Mitochondrial physiology within myelinated axons in health and disease : an energetic interplay between counterparts

Gerben Van Hameren

THÈSE POUR OBTENIR LE GRADE DE DOCTEUR DE L'UNIVERSITÉ DE MONTPELLIER

En Biologie Santé

École doctorale CBS2

Institut des Neurosciences de Montpellier

MITOCHONDRIAL PHYSIOLOGY WITHIN MYELINATED AXONS IN HEALTH AND DISEASE

AN ENERGETIC INTERPLAY BETWEEN COUNTERPARTS

Présentée par Gerben van Hameren
Le 23 Novembre 2018

Sous la direction de Dr. Nicolas Tricaud

Devant le jury composé de

Prof. Pascale Belenguer, Centre de Recherches sur la Cognition Animale Toulouse	Professeur d'université
Dr. Guy Lenaers, Mitochondrial Medicine Research Centre Angers	Directeur de recherche
Dr. Don Mahad, University of Edinburgh	Senior clinical lecturer

Invité

Dr. Marie-Luce Vignais, Institute for Regenerative Medicine & Biotherapy, Montpellier	Chargé de recherche

UNIVERSITÉ DE MONTPELLIER

Table of contents

List of abbreviations

AAV	Adeno-associated virus
AD	Alzheimer's Disease
AID	Activity-regulated Inhibitors of Death
AIS	Axon Initial Segment
ALS	Amyotrophic Lateral Sclerosis
Ang II	Angiotensin II
AnkG	Ankyrin G
ANT	Adenine Nucleotide Translocase
AP-1	Activating Protein-1
ATP	Adenosine TriPhosphate
CaM	Calmodulin
cAMP	cyclic AMP
CARS	Coherent Anti-stokes Raman Scattering
CMT	Charcot-Marie-Tooth
CNS	Central Nervous System
C/EBP	CCAAT-Enhancer-Binding Proteins
CFP	Cyan Fluorescent Protein
CoQ	Coenzyme Q
cpEGFP	Circularly permutated Endogenous Green Fluorescent Protein
dATP	deoxyadenosine triphosphate
DOA	Dominant Optic Atrophy
DRP1	Dynalin-Related Protein 1
ER	Endoplasmic Reticulum
ETC	Electron Transport Chain
Fabp7	Fatty acid binding protein 7
$FADH_2$	Flavin Adenine Dinucleotide
FEZ1	Fasciculation and elongation protein-ζ1
FIS1	Mitochondrial Fission Protein 1
FMN	Flavin Mononucleotide
FRET	Fluorescence Resonance Energy Transfer
FtMt	Mitochondrial Ferritin
GLUT1	Glucose Transporter 1
GPx	Glutathione Peroxidase
H_2O_2	Hydrogen Peroxide
HNE	4-Hydroxynonenal
HS	Heparan sulfate
IL-2	Interleukin-2
IP3R	Inositol 1,4,5-trisphosphate Receptor
ISCs	Iron-Sulfur Clusters
IT	Intrathecal
ITR	Inverted Terminal Repeats
JXP	Juxtaparanodes
KGDH	α-Ketoglutarate Dehydrogenase
KHC	Kinesin Heavy Chain
KIF	Kinesin superfamily protein
LOOH	Hydroperoxides

LPS	Lipopolysaccharide
MAM	Mitochondrial Associated Membranes
MBP	Myelin Basic Protein
MCT	Monocarboxylate Transporter
MCU	Mitochondrial Ca^{2+} Uniporter
MDA	Malondialdehyde
MDV	Mitochondria-Derived Vesicle
MEF2	Myocyte Enhancer Factor 2
MFF	Mitochondrial Fission Factor
MFN2	Mitofusin2
Miro	mitochondrial rho
Mn	manganese
mRNAs	messenger Ribonucleic Acids
MS	Multiple Sclerosis
mSC	myelinating Schwann Cell
mtDNA	mitochondrial Deoxyribonucleic Acid
NAD^+/NADH	Nicotinamide Adenine Dinucleotide
NCLX	NCX transporter
NCX	Na^+-Ca^{2+} exchanger
NF-κB	kappa-light-chain-enhancer of activated B cells
NMJ	Neuromuscular Junction
NO•	Nitric Oxide
NPC	Neuronal Progenetor Cell
NRF	Nuclear Respiratory Factor
NRG	Neuregulin-1
NSC	Neuronal Stem Cell
$O_2^{\bullet-}$	Superoxide anion
OH•	Hydroxyl Radical
$ONOO^-$	Peroxynitrite
OPA1	Optic Atrophy-1
ORF	Open Reading Frame
Orp1	Oxidant Receptor Peroxidase 1
PD	Parkinson's disease
PGC1	PPARγ coactivator-1
PKC	Protein Kinase C
PKM1/2	Pyruvate Kinase isozyme M1/M2
PLP	Proteolipid Protein
PMCA	Plasma Membrane Ca^{2+}-ATPases
PNJ	Paranodal Axoglial Junctions
PNP	Paranode-Node-Paranode
PNS	Peripheral Nervous System
PPAR	Peroxisome Proliferator-Activated Receptor
PT	Permeability Transition
RANBP2	RAN-Binding Protein 2
REEP1	Receptor Expression Enhancing Protein 1
RET	Reverse Electron Transport
RLR	RIG-I-like Receptor
roGFP	Redox sensitive Green Fluorescent Protein
ROOH	Hydroperoxide
ROS	Reactive Oxygen Species

SC	Schwann Cell
SCP	Schwann Cell Progenitor
SERCA	Ca^{2+}-ATPase
SOD	Superoxide Dismutase
SR	Sarcoplasmic Reticulum
SVZ	Subventricular Zone
rRNAs	ribosomal Ribonucleic Acids
RyR	Ryanodine Receptors
TCA	Tricarboxylic Acid
TLR	Toll-like Receptor
tRNAs	transfer Ribonucleic Acids
TRPV	Transient Receptor Potential
Trx	Thioredoxin
Ub	Ubiquitin
UPRmt	Unfolded Protein Response of mitochondrial proteins
UPS	Ubiquitin-Proteasome System
VDAC	Voltage-Dependent Anion Channel
VDCC	Voltage-Dependent Ca^{2+} Channel
YFP	Yellow Fluorescent Protein
ωas	anti-Stokes photon
ωp	pump photon
ωs	Stokes photon

Prologue

The human nervous system is the biological system that transmits signals between the brain and the rest of the body. It can be subdivided in two parts: the central nervous system (CNS), consisting of the brain and the spinal cord, and the peripheral nervous system (PNS). The PNS connects the brain and spinal cord with the organs and the limbs of the periphery. The neurons of the PNS, which cell bodies are located in the spinal cord and in dorsal root ganglia, cover a large topographical area of the body ranging from the ganglia, located just outside the CNS, to nerve endings in the farthest extremities of the body. To send signals from the CNS to the periphery, the PNS neurons depolarize and then conduct action potentials through their axons, which can be extremely long. Neuronal axons in the PNS have close functional interactions with the surrounding Schwann Cells (SCs), which support long-term axonal survival and peripheral nerve function through the myelin sheath. On the opposite, defects in SCs can cause axonal degeneration. SCs can be present in the PNS both in a myelinating and non-myelinating state. Myelinating SCs produce myelin, which is folded around the axon and is necessary for high nerve conduction velocity along axons. The axon is not myelinated in the space between two SCs and these unmyelinated areas, the nodes of Ranvier, are rich in ion channels, allowing action potentials to be regenerated.

When the PNS becomes damaged or does not function in a healthy way, this may lead to the development of peripheral neuropathies, such as hereditary Charcot-Marie-Tooth (CMT) diseases. In many patients that suffer from peripheral neuropathies, the interaction between neuronal axons and SCs is impaired, which often manifests as impaired motor or sensory functions. Several peripheral neuropathies indicate that mitochondrial physiology is critical for the maintenance of the PNS. Dysfunctional mitochondria are also involved in CNS diseases (such as Parkinson's disease, Multiple Sclerosis and Alzheimer's disease).

Mitochondria are organelles that are structured as two lipidic layers of discrete membranes and compartments in which proteins reside. These organelles are present in all human cells (except red blood cells), including neurons, and fulfill several functions that are essential for the cell to function in a healthy way, such as production of adenosine triphosphate (ATP) (the most-used energy form within cells), production of reactive oxygen species (ROS), and calcium storage. Mitochondrial function relies on a multitude of factors, including the structure of the mitochondrion, the composition of its membranes and the metabolites that are present in the cytosol. The vast majority of proteins (~99%) that define the mitochondrial structure and function are derived from transcription in the nucleus, translated in the cytosol and translocated into the mitochondria. Only a small proportion of proteins are derived from its own genetic material, the mitochondrial DNA (mtDNA). Most of the mtDNA genes code for proteins that are involved in the production of ATP and ROS.

ATP is produced via three metabolic pathways that use glucose or other metabolites: glycolysis in the cytosol, the tricarboxylic acid (TCA) cycle and the electron transport chain (ETC) in mitochondria. In short, glycolysis transforms glucose towards pyruvate, which can enter mitochondria and is used for the production of NADH and $FADH_2$ via a chain of enzymatic reactions. NADH and $FADH_2$ are used in the ETC as a source of electrons. These electrons are transferred from complex to complex within the mitochondrial inner membrane, while protons are exported in the intermembrane space to create a proton gradient towards the mitochondrial matrix. These protons re-enter the inner matrix of mitochondria via ATP synthase and this drives the ATP synthase to produce ATP from ADP and free phosphate.

The electrons that pass the ETC during the production of ATP may leak back into the inner matrix, and there it will reduce free oxygen to form ROS. ROS are mostly known for their role in DNA damage, protein oxidation and the oxidation of lipids. These are damaging processes, so an excess of ROS are considered toxic. However, ROS are not only damaging. They can regulate a whole range of cellular responses and therefore their role as a signaling molecule is more and more acknowledged. For example, ROS play important roles in immune responses, axonal regeneration and neurogenesis. Since mitochondria are central players in cellular function and viability, their involvement in many diseases, including peripheral neuropathies, is not surprising. Luckily, cells are equipped with competent antioxidant systems that can detoxify the cell by reducing the different types of ROS. Superoxide Dismutase (SOD), which is highly expressed in mitochondria, is an enzyme that reduces superoxide, which is a highly reactive type of ROS, to hydrogen peroxide (H_2O_2). Hydrogen peroxide is less reactive, hence it is less damaging, but it can also diffuse longer distances and oxidize cellular components more distally. Glutathione Peroxidase and catalase are the antioxidant enzymes that can reduce hydrogen peroxide further to water and dioxygen.

The shape of mitochondria is correlated with its function. Mitochondria are able to merge with other mitochondria, a process which is called mitochondrial fusion, resulting in larger mitochondria. This fusion process is correlated with a higher production of ATP. The opposite process, mitochondrial fission is also possible, leading to the presence of multiple smaller mitochondria. Besides changes in mitochondrial shape, also changes in mitochondrial position are important in defining mitochondrial function. They can bind to the cellular cytoskeleton and move towards regions where the need for energy is high so that they can replenish that area with ATP. Continuous depolarization and repolarization requires ATP and subsequently, the production of ATP in the node of Ranvier is crucial for repeated regeneration of action potentials in this area. Nonetheless, physiology and function of nodal mitochondria are still controversial. Besides, the method to recruit metabolites for mitochondria to produce ATP is not established. In the CNS, lactate may be delivered by astrocytes and oligodendrocytes, in a system that was called the lactate shuttle. However, such a transport has never been demonstrated in the PNS and the mechanism of lactate production by Schwann cells is unknown, since most cells use pyruvate for oxidative phosphorylation instead of lactate production.

In this PhD thesis, I will investigate what the role of Schwann cells is in mitochondrial metabolism in the axon and how Schwann cells can produce such amount of lactate to transport to the axon. Also how lactate shortage will influence neuronal function is studied. Then I will explore how a mutation in the mitofusin2 (MFN2) gene, a model for CMT2A disease, can cause neuronal deficits. For this, we looked how the endoplasmic reticulum (ER) and mitochondria are affected by this mutation. Finally, I focus on mitochondrial physiology and find out how mitochondrial production of ATP and ROS is influenced by a range of healthy and neuropathic stimuli, such as action potential firing, spatial localization and demyelination.

During this project I used *in vivo* techniques, because mitochondrial physiology changes very fast when the system is altered. These techniques involve fluorescent probes delivered by viral vectors, multiphoton microscopy, live imaging. Coherent anti-Stokes Raman Scattering (CARS) imaging is used to visualize myelin, which allows for detection of internodes and nodes of Ranvier and for the assessment of the myelin sheath status. These techniques are used for experiments *in vivo* using either wildtype or transgenic mice.

By presenting my original data, I will show that cytosolic lactate and glucose, or mitochondrial ATP and H_2O_2 levels can be measured *in vivo* using viral probes. When we looked for the mechanism how glial cells can produce enough lactate to feed the neurons they nurture, we found that the Warburg effect, which has previously been described mostly in cancer cells, can exist in the nervous system as well. The Warburg effect is a shift in metabolism from oxidative phosphorylation to aerobic glycolysis. Indeed, we showed that deleting Pyruvate kinase M2 (PKM2), the enzyme required for aerobic glycolysis, specifically in myelinating SCs in mice, resulted in correct myelin maintenance, but an alteration of the functions and the maintenance of myelinated axons of peripheral nerves. The lack of Warburg effect in glial cells becomes apparent only when neurons fire action potentials and thus require energy. In the PKM2 mutant mice, cytosolic lactate decreases following periods of induced action potential firing, which shows that lactate is used by mitochondria without replenishment of cytosolic lactate via the lactate shuttle. However, whereas mitochondria in healthy neurons upregulate ATP production upon nerve stimulation, mitochondria in lactate deprived neurons do not.

Secondly, by examining the effect of the $MFN2^{R94Q}$ mutation on neurons, I found that this mutation causes locomotor defects and neurite degeneration in motoneurons specifically. This phenotype correlates with increased ER stress and a decreased contact area between the ER and mitochondria, abnormal mitochondria morphology and an impaired transport of mitochondria through axons.

Then to investigate further the effects of nerve activity on axonal mitochondria physiology, I show that besides ATP, H_2O_2 levels increase as well when nerves are firing action potentials and energy need is higher. However, the dynamics of ATP is not the same as H_2O_2. Also, mitochondria are intrinsically more metabolically active in nodes of Ranvier than in internodes. Then, I will show how mitochondrial physiology changes in a couple of neuropathology models: the $MFN2^{R94Q}$ mutation to model CMT2A and a demyelination model. In both pathologies, a decoupling between ATP production and H_2O_2 production was observed.

Finally, I will provide a protocol on how to introduce transgenes into sciatic nerve cells. This protocol provides a list of the necessary equipment as well as a description of the surgical techniques to isolate the sciatic nerve in adult mice and mouse pups. In the next step, I will show how to inject viral particles into the nerve via micropulses and the procedure of closing the wound.

In conclusion, I will discuss these results in a larger context and create model on axon metabolism and axonal mitochondria physiology in normal and diseased conditions. I will also propose some perspectives for neuropathies and how mitochondria could be a therapeutic target.

All non-referenced figures are personally-made figures using Servier medical art, adapted with Microsoft Powerpoint and Adobe Photoshop 7.0.

Part A
Introduction

Chapter 1) Physiology and functions of mitochondria

The cells that build up the human body are filled with cytosol in which multiple cell components called organelles fulfill their specific role to ensure healthy cell function. The nucleus contains most of the cellular DNA and the Golgi apparatus and ribosomes fulfill their roles in protein synthesis. In this first chapter, I will introduce the origin, morphology and functions of mitochondria. These organelles are present in almost all human cells, where they play a role in several cellular processes. Mitochondria are often described as "the powerhouse of the cell", because of their function as energy producer. For this, mitochondria contain specialized groups of proteins that produce ATP, which is the most used energy source of human cells. How these proteins produce energy is also discussed in this chapter.

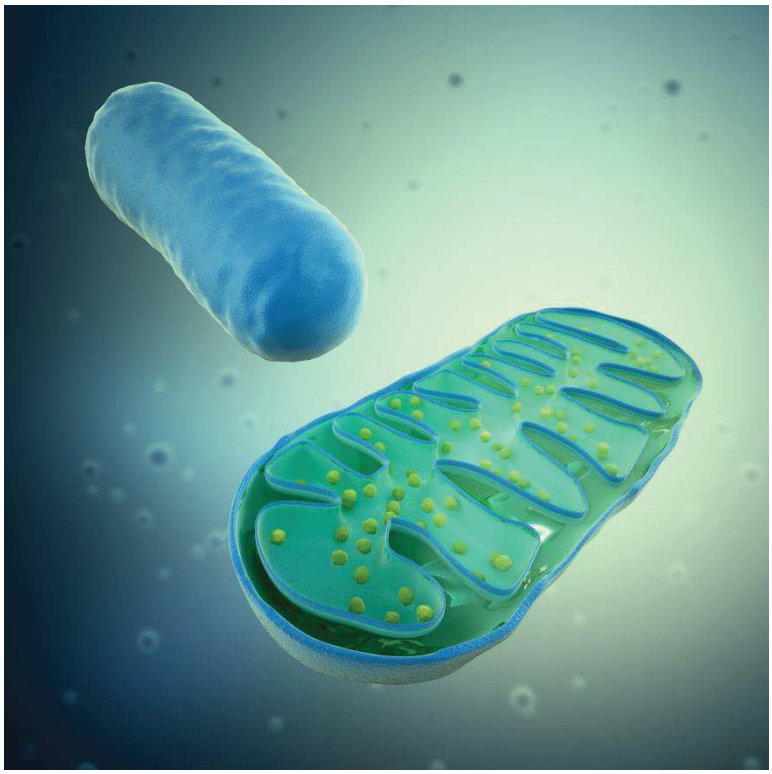

A mitochondrion

1.1 Mitochondrial biogenesis

According to the endosymbiont hypothesis, which is largely based on the genome that is contained within mitochondria, these organelles are of bacterial ancestry [1]. More specifically, the origin of mitochondria is the establishment of a phylum α-Proteobacteria as a symbiont into a host cell. Two main scenarios are hypothesized on how a phylum α-Proteobacteria has entered originally into a host cell. First, in the archezoan scenario, this host cell was a very primitive eukaryote, termed archezoan [2]. A second hypothesis, the symbiogenesis scenario, describes a single endosymbiotic event that involves the uptake of an α-Proteobacterium by a cell, resulting by the generation of mitochondria and as a consequence, the development of a nucleus and compartmentalization of this eukaryotic cell. An example of the symbiogenesis hypothesis is the hydrogen hypothesis [3]. The hydrogen hypothesis states that the origin of mitochondria is the result of symbiotic association between a strictly autotrophic archaebacterium, which is dependent on hydrogen, and an eubacterium that produces hydrogen as a byproduct of respiration through anaerobic heterotrophic metabolism. The host, the archaebacterim, depends on the hydrogen production of the symbiont, the eubacterium, which on its turn depends on the host's energy supply. A key point of symbiogenesis scenarios, including the hydrogen hypothesis, is that the complexity of the eukaryotic cell and its defining features emerged after the mitochondrial symbiosis, rather than before.

After this original genesis of a symbiont, these organelles have evolved, but its bacterial origin still has critical effects on mitochondrial function in humans. For example mitochondrial biogenesis results from the proliferation and growth of pre-existing mitochondria as the cell cannot produce mitochondria de novo. This is the reason why all our mitochondria are issued from the few mitochondria that were in our mother oocyte. Next to this autoreplication, mitochondrial biogenesis in human cells depends on fusion and fission. Mitochondria also contain their own DNA, called mitochondrial DNA (mtDNA), which code for 13 mitochondrial proteins [4]. Nonetheless, biogenesis of new mitochondria also involves the synthesis and import of 1000–1500 proteins that are encoded by the DNA in the nucleus [5]. A multitude of stimuli influences mitochondrial biogenesis, such as exercise, caloric restriction, low temperature, oxidative stress, cell division and renewal and differentiation. Because so many factors play a role, there is not only a large variety in numbers of mitochondria, but also in mitochondrial size and mass.

1.2 Lipids and proteins in the mitochondrial membranes

Mitochondria contain two bilipid layers that separate the compartments of the organelle [6]. The outer mitochondrial membrane separates the intermembrane space with the cytosol of the cell. The inner mitochondrial membrane separates the intermembrane space with the inner matrix of the mitochondrion (Fig. 1). The shape of the inner membrane involves many folds and notches, which are called cristae. The existence of two bilipid layers allows for the export of ions and other molecules from the inner matrix to the intermembrane space, which allow the formation of gradients, which is important for proper function of this organelle. During high respiratory activity, mitochondria have a small, condensed matrix volume, and the inner membrane is pulled away from the outer membrane, resulting in enlarged cristae, whereas when mitochondria are less active, they have a relatively large matrix volume with the inner membrane closely located to the outer membrane [7]. This shows that mitochondrial membranes actually have a really dynamic structure. The inner mitochondrial membrane is enriched in proteins and contains only about 20% of lipids, which is in contrast with the lipid-rich outer mitochondrial membrane [8]. Cardiolipin synthase, an enzyme located in the inner mitochondrial membrane, is involved in lipid biosynthesis by catalyzing the conversion of

phosphatidylglycerol to cardiolipin. Cardiolipin is an essential lipid in the mitochondrial membranes, because it regulates mitochondrial membrane permeability and protein import. Cardiolipin is also involved in mitochondrial fusion and fission, which is no surprise considering that the mitochondrial membranes have to fuse or separate during these two processes. Cardiolipin reacts with multiple mitochondrial membranes and stabilizes their confirmation. Next to cardiolipin, ceramide is another lipid that is strongly involved in mitochondrial function. In contrast with cardiolipin, which is mostly present in the inner mitochondrial membrane, ceramide is present mostly in the outer mitochondrial membrane. It enables the formation of protein-permeable channels through witch pro-apoptotic proteins can travel from the mitochondria into the cytosol. Therefore cardiolipin and ceramide are known regulators of mitochondrial shape and permeability.

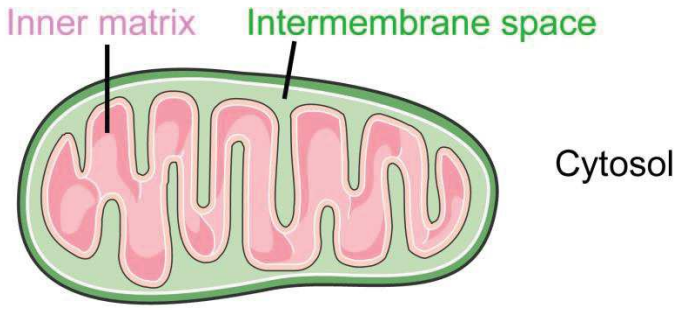

Figure 1 Structure of a mitochondrion. The inner matrix (pink) is separated from the intermembrane space (green) by a bilipid layer. A second bilipid layer separates the intermembrane space with the cytosol.

1.3 Fusion and fission

A part of mitochondrial biogenesis is the mechanism of mitochondrial fusion and fission (Fig. 2) [9]. Mitochondrial fusion and fission is a central mechanism that not only defines the mitochondrial number, but also the mitochondrial shape and size [10]. Even in other mitochondrial processes, including transport along axons and interactions with other organelles, such as the endoplasmic reticulum (ER), fusion and fission play a role. Mitochondrial dynamics involve the repartition of lipids, proteins or mtDNA within mitochondria and thereby these processes regulate the transport speed of these molecules through the cell [11].

Mitochondria adapt their shape continually through fusion, fission and motility in response to cellular stimuli, such as changes in energy demand [12]. Mitochondrial dynamics are essential to adapt mitochondria to different cellular functions, including maintaining cell viability or oppositely apoptosis. The fusion of mitochondria to form large mitochondria also increases the mitochondrial membrane potential and consequently increases the production of ATP [13]. In contrast, smaller mitochondria have a lower ATP production. Fission occurs when mitochondria become damaged, contain too high concentrations of deleterious components, such as mutated mtDNA [14], or endure too much cellular stress. This way the damaged or unviable parts of the mitochondria can be separated from the healthy parts of the mitochondria. The disposed mitochondria parts can be degraded in lysosomes through autophagy while the viable parts can continue to function. Reversely, mitochondrial fusion allows cells to repair defective mitochondria with healthy ones in order to regenerate the mitochondrial DNA (see paragraph 1.4).

Three dynamin-like GTPases are the central players in mitochondrial fusion. Mitofusin 1 and Mitofusin 2 (MFN1 and 2) are located in the outer membranes of mitochondria, while Optic Atrophy-1 (OPA1) is located in the inner membrane [10]. MFN1 and MFN2 interact with MFN proteins at the membranes of adjacent mitochondria. This interaction occurs via the formation of homo- and hetero-oligomers. Then, the outer membranes of the two mitochondria fuse. MFN1 interacts also with OPA1 for the fusion of the inner membranes of multiple mitochondria and the formation of cristae. Other proteins play a role in mitochondrial fission, which is the opposite process. Mitochondrial fission factor (MFF) and mitochondrial fission protein 1 (FIS1) are located at the outer membrane of mitochondria and act as ligands of dynalin-related protein 1 (DRP1), a cytoplasmic GTPase.

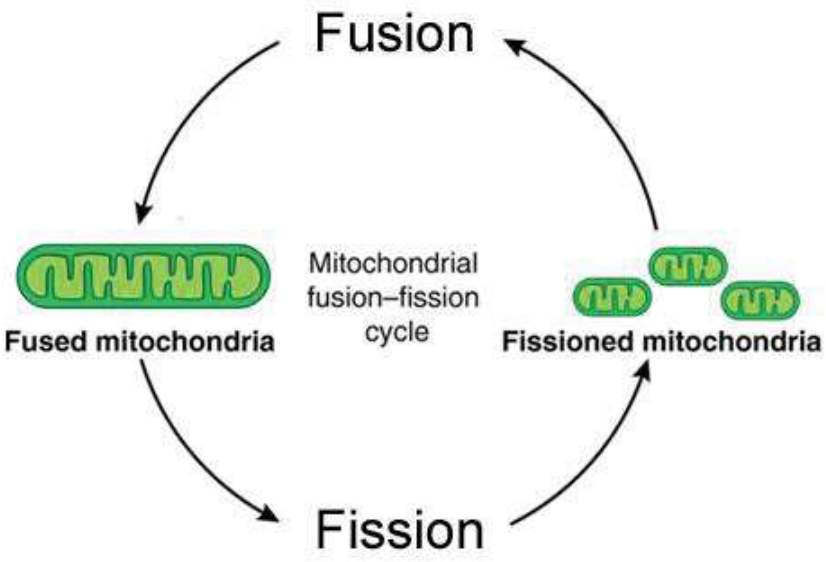

Figure 2: The process of mitochondrial fusion and fission [9]. Multiple small mitochondria can fuse to form one larger mitochondrion. The opposite reaction is mitochondrial fission, in which the large mitochondrion can separate to form multiple smaller mitochondria. These small mitochondria are more susceptible for degradation via mitophagy.

1.4 Mitochondrial DNA

A particular feature of mitochondria is the presence of mitochondrial DNA. mtDNA is circular shaped and consists of 16.5 kb. mtDNA contains 37 genes that code for 13 subunits of the ETC. In addition, mtDNA codes for 22 transfer ribonucleic acids (tRNAs) and 2 ribosomal RNAs (rRNAs) that are required for the translation of respiratory subunit messenger RNAs (mRNAs) within the mitochondrial matrix [15]. mtDNA is more susceptible to oxidative damage and as a consequence, mutations occur at a higher rate in mtDNA than in nuclear DNA. This high susceptibility is due to the high levels of ROS being generated by oxidative phosphorylation, lack of protective histones and a limited repair capacity for mtDNA damage. Intracellular ROS concentrations are correlated with changes in mtDNA copy number and the expression of mitochondrial respiratory genes. Increased oxidative stess during aging is as well associated with increased mtDNA copy number. Therefore, mitochondria require alternative protection methods to prevent accumulation of damaged mtDNA. One of the key protective measures is fusion and fission. Indeed, upon mitochondrial fusion, the mtDNA of each pre-existing mitochondrion is thought to recombine with each other [16]. This recombination of mtDNA allows healthy mtDNA to regenerate damaged mtDNA and thereby mitochondrial viability [17].

Although mtDNA contains a few genes that are important for mitochondrial function, most genes that code for proteins required for mitochondrial function are located in nuclear genome and these proteins are transported into mitochondria. Nuclear respiratory factors 1 and 2 (NRF1 and NRF2) are transcriptional regulators that act on nuclear DNA. There, it regulates transcription of subunits required for oxidative phosphorylation within mitochondria and genes that are involved in maintaining mtDNA copy number via mtDNA replication. NRF1 is a homodimer and binds to DNA to function as a positive regulator of gene transcription[14]. Many respiratory genes are regulated through NRF1 and NRF2, including complex I of the ETC, complex II, complex III and ATP synthase. In addition, NRF1 and 2 regulate proteins involved in mtDNA transcription and replication. Also, NFR1 and 2 are involved in regulating proteins that play important roles in the import of mitochondrial proteins into the organelle. Another important group of proteins that act as regulators of mitochondrial biogenesis is the PPARγ coactivator-1 (PGC1) family (PGC1a, PGC1b and PRC). This group of proteins acts mainly as coordinators of a multitude of transcription factors that are regulating the mitochondrial biogenesis process. Therefore, PGC1 proteins work in an indirect manner and they bind to other transcription factors, such as NRF1, NRF2 and PPARs to regulate their activity. This way, those transcription factors have an increased activity and can stimulate mitochondrial biogenesis.

The activity of transcription factors, including transcription factors that are involved in mitochondrial biogenesis, are influenced by ROS [14]. Human cells respond to defective respiratory function by increasing the expression of nuclear and mitochondrial genes. The upregulation of these genes is managed via an H_2O_2-dependent signaling pathway [12]. Treatment of mouse embryonic cells with H_2O_2 increases PGC1α and PGCβ mRNA levels [13]. PGC1α and PGC1β regulate gene expression of antioxidant genes such as catalase and superoxide dismutase. This shows that an interaction exists between mitochondrial biogenesis, ROS production and ROS defenses.

1.5 Mitochondrial functions in the cell

The main function of mitochondria is the production of ATP. The different components of the ETC have already been discussed shortly, but this system is actually the last phase in the production of ATP from metabolites. Glucose is the main energy source that is used by cells to produce ATP. Glucose is oxidized to carbon dioxide and water via glycolysis, the Kreb's cycle (also named the tricarboxylic acid (TCA) cycle), and the ETC. The latter two are referred to as oxidative phosphorylation. These are three synchronized pathways that involve a large range of enzymes and metabolic intermediates and result in the production of energy in the form of ATP [18]. The first pathway, glycolysis, is occurring in the cytosol and not in the mitochondria, but it is an important system in controlling mitochondrial metabolism.

1.5.1 Glycolysis

Glycolysis is the catabolism of glucose into pyruvate (Fig. 3) [19]. The formation of pyruvate from glucose also produces four ATP molecules, although two ATP molecules are used as well during this process, resulting in a net production of two ATP molecules. The produced pyruvate is being converted to lactate in anaerobic conditions, allowing the regeneration of nicotinamide adenine dinucleotide (NAD^+). Without NAD^+, glycolysis cannot continue further and glyceraldehyde3-phosphate is formed [18].

The function of glucose metabolism is to produce ATP and to provide carbon for reactions involving local activities [20]. In order for these pathways to be maintained, enough glucose needs to be present. Besides, there is a tight regulation of glycolysis via the presence of certain enzymes: hexokinase, phosphofructokinase and pyruvate kinase (PKM) [21]. Pyruvate kinase catalyzes the last step of glycolysis, converting phosphoenolpyruvate to pyruvate [22]. Several isoforms of pyruvate kinase exist, but the main two isoforms are PKM1 and PKM2. PKM2 is preferentially expressed by most types of cancer cells and it hypothesized that PKM2 promotes an alternative catalytic reaction that does not produce ATP, in contrast to the catalytic activity of PKM1 [23]. PKM2 is a known target of ROS for H_2O_2, diamide and hypoxia have all been shown to inactivate PKM2. In contrast, the reductant DTT restores PKM2 activity. In addition, the isoform PKM1 is not inhibited by oxidation. More specifically, Cys358 of PKM2 appeared to be especially susceptible for oxidation and Cys358 oxidation decreases the level of PKM2. As a response to oxidative stress, the mutated Cys358 induces PKM2 dissociation thus preventing its enzymatic activity. PKM2 inhibition results in the increase of NADPH production, which prevents the accumulation of intracellular ROS. In multiple pathological conditions that are characterized by mitochondrial dysfunction, mitochondrial ROS production is increased. In these same diseases, glycolysis is also enhanced while oxidative phosphorylation is impaired. This suggests that ROS is involved in glycolysis (dys)regulation [24].

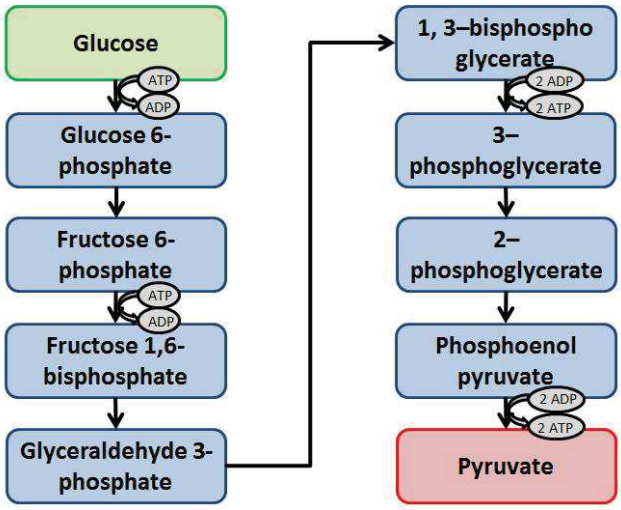

Figure 3: Schematic diagram of glycolysis

1.5.2 The Citric Acid Cycle

Under aerobic conditions, the pyruvate produced by glycolysis is used for oxidative decarboxylation, resulting in the production of acetyl-CoA (Fig. 4) [25]. In this reaction, pyruvate dehydrogenase is the driving enzyme. Acetyl-CoA binds to oxaloacetate and citrate synthase drives its conversion into citrate. This enzymatic reaction is the first step of the TCA cycle and oxidative phosphorylation. During the TCA cycle, three NADH molecules, and one 1,5-dihydro-flavin adenine dinucleotide ($FADH_2$) molecule are formed. These compounds serve as electron transporter into the complexes of the ETC. The electrons transferred to oxygen to form ROS by the ETC are actually originating from the NADH and $FADH_2$ that are formed during TCA cycle [18].

The TCA cycle consists of eight conversion steps [25]: The first step, the condensation step, has been mentioned above and involves the conversion of Acetyl-CoA to form citrate and is

catalyzed by citrate synthase. Then, citrate is converted to isocitrate by aconitase in a two-step conversion process. The third step involves the conversion of isocitrate to alpha-ketoglutarate by isocitrate dehydrogenase. This step is also the first step where NADH is produced as a cofactor, which is later used to drive the ETC. Step 4 is catalyzed by α-ketoglutarate dehydrogenase (KGDH). This enzyme generates succinyl-coA from α-ketoglutarate. Then, succinyl-coA is converted to succinate by succinic thiokinase, a reaction during which GDP is converted to GTP. The sixth step involves the succinate conversion into fumaric acid by dehydrogenase. During this conversion, $FADH_2$ is formed as well from FAD. $FADH_2$ is a second molecule that drives the ETC, next to NADH. In step 7, fumarate hydratase catalyses the hydration of the double C=C double bond of fumaric acid to form malate. Finally, malate is dehydrogenated to produce oxaloacetate by malate dehydrogenase. This is a second step where NADH is formed from NAD. The formed oxaloacetate reacts with acetyl-coA and forms citrate again, which is the first step of another round of the TCA cycle. The NADH and FADH2 molecules that are formed during this cycle are used by complexes of the ETC. Therefore, both glycolysis and the TCA cycle are important pathways in the production of NADH and $FADH_2$ that provide electron to the ETC.

Not only is the TCA cycle important for providing substrates for the ETC, it appears that intermediates of the TCA cycle can modulate the concentration of mitochondrial ROS [26]. The central intermediate in this TCA-cycle mediated ROS homeostasis is α-ketoglutarate and the enzyme KGDH (Fig. 4). Indeed α-ketoglutarate plays a role in ROS scavenging while reducing NADH production and decreasing the activity of KGDH allows ketoglutarate increase and drop ROS levels [26]. KGDH possesses a sensor function of oxidative stress as its oxidation leads to inactivation of its enzymatic activity. Actually, a reduced KGDH activity is reported in many disorders. For example, expression of mitochondrial KGDH is reduced in demyelinated axons [27]. Supposedly, the decreased KGDH activity is an adaptive mechanism in an effort to detoxify the cell of ROS. Nevertheless, the cell's ATP production is also impaired, so in healthy conditions the production of energy is always a compromise with the production of toxic ROS.

Metabolism is affected by oxidative stress, since excessive oxidation can cause inactivation of enzymes that are involved in glycolysis, TCA cycle and the ETC, which decreases cell viability [28]. However, metabolism has evolved to adapt to conditions of high oxidative stress. These adaptive mechanisms are often independent from transcription, but instead rely on thiol-based switches of enzymes, which change enzymatic activity fast. As a consequence, metabolic changes can occur relatively fast as well. Indeed, metabolic changes have been detected within minutes of oxidative stress.

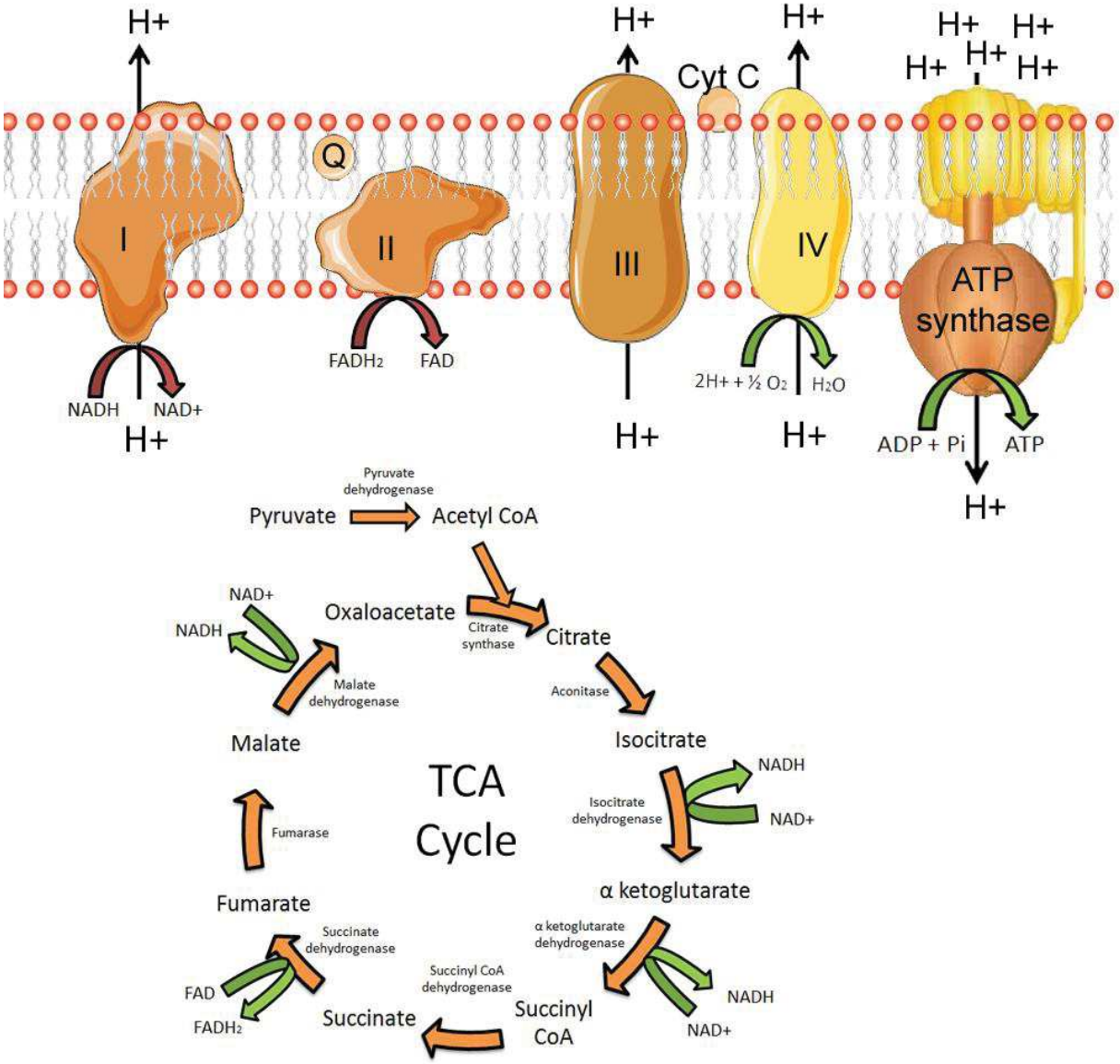

Figure 4: A schematic overview of oxidative phosphorylation. Pyruvate, produced by glycolysis, is transformed by Acetyl-CoA. Then, in a series of enzymatic reactions that form the TCA cycle, NADH and FADH is formed. These 2 compounds drive the electron transport chain to pump protons across the mitochondrial inner membrane. The resulting proton gradient is used to produce ATP.

1.5.3 Warburg metabolism

Most cells use both glycolysis and the citric acid cycle for the production of ATP. Nonetheless, when cells are in hypoxic conditions, not all pyruvate that is produced via glycolysis is being used by mitochondria [29]. Instead, a portion of the pyruvate is enzymatically transformed into lactate. In this condition, cells rely predominantly on glycolysis for the production of ATP. The hypoxia-induced transition of pyruvate production towards lactate is regulated by lactate dehydrogenase (LDH), which is the enzyme that converts pyruvate to lactate [30].

In the 1920s, the phenomenon of cells depending on glycolysis as the main source of ATP in aerobic conditions has first been described by Otto Warburg [31]. This aerobic glycolysis, also called Warburg metabolism, has first been demonstrated in several tumor types, including colorectal cancer, breast, lung and glioblastoma [32]. Several theories exist why switching to

Warburg metabolism is beneficial for tumor cells [33]. Warburg metabolism is potentially an adaptation mechanism to match the increased biosynthetic needs that are the result of uncontrolled proliferation [34]. Increased glucose consumption by the tumor cell and hence increased aerobic glycolysis is then a carbon source for the generation of more nucleotides, lipids and proteins. A second advantage of Warburg metabolism for tumor cells is the acidification of the microenvironment due to elevated glucose consumption and increased lactate secretion [35]. This decreased pH level in the tumor's microenvironment increases the invasiveness. Overall, the potential to switch to Warburg metabolism is an important feature of a cell and it is essential to understand how cell metabolism is regulated both in physiological conditions and in cancer.

An example of a known regulator of Warburg metabolism is pyruvate kinase. Tumor cells have been shown to express exclusively PKM2 [36]. Moreover, it has been demonstrated that a switch in splice isoform from PKM1 towards PKM2 is required for the shift in cellular metabolism to Warburg metabolism [37]. However, the exact mechanism how PKM2 regulates the transition towards Warburg metabolism has yet to be established.

1.5.4 Electron Transport Chain complexes

The inner mitochondrial membrane contains a set of proteins that cross this bilipidic layer. An important group of proteins located in the inner membrane includes the complexes of the ETC [38]. The role of the ETC in oxidative phosphorylation is to transfer electrons from electron donors to electron acceptors and the simultaneous transport of protons across the inner membrane in order to load the mitochondrial matrix with protons. These protons are then used as the driving force to produce ATP by ATP synthase. The ETC consists of 5 large protein complexes. These complexes are numbered as complex I (NADH dehydrogenase (ubiquinone), 45 protein subunits), complex II (succinate dehydrogenase, 4 protein subunits), complex III (ubiquinol-cytochrome C reductase, 10 protein subunits), complex IV (cytochrome C oxidase, 19 protein subunits), and complex V (ATP synthase, 19 protein subunits). It has been shown that these complexes are integrated in the inner mitochondrial membrane freely, but there is increasing evidence that the complexes can form respiratory chain supercomplexes [39]. Supercomplexes of two or even three respiratory chain complexes have been proposed, such as a complex III – complex IV supercomplex. Similar interactions include Complex I-III supercomplexes and further assembled interactions such as Complex I-III-IV [40]. The rate of supercomplex formation is different between different cell types, even between different cell types in the same tissue. It has been shown that neurons and astrocytes in the brain organize their mitochondrial respiratory chains differently, with a different proportion of respiratory chain complexes present freely or part of supercomplexes [41]. In astrocytes, complex I is assembled less frequently into supercomplexes resulting in more free complex I. In contrast, neuronal mitochondria contain less free complex I, since it is more frequently assembled into supercomplexes. An abundance of free complex I is caused by a low amount of complex III, which limits the amount of complex I that can be incorporated into supercomplexes.

ATP synthase is a multisubunit complex that functions in the last step of the ETC. The structure of ATP-synthase resembles a mushroom and the globular protein complex that forms the "head" of the mushroom contains its catalytic sites. This subunit is called the F1 domain [42]. A large difference in proton concentration across the inner membrane of mitochondria creates a membrane potential, also called the proton-motive force. ATP synthase uses this force to drive the conversion of ADP and phosphate into ATP [43].

The complexes of the ETC fulfill the main function of mitochondria: the synthesis of ATP. Besides, the activity of these complexes results in the production of ROS. The production of ROS is a central aspect of this dissertation hence their production by the ETC complexes will be discussed in detail in the next chapter.

1.5.5 Iron storage

Iron is used as a catalytic co-factor by proteins throughout the cell in various critical processes. It also acts as an epigenetic regulator as some promoters contain iron response elements [44]. A main source of cellular iron are mitochondria [45]. Synthesis of iron-sulfur clusters (ISCs) occurs within the matrix of mitochondria. Fe^{2+} is donated by frataxin to a scaffold protein. Sulfur, derived from cysteine via Nfs1/ISD11 complex-mediated desulfuration, also binds to the same scaffold protein. The resulting scaffold protein with Fe^{2+} and sulfur is the completed ISC. Then, the ISC is exported from mitochondria to the cytosol, although the exact export mechanism is still poorly understood. Possibly, the ATP binding cassette transporter Abcb7 enables the export of ISCs or ISC intermediates. Since ISCs are not stable, chaperones are required to export ISCs into the cytosol and protect them from degradation. However, ISCs have functions within mitochondria as well, for example in ETC complexes.

A particular mechanism in which ISCs are important is the production of heme, which is a compound required for the catalysis of several enzymatic activities such as a "storage" for electrons during electron transfer or redox chemistry. In addition, heme can store O_2 and O_2 oxidizing equivalents in the iron side chains for further selective oxidation of substrates [46]. In the first step of heme synthesis, aminolevulinic acid is produced from glycine and succinyl-CoA in the mitochondrial matrix [47]. ALAS2, an enzyme catalyzing this reaction, contains an iron response element and therefore the concentration of ALAS2 protein increases when iron is abundant. Aminolevulinic acid is transported into the cytosol, where it is metabolized into coproporphyrinogen III. Coproporphyrinogen III is imported back into the mitochondrial intermembrane space and converted into protoporphyrinogen IX, which is then transported into the mitochondrial inner matrix by the ATP binding cassette transporter Abcb6. In the inner matrix, protoporphyrin IX is then formed and protoporphyrin IX binds to Fe^{2+}, a reaction catalyzed by ferrochelatase. Next to the iron response elements of ALAS2, iron can influence heme synthesis via ISCs, because ferrochelatase needs ISCs for its stability. When ISC synthesis is impaired, this will lead to unstable ferrochelatase, which will result in incomplete heme synthesis [47].

Since mitochondria produce ROS via oxidative phosphorylation and import Fe^{2+} to be used in ISC and heme synthesis, this creates a particular situation regarding ROS homeostasis. Indeed the imported Fe^{2+} stimulates Fenton reactions (see Chapter 2), which amplify the production of ROS. To avoid this, mitochondria can either immediately use Fe^{2+} in synthetic pathways or store it in a storage protein complex consisting of oligomerized mitochondrial ferritin (FtMt) [45]. FtMt forms ferroxidase centers that oxidize Fe^{2+} to Fe^{3+}, which is less redox active. Importantly, the expression of the FtMt gene does not contain an iron response element, making it independent from iron concentrations. Overexpression of FtMt lowers ROS production and enhances cell viability, showing that FtMt has antioxidant features via inhibition of the Fenton reaction.

1.5.6 Calcium uptake

Calcium is essential for the respiratory function of mitochondria [48]. Indeed, Ca^{2+} has a stimulating effect on oxidative phosphorylation as it activates pyruvate dehydrogenase, isocitrate dehydrogenase, and KDGH [49], as well as stimulation of the ATP synthase [50], α-

glycerophosphate dehydrogenase [51], and the adenine nucleotide translocase (ANT) [52]. Mitochondria also participate to the regulation of intracellular calcium levels. Intracellular calcium concentrations can rise rapidly and mitochondria participate to the removal of Ca^{2+} from the cytosol. Alternatively, cytoplasmic Ca^{2+} can enter the sarcoplasmic reticulum or ER via its Ca^{2+}-ATPase (SERCA) and the sarcolemmal Na^{+}-Ca^{2+} exchanger (NCX) [53]. Cytoplasmic Ca^{2+} enters mitochondria passively via voltage-dependent anion channels (VDACs) and the mitochondrial Ca^{2+} uniporter (MCU). However, most of the mitochondrial calcium actually originates from the ER, which contains a much higher concentration of calcium. Calcium can be exchanged between mitochondria and the ER via the connection between these two organelles: mitochondrial associated membranes (MAM). The MAM is a domain of the ER that forms close contacts with mitochondria, where lipids are transferred from the ER to mitochondria next to the exchange of calcium [54]. The contacts between ER and mitochondria are dynamic and ER tubules can form contact areas ranging from 10% of the mitochondrial surface to a complete enveloping of the mitochondrion [55]. Under physiological conditions, Ca^{2+} influx into mitochondria is relatively low and stable. When cytoplasmic Ca^{2+} becomes too high though, the flux of Ca^{2+} into mitochondria increases. When this influx of Ca^{2+} becomes too high, the membrane potential of mitochondria is dissipated, resulting in the inhibition of further Ca^{2+} influx. In neurons, once intra-axonal homeostatic capability is exceeded, mitochondria are confronted with high Ca^{2+} levels, which triggers the mitochondrial influx of Ca^{2+} [56]. The mitochondrial NCX transporter (NCLX) enables the reverse transport of Ca^{2+} from the mitochondrial matrix into the cytosol. NCLX is a cotransporter and exports Ca^{2+} while importing sodium. Next to NCLX, the permeability transition (PT) pore is a route for Ca^{2+} to exit mitochondria, when the pore is open. The PT pore is an assembly of preexisting proteins within the mitochondrial inner and outer membrane. It has Ca^{2+} binding sites on the matrix side, which could regulate PT pore opening [57].

The uptake and release of calcium by mitochondria is important for neuronal function, because many cellular processes respond to the concentration of calcium within the cytosol. The processing of calcium in the cytoplasm is performed by sensor proteins that can bind to Ca^{2+}, which results in a reversible conformation change [58]. For example, the release of neurotransmitters by healthy neurons is dependent on calcium levels in the cell. Upon depolarization, voltage-gated calcium channels open and calcium enters at the axonal terminal. There, Ca^{2+} promotes fusion of synaptic vesicles with the presynaptic plasma membrane via acting on proteins of the SNARE superfamily. The fusion of synaptic vesicles and the plasma membrane results in a release of the vesicles' content, for example neurotransmitters, into the synaptic cleft.

1.5.7 Apoptosis

Finally mitochondria are also essential to trigger programmed cell death [56]. Release of cytochrome C from mitochondria regulates the assembly of caspase molecules and these caspases induce the cell degradation process. The exact export route of cytochrome C is not known, but its release is regulated by multiple proteins, such as proteins of the Bcl-2 family and Bax family [59]. Bcl-2 proteins block the release of cytochrome C and hence are anti-apoptotic. On the other hand, insertion of Bax proteins into the mitochondrial membrane stimulates cytochrome C release and promotes apoptosis.

Another regulator of cytochrome C release is opening of the PT pore. However, cytochrome C does not exit through the PT pore, and the way how the PT pore stimulates cytochrome C release is still unknown. The PT pore is triggered by high concentrations of Ca^{2+} within the

mitochondrial matrix and several other stimuli, including ROS and the depletion of ATP [48]. PT pore opening is accompanied by a burst of ROS production. This spike of ROS opens more PT pores, so an autoamplification process is induced. This burst of ROS may be the cause of cytochrome C release via the oxidation of cardiolipin. In addition to the release of mitochondrial Ca^{2+} into the cytosol through PT pores, it has been shown that cytochrome C binds to ER inositol 1,4,5-trisphosphate receptor (IP3R). This binding triggers the release of Ca^{2+} from the ER, so the concentration of Ca^{2+} into the cytosol increases even further. Overload of Ca^{2+} is the initial cellular trigger of the apoptotic cascade. The close proximity between the ER and mitochondria enables this cross-talk via cytochrome C.

1.6 Conclusion

So Mitochondria are highly dynamic organelles, since they are able to fuse with other mitochondria (mitochondrial fusion), split into two or more smaller mitochondria (fission), and migrate through cells by following the cytoskeleton. The shape and location of a specific mitochondrion define its functionality. In textbooks mitochondria are often referred to as "the powerhouse of the cell". Even though mitochondria indeed fulfill an important role in energy production, since oxidative phosphorylation produces much more ATP than cytosolic glycolysis, limiting the function of mitochondria to just being a battery is too reductive. After all, mitochondria fulfill an important role in iron storage, calcium homeostasis and regulation of apoptosis as well. In addition, mitochondria produce reactive oxygen species, which will be the topic of chapter 2.

Chapter 2) Reactive oxygen species

In chapter 1, the production of ATP by the electron transport chain has been presented. This process of proton transport coincides with the transport of electrons from complex to complex. Most of this electron transport results in the formation of water, but part of these electrons leak back into the mitochondrial matrix, where it oxidizes oxygen. Therefore, the electron transport chain produces reactive oxygen species (ROS) next to ATP. ROS can be present in different forms and these different forms have distinct features, although all of them can cause damage to the cell.

However, what is the exact mechanism how the transport of electrons gives rise to ROS? Besides, is ROS only produced by mitochondria or do other ROS sources exist? Furthermore, how do ROS interact with other molecules to cause damage?

In this chapter, we will introduce the different types of ROS and how they are produced. Then, the damaging effects of ROS will be described and how antioxidants can prevent this damage. Finally, the role of ROS as signaling molecules will be discussed.

Animation of ROS induced DNA damage

2.1 The different types of ROS

ROS are chemically reactive molecules derived from the reduction of molecular oxygen. In human cells, ROS are generated as a byproduct of oxidative phosphorylation in mitochondria. The first step of ROS production is the reduction of molecular oxygen (O_2) to anion superoxide ($O_2^{\bullet-}$).

H_2O_2 is a non-radical oxidant present in virtually all aerobic organisms. H_2O_2 is formed from $O_2^{\bullet-}$ by Mn-containing SOD that catalyzes the following reaction:

$$2O_2^{\bullet-} + 2H^+ \rightarrow H_2O_2 + O_2$$

H_2O_2 is considerably less reactive than $O_2^{\bullet-}$ [60]. Therefore, H_2O_2 can diffuse from the inner matrix of mitochondria through the mitochondrial membranes into the cell's cytoplasm. H_2O_2 can even diffuse in such a far radius that it is able to interact with the cell's nucleus. H_2O_2 is scavenged to water by glutathione peroxidase-1 (GPx) to limit its harmful effects [61].

The generation of the highly reactive hydroxyl radical (OH•) is catalyzed by iron via the Fenton reaction. OH• is an extremely reactive type of ROS [62]. It immediately attracts electrons from nearby molecules, turning them into a radical, which will result in a cascade of ROS. The classical Fenton mechanism predicts that H_2O_2 is reduced at the iron centers of the electron transport chain, which generates free OH•.

$$Fe^{2+} + H_2O_2 \rightarrow Fe^{3+} + OH^- + OH\bullet$$

The Fe^{2+} can be regenerated though the interaction of Fe^{3+} with $O_2^{\bullet-}$.

$$Fe^{3+} + O_2^{\bullet-} \rightarrow Fe^{2+} + O_2$$

The combination of these two reactions is called the Haber-Weiss reaction. As most other types of ROS, formation of HO• occurs mainly within mitochondria [63]. The reason for this is that the precursors of OH•, i.e. $O_2^{\bullet-}$ and H_2O_2, are being produced within mitochondria as well. The catalysts for OH• formation, low molecular weight iron, is also abundant there.

Next to the classical enzymatic conversion of $O_2^{\bullet-}$ towards H_2O_2, $O_2^{\bullet-}$ can react with nitric oxide (NO•), which is produced enzymatically by nitric oxide synthase in the cytosol and can diffuse freely into the mitochondria [64] to form peroxynitrite ($ONOO^-$) [65;66]. $ONOO^-$ can be generated in the cytosol as well, but the primary location of $ONOO^-$ formation is mitochondria. An alternative route for $ONOO^-$ formation is the reaction of nitroxyl anion with O_2, where the nitroxyl anion formation in mitochondria is the result of NO• reduction by mitochondrial electron donors such as ubiquinol or cytochrome C [67]. There, it can react with its targets, which results in oxidation, nitration and nitrosation of mitochondrial components. Since mitochondria contain many targets for $ONOO^-$ oxidation or nitrisatiation, such as metalloproteins, thiolgroups, and CO_2, intramitochondrially formed $ONOO^-$ has a shorter half-life than its counterpart formed in the cytosol. Like oxidation by $O_2^{\bullet-}$ or H_2O_2, oxidation by $ONOO^-$ significantly affect mitochondrial homeostasis and physiology. $ONOO^-$ reacts with complexes of the ETC as well, but these reactions are not the same as reactions between the ETC and NO•. Whereas NO• favors the inhibition of cytochrome C oxidase, $ONOO^-$ mainly reacts to complexes I, II and ATP synthase [68]. $ONOO^-$ reacting with complex I leads to inactivation, depending at least partially on thiol oxidation and the formation of a snitrosothiol-derivative of the complex. Complex II inhibition is most likely dependent on the

thiol oxidation of the succinate dehydrogenase that is present in the dicarboxylate binding site. Moreover, $ONOO^-$ inactivates and nitrates ATP synthase, potentially by targeting the critical tyrosine of ATP synthase, which would account for the decrease in activity. $ONOO^-$ may also diffuse over the mitochondrial membranes into the cytosol, since its mean diffusion distance has been shown to be 3-4 μm, which is larger than the mean mitochondrial length being 3 μm in length and 0.6 μm in diameter. However, $ONOO^-$ undergoes reactions during this diffusion. Protonisation of $ONOO^-$ results in ONOOH, which can be scavenged by GPx.

2.2 Mitochondrial ROS production

The production of ROS starts in the mitochondrial electron transport chain via a leak of electrons, mainly from complex I and complex III (Fig. 5), that reduce O_2 to $O_2^{\bullet-}$. Complex I pumps protons from the inner matrix to the intermembrane space. This export of protons creates a proton gradient, which is used for ATP formation by ATP synthase. Complex I is the entry point into the respiratory chain for electrons from NADH generated during the TCA cycle [38]. It contains a Flavin mononucleotide (FMN) cofactor that accepts electrons from NADH and passes them through to a Coenzyme Q (CoQ) reduction site. In between, the electrons pass a chain of seven iron-sulfur clusters (ISCs). These ISCs are located in the hydrophilic arm of Complex I and are shielded from O_2. This means that O_2 enters complex I at the FMN and Coenzyme Q sites and that is where electrons can reduce this O_2. The isolated complex I produces $O_2^{\bullet-}$ when the FMN site is fully reduced. Therefore the proportion of the FMN that is fully reduced is an important factor for ROS production. On its turn the proportion of reduced FMN is dependent on the ration of $NADH/NAD^+$. When complex I is impaired or inhibited, electrons flow back into FMN and this will produce an increased level of $O_2^{\bullet-}$ production. In addition, when NADH accumulates due to extremely low energy demand, this will lead to an increased $O_2^{\bullet-}$ production. However, only small amounts of $O_2^{\bullet-}$ are produced in normally respiring mitochondria, because the TCA cycle is not much active and therefore $NADH/NAD^+$ ratio is relatively low. A second mechanism of $O_2^{\bullet-}$ formation in complex I exists, named reverse electron transport (RET). Instead of an increased $NADH/NAD^+$ ratio or a fully reduced FMN site, RET occurs when CoQ is reduced [69]. With a sufficient proton motive force, electrons will then flow back into complex I and will reduce NAD^+ to NADH at the FMN site. When the electron supply to the CoQ pool originates from succinate, α-glycerophosphate or fatty acid oxidation, instead of pyruvate oxidation in the TCA cycle, a lot of ROS is created through this RET process. This particular respiration occurs in macrophages in response to bacterial infections and in cardiac and neuronal cells after ischemic periods [70].

Mitochondrial complex II is also called succinate dehydrogenase. It plays a role both in the ETC and in the TCA cycle, where it catalyzes the conversion of succinate to fumarate (see Chapter 1). Complex II consists of four subunits, including one subunit that contains a chain of three ISCs [71]. Apart from complex I, complex II is the second entry point for electrons. Succinate oxidation generates FADH, which gives rise to two electrons that are transferred from the flavin site of complex II, through the ISCs towards CoQ, which is then reduced to ubiquinol. The contribution of complex II to ROS production in healthy conditions is controversial [72], although increasing evidence is provided for its role in pathologic conditions, such as cancer [73].

Like complex I, complex III pumps protons over the mitochondrial membrane (Fig. 5). Complex III works via two reduction steps involving ubiquinonic structures [60]. First, two electrons are transferred from CoQ ubiquinone towards two cytochrome C molecules [38].

Then, two electrons are used to reduce quinone to quinol. During those processes, electrons leak back into the inner matrix, thereby participating in the formation of $O_2^{\bullet-}$ (Fig. 5) [74]. In contrast with complex I, complex III has just a single ISC. Another difference with complex I is that $O_2^{\bullet-}$ produced by complex III is not only leaking back into the inner matrix, but also into the intermembrane space [75]. However, the maximal amount of ROS produced by complex III is negligible when compared to the amount of ROS that can be produced by complex I through RET [38].This means that when complex I is producing high amounts of $O_2\bullet^-$, such as, then the extra ROS produced by complex III becomes irrelevant.

Complex IV, also called cytochrome C oxidase, catalyzes the final step of the ETC. This complex contains 13 subunits, of which three catalytic subunits, and four metal centers: Cu_A, Cu_B, Fe_a and Fe_{a3} [76]. Complex IV accepts electrons from cytochrome C and transfers them to the Fe_a metal center. From there, these electrons are transferred to the bimetallic center Fe_{a3}/Cu_B, where molecular oxygen is converted to water. Next to this electron transfer, complex IV also contributes to the generation of the mitochondrial proton gradient. During each reduction of O_2 to water, eight protons are taken up from the mitochondrial matrix, of which four are being used for water formation [77]. The other four protons are being pumped across the inner mitochondrial membrane.

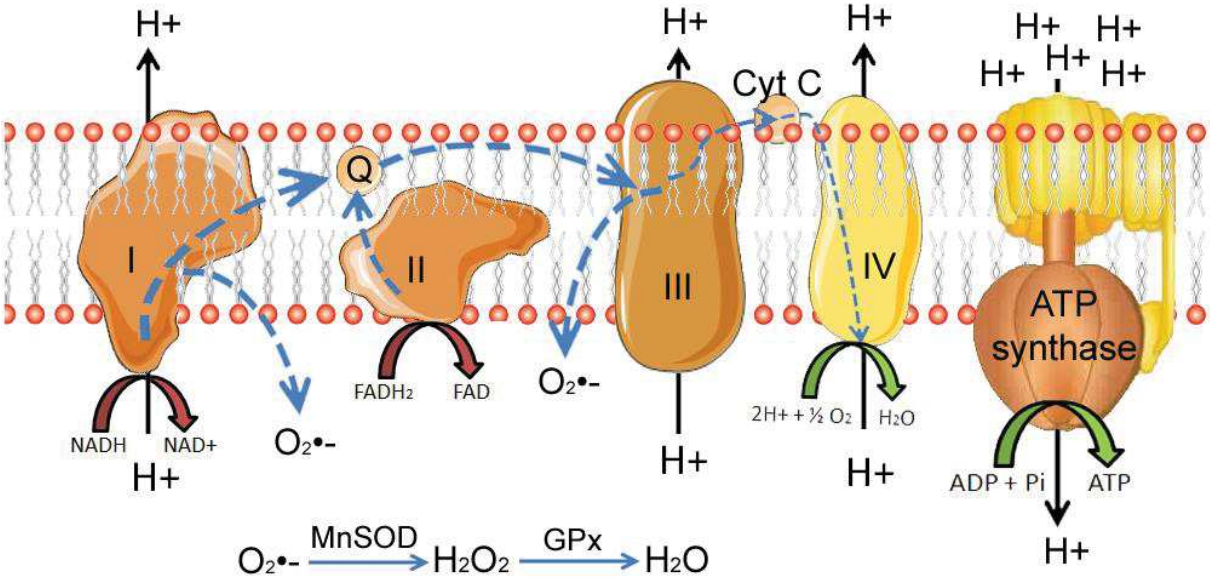

Figure 5: Schematic overview of the electron transport chain that depicts the sites of superoxide production. Protons are being translocated by complex I, III, and IV. In this process, free electrons are produced as well, which are delivered to coenzyme Q (Q), and further towards cytochrome C (Cyt C). Some electrons leak back into the inner matrix and those electrons reduce electrons to form superoxide. Superoxide can be enzymatically degraded towards H_2O_2 and further to H_2O.

Mitochondrial ROS production by the ETC is dependent on a multitude of stimuli. One of those stimuli is the concentration of a^{2+} within the cell. Indeed, cellular Ca^{2+} drives myocyte enhancer factor 2 (MEF2) expression through mitochondrial activation of caspase-3 [60], which on its turn increases the expression of NADH dehydrogenase, an essential complex I component. In addition, MEF2 also decreases the expression of antioxidant enzymes such as SOD and hydrogen peroxidase. The conformation of the ETC is another factor determining the amount of ROS that is produced in mitochondria. Indeed, when complex I is present freely, which is a situation that is more common in astrocytes than in neurons, ROS production is higher than when it is assembled into a supercomplex [41]. NADH-derived electrons are inefficiently transferred to ubiquinone by the free complex I, because the distance is larger. In addition, the low proportion of complex III in astrocyte mitochondria

inhibits the transfer of electrons to complex IV and deactivates complex I, because the ubiquinone pool is reduced.

2.3 NADPH oxidase

Although mitochondria are the main producers of ROS, this organelle is not the only origin of cellular ROS. NADPH oxidase is a plasma membrane bound enzymatic complex that can produce superoxide through the oxidation of NADPH [78]. While mitochondrial ROS is normally correlated with the production of ATP, ROS production is the main function of NADPH oxidase. In normal conditions, this enzyme is hardly active, but it is activated in particular conditions that require ROS production, such as the immune response mediated by neutrophils. Once the enzyme is activated, NADPH is oxidized to $NADPH^+$ and an electron is transferred to oxygen. This way, superoxide is produced to kill bacteria and fungi that are ingested inside the phagosomes. The activity of NADPH oxidase is strictly regulated and many intercellular signaling pathways are involved, but the strongest factor is the presence of Ca^{2+} in the cytosol, indicating that NADPH oxidase could also play a role in apoptosis and neurodegeneration [60].

NADPH oxidase activity and mitochondria can interact with each other [79]. For example, upon binding of Angiotensin II (AngII) on the AngII type 1 receptor, NADPH oxidase is activated through protein kinase C (PKC). Activated NADPH oxidase then produces ROS, which, among other effects, open mitochondrial K_{ATP} channels. The opening of these mitochondrial channels increases potassium influx into the mitochondria intermembrane space, swelling it and induces the production of mitochondrial ROS [80]. The interaction between NADPH oxidase and mitochondrial ROS can also work the other way around, making the pathway even more complex. Diazoxide, a mitoK_{ATP} channel activator, triggers the production of mitochondrial ROS [80], but ROS production by NADPH oxidase is also increased. As diazoxide does not directly affect NADPH oxidase activity, this suggests that production of mitochondrial ROS can influence NADPH oxidase activity. Inhibition of SOD2, which results in increased mitochondrial ROS levels, also increases NADPH oxidase activity and potentiate the effect of AngII [81]. In addition, increasing SOD2 levels decreased mitochondrial ROS production, which prevented AngII induced activity of NADPH oxidase. These results confirm that changes in mitochondrial ROS production affect the production of ROS by NADPH oxidase. Altogether, the activation of NADPH oxidases may increase the production of mitochondrial ROS and vice versa. This crosstalk between mitochondrial ROS and NADPH oxidases play an important role in the homeostasis of redox cell signaling. When ROS levels rise to excessive amounts due to overstimulation by AngII, high glucose, fat, or hypoxia for example, then a vicious cycle is triggered between mitochondrial ROS and NADPH oxidase resulting in more ROS production, which may contribute to the development of pathological conditions. Indeed, it has been shown that in some neurodegenerative diseases, such as Alzheimer's disease, Huntington's disease or Parkinson's disease, NADPH oxidase activity is increased [82] in addition to the production of mitochondrial ROS.

2.4 How ROS cause damage to DNA, proteins and lipids

ROS can damage cells in several of different ways. It can oxidize DNA inside the nucleus, but also proteins and lipids throughout the cell. DNA damage will trigger a general shutdown of RNA synthesis [83], although the expression of some genes may actually be increased [84].

2.4.1 DNA oxidation

The main components of DNA are the nucleobases that are held together by deoxyribose and phosphate groups. The four types of nucleobases, thymine, adenine, cytosine and guanine can be oxidized by ROS [85].

On thymidine, ROS oxidation adds a 5,6-pyrimidine covalent bond and substracts an H-atom from a methyl group. ROS preferably target C5 and to a lesser extent C6, which gives rise to the C6-yl and C5-yl radicals. These radical sites of thymidine react with O_2 to give rise to hydroperoxyl radicals [86]. The second pathway of ROS mediated thymine oxidation involves H-aton abstraction from the methyl group. This results in the 5-(uracilyl) methyl radical. Then, the 5-(uracilyl) methyl radical is converted into peroxyl radical after the reaction with O_2 and further to hydroperoxide radical. This radical is then reduced to 5-hydroxymethyluracil and 5-formyluracil, which can also react with guanine and adenine bases to produce intrastrand or interstrand cross-links between the methyl group of thymine and the C8 position of guanine or adenine.
ROS oxidation of cytosine and 5-methylcytosine also involves the formation of peroxyl radicals and hydroperoxides. Cytosine hydroperoxides rapidly decompose into intermediate compounds, such as uracil hydroperoxides and cyclic endoperoxide. These intermediates can form labile products such as cytosine glycol. The resulting products are analogues of uracil, which leads to altered transcription.
Guanine oxidation by ROS results in two main degradation products: 8-oxo-7,8-dihydroguanine and 2,6- diamino-4-hydroxy-5-formamidopyrimidine [85], which are then further degraded. Another type of guanine oxidation product is oxazolone [87]. The formation of oxazolone leads to base pair transversions and it creates stop points for DNA polymerase β, thereby blocking DNA synthesis [88].
The oxidation of adenine is similar to guanine oxidation, leading to 8-oxo-7,8-dihydroadenine and 4,6-diamino-5-formamidopyrimidine. The formation of both these oxidation products is initiated by addition of •OH to C8 and then either a one-electron or a reduction step [89]. Interestingly, the yield of the adenine oxidation products is approximately a ten-fold lower than guanine oxidation products. Possibly, the reason behind this disproportion is that the majority of initial oxidation reactions occur at C4 of adenine [90], leading to an adduct radical that undergoes rapid dehydration to Ade-N6-yl-radicals. However, these Ade-N6-yl-radicals induce reactions that involves electron of H-atom abstraction with normal adenine as a result. Thus, the adenine can be regenerated and this might explain the low yield of adenine oxidation products after DNA alteration by ROS. Besides, the strong oxidizing properties of Ade-N6-yl radicals may enable electron transfers in DNA thereby transferring damage from adenine to guanine, which is an alternative explanation for the low adenine oxidation yield.

These modifications to the DNA bases and oxidation of the deoxyribose backbone of DNA can lead to different types of DNA damage (Fig. 6), including, DNA single-strand breaks, DNA double-strand breaks [91], bulky adducts, abasic sites, interstrand and intrastrand crosslinking, insertions and deletions [92]. This DNA damage ultimately results in halted or false gene transcription and subsequently malformed proteins.

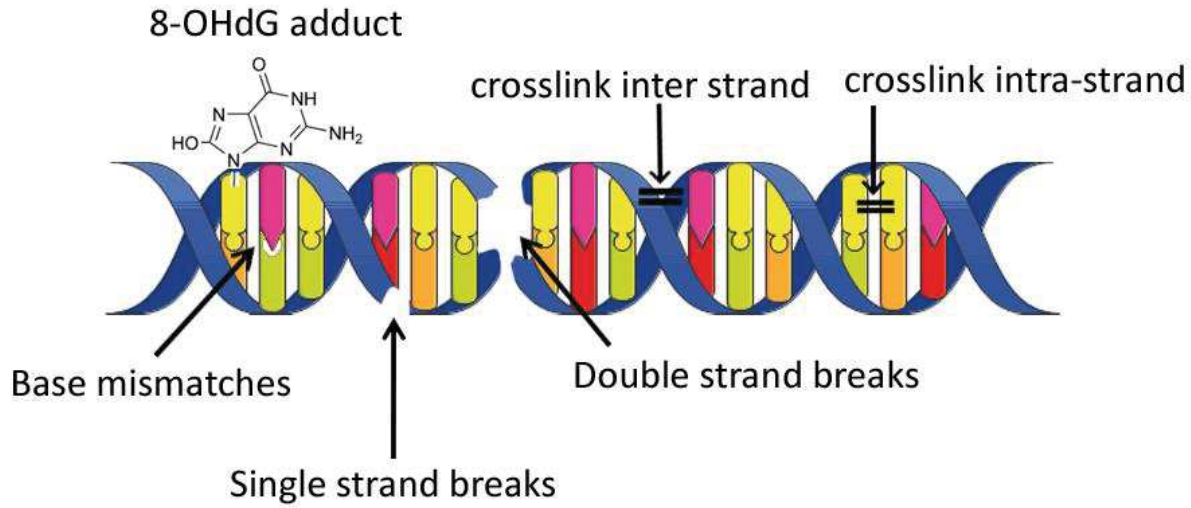

Figure 6 Types of DNA damage that can be the result of oxidation by ROS, being the formation of 8-OHdG adducts, mismatching of DNA bases, breaks of either 1 strand or both strands, and crosslinking between the different strands or within the same strand.

2.4.2 Protein oxidation

Next to DNA oxidation, ROS can also directly oxidize proteins forming protein oxidation products [93]. There are many different ways that ROS can induce protein oxidation, but metal catalyzed oxidation and amino acid oxidation are the main ones. Because several proteins interact with metal ions for their functions, the presence of H_2O_2 together with these metal ions, such as Fe^{3+} and Cu^{2+} ions, or Fe^{2+} and Cu^{+} , attack amino acid residues close to the metal binding site [94] inactivating the proteins.

Concerning amino acids oxidation, two different pathways, the diamide pathway and the α-amidation pathway, can induce cleavage of peptide bonds inside proteins. For example OH• reacts with proteins to form alkyl radicals [93;94]. Alkyl radicals can crosslink with each other to form protein aggregates or react with O_2 to generate alkylperoxide radicals. After reaction with Fe^{2+} or $HO_2^{\bullet}$, alkylperoxide can form alkoxyl radicals, which are capable of reacting with almost any organic substance [95] and therefore can attack the adjacent amino acids as well. The cleavage of the peptide bond can also be obtained more specifically by the reaction of OH• with the glutamyl, prolyl and aspartyl residues of the protein chain.

Several other amino acids can be specifically modified via side chain reactions with ROS. Amino acids that include aromatic side chain groups and those containing sulfydryl groups are most susceptible to react with ROS. Examples of aromatic amino acids are phenylalanine, tryptophan, histidine, and tyrosine. Upon oxidation, these amino acids can form mono- and di-hydroxy derivatives [93]. Hydroxyl derivative nitrotyrosine can interact with other tyrosine radicals within the same molecule or between other molecules and thereby inactivate the protein and form harmful protein aggregates. In addition, the oxidation of methionine and cysteine sulfhydryl residues form sulfoxide, sulfenic acids and disulfide bridges [96]. However, oxidation of cysteine and methionine residues is also reversible via the reduction of cysteine by thioredoxin and glutaredoxin and methionine by the methionine sulfoxide reductase system.

However, the main product of protein oxidation, whatever the type of protein oxidation, is the carbonyl residue. Carbonyl groups can be formed via secondary reactions with 4-hydroxynonenal (HNE) or with reducing sugars or their oxidation product [97]. Once formed, carbonyl groups can react with α-amino groups of lysine residues. These reactions lead to the

formation of intra- or inter-molecular crosslinks and the formation of protein aggregates. A main problem with protein aggregates is that they are unable to be degraded via normal protein degradation mechanisms, leading to further accumulation of oxidized proteins and cellular dysfunction.

2.4.3 Lipid peroxidation

In addition to DNA and proteins damage, lipids are a third cellular component that can be heavily damaged by ROS [98]. In general, lipids are damaged via lipid peroxidation, which involves the abstraction of a hydrogen from the carbon chain replacing it with an oxygen. This results in lipid peroxyl radicals and hydroperoxides. Glycolipids, phospholipids and cholesterol are the main targets of peroxidation. The process of lipid peroxidation includes three steps: initiation, propagation and termination. The first step involves a ROS-induced abstraction of allylic hydrogen, resulting in the carbon-centered lipid radical. Then, in the propagation phase, lipid radicals react with oxygen to form a lipid peroxy radical. The peroxy radical is able to induce the abstraction of hydrogen from another lipid molecule to form a new lipid radical. This creates a chain reaction of lipid radical formation and lipid peroxy radical generation. Another product formed during the propagation phase is lipid hydroperoxyde. During termination, antioxidants donate a hydrogen atom to the lipid peroxy radical to form nonradical products. Once lipid peroxidation is initiated, a propagation of chain reactions will take place until termination products are produced.

Lipid peroxidation can result in a variety of oxidation products. The main primary products are lipid hydroperoxides (LOOH). Many different aldehydes can also be formed as secondary oxidation products, including malondialdehyde (MDA), propanal, hexanal and HNE. MDA has been shown to be the most mutagenic type of lipid peroxidation product [99], whereas HNE is the most toxic [100]. This high toxicity is the result of the rapid reactions between HNE and thiol and amino groups. Besides, reactive aldehydes can act both as signaling molecules and as cytotoxic products. HNE acts as a signaling molecule for cell proliferation and/or differentiation, cell survival, autophagy, senescence, apoptosis, and necrosis by regulating several transcription factors sensible to stress, such as NRF2, activating protein-1 (AP-1), nuclear factor kappa-light-chain-enhancer of activated B cells (NF-κB), and peroxisome-proliferator-activated receptors (PPAR) [101].

2.5 ROS vs antioxidants

In many diseases, including neuropathies, ROS play a central role. However, this does not necessarily mean that the production of ROS has increased. Instead, antioxidant defenses, especially antioxidant enzymes, can be impaired. Multiple antioxidants exist in cells and each one is regulated independently, which allows a large range of scavenging of ROS. The main antioxidant enzymes are GPx, catalase and SOD proteins.

2.5.1 MnSOD

There are three SOD proteins in cells: the cytoplasmic Cu/ZnSOD (SOD1), the mitochondrial MnSOD (SOD2), and the extracellular Cu/ZnSOD (SOD3). All three isoforms are scavengers of H_2O_2, but I will focus on SOD2 in particular, because SOD2 is the only isoform present in the mitochondrial matrix. SOD2 is a mitochondrial manganese (Mn) containing enzyme (MnSOD), which is composed of a 96 kDa homotetramer [102]. The active site of SOD2 contains Mn in order to catalyze the disproportionation of $O_2^{\bullet-}$ to oxygen and H_2O_2. In SOD1 and SOD3, Cu or Zn respectively fulfills this catalytic function. The Mn is produced in the cytoplasm and then transported into the mitochondria, where it can fulfill its function. SOD2 contains a structure with a N-terminal helical hairpin and a C-terminal alpha/beta domain.

Both the hairpin and C-terminal domains direct the ligand of SOD2 to its catalytic Mn site. These active sites are stabilized by two identical four-helix bundles that are symmetrically assembled from the N-terminal hairpin to form a tetrameric interface.

In some pathological conditions, SOD2 can insert iron instead of Mn. Recently it has been shown that FeSOD2 actually does have enzymatic activity, but not as the traditional antioxidant that SOD is known for (Fig. 7) [103]. Bound to Fe, SOD forms an alternative isoform with peroxidase activity and the switch from Mn to iron binding allows FeSOD to promote oxidative stress at the expense of H_2O_2.

This shows that the binding of either Mn or Fe at its catalytic site is important for the regulation of SOD2 activity. However, the main regulation of SOD activity works via the expression of SOD genes. Indeed a multitude of transcription factors can regulate the expression of SOD. These transcription factors include NF-κB, AP-1, AP-2 and Sp1, as well as CCAAT-Enhancer-Binding Proteins (C/EBP) [104].

NF-κB is a redox-sensitive transcriptional factor that is considered a regulator of genes that acts as an "immediate responder" to harmful cellular stimuli. All three SOD genes have been shown to be regulated by NF-κB. In contrast with SOD1, which expression is not strongly regulated, SOD2 transcription can rapidly be modulated in response to oxidative stress. The NF-κB site is located within the second intron of the SOD2 gene, which implies a positive effect of NF-κB binding to SOD2 transcription [105]. Nonetheless, p50, which is another member of the NF-κB family, also regulates SOD2 expression but negatively.

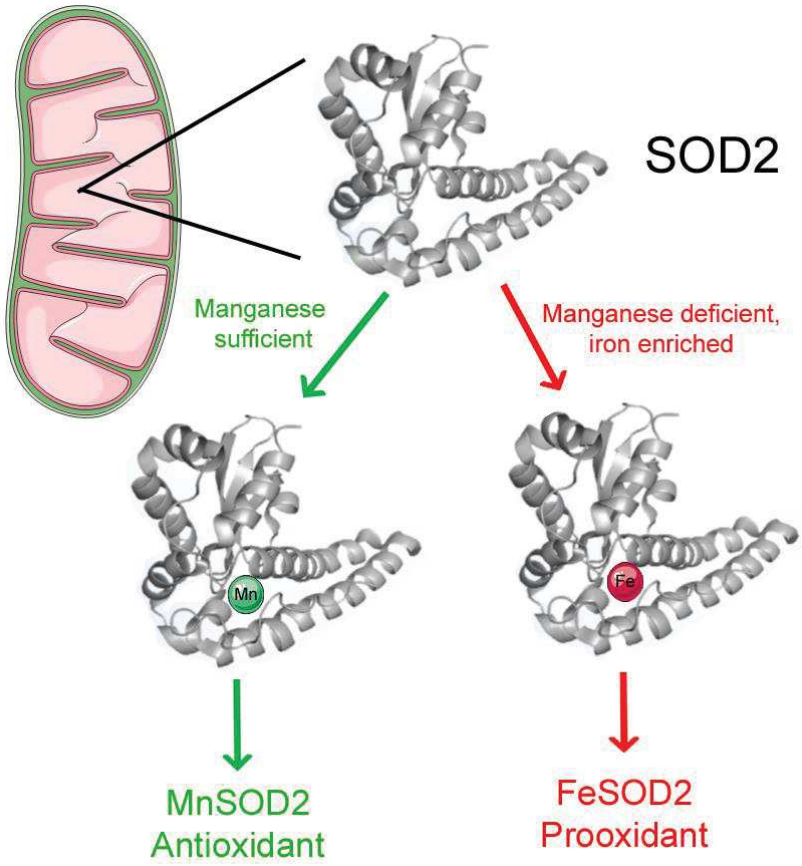

Figure 7: Incorporation of different cofactors in SOD results in opposite reactions. When Manganese is incorporated, SOD fulfills its known function as an antioxidant. However, SOD2 can function as a prooxidant in situations when manganese is deficient or iron is enriched in the environment. In these situations, SOD incorporates Fe.

Sp1 is a transcription factor that contains a zinc-finger domain that binds directly to the DNA. It stimulates gene transcription through one of its glutamine-rich domains. DNA domains that are rich in GC base pairs, such as the promotor regions of all 3 SOD genes, are targets for Sp1 binding. Multiple Sp1 binding sites are required to induce SOD2 expression [106]. The 5'-flanking region of the SOD2 gene contains a unique DNA looping structure allowing synergistically activation of transcription. This DNA looping structure is formed by the interactions between local and distant Sp1, indicating its influence on SOD2 expression. The unique single-strand structure of the SOD2 promoter modulates the interaction of transcription factors, such as NF-κB and Sp1, with the SOD2 promoter.

AP-2 is a family of transcription factors that can bind directly to the cis-element of its target gene. In addition, it can crosstalk with other transcription factors in order to change its target gene expression. AP-2 is an interesting transcription factor, since it can increase SOD1 transcription whereas it suppresses SOD2 by inhibiting Sp1-dependent transcription [107]. Methylation of the AP-2 site in the SOD2 promoter reduces AP-2 binding and subsequently SOD2 transcription is increased.

FOXO3a is a transcription factor that can bind to the 5'-flanking region of SOD2, and this way stimulates its expression. During ageing, Akt activity becomes increased, which is thought to be responsible for FOXO3a phosphorylation and hence its inactivation. This mechanism might be the cause of the age-related downregulation of MnSOD. Based on the overlapping binding sites with NF-κB, a dual NF-κB/FOXO regulation has been suggested [108].

Regulation of SOD2 expression and activity is essential in cellular function. For example, increased levels of SOD2 reduces the mitochondrial superoxide level, protects the mitochondrial morphology and functions, and provides resistance against oxidative cytotoxicity [109]. In contrast, complete ablation of SOD2 causes neonatal lethality in mice. These mice have inactivated ISCs in oxidative phosphorylation and TCA enzymes [110], which results in dilated cardiomyopathy and neurodegeneration [102], which soon cause the mice's death. In contrast, heterozygous mutant SOD2 animals have a partial oxidative phosphorylation defect involving a reduced respiratory control ratio. In these mice, the predisposition for opening of the PT pore is increased. The opening of the PT pore creates a channel through the inner and outer mitochondrial membranes that allows free diffusion of molecules of 1500 kDa or smaller. This results in the efflux of protons and the loss of the membrane potential. This leads in the swelling of the mitochondria and the initiation of apoptosis [110]. A dysregulation of SOD expression has been involved in several diseases and in particular in cancer. Oxidative stress is elevated when cancer is at an early stage and the amount of antioxidant enzymes is low. In this condition, the mutation of tumor suppression genes and activation of oncogenes is facilitated. Even though MnSOD initially has a tumor suppressor effect via mediation of ROS levels and the modulation of redox-related transcription factors, its role shifts during cancer progression [111]. Therefore, MnSOD expression is higher in aggressive cancer forms compared to benign cancers, when the disease is at a later stage. Next to alterations in gene transcription factors, polymorphisms in the SOD2 gene are the cause of affected SOD2 expression in cancer cells. Mutations in the SOD2 promoter region have been detected in various cancers, showing how this can be an underlying cause of the decreased MnSOD expression at the initial phase of the disease. These mutations create an extra DNA binding site for inhibitory transcription factor AP-2 and impair the interaction between DNA and proteins that are required for transcription initiation.

2.5.2 Glutathione Peroxidase

Human cells contain four major GPx isoforms [112]. The classical GPx (GPx1) is located in cytosol, nucleus and mitochondria of liver, lung and kidney cells, whereas GPx2 is located in the cytosol and nucleus (so not within mitochondria) of cells in the gastrointestinal tract. Plasma GPx (GPx3) is a secreted protein found in the cytosol in of cells located in many tissues including kidney, lung, epididymus, vas deferens, placenta, seminal vesicle, heart and muscle. Lastly, phospholipid GPx (GPx4) is present in the nucleus, cytosol and mitochondria and bound to membranes. GPx4 is broadly distributed in different tissues. GPx1, 2 and 3 act as homotetramers, whereas GPx4 is a monomer.

GPx catalyzes reactions that reduces H_2O_2 to water, and hydroperoxide (ROOH) is reduced to and the less reactive ROH alcoholic counterpart [110]:

$$H_2O_2 + 2GSH \rightarrow 2H_2O + GSSG$$
$$ROOH + 2GSH \rightarrow ROH + GSSG + H_2O$$

Although H_2O_2 is not the most reactive kind of ROS, it is involved in damaging Fenton reactions and is a direct precursor to the more reactive •OH. Therefore, mice lacking GP_X were thought to exhibit impaired mitochondrial function in tissues that express high levels of mitochondrial GPx1. However, initial studies in GPx1 mutant mice did not show any effect of the mutation indicating that loss of GPx1 is not sufficient to cause toxic oxidative stress. However, when challenged by paraquat or H_2O_2, the mutant mice appeared to be more susceptible to oxidative damage. Likely there is a compensatory mechanism for the GPx1 deficiency in place as well. Logically those compensatory mechanisms involve other GPx isoforms, such as Gpx4, or catalase.

It has been shown that mitochondrial ROS production is correlated to cellular protein disulfide content. In addition, it has been shown that cells overexpressing GPx also contain less protein with disulfide bonds. Moreover, GPx overexpression results in a reduction of the mitochondrial membrane potential, indicating that GPx acts on the mitochondrial electron flux over the mitochondrial membranes [113]. These are two strong indicators that GPx overexpression can alter the ROS production by mitochondria, which has a functional effect on proteins in the cytoplasm. It also suggests that other oxidation reactions, such as oxidation of lipids, can be diminished by GPx overexpression. Interestingly, another effect of the overexpression of GPx is the decrease in ATP levels. Therefore, an excess of GPx is thought to cause a reduction in proton-motive force, which results not only in less disulfide bonds in proteins, but also a decreased cellular ATP content. Since GPx is mainly an antioxidant, this pathway is driven by a reduction in ROS.

2.5.3 Catalase

Catalase is an enzyme that is found in almost all aerobically respiring organisms. Catalase consists of four protein subunits, each containing a heme group and a molecule of NADPH, which prevents deactivation [114]. Catalase is present in many tissues, but its activity is highest in liver, erythrocytes, kidney and adipose tissue, whereas its activity is relatively low in heart and brain. Catalase is the first antioxidant enzyme that has been characterized to catalyze the two stages of converting H_2O_2 to water and oxygen [115]:

$$catalase\text{–}Fe(III) + H_2O_2 \rightarrow compound\ I$$
$$compound\ I + H_2O_2 \rightarrow catalase\text{–}Fe(III) + 2\ H_2O + O_2$$

The kenetics of catalase is particularly high and therefore it is almost impossible to saturate catalase *in vivo*. Catalase can prevent mitochondrial permeability transitions by the transition of H_2O_2 to water and oxygen [116]. Catalase has also been shown to prevent a loss of mitochondrial depolarization, suggesting that the inner mitochondrial membrane permeabilisation is caused by mitochondrial H_2O_2.

Within cells, catalase is mainly located within peroxisomes and in the cytosol. In healthy neurons, this antioxidant can have major effects in cellular function, because it can efficiently regulate redox signaling by increasing or decreasing H_2O_2 concentrations. For example, catalase has been shown to regulate the influx of Ca^{2+} and Na^{+} via transient receptor potential V (TRPV) channels [117]. Intracellular ROS are potent activators of these plasma membrane channels, meaning that ROS will open TRPV channels through which Ca^{2+} and Na^{+} will enter the neuron. In heart and liver cells, catalase has been detected in mitochondria as well, but in neuronal mitochondria only extremely low catalase concentrations are found, compared to its concentration in the cytosol [118] In addition, as catalase inhibitors did not have an effect on the scavenging activity of ROS in mitochondria, this indicates that catalase is functionally irrelevant for brain mitochondria [119].

Changes in the catalase levels and polymorphisms in the gene coding for catalase are associated with many different diseases, such as hypertension, diabetes mellitus, insulin resistance, dyslipidaemia, asthma, bone metabolism or vitiligo [120].

2.6 The role of ROS as a signaling molecule

When ROS are being produced in physiological levels, those molecules are used in signaling pathways. These pathways include a wide variety of biological mechanisms, including cell proliferation, differentiation, and maturation. Compared to other signaling mechanisms, redox signaling is much less specific, since it can react on many different targets. Whereas the traditional method of signaling works via a receptor-ligand binding process, ROS signaling works via the oxidation of redox-sensitive amino acid residues. These residues are often located at the active sites or catalytic domains of protein tyrosine phosphatases. Since serine/threonine phosphatases are susceptible to oxidative inactivation, ROS can modulate signal transduction by decreasing phosphatase activity.

The signaling role is particularly important for H_2O_2 because it can diffuse over longer distances than the other types of ROS. For H_2O_2 to act as a signaling molecule, it must first evade reduction by the antioxidants that are present in between the mitochondrion and the proteins that are sensitive to H_2O_2 levels and then trigger a response of that peroxide-sensitive protein. Certain features of proteins make them susceptible to oxidation by H_2O_2. Because of the low pH of the cytosol, most cytosolic proteins are protonated and therefore protected from H_2O_2 oxidation. The few cytosolic proteins that do contain a deprotonated cysteine residue are specific targets for H_2O_2 and hence those proteins are suitable for being H_2O_2 sensors. Indeed, ROS induces the reversible oxidation of thiol groups of key cysteine residues in many proteins, including transcriptional regulators, kinases, phosphatases, structural proteins, metabolic enzymes, and SUMO ligases. The cysteine oxidation in these proteins often leads to altered activities.

2.6.1 ROS changes protein activity and gene expression in cells

The response of human cells to increased levels of H_2O_2 is an adaptation to the environment by stimulating the reduction of ROS [121;122]. This adaptation of the cell occurs via the control

of single enzymatic activities or via the control of transcription (Fig. 8) [123]. Moreover, H_2O_2 increases the transcription of antioxidant genes, which increases the concentration of oxidant reducing enzymes in the cell. Those antioxidants reduce the level of ROS and this negative feedback loop ensures the homeostatic balance of ROS within the cell. However, this negative feedback only occurs up to a threshold level of peroxide concentration. If the peroxide concentration rises above that threshold, despite the action of increased antioxidant production, different patterns of p53- regulated gene expression are initiated that stimulate the expression of pro-oxidants involved in apoptosis [124]. The negative feedback turns into a positive feedback that leads to apoptotic death of the cell.

Oxidation of the transcriptional activator OxyR is another remarkable example of H_2O_2 dependent regulation of gene expression. Oxidation of OxyR does not influence DNA binding per se, since both oxidized and reduced OxyR are able to bind DNA. However, only the oxidized form of OxyR can activate transcription of antioxidant genes [125]. It has been shown that activation of OxyR by H_2O_2 is dependent on the oxidation of cysteine 199, which results in a sulfenic acid derivative. The sulfenic acid derivative formation is sufficient to activate OxyR dependent transcription [126], but the activation becomes more stable by the formation of a more stronger disulfide bond between cysteines 199 and 208. One of the target genes of OxyR is glutaredoxin1, which becomes increasingly expressed upon OxyR activation. Glutaredoxin1 can reduce OxyR and deactivate it, thereby creating a negative feedback loop [127]

Transcription factors that contain Fe^{2+} are also suitable candidates for being a H_2O_2 sensor. H_2O_2 reacts easily with Fe^{2+}, which is functioning as a co-factor in several proteins. Indeed, the PerP transcriptional repressor reacts to H_2O_2 in a mechanism that is thiol independent. Instead, PerR works via the metal-catalyzed oxidation of histidine residues. It contains a structural Zn^{2+} binding site and a regulatory Fe^{2+} binding site [128]. When PerR binds to Fe^{2+} to its regulatory site, it connects to DNA and represses the expression of target genes. These target genes include antioxidant enzymes, such as catalase. H_2O_2 activates genes that were previously repressed by PerR, because Fe^{2+} coordinating histidine residues of PerR become oxidized. Therefore, PerR can no longer bind to Fe^{2+} or to DNA [129].The oxidation of the critical residues of PerP is on its turn catalyzed by Fe^{2+}, showing that PerR activity is modulated by both H_2O_2 and Fe. Whereas the oxidation of thiol groups is reversible, the oxidation of PerR histidine residues is not.

Next to regulation of ROS homeostasis, H_2O_2 can also activate signaling pathways to stimulate cell proliferation, differentiation, migration, or apoptosis. In addition, it can regulate the conjugation of proteins to the SUMO ubiquitin-like modifier in a concentration-dependent manner. Active macrophages produce H_2O_2 levels in a range that inhibits the conjugation of SUMO and hence reduces sumoylation. When H_2O_2 levels become elevated, the deconjugation of SUMO is inhibited. This causes an increased sumoylation rate [130]. Sumoylation is an important regulator of localization, activity, and stability of many proteins. Therefore, H_2O_2 can result in many biological responses via altered protein modification through sumoyliation.

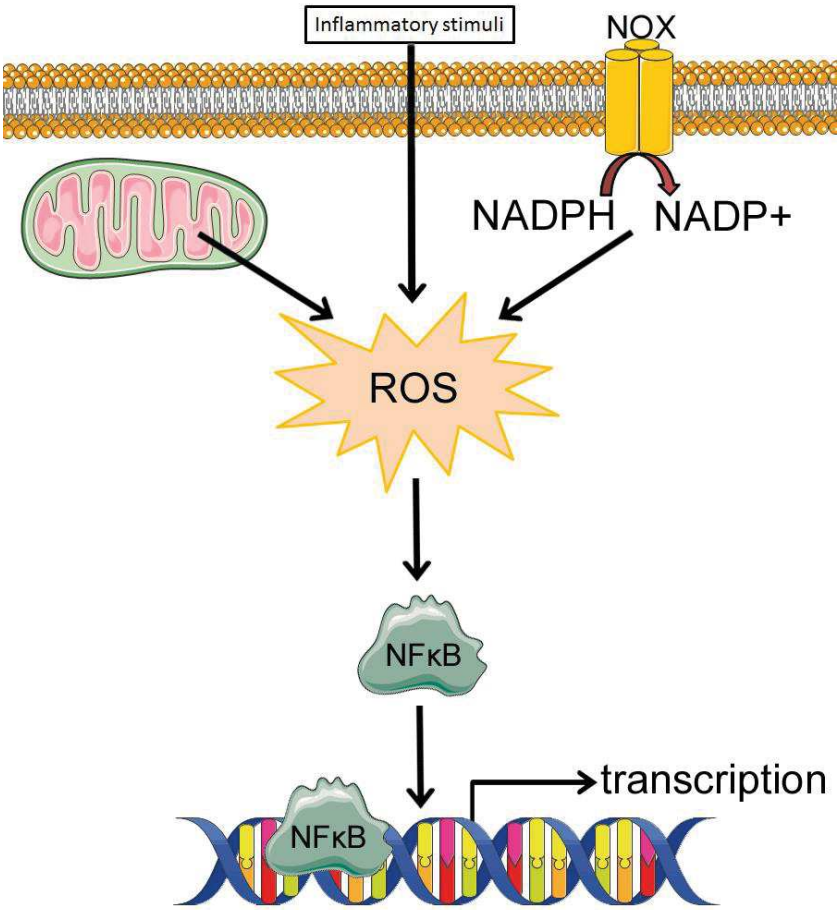

Figure 8: ROS can function as a signaling molecule and can change gene expression at the DNA level. When ROS is produced by mitochondria, NADPH oxidase or potential other sources, it stimulates the activity of transcription factors such as NF-κB. This will result in DNA binding of NF-κB and hence increased expression of certain genes, for example genes responsible for antioxidant functions or inflammatory responses.

2.6.2 The role of ROS in misfolded protein degeneration

The ubiquitin-proteasome system (UPS) is the main biological mechanism in the degradation of soluble proteins in cytosol and nucleus [131]. In the UPS, 26S proteasome is the major cellular proteolytic machinery. 26S proteasome degradation is not specific to nonfunctional proteins as it degrades folded and functional proteins as well in an ATP/Ub-dependent matter. Nonetheless, oxidative stress enhances the activity of 26S proteasome, in order to degrade nonfunctional proteins that are supposed to be present in abundance under conditions of high oxidative stress. The increased 26S proteasome activity should then protect the cells from these oxidatively damaged proteins. However, when ROS levels continue to be elevated, 26S proteasome disassembles and the UPS is deactivated. This gives rise to 20S proteasome, which is the core of 26S proteasome. Whereas 26S proteasome is ATP/Ub-dependent and relatively susceptible for oxidative stress itself, the 20S proteasome works in an ATP/Ub-independent way and it is more resistant against oxidation. Initially, the disassembly of 26S proteasome is still reversible when oxidative stress decreases, so the 26S proteasome can still reassemble. It has been observed that within several hours after reassemble of 26S proteasome, there is hyperactivation of the ubiquitinating system and proteolysis. If elevated oxidative stress is continued for a longer period of time, proteasomal activities are inhibited and new proteasomal components are being produced. This gives rise to newly-formed 20S and 26S. At one point, oxidative stress continues for too long or rises to a sublethal level, which impairs the proteolytic system and results in the accumulation of aggregates of damaged, abnormal proteins [132]. Besides its role in the degradation of damaged proteins, the

proteasomal system also controls the degradation of proteins that act as redox switches, some of which are discussed earlier, such as the transcription factors hypoxia-induciblefactor-1 (HIF-1), NRF2 or NFκB. The UPS itself is subjected to fluctuations in oxidative stress, even when those levels do not exceed concentrations that trigger 26S proteasome disassembly. Ubiquitination enzymes are inactivated by disulfide bond formation, S-nitrosylation, and S-glutathionylation. The proteolytic activity of the proteasome requires β-subunits in the catalytic 20S core with intact Cys-residues. These Cys-residues are extremely sensitive for oxidation.

A second mechanism of protein degradation is autophagy. Autophagy is an intracellular process that degrades cytosolic components inside lysosomes. Mild oxidative stress, redox-mediated signaling or oxidative modifications of macromolecules stimulate autophagy and hence prevent the aggregation of non-functional and damaging proteins and affected organelles. An oxidative stress-induced form of microautophagy has also been described, that involves mitochondria-derived vesicles (MDVs). These MDVs are transported to the lysosomes and contain mainly oxidized proteins. Oxidative stress induces the generation of MDVs [133]. Basal ROS levels contribute to healthy rates of autophagy, which is necessary to maintain protein turnover and proteostasis. This way, protein degradation via autophagy is actually a pro-survival mechanism. When oxidative stress increases, autophagy can either act as pro-survival function or contribute to cell death and the equilibrium between the two is tightly regulated. However, when oxidative stress exceeds a certain threshold, lysosomes release ROS and proteases into the cytosol and crucial cellular components are being degraded, eventually resulting in autophagy cell death [134].

2.6.3 ROS as a signaling molecule in the immune system

Substantial evidence has revealed that ROS are essential second messengers in innate and adaptive immune cells [135]. In the innate immune response, the toll-like receptor (TLR) ligand lipopolysaccharide (LPS) stimulates the production of ROS by NADPH oxidase and mitochondria. This increase in ROS levels activates inflammatory cytokines, is essential for immune response pathways induced by TLRs and optimizes the activity of macrophages. Furthermore, RIG-I-like receptors (RLRs) also signal through mitochondrial ROS and NLRP3, a component of the inflammasome, is activated by mitochondrial ROS. In adaptive immunity, ROS is an important activator of T-cells. ROS stimulates proliferation of T-cells and its production of the cytokine interleukin-2 (IL-2). As a response to initial T-cell activation by mitochondrial ROS, NADPH oxidase becomes involved to sustain T-cell activation. In addition to T-cell activation, ROS are also involved in B-cell activation. As discussed shortly in the role of H_2O_2 promoting either gene expression of antioxidants or promoting apoptosis, the amount of ROS is important in determining the effect of H_2O_2 as a signaling molecule in immune responses. A low amount of ROS production benefits immune responses by activation of T-cells and B-cells, and the immune response is more efficient without causing tissue damage [136]. However, when ROS levels rise higher, this can exacerbate the immune response via elevated levels of pro-inflammatory cytokines [137]. For example, NRG-deficient mice have higher levels of ROS and their immune response to pathogens is worse than wildtype mice, resulting in worsened pneumonia and sepsis. Thus, slight elevations in ROS levels may enhance immune system function, whereas high levels of ROS could promote a pathological response.

2.6.4 ROS as a signaling molecule in neurogenesis

Redox signaling plays an important role in the differentiation of various cell lineages from their respective precursors [138]. In addition, ROS levels play a role in clonal expansion of stem cells in the proliferative niches in the brain, such as the hippocampus and the subventricular

zone (SVZ). Because ROS regulate the proliferation and differentiation of neuronal stem cells (NSCs), tight regulation of ROS production is required to maintain stemness properties of the NSCs. In contrast, increased levels of ROS in neuronal progenetor cells (NPCs) in $p53^{-/-}$ mice induce a shift in the NPC differentiation balance towards the neuronal lineage [139].

2.6.5 ROS as a signaling molecule for neuronal calcium

Ca^{2+} is a central player in intracellular mechanisms and reactions and hundreds of proteins are involved in Ca^{2+} signaling [56;140]. Therefore, the intracellular concentration of Ca^{2+} is highly regulated. In human cells, there is close interaction between the levels of ROS, ATP and calcium and mitochondria are important regulating organelles that maintain the balance in this triad (Fig. 8) [56] . Stimuli that cause changes in cytoplasmic Ca^{2+}, ATP or ROS trigger feedback loops that should restore the balance in time or reach a new equilibrium. If a new balance cannot be obtained, this will lead to a decline of ATP levels, an increase of ROS production and increased intracellular Ca^{2+} concentration. ROS can act as a signaling molecule to regulate the intracellular Ca^{2+} concentration by acting on a variety of channels through which calcium can enter the cytosol. Important Ca^{2+} channels in neurons are the voltage-dependent Ca^{2+} channels (VDCCs). There are several subtypes of VDCCs and the reaction to ROS differs between subtypes. H_2O_2 accelerates the opening of P/Q-type of Ca^{2+} channels, so H_2O_2 stimulates the entry of Ca^{2+} into the cell. In contrast, ROS decreases the influx of Calcium through L-type Ca^{2+} channels in muscle cells, although no significant effect of H_2O_2 on L-type Ca^{2+} channels is reported in pancreatic β-cells.

Intracellular Ca^{2+} release from the ER or sarcoplasmic reticulum (SR) is mediated by ryanodine receptors (RyR) and IP3R. RyR and IP3R channels contain many cysteine residues. As mentioned earlier, deprotonated cysteine residues are especially susceptible to oxidation by ROS. Changes in the redox state of RyR and IP3R would affect their activities. ROS open RyR channels and this way enhances Ca^{2+} release from the ER. In neurons, activation of RyR subtype 3 by ROS might modify Ca^{2+}-dependent long-term potentiation and long-term depression. $O_2^{\bullet-}$ enhances IP3-induced Ca^{2+} release through IP3Rs from fractionated vascular smooth muscle SR, suggesting that, like RyR, ROS increase IP3R channel opening. Also ATP-dependent calcium channels, including the plasma membrane Ca^{2+}-ATPases (PMCA) and SERCA, as well as Na^+/Ca^{2+} exchangers NCX, are sensitive to ROS regulation. ROS effectively inhibits Ca^{2+} transport by SERCA in smooth muscle cells. H_2O_2 and $O_2^{\bullet-}$ can completely uncouple the hydrolytic reaction of PMCA and inhibit the hydrolytic reaction of SERCA [141]. The effect of ROS on NCX is not fully understood yet, because several contradictory results have been reported. An interesting feature of calcium signaling is that it can be administered intracellularly in Ca^{2+} sparks. Ca^{2+} sparks play an important role in local control of Ca^{2+} signaling in many types of cells. ROS also has a regulatory effect on the frequency that these Ca^{2+} sparks are occurring [142]. Like the general influx and efflux of calcium that has been described before, the effect of ROS on Ca^{2+} sparks vary depending on cell type.

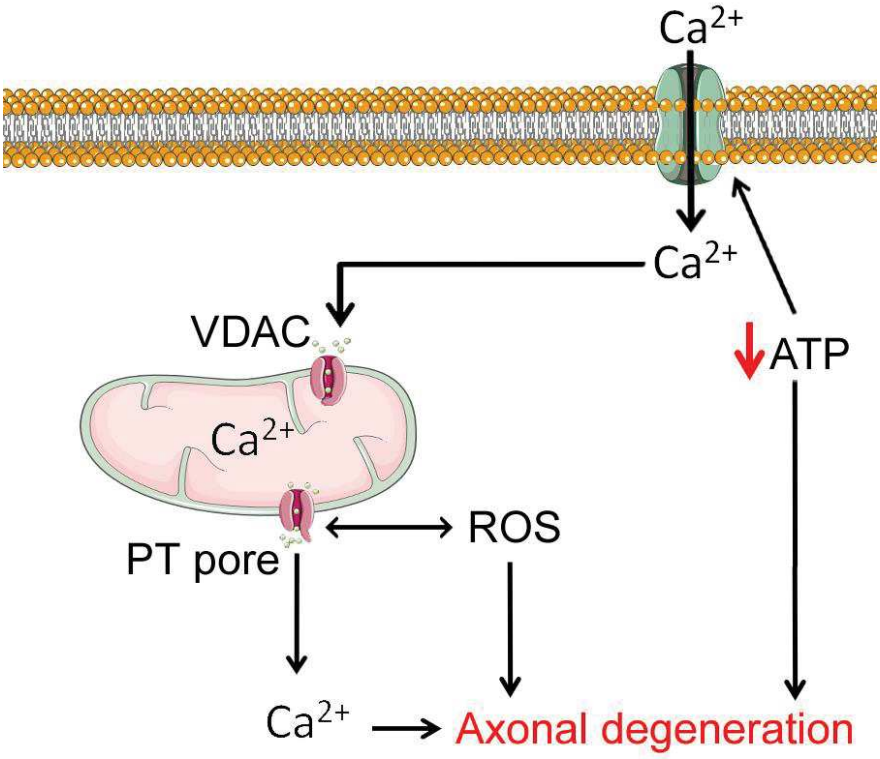

Figure 9: The ATP-ROS-calcium triad are important regulators in axonal degeneration. High cytosolic Ca^{2+} concentrations are a well-established stimulus that triggers a positive feedback loop leading up to Wallerian degeneration. Calcium can enter the axon, but then can be buffered by mitochondria. Decreased ATP levels induce intracellular calcium levels. Meanwhile ROS stimulates the opening of PT pores, resulting in an efflux of calcium into the cytosol. This way, ATP and ROS either prevent or stimulate axonal degeneration via cytosolic calcium levels.

2.6.6 ROS and wound healing and axonal regeneration

Although ROS are central players in neurodegeneration through pathways involving Bax, caspase, PARP and MAPKs, ROS also play an important role in tissue repair, including axonal regeneration. However, the production of this damage induced H_2O_2 production seems not to occur in mitochondria, but by the H_2O_2 producing enzyme Duox1, which is a type of NADPH oxidase and is present in epidermal cells. ROS signaling in regenerative tissue induces two parallel pathways. H_2O_2 triggers apoptosis, while activating the JNK pathway [143]. Both events are necessary for proliferation of epidermal cells around the wound and subsequently required for tissue repair. In addition, the reaction of tissue damage involves the recruitment of immune cells into the wound in order for tissue repair to occur. The H_2O_2 that is secreted by damaged tissue results in a gradient of H_2O_2, with a high concentration at the wound site and lower concentrations further away from the wound [144]. Because of the fast diffusion of H_2O_2, the damaged area can quickly be located by immune cells. Those immune cells follow the gradient of H_2O_2 and migrate into the wound site. ROS is involved in the regeneration of nerve tissue in the same way that H_2O_2 is triggering wound healing by signaling to epidermal cells and inducing repair pathways. It is shown that blocking H_2O_2 production by Duox1 prevents axonal regeneration after tissue damage [145]. Interestingly, a gradient of H_2O_2 that recruits leukocytes after tissue damage seems not to be required for promotion of axon regeneration [146].

The fact that mitochondrial ROS production seems not to play a central role in tissue regeneration nor axonal regeneration does not mean that mitochondria are not involved in regenerative mechanisms altogether [147]. The energy consumption during axonal regeneration is high, because many energy dependent processes, including the resealing of the cut

membrane, formation of a new growth cone and mobility, are happening. The nerve also requires energy to activate a growth program that involves the synthesis of new proteins, transport, and assembly to reorganize the new cytoskeleton of the regenerated axon. To accommodate the rise in energy demand after nerve injury, mitochondria are transported to the regeneration area of the axon. Both anterograde and retrograde transport of mitochondria in regenerating axons is increased within hours and is sustained for more than 21 days [148].

2.7 Conclusion

Several forms of reactive oxygen species are generated in cells and different forms have different features. For example, superoxide anions are highly reactive and therefore are acting extremely fast with molecules in its direct environments. On the other hand, hydrogen peroxide is a type of ROS that is less reactive, but can diffuse over longer distances and can oxidize distal targets.

ROS are often considered as a negative by-product of ATP synthesis by the electron transport chain in mitochondria. Indeed, mitochondria produce superoxide anions, which give rise to the other types of ROS, but mitochondria are not the only source of ROS. In general, ROS can be considered damaging for cells, because they oxidize DNA, proteins and lipids and these oxidation products are often non-functional or unstable. Fortunately, the cells are equipped with a competent antioxidant system that consists of a group of antioxidant enzymes, which reduce ROS to water.

However, defining ROS as a by-product of ATP synthesis is too reductive. Low amounts of ROS can have physiological signaling functions that can regulate gene expression.

Chapter 3) Mitochondria in the peripheral nervous system

As described in the prologue, our lab focuses on the biology of peripheral nerves. Several peripheral neuropathies indicate that mitochondria, both in the Schwann cells and in the peripheral axons of the nerves are critical for the maintenance of the axon-glia physiology. Compared to the CNS, PNS axons can be much longer and large axons are myelinated by a single Schwann cell. In the CNS, oligodendrocytes myelinate several axons and astrocytes, which are not myelinating, also participate to the metabolic maintenance of the axon. So if the overall principle of the metabolic maintenance of the axon-glia unit may be the same, some particularities may be specific for the PNS Schwann cell-axon unit.

One of the roles of Schwann cells is to form the myelin sheath that covers large axons that are critical for peripheral nerves function. The formation of the myelin sheath induces a spatial heterogeneity along the myelinated axons as specialized regions such as nodes of Ranvier form between two successive myelin segments. While one important functional particularity of the axon is to allow the transit of mitochondria from the cell body to the synapse, the presence of several domains along myelinated axons appears to change the dynamic of mitochondria movements. So in this chapter, I will discuss the development, features and functioning of the PNS. I will describe the role of Schwann cells and their roles in the nervous system. One of its roles is to form the myelin sheath that covers large axons that are critical for peripheral nerve function. The formation of the myelin sheath induces a spatial heterogeneity along the myelinated axons as specialized region such as node of Ranvier form between two successive myelin segments. While one important functional particularity of the axon is to allow the transit of mitochondria from the cell body to the synapse, the presence of several domains along myelinated axons appears to change the dynamic of mitochondrial movements. Finally, I will discuss how mitochondria can migrate towards different areas within the neuron and how nodes of Ranvier change the physiology and the movement of these axonal mitochondria.

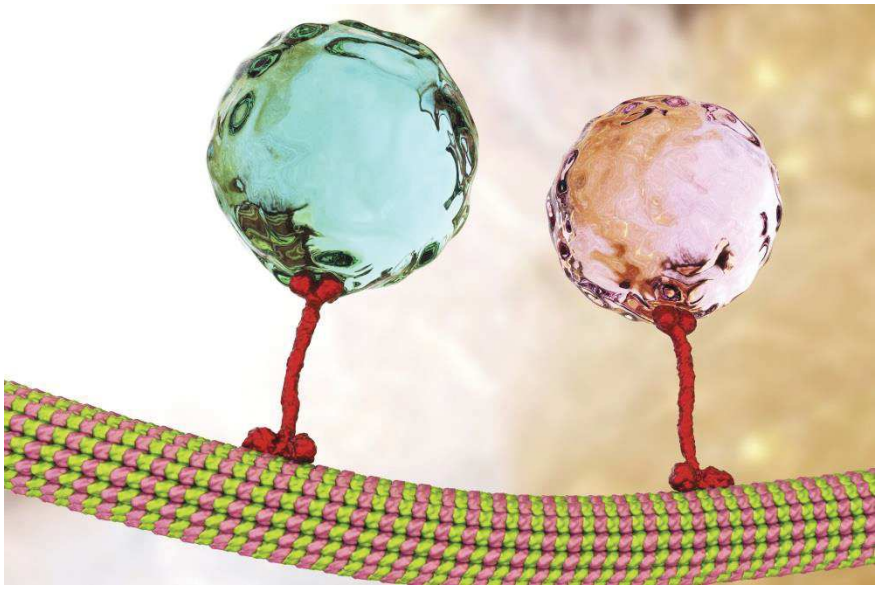

Transport of cargo through axons

3.1 Peripheral nervous system development

The PNS consists of two main cell types: neurons and myelinating Schwann Cells (mSC). Those two cell types have close functional interactions. Nevertheless, the development of these two cell types is not the same.

The development of peripheral nerves starts with migration and differentiation of neural crest cells towards neurons. These developed neurons then form axons that have to find their way to their peripheral targets [149]. The terminal point of the developing axon, the growth cone, leads the axon along its route. Initially, the first developing axons grow in an axon-free environment and form a path for later developing axons. However, because the axonal targets may be far away from the soma, later developing axons can use these paths to grow more efficiently by creating intermediate targets on specialized cells called guidepost cells and this way form axon networks. The individual segments that connect to intermediate targets are not longer than a few hundred micrometers. Guided and influenced by a contact attraction factors (secreted semaphorins and netrins), chemoattractants (netrins), contact repulsion factors (Eph ligands, transmembrane samaphorins and extracellular matrix proteins), and chemorepulsion molecules (Ig CAMs, cadherins and extracellular matrix proteins), the growth cone eventually finds the correct target of its respective axon [150]. All these mechanisms act simultaneously and in a coordinated manner for a proper pathfinding [151]. The definitive peripheral nerve contains axons with a diameter of 0.1-1.5 mm within large bundles surrounded by two cellular layers. The outer layer is made of migrating and proliferating SCs.

SC development starts, like neurons of the PNS, with migration and differentiation of neural crest cells [152]. Expression of Sox10, Neuregulin-1 (NRG1) [153], Pax3 [154], fatty acid binding protein 7 (Fabp7) and P0 [155] in neural crest cells drives the development towards SC lineage by stimulating differentiation of neural crest cells to Schwann Cell Progenitor (SCP) cells (Fig. 10) [156]. SCPs proliferate and migrate together with the developing axon [157] and during this process, the axon stimulates SCP survival. Once SCP migration stops, these cells differentiate into immature SCs, which is regulated by the expression of NRG1, Notch and ErbB2/3 [158]. Immature SCs determine which axons become myelinated and which axons become non-myelinated Remak bundles via a process called radial sorting. In the last phase of SC development, immature SCs either differentiate into myelinating SCs or non-myelinating Remak SCs. These Remak SCs are associated with C fiber nociceptors, post-ganglionic sympathetic and parasympathetic fibers, and motor nerve terminals at the neuromuscular synapses. Naturally, these classes of neurons have axons that are not myelinated. The differentiation of immature SCs into myelinating SCs requires signaling of a large variation of signaling factors, such as Krox20, NRG1, and BDNF [156].

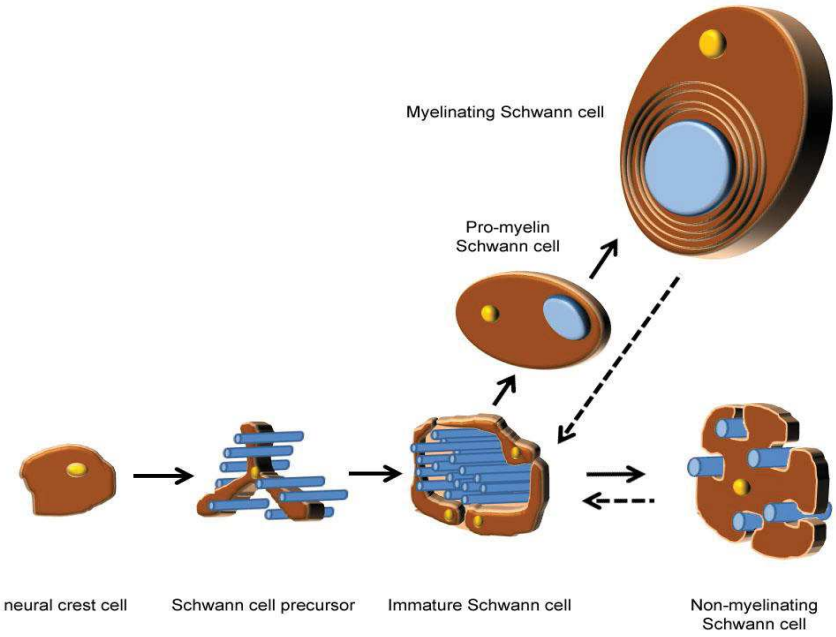

Figure 10 Schwann cell development. Neural crest cells differentiate into Schwann cell precursor cells and then into immature Schwann cells. These Immature Schwann cells either differentiate into pro-myelin Schwann cells and further into myelinating Schwann cells or into non-myelinating Schwann cells (Remak cells). After nerve damage, both myelinating and non-myelinating Schwann cells can dedifferentiate into Immature Schwann cells.

Neurons have a signaling role for survival of the developing SC precursors, but SCs have a role in neuronal development as well. This is exceptionally apparent in the development of the neuromuscular junction (NMJ). During development, one NMJ is innervated by multiple axonal nerve endings coming from the same neuron. During early post-natal development, most of these axonal nerve endings retract and the remaining axonal endpoint gets strengthened [159]. SCs play a central role in deciding which axonal endpoint gets supported. The perisynaptic SCs can detect the activity of the associated nerve ending by detecting intracellular Ca^{2+} levels in the perisynaptic SC. Additionally, these perisynaptic SCs can detect the release of neurotransmitters by the nerve ending as well [160;161]. Increased axonal activity leads to increased neurotransmitter release and increased intracellular Ca^{2+} levels. These factors are determining factors of the perisynaptic SCs for which nerve ending to support during competition between the nerve endings during post-natal development [162].

3.2 Myelination

The myelin sheath is a greatly extended plasma membrane of myelinating cells that wrap several times around axons (Fig. 11) [163]. It consists of 70% lipids in which proteins are embedded, with myelin basic protein (MBP) and proteolipid protein 20 (PLP20) being the most predominant. The myelin sheath is shaped as multiple layers (lamellae) of modified and compacted plasma membrane that are regularly breached by channels filled by cytoplasm (Schmidt Lantermann incisures). Cytoplasm containing membrane loops (paranodal loops) form the lateral extremities of the myelin sheath [164] . Longitudinal and transverse channels filled with cytoplasm (Cajal bands) are located at the outermost layer, where the myelin sheath adheres to the plasma membrane of the Schwann cell [165].

Once an initial contact between mSC and axon is made, the myelin membrane of the mSC advances in a spiraling motion [166]. The membrane extends along the entire axonal segment and then moves underneath the growing sheath to form the future internode [167]. The inner

tongue continues to advance underneath the earlier generated myelin layers, resulting in an increasing number of myelin layers (Fig. 11) [154]. Because the inner tongue generates the newest myelin membrane that leads to the radial growth of myelin, the newly synthesized membrane components need to be transported from the mSC soma through the developing myelin sheath to its innermost spiral. Therefore, the Schmidt-Lantermann incisures are made within the compact myelin, which create a helical path for transport [168;169]. For the lateral growth of the myelin layers, membrane components also have to be transported to the lateral sides of each myelin layer, the paranodal loops. At one point, many of the radial channels close, resulting in elevated transport of membrane components to the paranodal loops and hence, the internodal length increases. The final stage of myelin formation is the compaction of the myelin layers. This is achieved by the insertion of MBP into the membrane, which starts already when the myelin sheath is just a few layers thick. Although radial growth occurs in the innermost layer, compaction starts at the outermost layers.

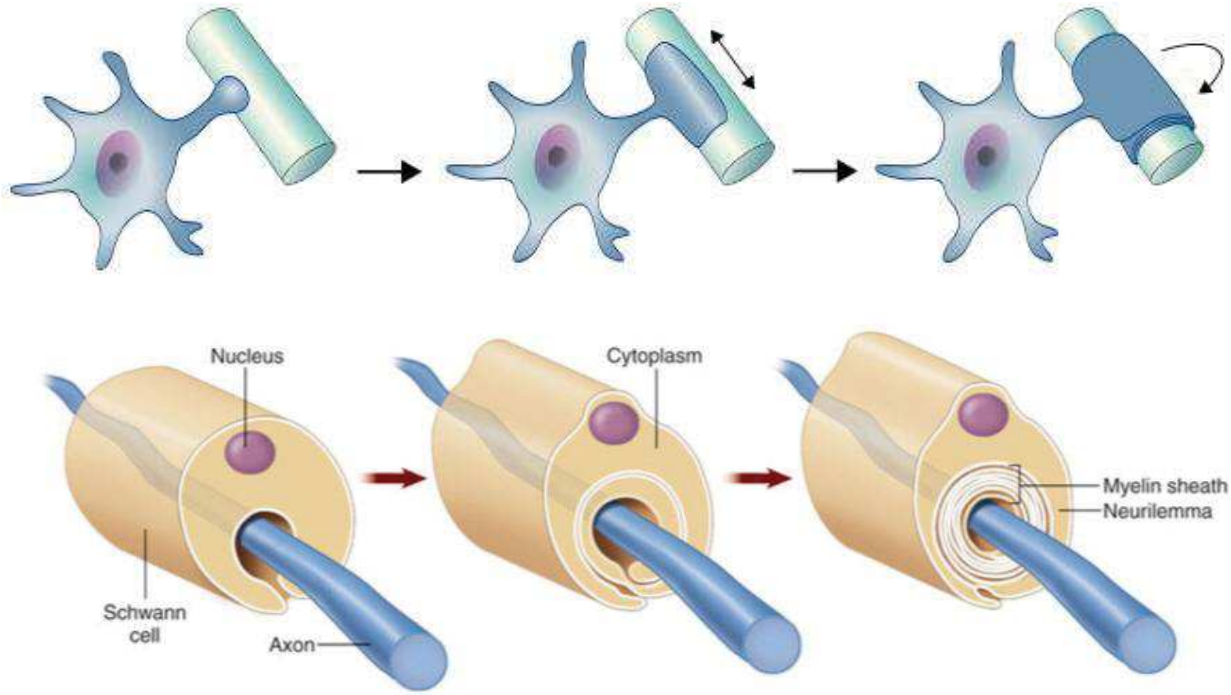

Figure 11 Schematic representation of myelination [154]. a) Oligodendrocyte myelination involves the creation of an outfolding that connects to the axon. Then this connection increases contact area and a myelin sheath is created by wrapping around the axon multiple times. b) Schwann cells engulf the axon and then wrap around axons to create a myelin sheath.

3.3 The role of Schwann cells

One role of myelin sheath formation by Schwann cells is to ensure efficient conduction of action potentials via electrical insulation. In between two Schwann cells are small areas where the axon is not myelinated called the nodes of Ranvier, which enable the fast propagation of action potentials from node to node (salutatory conduction). Another role of Schwann cells is to transport molecules to the axon to provide (metabolic) support.

3.3.1 The node of Ranvier

Myelinated axons are divided into distinct areas with different physiology, protein setup and sometimes different function within the PNS. These areas include the paranodal axoglial junctions (PNJ), juxtaparanodes (JXP) and internodes (Fig. 12) [170;171]. At the nodes of

Ranvier, microvilli emerge from the edges of the mSCs that myelinate the flanking internodes [172]. The nodes of Ranvier contain several sodium transporters that allow the generation of action potentials. Na^+/K^+ ATPases, Na^+/Ca^{2+} exchangers and voltage-gated Na^+ channels are all clustered within the node of Ranvier [173]. The α-subunit of Na^+ channels form a pore and β-subunits anchor this pore to both extracellular and intracellular components. In addition to Na^+ channels, nodes of Ranvier are enriched in K^+ channels [174] and the cytoskeletal and scaffolding proteins Ankyrin G (AnkG) and βIV spectrin. AnkG and spectrin connect the Na^+ and K^+ channels to the cytoskeleton of the node of Ranvier [175]. Additionally, the role of these scaffold proteins is to link Na^+ and K^+ to the extrinsic interactions, including interactions with the mSCs and the extracellular matrix (Fig. 12).

The formation of the node of Ranvier involves both axonal stimuli and stimuli coming from the mSC. Cytoskeletal proteins and ion channels are recruited to the place where mSCs connect to the axon. AnkG is an important neuronal regulator in the formation of the node, because AnkG is required for Na^+ channel clustering at the axon initial segment (AIS) that structurally and functionally resemble nodes of Ranvier. Nodal Na^+ channels, K^+ channels and bIV spectrin all contain Ankyrin-binding motifs, indicating that AnkG plays a central role in the accumulation of all these nodal factors to the same location, which is the developing node of Ranvier. When the AnkG-binding motif of Na^+ channels becomes phosphorylated by CK2, a protein kinase that is enriched in the node, the affinity for AnkG becomes much higher [176]. In accordance, mutations in βIV spectrin cause disrupted nodes, leading to ataxia and premature death [177]. When Na^+ channels initially cluster at the nodes, this is followed by the formation of the paranodal junction and then the clustering of K^+ channels at the juxtaparanodal region [178]. The initial Na^+ clustering occurs at sites adjacent to the SC extremities [179]. When the internodal regions become larger, these extremities displace the clusters of Na^+ channels until two clusters meet and fuse, forming 1 cluster where a new node of Ranvier is formed.

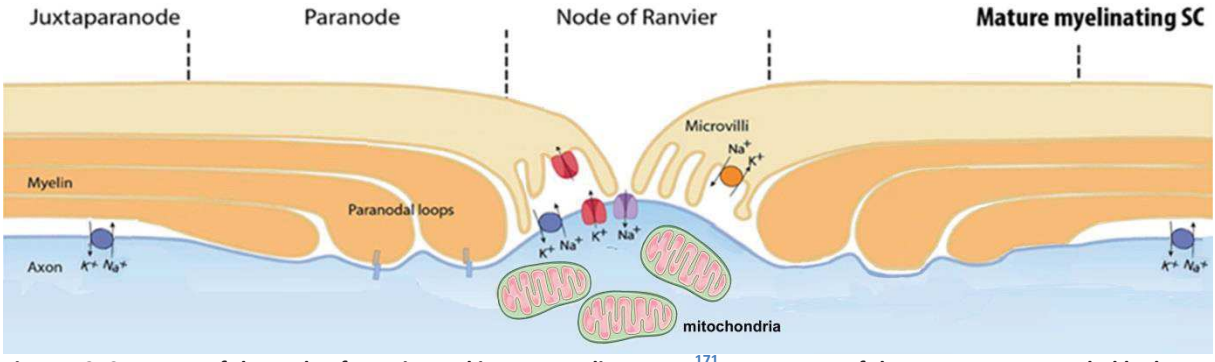

Figure 12: Structure of the node of Ranvier and its surrounding areas [171]. Most parts of the axon are surrounded by layers of myelin, although myelin is absent in small regions called the nodes of Ranvier. These areas are rich in iron channels, which enable salutatory conduction. Paranodes and juxtaparanodes are the regions flanking nodes of Ranvier. These regions contain the paranodal loops of myelin and K^+ channels at the axonal side.

3.3.2 Propagation of action potentials

The focus on the density of sodium and potassium channels in the node of Ranvier shows the importance of those channels in the function of the node of Ranvier. These ion channels are major players that allow fast propagation of action potentials from node to node. In the resting state, sodium channels are closed, whereas potassium channels are open, which creates a high concentration of potassium within the neuron, but a high concentration of sodium in the extracellular matrix. Overall, the cytosolic side of the membrane contains a negative potential. Regeneration of action potentials at the node of Ranvier follows the same four steps as

initiation of the action potential at the neuronal soma. Initially, opening of voltage gated Na^+ channels causes depolarization of the axonal membrane. Voltage-gated sodium channels are responsible for the rising phase of the action potential in membranes of neurons. Depolarization of the membrane induces a conformational change that opens the pore [180] and Na^+ enters the axon, raising the membrane potential by the increased concentration of positive ions in the cytosol of the axon. Meanwhile, the potassium channels remain closed. When the depolarization reaches a certain threshold, the other sodium channels open and a fast influx of sodium increases the membrane to a point that the membrane potential even becomes positive. Then, the sodium channels close while the potassium channels reopen, allowing the fast efflux of potassium towards the extracellular space. During this phase, the membrane potential decreases and at a certain point falls even lower than the resting state potential. The membrane potential recovers from this hyperpolarization to the equilibrium of the resting state potential by the sodium potassium ATPase that transfers sodium and potassium over the cell membrane against its concentration gradient. Voltage-gated sodium channels are located within the node of Ranvier whereas voltage-gated potassium channels are located at the juxtaparanode (Fig. 11). Sodium ions are transported out of the neuron by Na^+/K^+ ATPases. This ion-pump is located along the plasmalemma of PNS neurons and at the nodal, but not the paranodal or internodal, axolemma [173]. In the first step of the Na^+/K^+ ATPase reaction, binding of ATP accelerates the conformational transition that releases of K^+ in the cytosol. Upon potassium release, the ATPase becomes phosphorylated, which requires Mg^+ or ATP-Fe^{2+} as a co-factor and the binding of 3 Na^+ ions [181]. After phosphorylation, a reversion of the conformational transition occurs and the sodium ions are extruded from the cytosol.

3.3.3 Bioenergetics of the axon

Myelination enables fast propagation of action potentials along the axon, through the formation of the node of Ranvier and the electrical isolation that it provides along the internodes, forcing action potentials to jump from one node to the next. This is thought to save energy, because it limits the regeneration of action potentials, which is a highly energy demanding process [182;183], to the nodes of Ranvier. However, myelin synthesis and maintenance also costs energy [184]. Nonetheless, the fast signal transduction that myelination of axons enables, has big advantages in neuronal function. Tight wrapping of myelin around the axon is limiting entry of energy-rich metabolites, such as glucose, into the axon. Only at nodes of Ranvier, where no myelin is covering the axonal membrane, direct entry of metabolites is possible [185]. However, there are other transport systems occurring that allows the presence of sufficient metabolites inside the cytosol of the axon. This additional metabolic support is required, because next to basic survival mechanisms of the cell, neurons also require a lot of metabolites to produce enough ATP for depolarization and repolarization, which is constantly happening in firing neurons. Even though energy demand, and thus the necessity of the presence of metabolites, is higher in the node of Ranvier than in internodes, it is debated that Na^+/K^+ ATPases are present along the internode as well [186], indicating that metabolites need to be present in internodes too.

Besides action potential propagation, other critical ATP-dependent processes exist in the axon. Indeed, the intracellular transport of organelles, proteins, lipids and RNA along the axon is dependent on ATP, because axonal transport along microtubule tracks is mediated by two classes of ATP-dependent motor proteins (i.e. kinesins and dynein) [187]. Some authors suggest that this axonal transport energy cost can reach even 25% of the total energy consumption of the neuron [188]. The transport of mitochondria by these motor proteins to high-energy demand regions such as nodes of Ranvier is discussed in paragraph 3.5 and 3.6.

The abundance of mitochondria at the synapse indicates that these organelles also have functional roles in synaptic transmission as well. When the action potential reaches the axonal terminal, the depolarization of the cell membrane triggers opening of the voltage gated calcium channels. The influx of calcium at the synapse induces the fusion of synaptic vesicles filled with neurotransmitters with the cell membrane and the neurotransmitters are released in the synaptic cleft. The buffering of the calcium that entered the cell is one of the functions of mitochondria at the synapse. However, the production of ATP in this region is another important task, because the steps of synaptic transmission require energy [189]. The remobilization of synaptic vesicles, which are immobile before depolarization, and exocytosis are both ATP-dependent processes [189;190]. Then, ATP is also hydrolyzed for endocytosis, which is the production of new vesicles from the cell membrane, and for filling these new vesicles with neurotransmitter [189;190]. In addition, the membrane at the synaptic terminal contains Na^+/K^+ ATPase proteins, which use ATP like in the other parts of the axon. As synaptic terminals mitochondria can only come from the axon, this suggests that axonal transport of mitochondria is critical for the maintenance of the presynaptic terminals and therefore the maintenance of the axon itself.

3.3.4 Role of the Schwann cell and of the myelin sheath in the metabolic support of axons

Although glucose is the main energy metabolite for neurons, an alternative energy source exists in the form of lactate. Systemic administration of lactate maintains functional activity of neurons for several hours. In the CNS, the lactate that is required when the neuron is deprived of glucose was initially thought to be delivered only by astrocytes because they are also in contact with microvessels through their podocytes [191]. This transfer of lactate from astrocytes to neurons was called the lactate shuttle [192] (Fig. 13). When glutamatergic neurotransmission rates are changed, this lactate shuttle ensures that normal glucose utilization and energy consumption can continue. Glial cells have a higher glycolytic rate than neurons and some hypotheses even suggest that neurons depend completely on external lactate transfer and merely use glycolysis to maintain their antioxidant status and viability (via the production of NADPH for the reduction of glutathione). Since a myelin sheath limits free access of metabolites into the neurons, it has been suggested that next to astrocytes, also oligodendrocytes can be the source of lactate and play a role in the lactate shuttle. The most likely route for metabolites to be transferred from oligodendrocyte are small, extended spaces of non-compacted myelin that provides a connection between the glial cell's soma and the periaxonal space underneath the myelin. The products of glucose metabolism via glycolysis, pyruvate and lactate, can be released and taken up by monocarboxylate transporter proteins (MCTs). MCT1 is located in the myelin while MCT2 is located into the axonal membrane. Inhibition of MCT1 is not tolerated by neurons and results in axonal degeneration. This suggests that the transfer of lactate from oligodendrocytes to neurons is essential for neuronal viability. Although indications for the existence of the lactate shuttle exist in oligodendrocytes, a transfer of lactate between Schwann cells and neurons is unknown. The few indications of a lactate shuttle in the PNS are based on expression of MCT1 and MCT4 in Schwann cells, mainly in regions of noncompact myelin [193]. Downregulation of MCT1 in mSC/neuron cocultures increases myelination and decreases neurofilament, but a direct transfer of lactate has not been demonstrated.

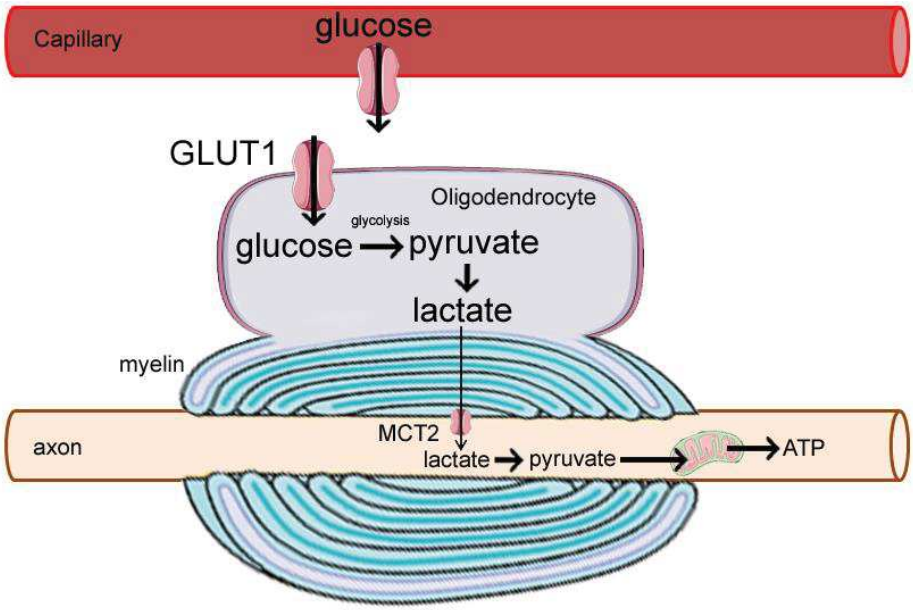

Figure 13: Schematic overview of the lactate shuttle from oligodendrocyte to neuron. Glucose, coming from the blood stream, is taken up by oligodendrocyte via GLUT1 transporters. Via glycolysis, this glucose is then transformed into lactate, which can be transported towards the axon through MCT1 and MCT2. In the axon, lactate is transformed back towards pyruvate, which can be used by axonal mitochondria to produce ATP via oxidative phosphorylation.

Neuronal or synaptic activity can influence the rate of the lactate shuttle and therefore is an important factor of mitochondrial function [194]. Synaptic activity induces these mechanisms via activating changes in gene expression, which results in long-lasting adaptation to this stimulus. Examples of such adaptive responses are activity-dependent dendritic remodeling and improving neuronal protection. The upregulated genes as a response of synaptic activity are called activity-regulated inhibitors of death (AID) genes. The exact working mechanisms on how these AID genes improve neuroprotection are not well understood. However, it seems that the functional changes induced by AID gene expression work via protection of mitochondria.

3.3 Schwann cell demyelination and remyelination

The state of the myelin relies on a balance between positive and negative regulators that modulate mSCs between myelination and dedifferentiation/demyelination. Whereas positive regulators stimulate transitions from immature SC toward mature mSC, negative regulators promote the reverse transition towards immature SC at the expense of myelination. Examples of positive regulators that support myelination are Krox-20, Sox10, NF-κB and cyclic AMP (cAMP). Promyelin transcription factors in mSCs, such as Krox-20/Egr2 are activated by axonal signals. On the other side of the myelination balance are the negative regulators c-Jun, Notch, Sox2 and NT3. For example, an upregulation of c-Jun is observed in nuclei of SCs in demyelinating diseases [195]. The promyelination factors and negative regulators can also interact with each other to form a pathway or feedback loops. At physiological levels, the anti-myelination factor c-Jun inhibits myelination via the inhibition of pro-myelination regulators Krox-20 or cAMP [196]. In contrast, the transcription factor CHOP inhibits myelination by its interaction with c-Jun. When the nerve becomes damaged, this balance between positive and negative regulators is disturbed. mSCs and non-myelinating Remak cells that surround axons respond to nerve damage and axonal degeneration by rapidly activating c-Jun [197], which induces the transdifferentiation of myelinating SCs and Remak cells into repair SCs distal to the nerve injury. Importantly, other factors such as Sox2 and Id2

are also upregulated after nerve damage, which suggest a role for these genes in the regeneration process as well and possibly in transdifferentiation of SCs. These repair SCs form regeneration tracks, also called bands of Bungner. The bands of Bungner guide regenerating axons along the nerve in order to reconnect the neuronal soma with its corresponding synapses. In addition to its function as a guide, repair SCs break down inhibitors of axonal regeneration. This works via myelin autophagy and by attracting macrophages to the injury site (Fig. 14) [198]. Moreover, repair SCs support survival of the regenerating neurons by secreting trophic factors. c-Jun is the driving force behind the transition into repair SCs by promoting expression of genes that fulfill all these support mechanisms. Inactivation of c-Jun in SCs results in a strong impairment of nerve regeneration after injury. Importantly, the shift towards a repair SC phenotype is reversible, since these Bungner cells associate with the axons they helped regenerating and then transform back to either a myelinating SCs or a Remak cell [199].

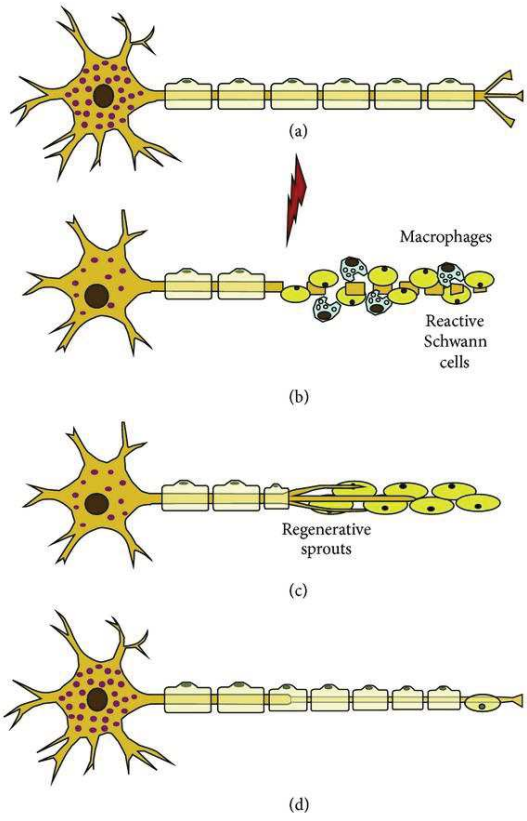

Figure 14: Demyelination and remyelination [198]. In healthy condition, axons are surrounded by a myelin sheath (a). However, damage to the axon can result in a destruction of myelin and possibly the axon itself (b). As a response repair SCs and macrophages become active and remove the damaged myelin debris. Then, repair SCs guide the regenerating axon towards its target (c). Then, a new myelin sheath is formed (d).

3.4 Difference of mitochondria in internodes and the node of Ranvier

As mentioned before, mitochondria are able to adapt their shape and function in response to their environment. Indeed, a couple of significant differences between SC mitochondria and axonal mitochondria have been observed. It has been reported that condensed mitochondria (indicating small matrix volume and high respiratory activity) are abundant in the axoplasm, but not in SCs [200]. Nonetheless, also the location within the same cell changes mitochondrial morphology. Since the nodes have particular energy needs, the roles of mitochondria that are located in or near the node of Ranvier are of interest. Even though majority of mitochondria (>90%) is located in internodes, internodes also contain the largest volume of the axon. Therefore, the density of mitochondria is a more interesting factor in investigating local energy homeostasis and energy homeostasis in nodes of Ranvier in particular. Although the

density of mitochondria is already high throughout the axons in PNS neurons, the mitochondrial density is shown to be even higher at the paranode-node-paranode (PNP) region. Mitochondria residing in the PNP are also smaller than internodal mitochondria. Furthermore, these mitochondria contained fewer cristae compared to mitochondria residing in internodes. The higher density in the nodal axoplasm has not been observed in the CNS. In contrast, mitochondria are absent in 39% of nodes of Ranvier in the cerebellum and even 66% of nodes in the optic nerve [201]. Axonal firing appeared to decrease mitochondrial motility of mitochondria within PNP regions, whereas the motility of internodal mitochondria is not influenced [201]. As a result, the density of mitochondria in the nodal axoplasm increases in response to axonal firing.

The high density of mitochondria at PNPs suggests a need for ATP production at these regions. This would suggest that mitochondria produce more ROS in nodes of Ranvier as well. Another indication for increased ROS production by mitochondria located in the node of Ranvier is the observation that nodes of Ranvier are the initial sites of mitochondrial damage induced by oxidative stress [202]. In nodes of Ranvier, oxidative stress initially induces depolarized mitochondria, resulting in changes in the morphology of mitochondrial membranes and disruption of cristae. Mitochondrial transport also becomes impaired as a result of these morphological disruptions. This shows that nodes of Ranvier are sensitive to oxidative stress, which is possibly the result of an already elevated ROS concentration due to a higher mitochondrial density. The mitochondrial changes induced by oxidative stress expanded from the nodes of Ranvier bidirectionally into internodes, showing that mitochondria are more sensitive to ROS the closer they are located to nodal areas.

3.5 Anterograde and retrograde mitochondrial movement

Mitochondria are dynamic organelles and their shape can be changed mainly via fusion and fission. Nonetheless, another important feature of neuronal mitochondria is their transport along the axon, using the cytoskeleton as guidance. Estimations on the percentage of motile mitochondria ranges between 10% and 30% and this transport is not continuous for mitochondria can frequently change direction, pause or stop completely [203]. These mobility patterns are possible because of the ability of mitochondria to connect to anterograde or retrograde motor proteins and to a docking and anchoring machinery. This connection between mitochondria and motor proteins usually involves receptors located at mitochondrial membranes (Fig. 15) [204].

Kinesin superfamily protein (KIF) is a family of proteins guiding mitochondrial transport by converting ATP energy into unidirectional motion along microtubules [205]. For example, KIF5 proteins play a key role in anterograde transport of neuronal mitochondria. Each KIF5 heavy chain contains an amino-terminal motor domain, whereas carboxy-terminal domain connects to kinesin light chains or directly to mitochondria or mitochondrial adaptor proteins. Mutations in the KIF5b gene result in clustering of mitochondria in the soma, due to impaired transport along the axon towards synapses. In addition to KIF5, two members of the kinesin-3 family, KIF1B-α and KLP6, modulate mitochondrial transport, since it has been shown that mutant forms of KIF1B- α and KLP6 decrease their migration velocity and the density of mitochondria within the axon[206]. The protein Milton is involved in mitochondrial transport in neurons by association with KIF5. Milton not only connects to KIF5, but also with mitochondria via the interaction with mitochondrial rho (Miro), which is a Rho family GTPase located in the mitochondrial outer membrane. Miro contains two Ca^{2+}-binding sites and two GTPase domains and connects mitochondria to Milton and KIF5. As a result, the

Miro-Milton complex connects mitochondria to its motor protein and thus this complex is required for anterograde transport of mitochondria. Mutations in genes coding for Milton or Miro result in impaired mitochondrial transport and depletion of mitochondria in synapses. Two Milton orthologues (TRAK1 and TRAK2) have been identified in mammals that interact with KIF5 [207]. Interestingly, these Milton proteins not only transport mitochondria, but are also involved in transporting other organelles through neurons. Another protein that can connect mitochondria to KIF5 is called syntabulin, which binds directly to the cargo-binding site of KIF5 and attaches to the outer mitochondrial membrane via its C-terminal domain [208]. Fasciculation and elongation protein-ζ1 (FEZ1) is a protein responsible for axonal outgrowth. FEZ1 is yet another KIF5 adaptor protein that is involved in axonal transport of mitochondria. Finally, RAN-binding protein 2 (RANBP2) can bind mitochondria to KIF5 to undergo anterograde transport. Inhibition of RANBP2 and KIF5B or KIF5C has been shown to result in mitochondrial clustering near the nucleus, although the role of RANBP2 in neurons has not been established.

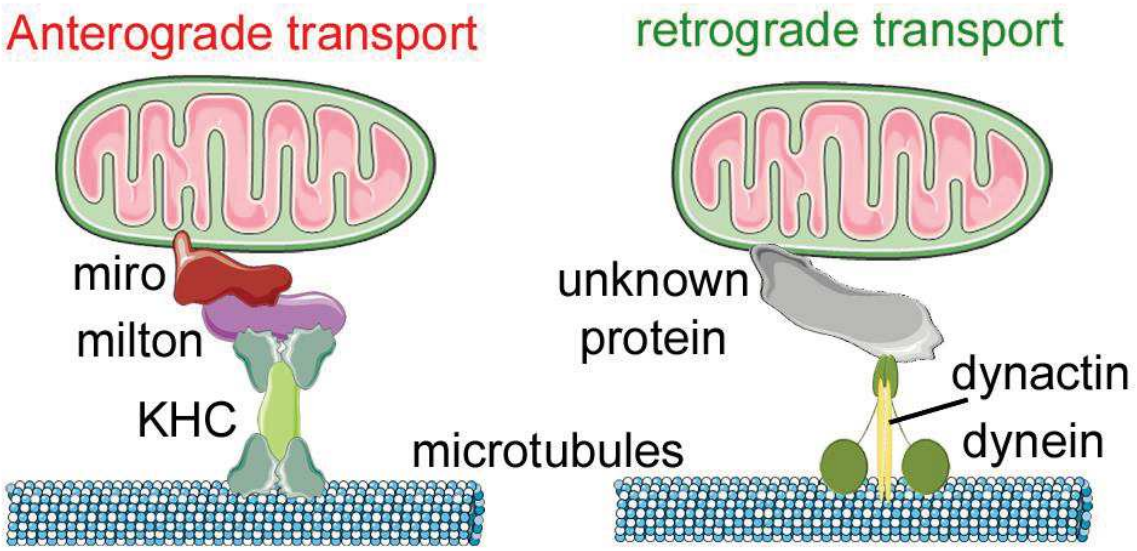

Figure 15: Transport of mitochondria along the cytoskeleton. Different motor proteins are involved in different transport direction. For anterograde transport, mitochondria recruit the Miro-milton complex and binds to KHC to connect to microtubules (a). In contrast, retrograde transport involves dynein proteins, but the proteins located within mitochondrial membranes that can connect to dynein are still not identified (b).

Opposed to anterograde transport, mitochondria can also move in a retrograde direction. Instead of kinesin proteins that regulate anterograde mitochondrial transport, it is cytoplasmic dynein that is the driving protein in retrograde transport. Cytoplasmic dynein consists of two dynein heavy chains and several dynein intermediate chains, dynein light intermediate chains and dynein light chains. Dynein mutations located in heavy chains impair retrograde mitochondrial movement regarding migration velocity and run length [209]. The interaction between mitochondria and dynein is much less described than mitochondria's interaction with kinesin. Supposedly, the dynein light chain protein TCTEX1 binds to VDAC1, which is located in mitochondrial outer membrane. Dynactin binds to both cytoplasmic dynein and to microtubules via its p150 component, which can regulate the interaction between dynein with its cargo. It has been shown that dynactin can bind to mitochondria as well *in vitro*. However, *in vivo* analysis showed that dynactin only has a coordinating function in bidirectional movement of organelles and is not required to link those organelles to dynein. Snaptin is another motor adaptor protein that links endocytic organelles to dynein in neurons. However, an involvement of snaptin in mitochondria-dynein connection has not been established, so a clear demonstration of a stable connection between this organelle with dynein is still lacking.

Nonetheless, dynein-mediated retrograde transport of mitochondria seems to require the action of Miro as well. Next to Miro's effect on anterograde transport through kinesin, loss of Miro gene impairs dynein-mediated mitochondrial transport. This shows that Miro has more roles than being a KIF5 adaptor protein, even though a Miro-dynein association has not been established either.

3.6 Mitochondria movement to high energy demand regions

The functional reason behind migration of mitochondria is that ATP has a limited diffusion capacity, which causes problems in long axons in particular. To avoid ATP shortages in the distal synapses, mitochondria migrate along axons. For the same reason, mitochondria are able to dock at locations where energy dependency is high and be released when they have to move somewhere else or to be regenerated for example.

Transport and spatial distribution of mitochondria over the axons is directly correlated with synaptic activity. The driving forces behind mitochondrial transport to high demand regions such as synapses and nodes of Ranvier in response to synaptic activity are ATP and Ca^{2+} [210]. Mitochondrial velocity increases when they enter cellular regions with high ATP levels and decreases when local ATP concentrations are low. Due to the high use of energy in synapses and nodes of Ranvier, ATP is depleted in these regions, and hence mitochondria slow down. Similarly, mitochondrial movement decreases when local Ca^{2+} concentrations increase. Local Ca^{2+} increases are mostly the result of Ca^{2+} influx through voltage-dependent Ca^{2+} channels at presynaptic terminals or nodes of Ranvier. In other words, action potentials open these Ca^{2+} channels, Ca^{2+} enters the neuron and mitochondrial velocity decreases [211].

The notion that ATP and Ca^{2+} influence mitochondrial velocity suggests that these molecules are influencing motor proteins, motor adaptor proteins or their interaction with mitochondria. The paradigm on why mitochondrial binding to these classes of proteins involves multiple adaptor proteins is that neurons are able to regulate mitochondrial transport by different mechanisms in response to different physiological signals. Indeed, it has been shown that ATP/ADP and Ca^{2+} can influence the interaction of mitochondria with KIF5 through these adaptor proteins, which shows that mitochondrial transport and distribution is regulated to fulfill mitochondrial functions at the location where it is most needed. In addition, Miro protein has been identified as a Ca^{2+} sensor[212]. In neurons expressing Miro with mutations in its Ca^{2+} sensing domains, mitochondria no longer slow down in areas with high Ca^{2+} levels. These mutated Miro proteins cannot bind Ca^{2+}, showing that Miro is an important candidate as the main regulator of mitochondrial movement to and recruitment at the nodes of Ranvier and activated synapses in response to increased action potential firing.

Next to variable mitochondrial speeds, mitochondria can become stationary and reversely, stationary ones can be remobilized and redistributed. Factors that can change mitochondrial velocity can similarly switch stationary mitochondria to mobile ones. These factors include changes in axonal physiology, but also changes in axonal activity. Vice versa, the state of mitochondria is an important factor in axonal and synaptic function. For example, mitochondrial anchoring is required for synaptic transmission and for axonal branching and maintenance. The requirement for mitochondrial docking provides a need for factors that regulate mitochondrial docking as well. Syntaphilin acts as a static anchor that immobilizes mitochondria. Synaptaphilin contains a carboxyl-terminal mitochondria-targeting domain and an axon-sorting sequence, which make it possible to be located in the mitochondrial outer membrane of mitochondria that are targeted to axons. Syntaphilin arrests mitochondrial

movement by coupling mitochondria to microtubules. Deletion of syntaphilin in mice results in an increase of motile mitochondria but a reduction of mitochondria within axons. Conversely, over-expression of syntaphilin results in immobile mitochondria. Syntaphilin is also involved in activity-dependent immobilization of axonal mitochondria. In neurons that fire action potentials, the Miro-Ca^{2+} pathway is activated, but this does not result in reduced mitochondrial velocity or mitochondrial docking in syntaphilin deficient mice. On the other hand, dendritic mitochondria are immobilized, showing syntaphilin's selectivity for axonal mitochondria. Syntaphilin specifically binds to the KIF5 C-terminal tail and this binding is facilitated via Miro-Ca^{2+}. Binding of syntaphilin to KIF5 inhibits ATPase activity and prevents the assembly of the Miro1-TRAK2-KIF5 transport complex. Interestingly, neuronal activity stimulates the recruitment of syntaphilin into the mitochondrial membrane, suggesting that syntaphilin undergoes dynamic translocation in response to neuronal activity.

The central role that calcium appears to play in mitochondrial function and mitochondrial movement points to the ER with its MAM as a potential regulator of these processes.[213] However, the influence of the ER on such distally located mitochondria depends on the presence of ER all the way throughout the axon. Reticulon-4 is a protein that promotes ER tubulation, and subsequently influences ER-mitochondria interactions in the axon[214]. Other ER tubulation enzymes fulfil a similar function, including receptor expression enhancing protein 1 (REEP1), which is a known regulator of both ER network formation and mitochondria membrane dynamics. Likewise, the microtubule severing protein spastin plays a role in connecting ER tubules to the cytoskeleton and in the trafficking of mitochondria along axons. Hence, migration of mitochondria and tubulation of the ER go hand in hand, suggesting the role of the ER in mitochondrial movement to energy dependent areas.

3.7 Conclusion

Myelinating Schwann cells have several functions to support neuronal functions and axonal mitochondria. The myelin sheath has metabolic advantages and increases action potential conductivity, but it also creates spatial differences in the axon and the effects of these spatial differences on mitochondrial physiology have only partially been investigated.

Also the lactate shuttle is a process that has not been fully understood yet. Since most cells use pyruvate for oxidative phosphorylation, instead of transforming it to lactate, the origin of lactate that is transported from Schwann cells to axons is not established. Also the effect of the lactate shuttle on neuronal function and mitochondrial function is unknown.

Furthermore, the movement of mitochondria along the axon to their target destination has been shown to be a complex mechanism. The connection between mitochondria and the cytoskeleton works via a complex of multiple proteins, but the regulation of this complex has to be investigated further.

Chapter 4) Mitochondria and ROS in neuropathies

The role of nervous system is to send signals from the brain to the organs and back. In the conduction of these signals, mitochondria play an important role. However, the nervous system can become damaged or may not function properly, which may result in the development of neuropathies. Multiple sorts of neuropathies exist, depending on the mechanism that causes the neuropathy and the cell type and region of the nervous system that is affected. These different sorts of neuropathies have different symptoms.

Several of the most important neuropathies both in the CNS and PNS involve mitochondria and dysfunctional mitochondrial functions and/or physiology. In this chapter I will discuss the role of mitochondria and ROS in amyotrophic lateral sclerosis, Alzheimer's disease, Parkinson's disease, multiple sclerosis and Charcot-Marie-Tooth diseases.

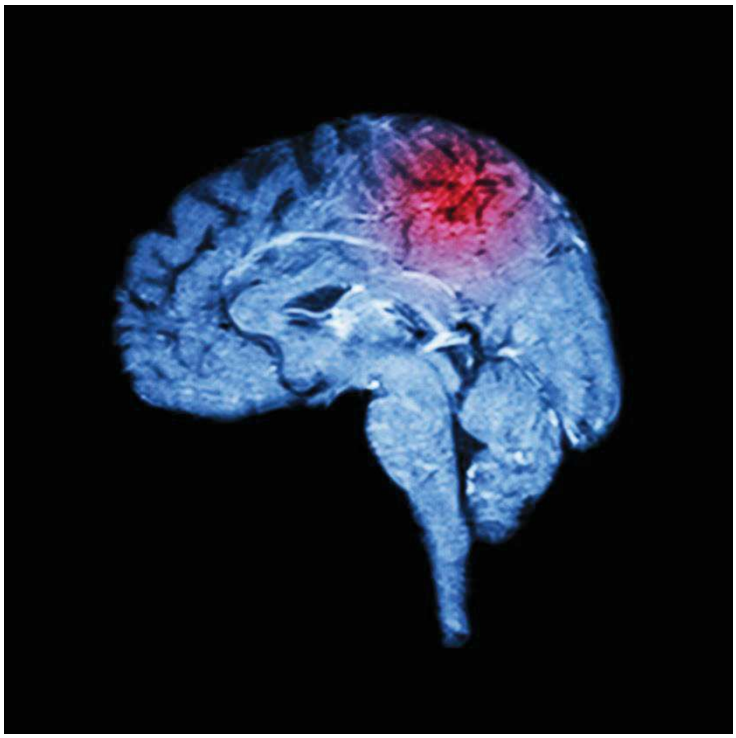

4.1 Amyotrophic lateral sclerosis

Amyotrophic lateral sclerosis (ALS) is a neuronal disease that progressively affects motor functions [215]. The incidence rate of ALS is 2.7 per 100,000 people and patients suffer from muscle weakness, twitching, and cramping. Most cases are sporadic, although 5% of the cases showed a hereditary component [216]. While the exact pathological mechanisms remain unclear, the role of mitochondria and the ROS they produce have been demonstrated.

Most studies point towards ROS as a central player in ALS pathology. Mutations in the SOD1 gene have been detected in around 20% of familial ALS cases [217]. SOD1 mutations decrease the quenching capacity of H_2O_2, which can have several downstream effects. Indeed, numerous studies demonstrated a correlation between ALS and increased oxidative stress. Increased protein carbonyl levels, indicating elevated oxidative damage to proteins, have been detected in both the spinal cord and motor cortex of ALS patients [218]. In addition, increased 3-nitrotyrosine levels have been measured within large ventral horn neurons [219]. Next to protein oxidation, lipid oxidation was detected in motor neurons, astrocytes and macrophages. Oxidative damage to DNA has been found to be elevated in the spinal cord of ALS patients, especially in the ventral horn. Not only neurons, but also other brain components can contain more oxidative damaged DNA, proteins or lipids, including the CSF [220]. Next to increased oxidative stress, other mitochondrial abnormalities, such as disrupted axonal transport, have been reported in ALS patients. The SOD1 mutations in ALS patients correlate with reduced astroglial glutamate transporter EAAT2, which leads to over-stimulation of glutamate receptors of neurons and excessive neuronal firing. In addition, this glutamate excitotoxicity causes excessive calcium influx, which results in neurodegeneration.

Interestingly, in transgenic mice with mutant SOD1, the most severely oxidized protein appeared to be SOD1 itself [221]. This finding suggests that mutant SOD1 is not only incapable of quenching oxygen radicals, but also inhibits the function of normal SOD1 expressed by the normal allele. Nevertheless, some SOD1 mutations involved in ALS have been shown to leave the reducing capacity of the protein intact, suggesting that alternative mechanisms are probably existing.

4.2 Alzheimer's disease

Alzheimer's disease (AD) is a dementia disorder with progressive deterioration of cognitive function and memory loss. In Europe, 11.08 per 1000 persons are diagnosed with Alzheimer every year [222]. The exact pathological pathway is not known due to the many genes that have been shown to be involved. Nonetheless, two major causes have been characterized being the formation of amyloid plaques and the formation of intracellular neurofibrillary tangles.

ROS have been linked to AD as well [223]. For example, DNA and RNA oxidation is increased in AD brains. Also increased protein carbonyl levels have been observed in AD frontal lobe, hippocampus and superior middle temporal gyrus. Besides, nitrotyrosine and dityrosine cross-linked proteins are elevated 8-fold and 3-fold respectively in hippocampal and neocortical regions of AD brain. Oxidation-induced crosslinking of proteins may result in the resistance of lesions against degradation, even though there is abundant ubiquitination of these proteins. Lipid peroxidation and the subsequent altered phospholipid composition have also been detected in AD brains. Interestingly, the antioxidant response by SOD is elevated in AD brains, which suggests that the normal compensatory mechanisms against ROS may be insufficient in AD patients.

The increased ROS levels and oxidative stress in AD brains is correlated with mitochondrial dysfunctions. For example, mutations in the MFN2 gene in AD patients result in a disbalance in mitochondrial fusion and fission and an abnormal distribution of mitochondria in the hippocampus [224]. Knockout of MFN2 in mice resulted in neurodegeneration in the hippocampus. This phenotype resembles many of the characteristics of AD. Another explanation of mitochondrial dysfunction in AD is a dysfunctional ER-mitochondria interaction. MAM are uniformly distributed throughout the hippocampal neurons and impaired MAM function results in neuronal degeneration. Interestingly, MAM function appeared to be upregulated in AD patients, leading to increased ER-mitochondrial interaction [225]. Similarly, neuronal cells exposed to amyloid β, an AD mouse model (APPSwe/Lon) and cortical tissue from AD patients all showed affected MAM. In mice, MAM-associated proteins are upregulated already at 2 months of age, which is before the presence of visible amyloid plaques [55]. In an early stage of AD, the increased expression of MAM proteins could indicate a stress response, where neurons try to maintain proper function. Although most MAM-associated proteins were shown to be upregulated, σ1R, a molecular chaperone located in the ER–mitochondria interface, was significantly decreased. In accordance, decreased σ1R was detected in hippocampus tissue from AD patients.

4.3 Parkinson's disease

Parkinson's disease (PD) is a progressive neurodegenerative disorder that results in the loss of dopaminergic neurons of the substantia nigra that project to the putamen [226]. The incidence of Parkinson's disease is 17.2 per 1000 persons per year [227] and patients suffer mainly symptoms that impair motor functions, such as tremor at rest, rigidity, akinesia or bradykinesia and postural instability [228].

A defective ETC has been an established marker of Parkinson's disease. In particular a defective complex I has been associated with the pathogenesis of PD. Blocking complex I by 1-methyl-4-phenyl-1,2,3,4-tetrahydropyridine or rotenone results in neurodegeneration selectively in the substantia nigra pars compacta, which are also the cells that are most affected by PD pathology. Moreover, decreased complex I activity was shown in brains of patients with sporadic PD [229]. A decreased complex I activity may lead to decreased ATP production and an increase in the production of ROS. Some studies reported only a 25-30% decrease in complex I activity in PD patients, which is not sufficient to cause ATP depletion [230], although others have shown a decrease up to 60% [231]. Nonetheless, increased oxidative damage to proteins, lipids, and DNA has been observed in postmortem brain samples from PD patients [232]. However, this oxidative damage and increased levels of ROS may be derived from sources other than the neuronal mitochondria. For example, neighboring glial cells may be causing the observed damage to PD brains. In addition to possible decreased ATP and increased ROS production, calcium homeostasis is affected by PD pathology. It has been shown that PINK1, a regulator of calcium release via the mitochondrial Na^{+}/Ca^{2+} exchanger, is affected in PD. PINK1 ablation indeed results in impaired Ca^{2+} efflux from mitochondria, accumulation of mitochondrial $Ca^{2+,}$ increased production of mitochondrial ROS, decreased mitochondrial respiration and a lowered threshold for Ca^{2+}-dependent opening of the mitochondrial permeability transition pore complex in dopaminergic neurons. This results in increased apoptosis [233]. Another protein that is connected to PD is parkin. Mutant parkin results in morphological and functional mitochondrial defects, including a decrease in the membrane potential (by 30%), complex I activity (by 45%), ATP production (by 58%) and an increase mitochondrial fragmentation [234]. This shows that mitochondrial morphology is also different in PD mitochondria.

Finally, a protein that plays an important role in Parkinson's disease is α-synuclein. In Parkinson's disease, aggregates of α-synuclein accumulate in Lewy bodies located in neurons and these aggregates are thought to contribute to neuronal loss. In healthy neurons, α-synuclein is associated with mitochondria as it regulates the balance between mitochondrial fission and fusion [235]. However, overexpression of α-synuclein increases the flux of calcium from the ER to mitochondria, and the number of ER-mitochondria contact sites increases [236]. These observations show that MAM are involved in mitochondrial physiology in Parkinson's disease, including calcium homeostasis [237].

4.2 Multiple Sclerosis

Multiple Sclerosis (MS) is a chronic inflammatory disease of the CNS with a crude prevalence of 151.2 per 100,000 French inhabitants [238]. MS is characterized by the presence of demyelinated lesions in both white and gray matter and it progresses in episodes of exacerbated immune responses followed by remission periods [239]. These immune responses involve widespread microglial activation. Over time, MS patients develop neuronal and axonal degeneration with extensive cortical demyelination. MS pathology manifests by a variety of symptoms including fatigue, numbness and tingling muscle spasms, stiffness and weakness, motor problems, and organ failure.

The activated microglia and macrophages are thought to be the initial source of ROS that cause damage in MS lesions [240]. Iron mediated ROS has been shown to cause oxidative stress in MS lesions [241], since iron is abundant in myelin [241;242] and during demyelination, this iron becomes accessible for ROS [242] to induce damage to lipids and proteins. Indeed, MS patients that were treated with iron chelator deferoxamine showed an improvement of their condition. It is thought that by chelating the iron deferoxamine prevents the production of hydroxyl radical from H_2O_2 and $O_2^{\bullet-}$. Mitochondrial dysfunction and an increase of mitochondrial ROS contribute as well in progressive MS. Indeed, activity of mitochondrial complex IV is increased in active MS lesions even though mitochondrial mass is also increased in MS lesions [243].

Cuprizone treatment is used in animal studies as a model for toxic demyelination, like in MS [244]. Cuprizone treatment and the resulting demyelination in the nervous system causes changes in mitochondria, such as increased complex IV activity [245] and increased ROS levels. Additionally, decreased mnSOD and CuZnSOD are measured [246], indicating that the elevated ROS levels are possibly caused via both increase mitochondrial activity as antioxidant failure. Cuprizone also induced decreased levels of glutathione, the main electron donor of the antioxidant GPx, which leads to low GPx activity.

Cuprizone treatment eventually affects ER function. Also Rab32, a known regulator of the MAM, is highly expressed in active MS lesions of both human MS patients and mouse models [247]. The high expression of Rab32 leads to changes in mitochondrial physiology and the induction of apoptosis. Impaired ER function disrupts protein and lipid synthesis as well, including proteins and lipids that would build up the myelin sheath in a healthy condition. Therefore MAM function, including the exchange of Ca^{2+} between ER and mitochondria, contributes to the further breakdown of the myelin sheath and controls neuronal degeneration in active MS lesions [247]

During inflammatory events, the increase of ROS induces further mitochondrial damage and reduced ATP production, which inhibits axonal mitochondrial transport. Also transport of other axonal compounds is inhibited in MS, which affects axonal integrity [239].

All these mechanisms indicate that the pathologic immune response in MS triggers a feedback loop that involves demyelination, mitochondrial dysfunction, elevated ROS production and ER failure (Fig. 16) and this mechanism progressively destroys the myelin sheath and eventually results in neuronal death.

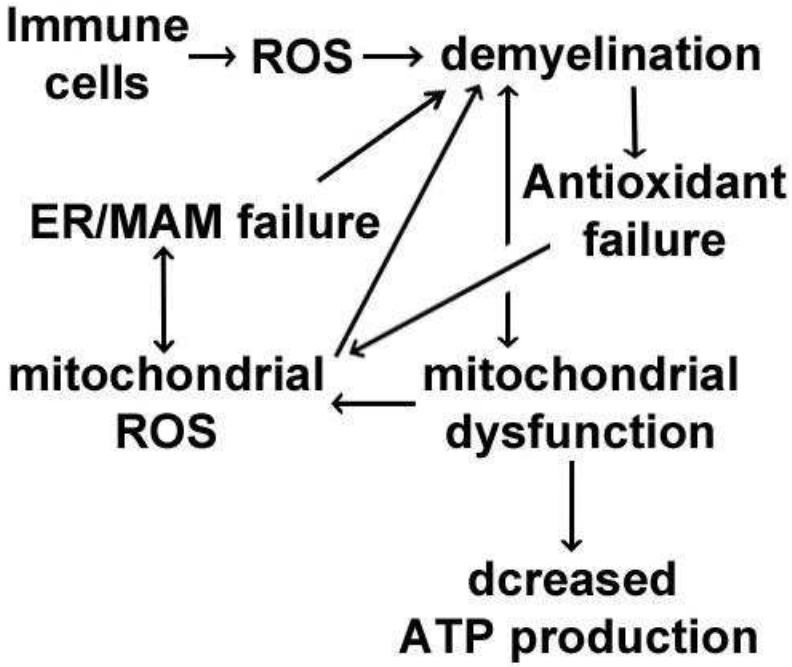

Figure 16: Steps in the development of MS pathology that form a feedback loop. Immune cells produce ROS that induces demyelination. This demyelination causes mitochondrial dysfunction in oligodendrocytes and neurons, which elevates ROS levels. This mitochondrial ROS causes damage to the endoplasmic reticulum and mitochondrial associated membranes. The failure of the ER on its turn contributes to the demyelination and mitochondrial dysfunction. Demyelination also induces antioxidant failure which exacerbates ROS. Mitochondrial dysfunction affects ATP production.

4.5 Charcot-Marie-Tooth disease

CMT disease is a genetically and phenotypically heterogeneous group of disorders with a prevalence of CMT is 1 per 2500 people [248]. The first signs of CMT are found distally in the feet and progress proximally. Symptoms of CMT patients include a combination of peripheral nerve related motor and sensory deficits, high foot arches and curled toes. These symptoms present themselves as length-dependent paresis, muscle atrophy and areflexia. The chronic nature of CMT leads to the development of foot deformities, hammertoes and high-arched feet in approximately 70% of patients. As the disease progresses, the hands may also become deformed. Sensory system symptoms are common as well, which include loss of vibration and joint position sense and decreased pain and temperature sensation. Patients also report numbness and tingling in their feet and hands. Scoliosis occurs in approximately one-third of CMT cases.

CMT can be divided in demyelinating forms (CMT type 1) and axonal forms (CMT type 2) [249]. Interestingly, clinical symptoms are not different between the demyelinating or axonal

forms. The age of onset of both CMT1 and CMT2 is in the first or second decade of life, but the severity of the disease can be highly variable with some patients suffering severe symptoms at an early age and others showing only mild features in their whole lifetime. For example, patients with CMT1A, which is the most common form of CMT, rarely will ever need the use of a wheelchair. On the other hand, CMT2A has greater severity with most patients requiring a wheelchair at a young age [250]. Details about the genetic bases of CMT diseases and the pathomechanisms can be found in Sziget & Lupski, 2009 [239].

Diagnostic tests may include electrophysiological tests and sural nerve biopsies. These electrophysiological tests are especially helpful to distinguish between demyelinating CMT type 1 and axonal CMT type 2, the former showing a NCV below 38 m/s and the latter being associated with normal NCV [250], but reduced compound muscle action potential. Sometimes an intermediate CMT is classified when the patient cannot be classified confidently as either CMT1 or CMT2 [251]. These intermediate CMT patients have features of both demyelination and axonopathy. Sural nerve biopsies from CMT1 patients reveal segmental demyelination and onion bulb formation. CMT2 patient sural nerves show axonal degeneration, but a healthy myelin sheath.

4.5.1 CMT Type 1

Although CMT1 and CMT2 cannot be distinguished based on the patients' symptoms, the cellular deficits that cause these symptoms differ between the two forms. This is also reflected by the detection of genetic factors, which are different between CMT1 and CMT2. Not surprising, the demyelinating forms of CMT show mutations in genes involved in myelin production or its regulation. For example, it has been shown that elevating cJun in SCs of a CMT1A mouse model prevents myelin loss of myelinated sensory axons [252]. This prevention is correlated with an improvement of behavioral symptoms in these mice. Sox2 has also been identified to be a physiological regulator of SC myelination *in vivo* that is implicated in myelination disorders in the PNS, such as CMT1 [253]. Next to hereditary causes, acquired inflammatory etiologies, exposure to toxic compounds such as lead or chemotherapeutic agents or vitamin deficiencies as thiamine or B12, are factors that contribute to CMT disease development.

Deletion of serine 63 from P0 glycoprotein (P0S63del) causes CMT1B neuropathy in humans and a CMT1-like phenotype in mice. As a result of a misfolded P0S63del, SCs develop an increased unfolded protein response and increase the expression of CHOP. This transcription factor has previously been associated with apoptosis in ER-stress and apoptosis. However, ablation of CHOP in S63del mice rescues their motor deficit and partially prevents from demyelination, indicating that S63del causes the phenotype effects through CHOP [254]. Next to myelination problems, mitochondrial deficits have been correlated with c-Jun, CHOP and the unfolded protein response. Upon activation of c-Jun and CHOP-10, expression of genes that are involved in the unfolded protein response of specifically mitochondrial proteins (UPRmt) is increased. UPRmt involves mitochondrial chaperones and proteases that remove dysfunctional proteins from the mitochondrial matrix [255].

4.5.2 CMT Type 2

The genetic causes of CMT2 are partially distinct from CMT1. The most common mutations observed in CMT2 are in genes encoding for MPZ, HSPB1 and MFN2 [256]. The detection of MPZ mutations in CMT2 patients is remarkable, because MPZ is a protein component of compact myelin in the PNS, where it plays a crucial role in myelin formation and adhesion [257]. CMT2 patients with mutations in the MPZ gene have been shown to suffer from severe axonal neuropathy with Wallerian-like degeneration and clusters of regeneration. However,

no evidence of demyelination was observed in these patients. The precise mechanism on how this myelin related gene causes the axonal CMT2 is not fully understood. HSPB1 belongs to a family of heat shock proteins and is involved in a multitude in cellular mechanisms. In peripheral nerves however, its most prominent role is the stimulation of neurofilament formation and dynamics of cytoskeletal proteins [258]. This finding links HSPB1 mutations with impaired transport of cargo, and possibly impaired mitochondrial transport, which has also been reported in CMT2.
More than 60 mutations in the MFN2 gene have been identified in CMT2A patients [259] and almost all these mutations are single point mutations in the coding sequence that cause an amino acid substitution. MFN2 mutations mainly cause autosomal dominant CMT, though families with homozygous or compound heterozygous mutations have been identified [260]. Especially the amino acid residue at position 94 of the MFN2 gene appeared to be highly susceptible to be mutated in CMT2A patients. The most common substitutions reported at this position are the R94Q and R94W point mutations. Hence, models mimicking the R94Q mutation *in vitro* or *in vivo* have been useful to research the biological effects [261]. Interestingly, MFN2 mutant mice show an increased proportion of small and medium sized axons. Fusion impairments have been reported to cause neurite atrophy in purkinje cells [262], so possibly MFN2 related fusion impairments also cause the shift towards smaller nerve fibers. The presence of smaller nerve fibers does not indicate that axons are lost. Indeed, CMT2A patients with MFN2 mutations, as well as $MFN2^{R94Q}$ mice models, do not show any sign of axonal loss [263].

One murine model of CMT2A, overexpressing $MFN2^{T105M}$ shows an improper mitochondrial distribution and tight clusters of mitochondria within axons of motorneurons [264]. However, this result was thought to be the result of increased expression of this mutant MFN2 and the subsequent accumulation of this protein, rather than the mutation per se.

In other mouse models and in CMT2A patients, neither such extreme overexpression of MFN2, nor a depletion of mitochondria in axons has been observed. In contrast, a 30% increased number of mitochondria in axons have been detected in mutant MFN2 expressing neurons in the sciatic nerve. The increase in mitochondrial density in axons of MFN2 mutant mice can be caused by multiple reasons, including impaired retrograde transport of mitochondria and an increased number of fission events, while fusion is impaired.

OPA1, the other protein involved in the mitochondrial fusion process, interestingly is not involved with CMT2A. Instead mutations in the OPA1 gene cause another neuropathy being dominant optic atrophy (DOA) [265] . These patients suffer from visual loss, central visual field deficits and problems with color vision. These symptoms develop due to atrophy of the optic disc and retinal ganglion cells [266]. Secondary symptoms that only occur in a minority of patients include neurosensory hearing loss, myopathy, peripheral neuropathy and multiple sclerosis-like illness. DOA patients also show heterogenous mitochondrial network and clumps in discrete areas of the cytoplasm [265], so the abnormal distribution of mitochondria in these patients may cause the pathology. Furthermore, OPA1 mutant fibroblasts show a higher percentage of mitochondria containing balloon-like structures and complete fragmented mitochondria [267]. Since both MFN2 and OPA1 are involved in mitochondrial fusion, it is striking that mutations in the respective gene causes such different pathology. This suggests that next to mitochondrial fusion, OPA1 and MFN2 have other functions in the cell.

MFN2 is required for axonal mitochondrial transport [268]. In neurons derived from MFN2 knockout mice or neurons expressing mutant MFN2, migrating axonal mitochondria undergo pauses that take a longer time than axonal mitochondria in healthy neurons. In addition, anterograde and retrograde migration speed is decreased in mitochondria with defect MFN2. That result suggests that the attachment to microtubules becomes impaired when MFN2 is not present of mutated. Importantly, MFN2 defects do not affect the transport of other organelles, showing that the effect is specific to mitochondria. Knockdown of Miro2 results in identical mitochondrial transport deficits, suggesting that mitochondria in MFN2 mutants are no longer able to connect to Miro2 and hence the kinesin motors. Mutations in Opa1, the other protein required for mitochondrial fusion, results in impaired fusion, but not in decreased mitochondrial transport, indicating that mitochondrial fusion and mitochondrial transport are not inherently connected.

Changes in the physiology of mitochondria caused by MFN2 mutations have an effect on the functionality of these mitochondria [269]. Changes in cellular energy metabolism, calcium homeostasis and other cellular functions are possible. Indeed, mutations in the MFN2 gene result in a reduced mitochondrial respiration and a decrease in respiratory complex subunits. Importantly, a decrease in the mitochondrial membrane potential is observed. This is correlated with a reduction of the efficacy of oxidative phosphorylation [270]. In contrast, oxygen consumption is increased in MFN2 mutant cells in certain conditions and cell types, showing that the effect of mutations in the MFN2 gene can be highly variable between cell types. However, a stable depletion of the MFN2 gene induces adaptive processes that counteract disorganization of cell metabolism and function. The reduced oxidative phosphorylation efficiency is compensated by increased glycolysis [269].

Differences in energy metabolism in MFN2 mutant mitochondria can result in downstream effects, including altered ROS production. Sebastian et al. reported that in muscle and liver tissue, MFN2 deficiency leads to increased H_2O_2 concentrations, differences in ROS response and mitochondrial dysfunction [271]. This is possibly due to a dysregulated antioxidant response, because the mutation c.140A>G, p.His47Arg in SOD1 is connected to CMT2 like pathologies [272]. Also $SOD1^{-/-}$ mice develop a peripheral neuropathy phenotype that affects mostly motor neurons, while sensory neuron function remain normal [273]. Nerve conduction velocity in these $SOD1^{-/-}$ mice is impaired in mostly motor nerves, whereas the sensory sural nerve is unaffected. The effect of increased ROS production by MFN2 mutant mitochondria is an increase in JNK phosphorylation and IRS1 phosphorylation, which leads to insulin resistance. In addition, palmitate induced ROS production is reversed by upregulating the expression of MFN2. Also in the reverse experiment, knockdown of MFN2 by antisense MFN2, an increase in ROS production was detected. These results show that mitochondrial ROS production is increased when MFN2 function is impaired, but the underlying mechanism is not well understood.

In addition to increased ROS production caused by MFN2 mutations, changes in ATP production in MFN2 mutant mitochondria have been observed. However, this might not be the downstream effect of different energy metabolism. In mouse models for CMT2, several mutations in the gene coding for ATP synthase are observed[274]. A specific mutation that is found to be correlating with disease severity is m.9185T>C. Remarkably, ATP synthase activity is measured but in the reverse direction, meaning that ATP is hydrolyzed to produce ADP and inorganic phosphate. In addition, the m8993T>G mutation is associated with impaired assembly and stability of ATP synthase with reduced the activity of ATP synthase in mice. Same impairments in ATP synthase, either impaired assembly, impaired function, or

both are detected in CMT2 patients that appeared to have the m.9185T>C mutation. Even though the direct link between ETC deficits and neuronal degeneration is not fully described yet, several hypotheses are proposed. Possibly, axonal degeneration is caused by a decreased axonal membrane potential due to Na^+/K^+-ATPase failure caused by a decrease in ATP production by MFN2 mutant mitochondria. On the other hand, even though a decrease in mitochondrial ATP production is detected in MFN2 mutant fibroblasts due to a less efficient oxidative phosphorylation, total cellular ATP production is found to be unchanged, because other ATP producing mechanisms, such as glycolysis, compensate for the lack of mitochondrial ATP [270]. However, these compensatory mechanisms require greater oxygen consumption, so ATP production may still become impaired due to MFN2 deficits in situations when the cell is located in a low oxygen environment or when the cell is very active such as firing axons.

4.6 Conclusion

Mitochondria and ROS play an important role in the nervous system and when mitochondria malfunction or when the equilibrium between ROS and antioxidants becomes in disbalance, neuropathies can develop such as Amyotrophic Lateral Sclerosis, Multiple Sclerosis, Alzheimer's disease and Parkinson's disease. In the PNS, peripheral neuropathies such as Charcot-Marie Tooth diseases can develop due to mitochondrial dysfunction and an excess of ROS. Some diseases, such as ALS and CMT2, are the result of neuronal malfunctioning or neurodegeneration, whereas pathologic demyelination is the cause of MS and CMT1 for example. However, our understanding of the effect of pathological conditions on mitochondrial function is still lacking. Especially knowledge about changes of mitochondrial physiology in pathologic conditions *in vivo* is limited.

Chapter 5) In-vivo imaging of peripheral nerve mitochondria

The biological mechanisms in the PNS and the role that mitochondria play in these mechanisms appear to be complex. Importantly, when these mechanisms do not function correctly, this can lead to neuropathies. Therefore, there is a need to better understand the biological processes in the PNS and what goes wrong on a cellular and molecular level. Because mitochondrial function is greatly different in an *in vitro* setting or in dissected nerve tissue than in a living organism, it is important to observe what happens in healthy and diseased nerves *in vivo*. For this, advanced research tools are developed. During my thesis I contributed to develop such techniques to decipher the role of mitochondria and metabolic changes that occurs in healthy and diseases peripheral nerves.

In this chapter I will discuss several techniques that can be used for *in vivo* imaging. These techniques include viral vectors with fluorescent probes, multiphoton microscopy, FRET imaging and CARS imaging.

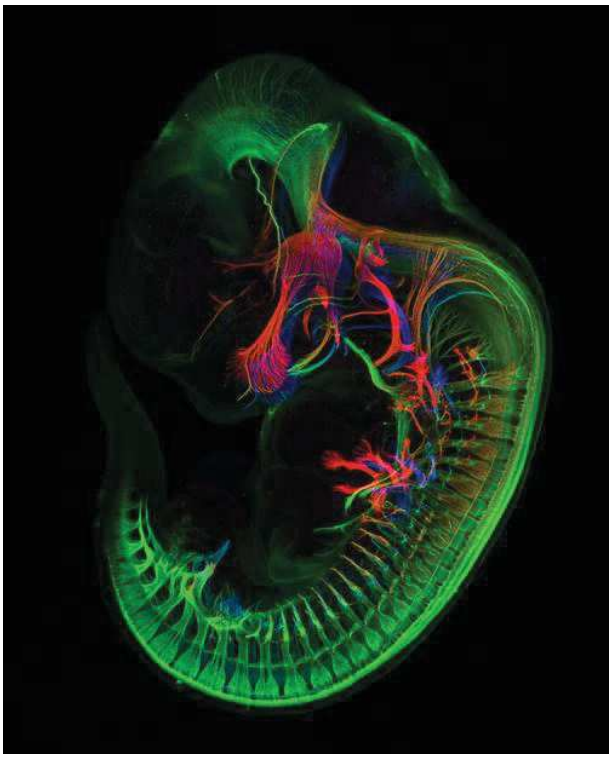

Expression of fluorescent markers in the developing mouse embryo

5.1 Fluorescent probes

To measure cellular processes, genetically-encoded probes can be used that emit fluorescent signals. These fluorescent probes can either be cytosolic or targeted to cellular compartments such as mitochondria. Manufactured probes include mito-AT1.03, Laconic, FLII12Pglu-δ6, mito-GCaMP2 and mito-roGFP2-Orp1.

5.1.1 AT1.03

AT1.03 is a genetically-encoded fluorescence probe based on fluorescence resonance energy transfer (FRET) that detects ATP (Fig. 17) [275]. FRET is a distance dependence physical process by which energy is transferred from an excited fluorescent molecule, an energy donor, to another fluorophore, an energy acceptor [276]. The efficiency of FRET is dependent on the distance between the energy donor and acceptor fluorophores, making it a sensitive technique for investigating a variety of biological mechanisms that induce changes in molecular proximity. FRET microscopy captures fluorescent signals from the interaction of the labeled molecules [277]. This interaction includes quenching of donor channel signals and increase of the acceptor channel signal. Several FRET microscopy techniques exist and are used to test various biological mechanisms such as organelle structure, conjugated antibodies, cytochemical identification, and oxidative metabolism.

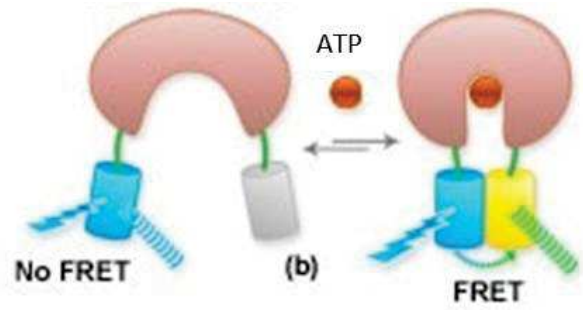

Figure 17 Schematic representation of AT1.03

AT1.03 consists of the cyan fluorescent protein (CFP) mseCFP, the yellow fluorescent protein (YFP) variant monomeric Venus, both linked at the ε-subunit of the Bacillus subtilis FoF1-ATP synthase. In presence of ATP, the ε-subunit retracts to bring the two fluorescent proteins close to each other, thereby increasing FRET efficiency. The conformational change is reversible. Relative ATP levels are measured using the YFP/CFP fluorescence ratio. AT1.03 appeared to have a sensitive range between 1 and 10 mM at 37 °C. It is sensitive to ATP selectively, since addition of up to 10mM GTP or ADP has been shown not to have an effect on the YFP/CFP fluorescent ratio, in contrast what is observed with the addition of ATP. Even deoxyadenosine triphosphate (dATP) does not change the fluorescent ratio of AT1.03. Within the pH-range of 7.1 to 8.5, pH variations does not influence the emission ratio of AT1.03. This indicates that small pH fluctuations around the normal cytoplasmic pH (which is near 7.3) or mitochondrial pH (7.8) will not affect the AT1.03 fluorescent ratio. Nonetheless, temperature changes appeared to have a stronger effect on the AT1.03 sensitivity. The dissociation constant elevates approximately five-fold by an increase of 10 °C. Next to its specificity and sensitivity, the kinetics of ATP binding and dissociation are important factors of AT1.03 functionality. The rate of ATP binding was established at 1.7 x 10^{-2} $mM^{-1}s^{-1}$ and the rate of ATP release at 9.8 x $10^{-2}s^{-1}$. This indicates that ATP can be monitored with rates up to 0.1 s^{-1}. AT1.03 targeted to cellular compartments, showed that differences in ATP concentration were present in different cellular structures. Surprisingly, AT1.03 located in the mitochondrial matrix has been shown to have significant lower YFP/CFP emission ratios than in the cytoplasm or in the nucleus. The nucleus also shows a lower AT1.03 emission ratio than the cytoplasm, but to a smaller extent, suggesting that ATP can pass the nuclear membrane almost freely. The mitochondrial target sequences should not impair AT1.03 sensitivity as the target sequence is cleaved after transport into mitochondria. Although that observation seems paradoxical, considering mitochondria being

the main producer of ATP, possibly the nucleotide translocator pumps ATP from the mitochondrial matrix into the cytosol, thereby maintaining a relative high ADP/ATP ratio, which is preferable for ATP synthase to produce ATP from ADP and phosphate.

5.1.2 Laconic

Laconic is a FRET-based probe as well, with the FRET pair being mTFP and Venus, bound to the DNA-binding domain of LldR, which is a bacterial transcription regulator that also contains a lactate-binding/regulatory domain [278]. mTFP is located at the N-terminus of LldR flanked by linkers, and Venus located at the C-terminus. Opposite to AT1.03, FRET efficiency decreases upon binding of lactate, meaning that the mTFP/Venus fluorescent ratio decreases when lactate is bound. Laconic detection is sensitive for a large range: from at least 1 µM up to 10 mM. Also opposite to AT1.03, laconic shows some change in specificity in milieus of different pH. Although *in vitro*, some interference was observed from pyruvate and citrate, this should not have significant effects in other conditions. Pyruvate only showed interference at high concentration, whereas in a physiological condition, pyruvate concentration is 10-50 times lower than lactate, indicating that endogenous pyruvate should not interfere with lactate sensing under physiological conditions. Citrate increased FRET ratio at a concentration of 1 mM, although no effect was measured at lower concentrations. Like pyruvate, cytosolic citrate levels are below the concentration in which it affects Laconic. However, mitochondrial citrate is 10 times higher than in the cytosol, suggesting that mitochondrial citrate may affect mitochondrial lactate sensing by mitochondria-targeted Laconic. Extreme redox changes did not change the Laconic emission ratio.

5.1.3 FLII12Pglu-δ6

FLII12Pglu-δ6 is another FRET based probe, connecting eCFP and citrine to the glucose/galactose binding protein of Escherichia coli (MglB) [279]. Citrine was inserted into the backbone of MglB in order to reduce rotation of citrine and hence preventing limited resonance energy transfer. To limit this rotation even further, a number of amino acids of the linker domains was reduced. For FLII12Pglu-δ6, 6 amino acids were deleted (hence δ6). FLII12Pglu-δ6 is a probe that detects glucose and it has a high dynamic ratio *in vitro* and *in vivo*. FLII12Pglu-δ6 appeared to be sensitive to glucose levels from 0.05 mM to 9.6 mM, with a $K_{0.5}$ at 600 µM *in vivo* and a normalized Δratio of 0.74. In the cytosol of *HepG2 cells in vitro*, FLII12Pglu-700µδ6 showed saturation over 10 mM glucose. The kinetics of FLII12Pglu-700µδ6 showed a $K_{0.5}$ of 1.54±0.30 mM glucose, and a Vmax of 3.91 ± 0.22 Δratio/min. These values are in accordance with the GLUT1 affinity to D-glucose on plasma membrane.

5.1.4 RoGFP2-Orp1

Redox sensitive GFPs (roGFPs) are ratiometric probes that detect the redox status of its environment (Fig. 18). roGFPs harbor an engineered dithiol/disulfide switch on their surface, which determines their wavelength of excitation [280]. RoGFP2 can be converted into an H_2O_2 specific probes by fusion with the microbial H_2O_2 sensor Oxidant Receptor Peroxidase 1 (Orp1) [280;281]. Orp1 is known to respond to H_2O_2 with high specificity. Because of this, the fusion protein roGFP2-Orp1 is also highly sensitive to H_2O_2, as it has shown not to react with other oxidants, such as GSSG, cysteine, hydroxyethyl disulfide or hydroascorbic acid, but a significant ratiometric change could be observed induced by H_2O_2. Upon detection of H_2O_2 by Orp1, de resulting disulfide bridge on Orp1 is transferred to the roGFP subunit, which then can be detected as the conformational shift alters the excitation spectrum of roGFPs. The oxidized roGFP that contains disulfide bridges is detected with an excitation peak at 405 nm, whereas the excitation peak of the reduced roGFP (that contains –SH groups) is at 488 nm [282]. The formation of disulfide bridges on roGFP is reversible via reduction by cellular

thioredoxin (Trx) or GRx/GSH [283]. RoGFP2-Orp1 appeared to be sensitive to H_2O_2 levels in a range between 0.1–10 µM *in vitro* and 1-50 µM in living cells [281].

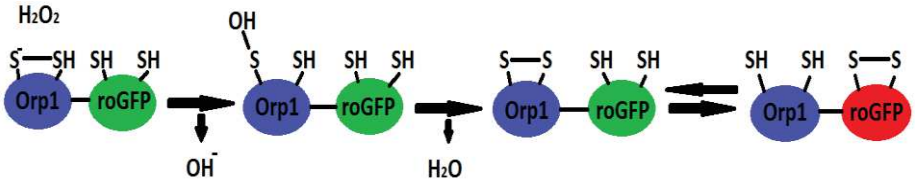

Figure 18 Schematic representation of roGFP-Orp1

5.1.5 GCaMP2

To measure cellular and mitochondrial calcium levels, a fluorescent indicator for Ca^{2+} was developed: GCaMP2. These calcium sensors include a M13 fragment from myosin light chain kinase, a circularly permutated EGFP (cpEGFP) and calmodulin (CaM) located N to C terminally. When Ca^{2+} binds to CaM, conformational changes due to the Ca^{2+}–CaM–M13 interaction induce a subsequent conformational change in cpEGFP, so that the fluorescence intensity increases [284]. Indeed, GCaMP is sensitive to Ca^{2+} levels with a Kd of approximately 235 nM [284]. The Kd of mitochondria-targeted GCaMP2 is slightly variable from one cell to another, since the Kd has been established at 136 nM in HéLA cells and 189 nM in cardiac myocytes [285]. The effect of pH on mito-GCaMP2 is shown to be minimal [285].

5.2 Viral vectors

These fluorescent probes may be useful tools to detect physiological changes in cells, but they need to be expressed in living cells first. To detect fluorescent probes *in vivo*, genetically modified mice expressing DNA that codes for the fluorescent proteins are generally needed. Conventionally, DNA plasmids coding for fluorescent proteins were introduced into embryonic stem cells or into mouse embryos and then mice have to be bred. However, a faster and easier method is injecting viral vectors that contain DNA coding for fluorescent probes into mice postnatally. Efficient gene transfer and stable transgene expression are important features to bring DNA into cells and express this newly delivered DNA [286].

Adeno-associated virus (AAV)-derived vectors are excellent vectors for gene delivery *in vivo*, because of their low toxicity and low immunogenicity, highly efficient gene transfer and long-term expression in several cell types, including neurons. AAVs are non-enveloped, helper-dependent parvoviruses with a capsid architecture of ~25 nm in diameter [287]. AAVs package ~4.7 kb genome flanked by ~145 bp inverted terminal repeats (ITRs) on the 5 and 3 ends. Wildtype AAV genome is a linear single stranded DNA consisting of two open reading frames (ORFs). This wildtype AAV requires coinfection by adenoviruses or herpes simplex viruses to transfect neurons successfully. It has been shown that wildtype AAV is able to integrate into the (human) host genome at a specific locus in chromosome 19. The integration of AAVs at this specific locus is mediated through its ITR and Rep68 or Rep78 proteins. However the rep gene is undesirable for AAV transducing vectors, since it strongly inhibits gene expression and cell growth [288]. Recombinant AAVs lack endogenous viral genes [289], so it allows for transduction of a wide variety of cells at a high titer with a low risk insertional mutagenesis and immunogenicity. Twelve AAV vector serotypes with different transduction profiles have been constructed. For example, AAV5 is mainly used for transfection of sensory neurons, whereas AAV2, 6 and 9 is used for spinal motor neurons.

Successful transduction by AAV vectors occurs in several steps [290]. To target primary sensory and motor neurons, two routes of delivery have successfully been used, depending on the

target location. AAVs can be delivered via direct intraganglionic or intraspinal injection. Direct intraganglionic injection of an AAV vector results in expression of the AAV in sensory neurons with very little expression in other locations [291]. The second route is intrathecal (IT) delivery. IT delivery results in transduction of sensory and spinal cord neurons, but also in other non-neuronal cell types [292]. When the AAV vectors are injected, the virus has to enter the neurons. First, AAVs bind to the receptors located on the cell surface. Surface exposed regions on the AAV capsid mediate this initial interaction with the host cell surface (Huang et al., 2014). In addition, cell surface glycans have been identified as the preferred receptor to bind to by many AAV serotypes. AAV serotypes 1, 5, and 6 bind N-linked sialic acid (SA), whereas AAV4 is the only natural AAV isolate that binds O-linked SA moieties on mammalian cell surfaces [293]. AAV serotype 1,5 and 6 bind N-linked SA, whereas AAV4 binds O-linked SA moieties and AAV2, AAV3 and AAV6 bind heparan sulfate (HS) proteoglycans. AAV9 requires N-terminal galactose residues to perform successful gene transfer [294]. Then, the AAVs are taken up into the cell and translocated towards the nucleus. This translocation is followed by entry into the nucleus, uncoating of the capsid and release of the new genome. Finally, a second strand of DNA needs to be synthesized and gene transcription needs to occur for successful gene expression.

5.3 Multiphoton microscopy

Conventional fluorescent microscopy is based on a linear effect: One photon is absorbed by the fluorescent molecule and then emits a single fluorescent photon [295]. In conventional fluorescence, if the excitation power is increased by a factor of two, then twice the amount fluorescence is generated as well. Multiphoton microscopy is not based on this linear effect, but relies on nonlinear interactions between the excitation laser and the fluorescent molecule. Two-photon excitation is the most commonly used multiphoton non-linear imaging technique. Two-photon absorption is the interaction of two photons with the same molecule within a time interval less than 10^{-18} seconds. With normal light illumination the probability of two-photons arriving within this time interval is extremely low. Therefore, fluxes in the range of 10^{20}-10^{30} photons per centimeter per second are necessary to generate a two-photon interaction. In microscopy, powerful pulsed lasers generate photon fluxes with such a high density. Actually, the average laser power is kept relatively low, but since the laser photons are condensed in small time packets, these pulses contain a power high enough to produce high density photon fluxes. To compress photons not only in time, but also in space, high numerical aperture objectives are used. The combination of concentration the photons in time and in space, increases the probability of a nonlinear excitation event. Because a two-photon excitation event requires two photons to interact with the same particle at the same time, the probability of an absorption event is not linearly dependent on the excitation intensity. Moreover, the excitation light is focused at a small area. These two factors sharply decrease the probability of absorption events outside the focal area. Therefore, no pinhole is required to reduce light originating from different parts of the sample, such as in a two-photon setup, which is in contrast to a conventional confocal setup. This property allows more of the excitation laser beam to reach deep into the sample as well.

Although two-photon excitation can be used for several kinds of optical transition, it is most often used to generate fluorescence. Fluorescence is the absorption and re-emission of light by a molecule. In a standard fluorescence process, photons of the right energy interact with a sample molecule and are absorbed. This absorption of the photon and the energy it contains cause the sample molecule to transition to an excited electronic state (Fig. 19) [295;296]. This excited state is unstable and within 10^{-8} seconds or shorter, the molecule returns to its ground

state by emitting a new photon [297]. During this process, energy is lost, so the emitted photon contains less energy than the photon that the molecule absorbed earlier. Since the wavelength of photons is inversely correlated to the amount of energy these photons contain, the wavelength of the emitted photon is therefore longer than the excitation photons. In two-photon microscopy, each photon of the excitation laser has just one-half of the energy that is necessary to excite the molecule. Therefore the wavelengths of these excitation photons is around two times longer than the wavelength required for conventional fluorescent microscopy. Molecules that are excited by two-photon excitation emit photons with the same features as after one-photon excitation, including the same wavelength. The consequence is a reverse Stokes shift, meaning that the emitted photons contain more energy than each of the two photons that were necessary for excitation. This means as well that wavelength of emitted photons have a shorter wavelength than the excitation photons. The biphoton setup therefore requires an appropriate filter to collect the fluorescence of interest.

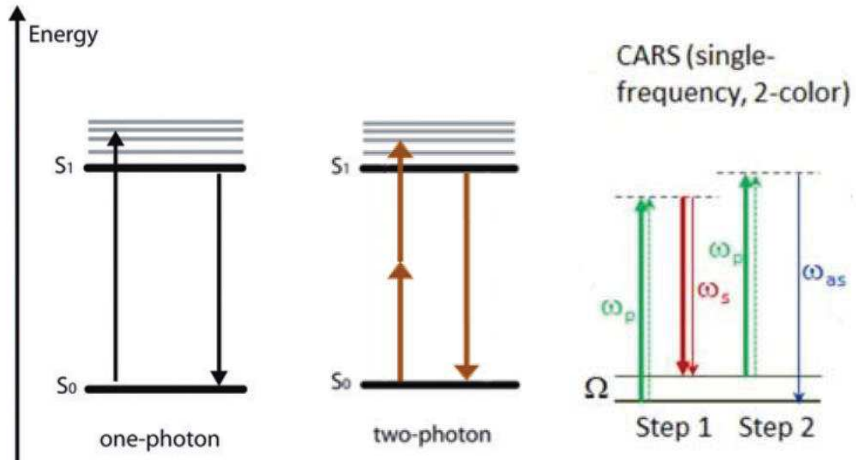

Figure 19: Energy-level diagrams of four different microscopy techniques: One-photon fluorescence microscopy, two-photon fluorescence microscopy, 3-color CARS microscopy and 2-color CARS microscopy). In One-photon microscopy, the sample molecule reaches a higher energetic state upon excitation. After loss of energy, a lower energy photon is re-emitted. In two-photon microscopy, two low-energy photons are used to reach this same high energetic state of the sample molecule, although the same emission is obtained. This means that the excitation photons contain less energy than the emitted photon. CARS imaging requires two steps. First, a pump photon excites the sample, followed by a Stokes photon that induces electron scattering, which results in a vibrational sub-state. In step 2, the pump photon excites the sample again, now to an energetic state that is high enough to emit an anti-Stokes photon, which can be detected.

Two-photon imaging is the best option for imaging structures *in vivo*. It allows deeper imaging compared to confocal microscopy, which is a strong advantage when excision of the sample is not possible [298]. Two-photon microscopy also has less phototoxicity, because first the use of two photons with a shorter wavelength allows to use infrared light and second only a small part of the sample is illuminated. Although two-photon excitation allows imaging in deeper samples and is preferred for *in vivo* imaging, it also has a set of limitations. Aside for the higher costs, accelerated photobleaching can cause problems in two-photon imaging [299]. Higher photon density activates more photobleaching pathways, even though this photobleaching is condensed to the imaging area and does not affect the path between laser and focal point, which is the case in confocal imaging. The photobleaching in two photon microscopy is especially detrimental in thin slices of less than 10 µm. Besides, two-photon excitation can lead to interaction with chromophores that are naturally present in the sample.

5.4 CARS imaging

CARS is a third-order nonlinear optical process consisting of two stimulating scattering steps [296]. In the first step, a pump photon (ωp) excites molecules in the the sample and brings it to a higher energetic state, but this elevated energetic state is not high enough to emit a detectable emission photon. Instead a Stokes photon (ωs), coming from a second laser beam, causes a scattering of photon on the molecules' electrons and thereby decreasing the sample's energy. Depending on the chosen wavelengths of pump and stoke photons, the sample molecules become in a vibrational sub-state, which is specific to the chemical properties of the molecules. Coherent generation of anti-Stokes photons by another pump photon illumination can only be efficient when the frequency difference between the pump and the Stokes photons is equal to the vibrational frequency of the sample. Then, the pump photon excites the sub-state sample again in a specific set of molecules. Whereas the first excitation resulted in an energy state that was not high enough for the sample to emit a photon, the second excitation elevates the energy state even further, because the sample was already in a vibrational sub-state. After the second excitation by the pump photon, the sample will emit a blue-shifted anti-Stokes photon (ωas). The anti-Stokes signal can be detected by the detector of a microscope (Fig. 20) [300]

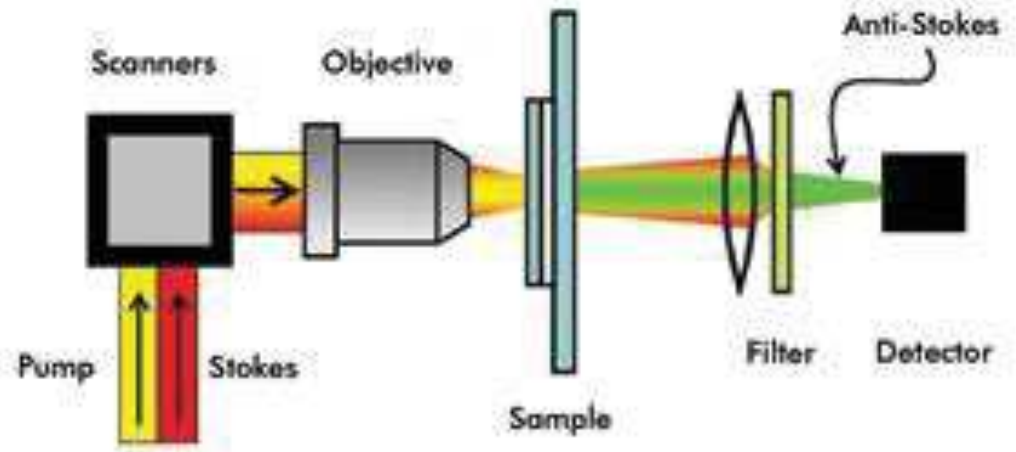

Figure 20: The setup of a microscope equipped with lasers for two-color CARS imaging. The two laser beams, the pump beam and the Stokes beam, are directed through the objective to the sample. After passing through a filter, the created anti-Stokes emitted photons are detected by the microscope's detector.

5.5 The effect of anesthesia

Using multiphoton microscopy for *in vivo* experiments requires the connection to an anesthesia supply system. A regular anesthetic used for rodent *in vivo* experiments is isoflurane, which is a general anesthetic and needs to be inhaled by the animal. Therefore a constant flow of isoflurane needs to be administered to the animal, while it is examined by multiphoton microscopy. However, in experiments that test mitochondrial function, the effect of isoflurane on mitochondria needs to be considered.

It has been shown that isoflurane induces ROS accumulation in HEK-293 cells [301]. However, the duration of treating mitochondria appeared to be an important factor in ROS accumulation. Treatment of HEK-293 cells with 2% isoflurane for 15 to 30 minutes does not induce ROS accumulation, but treatment for a longer period of time (60 to 90 minutes) increases ROS levels. Other studies have shown that isoflurane can induce a range of other changes to cells and mitochondria, such as an increase in cytosolic calcium concentration,

opening of mitochondrial PT pores, decreasing mitochondrial membrane potential and release of cytochrome C. These pathways might actually describe the pathway in which isoflurane induces ROS accumulation and potential activation of caspase-3.

On the other hand, isoflurane has also been reported to activate cardioprotective signaling through ROS sensitive pathways, because only low concentrations of ROS are induced by isoflurane [302]. These low ROS concentrations activate preconditioning pathways such as PKC, Akt, and glycogen synthase kinase β pathways. These pathways can actually lead to a delay in opening of mitochondrial PT pores, which is in contrast with the results reported by Sun et al.[301]. Previous studies also demonstrated that ROS scavengers actually abolish isoflurane-induced reduction of myocardial infarct sizes. Isoflurane increases ROS generation with complex I-, but not complex II-linked substrates in submitochondrial particles. Besides, isoflurane only alters activity of complex I, but not of the other complexes in solubilized mitochondria. Interestingly, in the presence of complex I inhibitors, isoflurane actually enhances ROS production from complex I-linked substrates. In this situation, the inhibitory effect of isoflurane on complex I is enhanced, resulting in isoflurane induced ROS production. Even though isoflurane does not alter complex II activity, isoflurane induced ROS production by complex III has been observed as well. However, an increased ubiquinone/ubiquinol ratio enhances ROS generation at complex III. Electrons are transferred to oxygen from reduced downstream cytochrome b_L to oxygen in a reverse reaction via oxidized ubiquinone. Indeed, exogenous ubiquinone enhances ROS generation at complex I. In addition, inhibition of complex I by isoflurane further increases the ubiquinone/ubiquinol ratio by decreasing complex I activity and forming reduced ubiquinol, thereby enhancing ROS generation at complex III. In a similar way, inhibition of complex II increases ubiquinol and also enhances ROS generation by complex III. This shows that inhibition of upstream complexes of the ETC, including inhibition of complex I by isoflurane, can increase ROS production by complex II through changes in the ubiquinone/ubiquinol ratio.

However, isoflurane has not been shown to influence mitochondrial function in the peripheral axons *in vivo.* Besides, only long-term exposure of isoflurane to the direct environment of cells showed an effect of the anesthetic. In addition, I checked the impact of the isoflurane anesthesia on my imaging experiments changing the anesthesia protocol to ketamine/xylazine and found no effect. This indicates that isoflurane can be used in the experiments that are discussed in part B of this thesis.

5.6 Conclusion

To investigate cellular and mitochondrial function *in vivo* several techniques have been developed. For example, the use of viral vectors allows for the introduction of fluorescent markers in the nervous system. These viruses, such as AAVs, will infect neurons or Schwann cells and the fluorescent proteins will be expressed at their target location, which could be the cytosol or an organelle. These fluorescent markers can be detected by microscopes that can detect fluorescent light. Since fluorescent light of various colors exist, it allows for the detection of multiple cellular structures when labelled with fluorescent tags of a different color. More recent advancements of fluorescent microscopy involve fluorescent markers that shift color in different conditions. Examples of those types of fluorescent markers are redox-based fluorescent probes and Fluorescence Resonance Energy Transfer (FRET) based fluorescent probes. Next to standard fluorescence, label-less imaging techniques can be used for *in vivo* microscopy, which create a detectable fluorescent signal based on the molecular properties of the specific samples. An example of a label-less imaging technique is Coherent

Anti-Stokes Raman Scattering (CARS), which can be used to visualize the myelin sheath, based on the lipid-rich structure of myelin. The type of anesthesia is an important factor in *in vivo* studies, but isoflurane can safely be used without impacting the results.

Part B
Results

Chapter 6) Cancer-like metabolism in myelinating glia protects axons

The previous chapters provided a biological and technical background for the results that will be explained in the following chapters. These chapters are either published or under review or in preparation for publication at the time of writing. Therefore, chapter 6 till 9 are presented as separate sections with their own (short) introductions, figure numbering and reference sections.

First, I will present my research on the metabolic support of Schwann cells to axons. In chapter 3, I discussed how astrocytes, oligodendrocytes and supposedly SC could provide lactate to the axon, which axonal mitochondria can use for oxidative phosphorylation. This transport of lactate is named the lactate shuttle. However for this lactate shuttle to occur, glial cells need to produce sufficient amount of lactate. In most cells, including neurons, mostly PKM1 is expressed while PKM2 is not expressed, leading to the production of pyruvate, which is used in the TCA cycle within mitochondria to produce ATP. However in a small number of cell types, such as cancer cells, a shift from oxidative phosphorylation towards aerobic glycolysis has been observed, which is correlated with a shift in the balance from PKM1 towards PKM2. The metabolic shift from oxidative phosphorylation to glycolysis as the main source of ATP in cancer cells has been referred to as the Warburg effect and this allows for the production of ATP via aerobic glycolysis. Therefore, the Warburg effect provides a condition in which the cancer cells can proliferate faster.
A healthy use of the Warburg effect has recently been proposed in the nervous system. Similar to cancer cells, it has been shown that oligodendrocytes can rely completely on glycolysis instead of oxidative phosphorylation and still remain viable. In contrast, completely glycolytic neurons are not viable. Moreover astrocytes or oligodendrocytes that cannot provide lactate to neurons induce neuronal degeneration [303], suggesting that the eventual Warburg effect in glial cells would be essential for the maintenance of the nervous systems. This suggests that the shift in metabolism towards glycolysis that occurs in oligodendrocytes is an important mechanism for neurons. The Warburg effect allows for the production of lactate that can be transferred towards neurons. However, a direct demonstration of the role of the Warburg effect in glial cells in order to support neuronal function and survival is lacking.

In this chapter, we will demonstrate the Warburg effect in the PNS. We also show that a defective Warburg effect, which is induced by a specific and conditional knockout of PKM2 in myelinating SC, results in impaired neuronal function and defective ATP synthesis by axonal mitochondria. For this we will use viral vectors that will induce expression of fluorescent probes that detect cytosolic glucose or lactate or mitochondrial ATP.

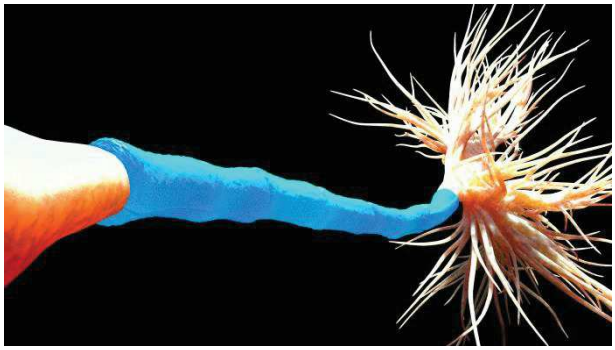

A neuron with Schwann cells surrounding the axon intermitted by nodes of Ranvier

Warburg effect is required in myelinating Schwann cells to sustain axonal metabolism and function

Marie Deck[1], Gerben Van Hameren[1], Nathalie Bernard-Marissal[2], Jérôme Devaux[1], Graham Campbell[1], Jade Berthelot[1], Alise Lattard[1], Jean-Jacques Médard[3], Roman Chrast[3], Nicolas Tricaud[1]

[1] Institut des Neurosciences de Montpellier, Université de Montpellier, 80 Rue A. Fliche, 34090 Montpellier, France

[2] Aix Marseille Université, INSERM, MMG, 13385 Marseille, France

[3] Departments of Neuroscience and Clinical Neuroscience, Karolinska Institutet, Stockholm 17177, Sweden

1. Introduction

Metabolism is an essential parameter of neurons' function and survival [1,2,3]. Glial cells play a critical role in this matter as they metabolize glucose into lactate and export it to the axon as a rapid fuel for mitochondria [4,5,6]. Recently mitochondrial respiration was shown to be dispensable for myelinating oligodendrocytes suggesting these cells uses aerobic glycolysis for ATP production. This glycolytic metabolism also named Warburg effect, almost exclusively used by cancer cells, has the particularity to produce lactate instead of pyruvate [7,8,9]. So, do myelinating cells use a cancer-like metabolism to support axonal physiology? Here we show that PKM2, the glycolytic enzyme required for Warburg effect [10], is expressed in mature myelinating Schwann cells (mSC), oligodendrocytes and astrocytes. Genetic ablation of PKM2 in mature mSC results in lactate shortage in nerves and in active myelinated axons. Despite an increased glucose mobilization, stimulated axons of mutant mice failed to upregulate mitochondrial ATP production. While the myelin sheath was correctly maintained mutant mice had reduced motor performances. Axonal electrophysiological properties were maintained but axon terminals retracted and motor neurons showed an increased expression of neuronal stress marker caspase 3. Further challenging lactate production using dichloroacetate prevented mutant mice functional recovery after inducing peripheral neuropathy. Our results show that mSC provide lactate to axons to maintain their physiology and this requires an aerobic glycolysis metabolism to produce the critical lactate. As oligodendrocytes and astrocytes also express PKM2 in mature brain, it is likely that a similar unusual metabolism exists in the brain. Such as in cancer cells, this may dramatically change the response of the nervous system to many external stimuli and metabolic perturbations, suggesting that part of the neurodegenerative disorders' particularities results from this metabolism of glial cells [11, 12, 13].

2. Results

2.1 Schwann cell metabolism shifts to aerobic glycolysis upon maturation

In order to investigate the role of Warburg effect in glial cells functions *in vivo* in mice, we focused on myelinating Schwann cells (mSC). Indeed, these glial cells are the main cellular partner of peripheral nerves axons, so perturbations of mSC Warburg effect is likely to directly affect them. In addition, live imaging of these axons is more amenable than in the central nervous system. As most cells express PKM1, we first investigated a potential shift from PKM1 to PKM2 expression during the maturation of the mSC, when glial cells are

required to maintain axonal homeostasis [14]. We collected nerve samples that contain mostly glial cells mRNA and we investigated PKM mRNA expressions using quantitative RT-PCR. PKM1 mRNA was downregulated from day 2 to day 28 while PKM2 expression on the opposite increased at the same time (Fig. 1A). To go further we immunostained sciatic nerve cross-sections with PKM1 or PKM2 specific antibodies together with E-cadherin and 2H3 antibodies, as marker of mSC and axons respectively (Fig 1B). At day 4, E-cadherin and 2H3 were not yet well expressed but PKM1 and PKM2 were both expressed in the cytoplasm of mSC that surrounded axons (Fig. 1B a,b). A similar distribution was seen in mSC at day 15 with a more explicit localization of E-cadherin (Fig. 1B c,d). 2H3 colocalized with PKM2 in axons (Fig.1B d). At day 30 PKM2 replaced PKM1 in the cytoplasm of mSC while the reverse occurred in axons (Fig. 1B e,f). This shift from PKM1 to PKM2 expression in mSC was confirmed in fully adult mice at 5 months (Fig. 1B g,h). So both at mRNA and protein levels PKM expression in glial cells shifted from PKM1 to PKM2 isoforms when the myelin-axon couple enters the maintenance stage, suggesting mature mSC enter the Warburg effect metabolic mode.

To investigate the role of this Warburg effect in mSC we then specifically and conditionally deleted PKM2 isoform in myelinating glia of mice. A mouse strain expressing floxed PKM2 intron alleles [15] was crossed with mice expressing the Cre recombinase under the inducible and myelinating cells-specific promoter PLP-ERt [16]. Injecting tamoxifen in Cre positive and floxed PKM2 positive mice (mutant) at 1 month postnatal resulted in a significant decrease of PKM 2 expression in sciatic and saphenous nerves as seen in immunoblotting (Fig. 1C), quantitative RT-PCR (Fig. 1D), and immunostaining (Fig. 1E j,l). We used cre-negative PKM2-floxed positive littermates injected with tamoxifen in the same conditions as control animals. Both immunostaining and RT-PCR indicated that PKM1 was re-expressed in PKM2-deleted mSC (Fig. 1E i,k), suggesting that these recombined cells practiced mitochondrial respiration instead of Warburg effect. In order to check whether this reversal of the metabolism had an impact on the production of lactate by the mSC we measured free lactate in sciatic nerves of mutant and control mice. Mutant mice had significantly less lactate that control ones (Fig. 1F). So, the increased consumption of pyruvate by mitochondrial respiration in mSC of mutant mice resulted in a shortage of lactate production.

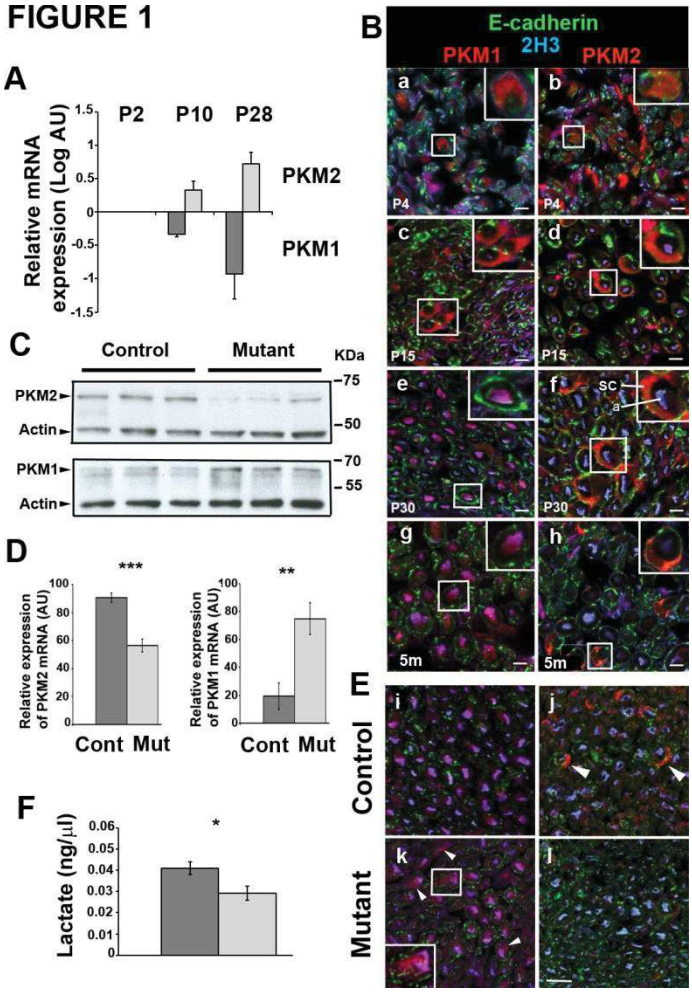

FIGURE 1 PKM2 is efficiently deleted in mature mSC of Mutant mice.
A- Quantitative RT-PCR shows decreased PKM1 and increased PKM2 expressions during mSC maturation (P: postnatal days). Normalized on P2 values. n=4 animals. **B**- Immunostaining on mouse sciatic nerve sections shows decreased PKM1 (left panels) and increased PKM2 (right panels) expressions in mSC (E-cadherin) during maturation. m: months. sc=Schwann cell; a=axon. **C**- Western blots show lower PKM2 and higher PKM1 amounts in Mutant versus Control mice sciatic nerves. Actin serves as loading control. KDa=Kilo Dalton. n=3 mice. **D**- Quantitative RT-PCR shows decreased PKM2 and increased PKM1 expressions in Mutant (Mut, n=7) versus Control (Cont, n=5) mouse sciatic nerves. **E**- Immunostainings, as described in B, show PKM2 lower in Mutant mSC (panel l) while PKM1 is higher (arrowheads and Insert panel k). **F**-Biochemical measure of lactate shows a reduced concentration in Mutant versus Control sciatic nerves (n=6 mice) and 12 months old). All scale bars = 10µm. Statistics show two-tailed Student t-test. Error bars represent SD in A and D, and SEM in F. AU=arbitrary unit.

2.3 Neuronal physiology is affected by PKM2 deletion in Schwann Cells

According to the lactate shuttle theory this lack of lactate should also result in shortage of axonal lactate. We investigated this assumption expressing a lactate-detecting probe (Laconic, [17]) in peripheral axons using an AAV transduction approach. An AAV9 expressing the probe was injected in the spinal cord of new born mutant and control mice that were then treated with tamoxifen at one month. We performed live-imaging of probe-labelled axons that cross

the sciatic nerve of 7 to 9 weeks old anesthetized mice (Suppl. Fig. 1). In basal conditions no difference could be seen between control and mutant animals (Suppl. Fig. 2). However when axons were challenged with electrical stimulations axonal lactate significantly dropped in mutant mice while control mice axons were able to maintain their lactate homeostasis (Fig. 2A), showing that mSC lactate is required for lactate homeostasis in axons. Beside lactate, another way axons feed their mitochondria to produce ATP is glucose-derived pyruvate. Thus, we also investigated the glucose content in axons in the same conditions using a virus expressing a glucose-specific probe (Δglu6, [18])(Suppl. Fig. 1B). Upon electrical stimulations glucose increased in axons of mutant mice while it remained stable in control mice (Fig. 2B). This indicated that mutant mice axons mobilized glucose upon stimulations while this was not necessary in control mice axons. Taken together we conclude that mutant mice axons, unable to maintain their lactate homeostasis, mobilized glucose instead in order to sustain the production of ATP. We next investigated the production of ATP by axonal mitochondria *in vivo* using a mitochondria-targeted fluorescent probe detecting ATP (ATeam, [19]). When axons were electrically stimulated to challenge axonal metabolism mutant mice mitochondria failed to increase ATP production while this production increased in control mice (Fig. 2C). Thus, in absence of Warburg effect in mSC, lactate homeostasis in axons is impaired and, despite the mobilization of glucose, axonal mitochondria respiration is impaired.

FIGURE 2

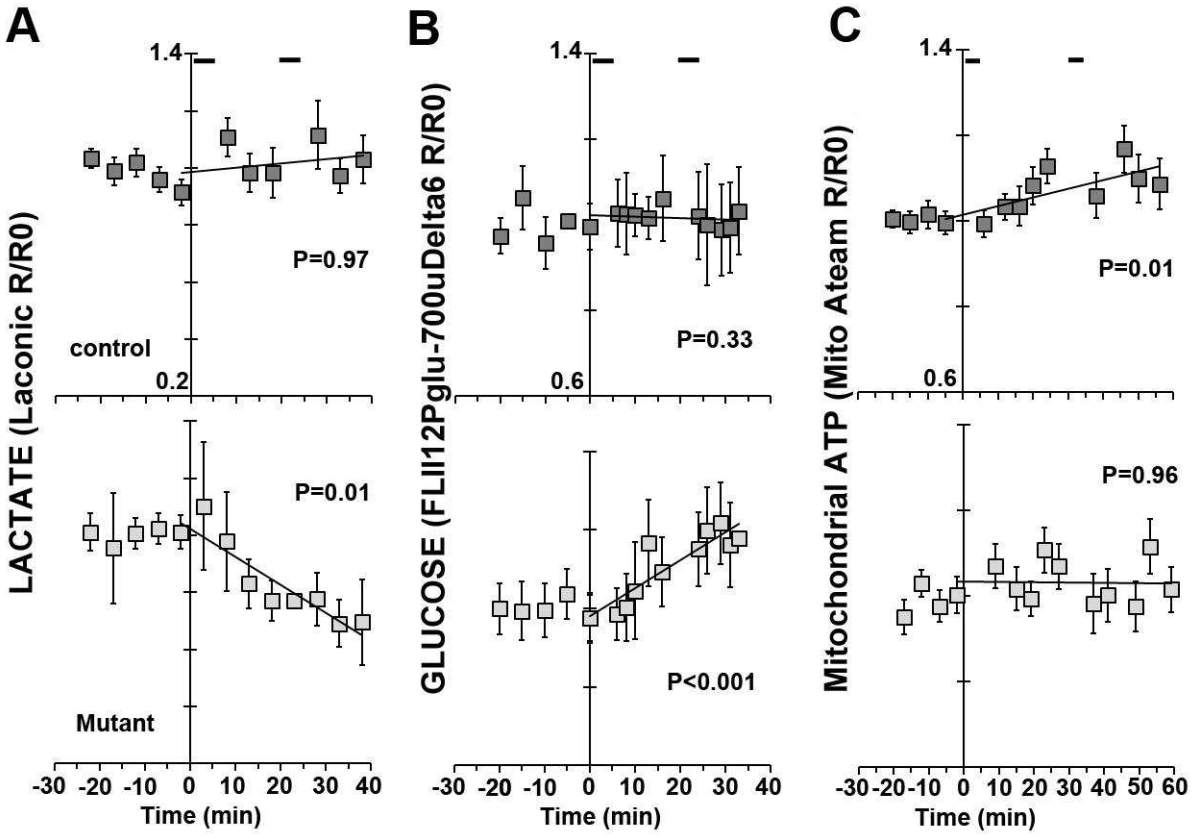

FIGURE 2 Mutant mice axons display an altered metabolic response to electrical stimulations.
The ratio of fluorescent probes (R) was normalized over the average ratio at time points before the first stimulation (R0). Segments at the top of each Control mice graphs show stimulation periods. Lines show linear regressions of the values over time starting with the last value before the first stimulation. P-values indicate the statistical significance of the linear regression test: is there a relationship between x and y (if regression line is y=ax+b, the null hypothesis is b=0)?
A- Axonal lactate increased after stimulations and remained stable on the long term in Control mice (n= 20 axons, 7 mice) while it decreased in Mutant mice (n= 7 axons, 4 mice) .
B- Axonal glucose remained stable over time upon stimulations in Control mice while it increased in Mutant mice (n= 6 and 9 axons respectively, 3 mice).
C- Mitochondrial ATP increased over time upon stimulations in Control mice axons while it remained stable in Mutant mice axons (n= 16 and 14 axons, respectively 5 mice each).
Error bars represent SEM.

2.4 Unbalanced axonal metabolism affects motor performance

Does this unbalanced axonal metabolism affect peripheral nerves functions? To answer this question, we investigated the motor behavior of mutant and control mice using Rotarod and grip test. The longitudinal analysis of mutant mice revealed a significant deficit in both tests starting 4 (Rotarod) and 10 months (grip test) after birth (respectively 3 and 9 months after PKM2 deletion in mSC) (Fig. 3A, B). So Warburg effect suppression in mSC impairs peripheral nerves functions. We also measured the nerve conduction velocity of sciatic nerves and no deficit was found (Fig. 3C). As nerve conduction velocity reflects the myelination status of the nerves, this suggested that the myelin sheath was not affected by PKM2 deletion. These data indicated that impaired peripheral nerves functions did not result from a defective myelination but more likely from axonal dysfunctions.

FIGURE 3

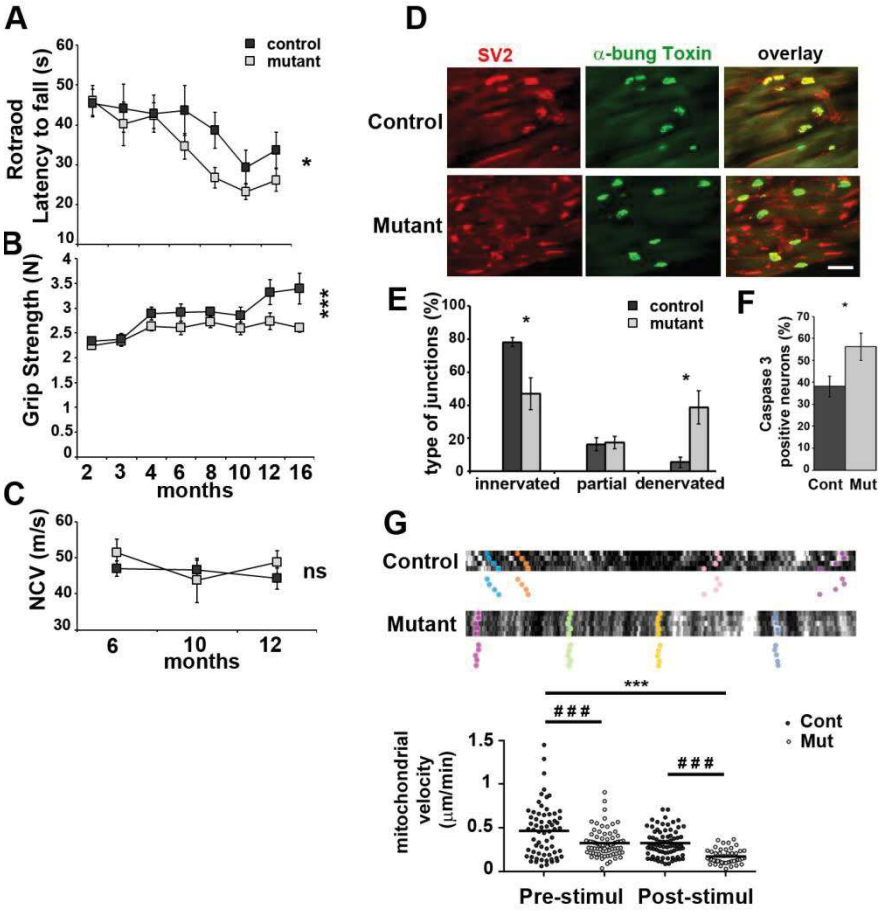

FIGURE 3 Mutant mice show motor deficit and display axonal defects.
A- Rotarod latency to fall and **B-** grip strength were measured between 2 and 12 or 16 months postnatal respectively on Control (n=21) and Mutant (n=25) mice. Statistical tests show two-way non–repeated ANOVA Sidak's post-hoc tests. **C-** Nerve conduction velocity (NCV) measured in Control and Mutant mice (n=10) at 6, 10 and 12 months postnatal show no significant difference (ns, two-way non-repeated ANOVA statistical tests, Sidak's post-hoc tests). **D-** Soleus muscle neuromuscular junctions of 12 months old Mutant and Control mice were stained for presynaptic SV2 and postsynaptic acetylcholine receptor (α-bungarotoxin). Scale bar= 100μm. **E-** Innervated (complete overlap), partially innervated (partial overlap) and denervated (no overlap) junctions were counted on sections as shown in D for Mutant mice and Control mice. Two tailed Student t-test. n= 4 mice (12 months). **F-** Spinal cord sections of Mutant (Mut) and Control (Cont) mice were immunostained for Caspase 3, motor neurons markers ChAT and Neurofilament (see Figure S3). Caspase 3/Neurofilament-positive neurons are more abundant in Mutant (n=20 images, 3 animals) than in Control (n= 14, 2 animals). Two tailed Student t-test. **G-** Axonal mitochondria labelled with mito-Dsred2 were imaged *in vivo* before and after electrical stimulation. **Upper panels** show typical kymographs. Tracked mitochondria are shown with colour dots. Mutant mice mitochondria follow a straight pattern indicating they are immobile or slowly moving. **Lower panel**: Mitochondria speed was plotted according to the genotype before and after stimulation. Statistical analysis show one-way ANOVA Tukey's post-hoc test. n are provided in Material and Methods. Error bars represent SEM.

We next investigated the electrophysiological properties of sciatic nerve axons *ex vivo* in artificial CSF looking at fibers recruitment, refractory period and fatigability at high frequency stimulation trains. No significant difference could be detected between mutant and control mice nerves (Suppl. Fig. 2), suggesting that peripheral nerves defects observed in mutant mice do not result from an altered conduction of action potentials along axons. However, mutant mice showed an increased number of retracted neuromuscular junctions at 12 months of age (Fig. 3D,E) and their spinal cord motor neurons displayed a higher expression of caspase 3 (Fig. 3F, Suppl. Fig. 3), a marker of neuronal stress and axonal degeneration [20], suggesting an alteration of the axonal physiology and maintenance. Several axonopathies indicate that mitochondrial trafficking is essential for the axonal maintenance. However, tracking axonal mitochondria *in vivo* revealed no significant decrease in their movements in mutant mice versus control. (Fig. 3G). Mitochondrial movement decreased after nerve stimulation (Fig. 3G), suggesting their docking along the axon. Indeed, a temporary docking of mitochondria in active nerves has been observed in previous studies *in vitro* [21;22;23;24], which is thought to promote replenishing cytosolic ATP. Taken together these data indicated that Warburg effect in mSC is required for the maintenance of trafficking of mitochondria in myelinated axons. This defect is correlated with neuronal stress linked to axonal dysfunction and retraction of presynaptic terminals at neuromuscular junctions.

2.5 Effect of dichloroacetate on peripheral nerve function

To investigate this further, we treated mutant and control mice with dichloroacetate (DCA), a drug that inhibits pyruvate dehydrogenase kinase (PDK) and therefore promotes pyruvate dehydrogenase activity (PDH) (Fig. 4a). As this enzyme catalyzes the production of acetyl-CoA from pyruvate, DCA promotes the mitochondrial consumption of pyruvate and decreases the production of lactate [25]. Thus, DCA treatment has been considered for patients suffering congenital lactic acidosis [26]. This treatment however leads to a reversible peripheral neuropathy, which is mimicked in rodents [27], suggesting DCA prevents lactate supply to peripheral axons. We analyzed DCA-treated mutant and control mice behavior using the Rotarod test and measured nerve conduction velocity. Over the three weeks of treatment Rotarod performance significantly decreased but independently of the genotype (Fig. 4b). When we stopped the treatment control mice recovered over 3 weeks on the Rotarod while mutant mice did not (Fig. 4B), showing that axonal function was definitely damaged in these mice. These data confirm that Warburg effect in mSC is required for the long-term maintenance of peripheral axons physiology.

FIGURE 4

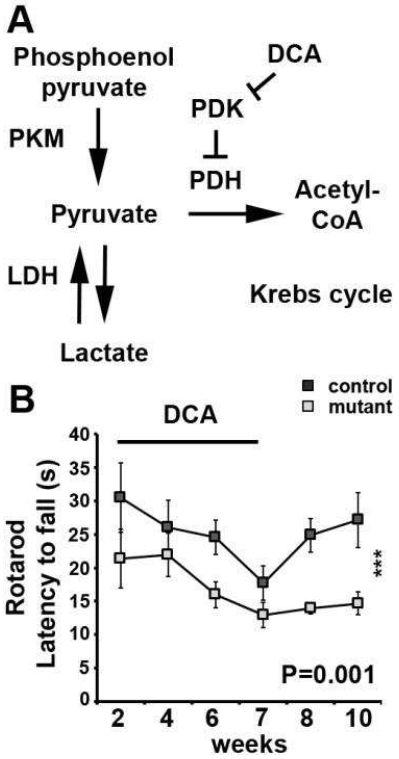

FIGURE 4 PKM2 deletion in mSC impairs motor performance recovery after DCA treatment.

A- Metabolic pathways directly affected by the manipulations. LDH: lactate dehydrogenase; PDH: pyruvate dehydrogenase; PDK: PDH kinase. DCA inhibits PDK, which inhibits PDH.

B- Rotarod latency to fall was measured in Control and Mutant mice during a 7 weeks daily treatment with DCA and then during a three weeks recovery period without treatment. Statistical analysis show two-way non-repeated ANOVA Sidak's post-hoc test from week 7 to week 10. n= 5 animals for each genotype. Error bars represent SEM.

3. Conclusion

Mutant mice phenotype was close to axonal peripheral neuropathy such as CMT2 diseases and ageing in the behavior and to ALS, Parkinson and Alzheimer diseases in the molecular aspects (altered mitochondrial physiology, altered axonal metabolic homeostasis, neuronal stress, axon terminals defects). Therefore, we propose that myelinating cells alter their metabolism in adult animals toward the cancer-like aerobic glycolysis in order to produce the lactate required for the long-term maintenance of axonal physiology. While such metabolic switch is pretty common in cancer cells, Warburg effect has been shown to occur in activated macrophages [28], adult stem cells [29] and retinal cells [30]. This uncommon property appears to be an adaptation to particular physiological cell conditions [31]. However, this dramatically changes the response of the system to many external stimuli and perturbations, suggesting that part of the neurodegenerative diseases particularities results from this exceptional metabolism of glial cells.

4. Material and Methods:

Animals

Schwann cell specific ablation of PKM2 in adult mice (*Plp1-cre^{ERT};PKM2$^{f/f}$*) was obtained by crossing *Plp1-cre^{ERT}* (JAX: 005975)[16] mice with *PKM2$^{f/f}$* (JAX: 024048) [15] to generate *Plp1-Cre^{ERT};Pkm2$^{+/f}$* animals, which were in turn backcrossed with *PKM2$^{f/f}$* mice. All transgenic lines were kept in C57/Bl6 background. Genotyping for all mutants was performed by PCR strategies using standard procedures and appropriate primers. Animals were kept under French and EU regulations, following recommendations of the local ethics committee.

Tamoxifen administration: The recombination of the floxed allele was induced by intraperitoneal injection of tamoxifen (Sigma, T-5648) dissolved in corn oil (Sigma, C-8267) once every 24 hours for a total of 5 consecutive days, in 1 month animals at 180 µg/ gram mouse weight.

DCA administration: dichloroacetate (DCA, Sigma) dissolve in water was administrated by gavaging six days per week during seven weeks, at 500 mg/ kg mouse weight.

Behavioural studies

Rotarod tests: Locomotor coordination was performed with a rotating rod apparatus (Bioseb). Mice from 2 to 12 month were placed on the rotating rod and challenged using the following step: on day 1, mice was familiarized to the behavioral room and learned to stay on the Rotarod at constant speed of 8 rpm for 2 min. At day 2, locomotion performance was assessed on the accelerating Rotarod with a rate of 4 to 40 rpm for 2 min. Latency to fall was recorded on 3 trials separating by at least 15 min pauses. Data are expressed as the means from the 3 trials for each animal, normalized according to animal weight, +- standard error of the mean (SEM).

Griptest: muscular strength for the 4 limbs was assessed with a grip test apparatus (Bioseb). Mice were held by the tail and allowed to grab the grid and then pulled backwards in a horizontal plane. The maximum force (measured in Newtons) applied to the grid was recorded. Data are expressed as the means from 3 trials for each animal, normalized according to animal weight, +- standard error of the mean (SEM).

Hotplate test: sensitivity was tested with a hotplate (Bioseb). The mouse was placed on the surface of the plate heated at 55°C and the timer was started. The timer is stop at the instant the animals was reacting to discomfort by lifting its paw from the plate and shaking or licks its paw or jumps off. A maximal cut-off time of 20 s was used to prevent tissue damage. Data are expressed as the means from 2 trials for each animal separated by at least 30 min pauses, +- standard error of the mean (SEM).

Motor nerve conduction velocity measurement: mice were anesthetized with 2% isoflurane and maintain at 37°c on a hotplate. Left and right sciatic nerves were successively stimulated at the sciatic notch (proximal stimulation) and the ankle (distal stimulation) via a pair of steel needle electrodes (AD Instruments, MLA1302) with supramaximal pulses (7V) of 0.05 milliseconds delivered using a PowerLab 26T (AD Instruments ML4856). The distance between the 2 sites of stimulation was measured alongside the skin surface with fully extended legs. The latencies of the CMAP were recorded with a second pair of electrodes

inserted between the digits of the hind paw and measured from the stimulus artefact to the onset of the M-waves deflection. NCV was calculated by dividing the distance between sciatic notch and ankle sites of stimulation by the subtraction of the distal latency from the proximal latency.

Histological analysis

Immunohistochemistry

For immunohistochemistry on cryosection, nerves were dissected and fixed 2hours in PFA4% at 4°C. For spinal cord and DRG, mice were first perfused transcardially with PBS, and spinal cord and DRG were dissected and fixed in PFA4% overnight or 10min respectively. All tissues were then transferred to 30% sucrose overnight before embedding into Optimum Cutting Temperature (OCT, Tissue-Tek) medium. Cryostat sections of nerves or spinal cord (12 µm) were dried at room temperature (RT) for 15 min, washed in PBS, incubated 1h at RT in a blocking solution (0.25% Triton X-100 and 10% normal Goat serum in PBS) and incubated with primary antibodies in blocking solution overnight at 4°C. For immunochemistry on teased fibers, nerves were isolated from mice, fixed for 10 min in Zamboni's fixative, washed in PBS and subsequently teased on glass slides. Slides were then dried overnight at RT and immunostained as described above. Primary antibodies: PKM1: 1/2500 (NBP2-14833, Novus Biologicals); PKM2 1/500 (SAB4200095, Sigma Aldrich); 2H3:1/80 (DSHB); Cleaved caspase3 1/400 (Cell Signaling); SMI32 1/1000; E-Cadherin 1/300 (MABT26, Merck); SV2 1/100 (DSHB). Secondary donkey antibodies coupled to Alexa Fluor 488, Alexa Fluor 594, or Alexa Fluor 647 1/1000 (Invitrogen) and TO-PRO-3 iodide 1/1000 (Invitrogen, T3605). Imaged were acquired with a Zeiss confocal microscope LSM710.

For neuromuscular junctions immunostaining, soleus and gastrocnemius muscles were dissected and fixed 20 minutes in PFA4% and incubated in 25% sucrose solution at 4°C for 24 h. Tissues were embedded in OCT and stored at -80°C before processing. Neuromuscular Junctions (NMJ) occupancy was quantified on 25-µm and 16-µm thick longitudinal tibialis and soleus sections, respectively. Muscle sections were incubated overnight at 4°C in blocking solution (2% BSA, 10% NGS, 0.1% Triton and PBS) with mouse anti-SV2 (Developmental Hybridoma Bank, 1/50). Sections were next incubated with goat anti-mouse IgG1 Cy3-conjugated antibody (Jackson ImmunoResearch, 1/500) and Bungarotoxin-488 (Molecular Probes, 1/500), and mounted in Mowiol mounting medium. NMJ were imaged on Axioplan fluorescence microscope (Zeiss) with a 20x objective.

Image analysis was done on tissue sections of at least 3 mice. Images that did show at least one caspase3 positive cells were not included in the statistical analysis.

Electron microscopy

Sciatic nerves were isolated from mice and immediately fixed in 2.5% glutaraldehyde and 4% PFA for 2h at RT, and postfixed in 2.5% glutaraldehyde in PHEM buffer (1X, pH 7.4) overnight at 4°C. They were then rinsed in PHEM buffer and post-fixed in a 0.5% osmic acid for 2h at dark and room temperature. After two washs in PHEM buffer, the cells were dehydrated in a graded series of ethanol solutions (30-100%). The cells were embedded in EmBed 812 using an Automated Microwave Tissue Processor for Electronic Microscopy, Leica EM AMW. Thin sections (70 nm; Leica-Reichert Ultracut E) were collected at different

levels of each block. These sections were counterstained with uranyl acetate 1.5% in 70% Ethanol and lead citrate and observed using a Tecnai F20 transmission electron microscope at 200KV in the CoMET MRI facilities, INM, Montpellier France.
Semithin (1 µm) cross section were stained with toluidine blue (Sigma-Aldrich, 89640-5G) and observed with a Nanozoomer Hamamatsu. The g-ratio was determined using the ImageJ GRatioCalculator plug-in (CIF, UNIL).

Lactate assay

To measure lactate content in sciatic nerves of Control and Mutant animals of 4 months and 12 months, equal-length nerves of 2 cm were dissected and immediately homogenized with Lysing Matix D tubes (MP Biomedical) in the lactate assay buffer and proceed according the instruction of the lactate assay kit (MAK064, Sigma-Aldrich).The absorbance at 570 nm was measured with microplate reader (CLARIOstar, BMG Labtech)

Western Blot

Sciatic nerves were dissected from mice, after removal of the epineurium and perineurium, the nerves were frozen in liquid nitrogen and conserved at -80°C. Protein were extracted from whole sciatic nerves after homogenization by sonication in standard RIPA lysis buffer and the protein concentration was measured using a BCA protein assay kit (Pierce). 20 µg proteins were directly analyzed by western blot using standard procedures with 12% SDS–PAGE and transferred on PVDF membranes for immunoblotting. Primary antibodies: Rabbit anti-Pkm1 1/2500 (NBP2-14833, Novus Biologicals); Rabbit anti-Pkm2 1/2500 (SAB4200095, Sigma Aldrich); Mouse anti-α-β-Actin 1/10000 (C1.AC-15, #A1978, Sigma Aldrich). Secondary antibodies, Peroxidase Goat anti Rabbit or Mouse (H+L) (Jackson Immuno Research) were used at 1/10000 dilution.

Semi-quantitative rtPCR

Whole sciatic nerves from 2 and 10 days old mice (P2 and P10) or endoneuria from 1 (P28), 3 and 12 months-old mice were dissected at indicated time-points. Tissues were lysed using Trizol reagent and mechanical homogenization (TissueLyser II, Qiagen). Total RNA was extracted with the RNeasy lipid tissue kit (Qiagen), and RNA quality and concentration were verified by ND-1000 spectrophotometer (NanoDrop). cDNA was synthesized using 70-200ng of the RNA with the PrimeScript RT kit (Takara), following manufacturer's protocols. PKM1 and PKM2 splicing assays at different developmental time-points were conducted as previously described in Clower et al.[32] using the following primers PKM-F: 5'-ATGCTGGAGAGCATGATCAAGAAGCCACGC-3' and PKM-R: 5'-CAACATCCATGGCCAAGTT-3' with PCR annealing step at 60°C during 35 cycles and using HotStart Taq Polymerase (Qiagen). Digestions of cleaned 502bp-PCR products (with DNA Extraction kit, Qiagen) by NcoI (NEB), producing approx. 250 bp bands revealing PKM1 transcript, and PstI (NEB), producing approx. 280+220 bp bands revealing PKM2 transcript), were performed for 2h at 37°C. Digested PCR products were resolved on a 2% agarose gel, imaged by ChemiDoc XRS+ system and quantified using Image lab software version 3.0 (Biorad). The ratio between detected intensity of uncut and cut products was used to assess relative amount of PKM1 and PKM2.

Probes construction and AAV preparation

pAAV-Laconic and pAAV-ΔGlu6 were obtained by digesting Laconic/pcDNA3.1(-) (gift from Luis Felipe Barros; Addgene plasmid #44238)[17] and pcDNA3.1 FLII12Pglu-700uΔ6 (gift from Wolf Frommer; Addgene plasmid # 17866)[18] by BamH1/HindIII (NEB) and cloned into pAAV-MCS (Cell Biolabs, Inc.) under of a CMV promoter. Clones were validated by sequencing. pcDNA-mito-AT1.03 (from H. Imamura, Tokyo, Japan)[19] was digested with XhoI/HindIII (NEB), blunted and cloned into the CMV promoter controlled pAAV-MCS. Mitochondria-targeting tags were two tandem copies of CoxVIII. pAAV9 were produced at UPV, Universitat Autonoma de Barcelona or at INSERM U1089 University of Nantes, France.

In vivo injection in spinal cord

The pups between 1 and 3 days were covered in aluminum foil and completely surrounded in ice for 3–4 min, until a completely cryoanesthetizia. Cryoanesthetized neonates were injected using a thin glass needle filled with colored viral and hold by a micromanipulator (IM—3C, Narishige Japan Group) directly in the spinal cord. 1 µL of the viral solution was injected slowly with short pressure pulses using a microinjector (Pneumatic Picopump PV820, World Precision Instruments) coupled to a 3 MHz function pulse generator (GFG8215, Langlois). The injection site was then cleaned with betadine (Vetoquinol, cat. No. 3042413) and pups were warmed in hands. When fully awake, pups were put back to the mother and the littermates.

Imaging and stimulation of saphenous nerves in living mice

3-4 weeks after the viral injection, mice were anesthetized with a constant low (1.5 l/min) of oxygen+ 5% of isoflurane in an anesthesia induction box (World precision Instrument, Ref.EZ-B800) for 5 min. Thereafter the anesthesia was maintained with a mask delivering 2% isoflurane at 0.8 L/min. The eyes were protected with Ocry-gel (TVM, cat. No. 48026T613/3). The mouse was placed on the back in a silicone mold, the hind leg was shaved and the paws were immobilized using small pins. The incision area was disinfected with betadine (Vetoquinol, cat. No. 3042413). After incision of the skin of the thigh, connective tissue was carefully removed to expose the saphenous nerve. For electrophysiological experiments, the saphenous nerve was lifted up in the middle of the thigh and isolated electrically from the surrounding muscle tissue using a plastic trip. A pair of stimulating platinum electrodes (World precision Instrument, PTM23B05KT) held by micromanipulators (U-31CF, Narishige) was carefully placed under the saphenous nerve, at the ankle. The recording electrode (AD Instruments, MLA 1203) was placed at the groin. A reference needle electrode was inserted in the groin area and a ground electrode is placed in the tail. Once the electrodes were positioned the animal was transferred in a chamber at 37°C under the two-photon microscope (LSM 7 MP OPO, Zeiss), electrodes are connected to a Powerlab 26T (AD Instrument; ML4856). Supramaximal stimulus (between 4 and 12 mA, 150 µs) was delivered at a frequency of 10 Hz during 5 min. Time-lapse of the middle portion of the exposed nerve in the thigh were acquired every 5 min during 1 h with 20X objective lens (LD CApochromat, 421887-9970, Zeiss. For Laconic, ΔGlu6, and mito-ATeam alike, a 870 nm excitation wavelength was used to obtain both emission wavelength 475 nm for mTFP (Laconic) or CFP (ΔGlu6, mito-Ateam) and emission wavelength 527 nm for Venus (Laconic, mito-ATeam) or YFP (ΔGlu6).

Image analysis

We used ImageJ software to analyze the relative lactate, glucose or mitochondrial ATP levels in peripheral axons. The acquired images for each wavelength (em. 475 nm for mTFP or CFP and em. 527 nm for Venus or YFP) were aligned using the Template Matching plugin. We defined a Region of Interest (ROI) encompassing the cytosolic area of one axon or encompassing all labelled mitochondria of one axon and the mean fluorescent intensity in the ROI was measured on both images. These light intensities were then corrected for background light intensity determined as an area within the nerve where no fluorescent signal from the viral probe can be observed. The Citrine/CFP (ΔGlu6) or Venus/mTFP (Laconic) or Venus/CFP (mito-Ateam) ratio was then calculated from the 2 values for mean light intensity. The MTrackJ plugin in ImageJ was used for analysis of mitochondrial movement. For at least 5 images over a time span of 20 minutes, the location of the same mitochondrion was marked, the distance between marked locations was measured and migration velocity was calculated. n= 65 (Control before stimulation), 75 (Mutant before stimulation), 76 (Control after stimulation), 45 (Mutant after stimulation) mitochondria.

Ex vivo nerve electrophysiology

Sciatic nerves were dissected out and transferred into oxygenated artificial cerebrospinal fluid (ACSF) containing 126 mM NaCl, 3 mM KCl, 2 mM $CaCl_2$, 2 mM $MgSO_4$, 1.25 mM NaH_2PO_4, 26 mM $NaHCO_3$, and 10 mM dextrose, pH 7.4-7.5. The nerves were desheated, and cut into 2 cm segments. Nerves were then placed in a three compartment recording chamber and perfused (1-2 ml/min) in 36°C ACSF equilibrated with 95% O_2-5% CO_2. The distal end was stimulated supramaximally (40 µs duration) through two electrodes isolated with Vaseline, and recordings were performed at the proximal end. Signals were amplified and digitized at 500 kHz. Measurements were made once the effects had reached a steady state. The delay and duration of compound action potentials (CAPs) were calculated at half the maximal amplitude and at the maximal amplitude. For recruitment analysis, the amplitude of CAPs was measured and plotted as a function of the stimulation intensity. For refractory period analysis, two stimuli were applied at different intervals, and the amplitude of the second CAP was measured and plotted as a function of the stimulus interval. To ensure that the amplitude of the second response was accurately assessed, the first response was subtracted from all the recordings. For train stimulation, nerves were stimulated for 200ms at frequencies ranging from 100 to 1 kHz. The amplitude of each evoked CAP was measured and plotted as a function of time. Conduction velocities were estimated from latencies.

Statistical significance

*= P value<0.05; **= P value<0.01; ***= P value<0.001.
#= P value<0.05; ##= P value<0.01; ###= P value<0.001.

5. References

1. Harris, J. J. & Attwell, D. The energetics of central nervous system white matter. *J. Neurosci. Off. J. Soc. Neurosci.* **32,** 356–371 (2012).

2. Attwell, D. & Laughlin, S. B. An Energy Budget for Signaling in the Grey Matter of the Brain. *J. Cereb. Blood Flow Metab.* **21,** 1133–1145 (2001).

3. Alle, H., Roth, A. & Geiger, J. R. P. Energy-Efficient Action Potentials in Hippocampal Mossy Fibers. *Science* **325,** 1405–1408 (2009).

4. Magistretti, P. J. & Allaman, I. A Cellular Perspective on Brain Energy Metabolism and Functional Imaging. *Neuron* **86,** 883–901 (2015).

5. Funfschilling, U. *et al.* Glycolytic oligodendrocytes maintain myelin and long-term axonal integrity. *Nature* **485,** 517–521 (2012).

6. Lee, Y., Morrison, B. M. & Rothstein, J. D. Oligodendroglia metabolically support axons and contribute to neurodegeneration. *Nature* 443–448 (2012).

7. Vander Heiden, M. G., Cantley, L. C. & Thompson, C. B. Understanding the Warburg Effect: The Metabolic Requirements of Cell Proliferation. *Science* **324,** 1029–1033 (2009).

8. Hanahan, D. & Weinberg, R. A. Hallmarks of Cancer: The Next Generation. *Cell* **144,** 646–674 (2011).

9. Frezza, C. & Gottlieb, E. Mitochondria in cancer: Not just innocent bystanders. *Warbg. Eff. Re-Discov. Importance Aerob. Glycolysis Tumor Cells* **19,** 4–11 (2009).

10. He, X. *et al.* PKM2 in carcinogenesis and oncotherapy. *Oncotarget* **8,** 110656–110670 (2017).

11. Chen, Z., Liu, M., Li, L. & Chen, L. Involvement of the Warburg effect in non-tumor diseases processes. *J. Cell. Physiol.* **233,** 2839–2849 (2017).

12. Procaccini, C. *et al.* Role of metabolism in neurodegenerative disorders. *Metabolism* **65,** 1376–1390 (2016).

13. Pathak, D., Berthet, A. & Nakamura, K. Energy Failure: Does It Contribute to Neurodegeneration? *Ann. Neurol.* **74,** 506–516 (2013).

14. Pellerin, L. & Magistretti, P. J. Glutamate uptake into astrocytes stimulates aerobic glycolysis: a mechanism coupling neuronal activity to glucose utilization. *Proc. Natl. Acad. Sci. U. S. A.* **91,** 10625–10629 (1994).

15. Israelsen, W. J. *et al.* PKM2 isoform-specific deletion reveals a differential requirement for pyruvate kinase in tumor cells. *Cell* **155,** 10.1016/j.cell.2013.09.025 (2013).

16. Puckett, C. *et al.* Myelin-specific proteolipid protein is expressed in myelinating schwann cells but is not incorporated into myelin sheaths. *J. Neurosci. Res.* **18,** 511–518 (1987).

17. San Martin, A., Ceballo, S., Ruminot, I. & Barros, L. F. A genetically encoded FRET lactate sensor and its use to detect the Warburg effect in single cancer cells. *PLoS ONE* e57712 (2013).

18. Takanaga, H., Chaudhuri, B. & Frommer, W. B. GLUT1 and GLUT9 as major contributors to glucose influx in HepG2 cells identified by a high sensitivity intramolecular FRET glucose sensor. *Biochimica et Biophysica Acta - Biomembranes* 1091–1099 (2008).

19. Imamura, H. *et al.* Visualization of ATP levels inside single living cells with fluorescence resonance energy transfer-based genetically encoded indicators. *Proc. Natl. Acad. Sci. U. S. A.* **106,** 15651–15656 (2009).

20. Mukherjee, A. & Williams, D. W. More alive than dead: non-apoptotic roles for caspases in neuronal development, plasticity and disease. *Cell Death Differ.* **24,** 1411–1421 (2017).

21. Sheng, Z.-H. Mitochondrial trafficking and anchoring in neurons: New insight and implications. *J. Cell Biol.* 1087–1098 (2014).

22. Sheng, Z.-H. & Cai, Q. Mitochondrial transport in neurons: impact on synaptic homeostasis and neurodegeneration. *Nat Rev Neurosci* 77–93 (2016).

23. Liu, X. & Hajnóczky, G. Ca2+-dependent regulation of mitochondrial dynamics by the Miro–Milton complex. *The International Journal of Biochemistry & Cell Biology* 1972–1976 (2009).

24. Schwartz, T. Mitochondrial Trafficking in Neurons. *Cold Spring Harb Perspect Biol* a011304 (2013).

25. Itoh, Y. *et al.* Dichloroacetate effects on glucose and lactate oxidation by neurons and astroglia in vitro and on glucose utilization by brain in vivo. *Proc. Natl. Acad. Sci.* **100,** 4879–4884 (2003).

26. Stacpoole, P. W., Barnes, C. L., Hurbanis, M. D., Cannon, S. L. & Kerr, D. S. Treatment of congenital lactic acidosis with dichloroacetate. *Arch. Dis. Child.* **77,** 535–541 (1997).

27. Calcutt, N. A. *et al.* Peripheral Neuropathy in Rats Exposed to Dichloroacetate. *J. Neuropathol. Exp. Neurol.* **68,** 985–993 (2009).

28. Kelly, B. & O'Neill, L. A. Metabolic reprogramming in macrophages and dendritic cells in innate immunity. *Cell Res.* **25,** 771 (2015).

29. Shyh-Chang, N., Daley, G. Q. & Cantley, L. C. Stem cell metabolism in tissue development and aging. *Dev. Camb. Engl.* **140,** 2535–2547 (2013).

30. Ng, S. K. *et al.* Cancer-like metabolism of the mammalian retina. *Clin. Experiment. Ophthalmol.* **43,** 367–376 (2014).

31. Burns, J. S. & Manda, G. Metabolic Pathways of the Warburg Effect in Health and Disease: Perspectives of Choice, Chain or Chance. *Int. J. Mol. Sci.* **18,** 2755 (2017).

32. C. V. Clower et al., The alternative splicing repressors hnRNP A1/A2 and PTB influence pyruvate kinase isoform expression and cell metabolism. Proc Natl Acad Sci U S A. 107, 1894–1899 (2010).

Supplemental Figures

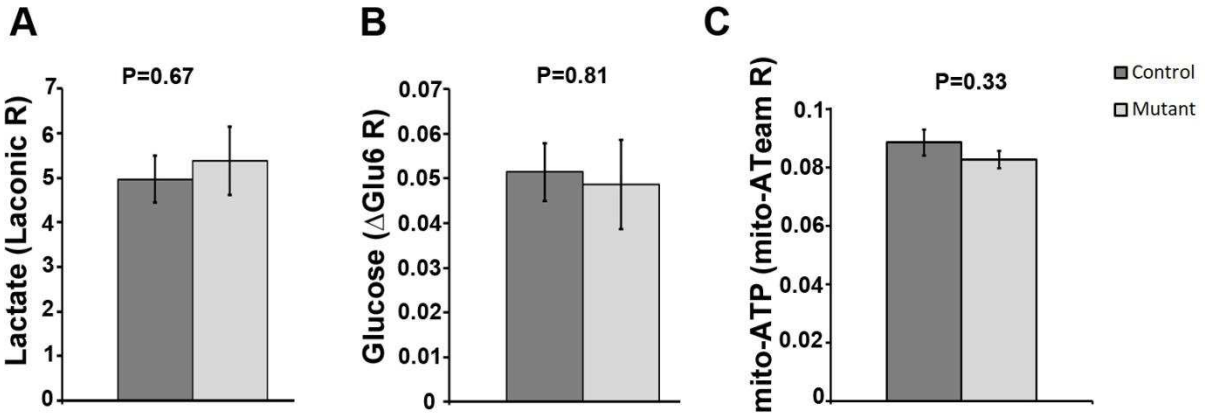

FIGURE S1 Lactate, glucose and mitochondrial ATP levels in resting axons of Mutant and Control saphenous nerves are not different.
As described in Figure S3, Laconic (**A**), δGlu6 (**B**) and mito-Ateam (**C**) fluorescence ratios were measured in resting axons of the saphenous nerves of Mutant and Control mice. No significant differences could be detected in these conditions. P-values show two-tailed unpaired Student T-test. A: n=20 axons in 7 Mutant mice, 7 axons in 4 Control mice. B: n=9 axons in 3 Mutant mice, 15 axons in 6 Control mice. C: n=14 axons in 5 Mutant mice, 16 axons in 5 Control mice. Error bars represent SEM.

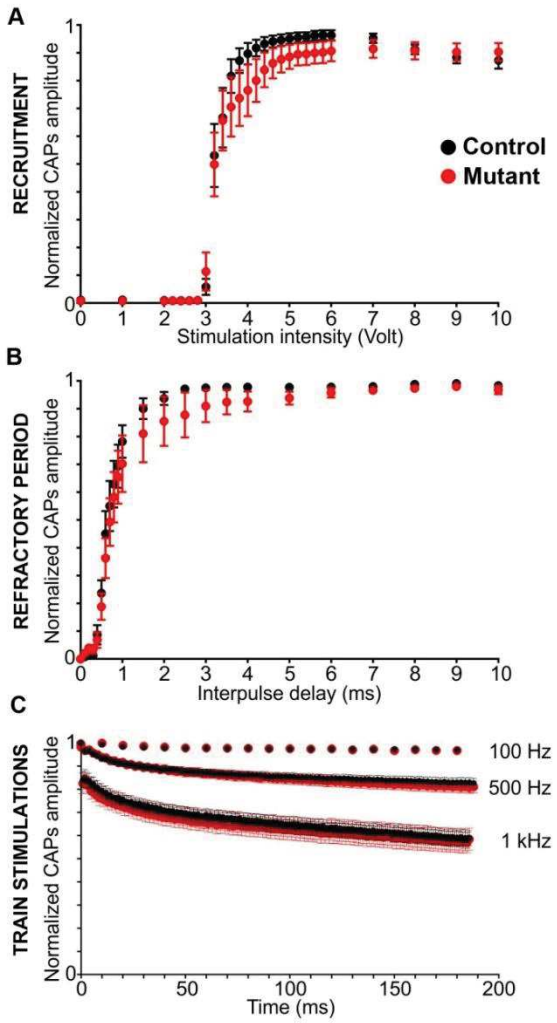

FIGURE S2 Electrophysiological analysis of Control and Mutant sciatic nerves show no significant alteration of the action potential propagation along axons.
A, B- The recruitment (**A**) and refractory period (**B**) of sciatic nerves from Mutant mice (n = 10 nerves from 5 mice) is not significantly different from those of Control mice (n = 10 nerves from 5 mice) (P>0.05 by two-tailed t-tests for two samples of equal variance). **C**- Nerves were stimulated with train of stimuli ranging from 100 to 1 kHz in order to monitor the sustainability of the response. No difference was observed between Control and Mutant mice. Error bars represent SEM.

TABLE S Electrophysiological characteristics of Control and Mutant mice.

	Control	Mutant
Amplitude (mV)	2.5 ± 1.8	3.2 ± 2.5
Duration (ms)	0.34 ± 0.06	0.37 ± 0.09
$CV_{V½}$ ($m.s^{-1}$)	52.1 ± 15.8	45.2 ± 16.1
CV_{Vmax} ($m.s^{-1}$)	33.8 ± 8.5	30.6 ± 9.4
n	10 (5 animals)	10 (5 animals)

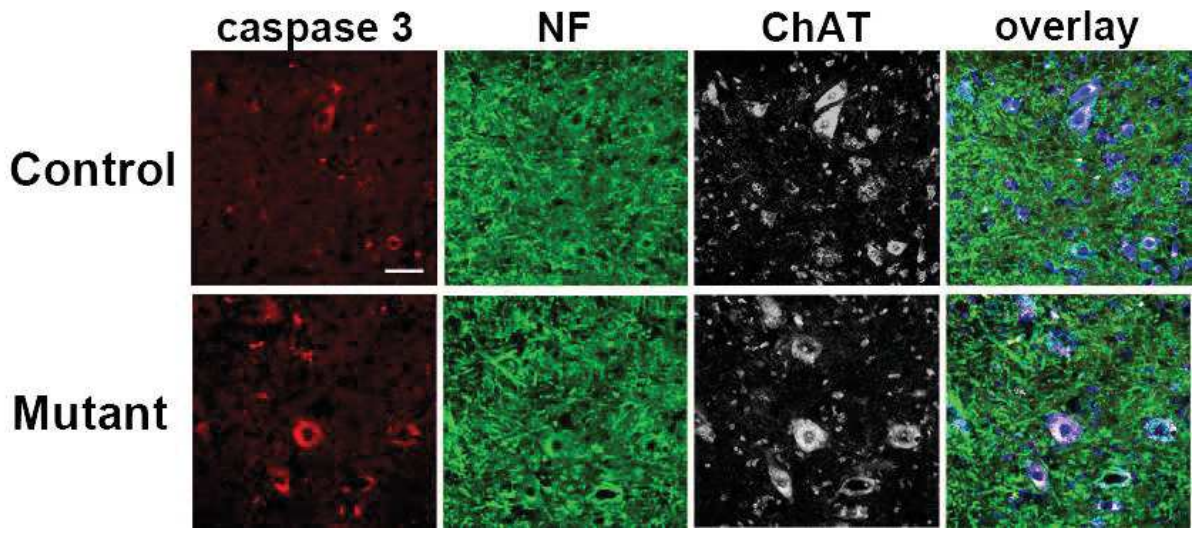

FIGURE S3 Mutant mouse motor neurons display neuronal stress marker Caspase 3. Spinal cord cryosections of Mutant and Control mice were immunostained for neuronal stress marker Caspase 3 (red), neuronal marker Neurofilament (NF, green) and motor neurons marker ChAT (blue). While Neurofilament staining is not different, more motor neurons express Caspase 3 in Mutant mice than in Control mice. Scale bar= 50μm.

Chapter 7) Altered MAM in CMT2A neuropathy

In the previous chapter, we showed that Schwann cells produce lactate via the Warburg effect and transport this lactate to the neuron where it is used in mitochondrial respiration. Mitochondrial physiology in neurons also depends on intraneuronal cues, for example the connection between mitochondria with the endoplasmic reticulum (ER). The ER is an organelle that contains a large amount of calcium, which can be transported into the mitochondrial matrix through pores in mitochondria associated membranes (MAM). Calcium regulates multiple functions within mitochondria, such as improving the activity of enzymes that are part of oxidative phosphorylation and changing conformation of proteins that form the interaction between mitochondria and the cytoskeleton.

The MAM is an area of the ER with a high density of calcium pores, but interestingly MFN2 protein, which is a protein involved in mitochondrial fusion, is also located in there. This suggests that MFN2 also has a role in calcium transport. MFN2 mutations can cause the peripheral neuropathy CMT2A, so possibly calcium transport towards mitochondria is impaired in patients suffering from this disease. However, the effect of MFN2 mutations on ER-mitochondria interaction is not known.

In this chapter, our results on ER-mitochondria interactions in a model for CMT2A neuropathy with MFN2 deficient mitochondria will be presented and discussed as well as downstream effects such as dendrite length, neuronal survival and mitochondrial morphology.

A nucleus surrounded by an endoplasmic reticulum

Altered interplay between endoplasmic reticulum and mitochondria in Charcot-Marie-Tooth type 2A neuropathy

Short running title: Altered MAM in CMT2A neuropathy

Nathalie Bernard-Marissal[a,b,1], Gerben van Hameren[c], Manisha Juneja[d,e], Christophe Pellegrino[f], Cylia Rochat[a], Omar El Mansour[a], Jean-Jacques Médard[g], Marie Croisier[h], Catherine Maclachlan[h], Olivier Poirot[i], Vincent Timmerman[d,e], Nicolas Tricaud[c], Bernard L. Schneider [a,1,2], Roman Chrast [g,1,2]

[a] Brain Mind Institute, Ecole Polytechnique Fédérale de Lausanne (EPFL), 1015 Lausanne, Switzerland

[b] Aix Marseille Univ, INSERM, MMG, 13385 Marseille, France

[c] INSERM U1051, Institut des Neurosciences de Montpellier (INM), Université de Montpellier, 34295 Montpellier, France

[d] Peripheral Neuropathy Research Group, Department of Biomedical Sciences, University of Antwerp, 2610 Antwerp, Belgium

[e] Institute Born Bunge, 2610 Antwerp, Belgium

[f] INMED, Aix-Marseille Univ, INSERM, 13385 Marseille, France

[g] Departments of Neuroscience and Clinical Neuroscience, Karolinska Institutet, Stockholm 17177, Sweden

[h] Centre of Interdisciplinary Electron Microscopy, EPFL, 1005 Lausanne, Switzerland

[i] Department of Medical Genetics, University of Lausanne, 1005 Lausanne, Switzerland

[2] These authors equally contributed to this work

To whom correspondence should be addressed:

[1]Roman Chrast, Department of Neuroscience, Karolinska Institutet, Solnavägen 9, 171 65 Stockholm, Sweden; Tel: +46852487825, Email: Roman Chrast, roman.chrast@ki.se

Correspondence may also be addressed to:

Nathalie Bernard-Marissal; Email: nathalie.bernard.1@univ-amu.fr

Bernard L. Schneider; Email:bernard.schneider@epfl.ch

Abstract

Mutations in the *MFN2* gene encoding Mitofusin 2 lead to the development of Charcot-Marie-Tooth type 2A (CMT2A), a dominant axonal form of peripheral neuropathy. Mitofusin 2 is localized at both the outer membrane of mitochondria and the endoplasmic reticulum, and is particularly enriched at specialized contact regions known as mitochondria-associated membranes (MAM). We observed that expression of $MFN2^{R94Q}$ induces distal axonal degeneration in the absence of overt neuronal death. The presence of mutant protein leads to reduction in endoplasmic reticulum and mitochondria contacts in CMT2A patient-derived fibroblasts, in primary neurons and *in vivo*, in motoneurons of a mouse model of CMT2A. These changes are concomitant with endoplasmic reticulum stress, calcium handling defects and changes in the geometry and axonal transport of mitochondria. Importantly, pharmacological treatments reinforcing endoplasmic reticulum-mitochondria crosstalk, or reducing endoplasmic reticulum stress, restore the mitochondria morphology and prevent axonal degeneration. These results highlight defects in MAM as a new cellular mechanism contributing to CMT2A pathology mediated by mutated MFN2.

Significance Statement

Interactions between mitochondria and the endoplasmic reticulum (ER) at the level of mitochondria-associated membranes (MAM) constitute a key signaling hub emerging as a shared target altered in multiple neurodegenerative diseases. We use both in *in vivo* and *in vitro* models of Charcot-Marie-Tooth type 2A, an axonal form of neuropathy, to demonstrate that the presence of mutated Mitofusin 2 leads to altered MAM. In neurons, these modifications occur concomitantly with activation of ER stress response, dysregulated calcium handling and alterations in mitochondrial morphology and transport, collectively contributing to axonopathy. Importantly, the reported results indicate that the pathological consequences of mutated Mitofusin 2 may be targeted with drugs reinforcing the ER-mitochondria crosstalk and/or reducing ER stress.

Keywords

Motor and sensory neurons, endoplasmic reticulum, mitochondria, CMT2A, neuropathy

Introduction

Charcot-Marie-Tooth (CMT) disease, also known as hereditary motor and sensory peripheral neuropathy, represents a clinically heterogeneous group of inherited neurological disorders with a prevalence of 1 in 2500 (1, 2). These diseases result from defects in axons or in myelin or in both. Among the axonal forms of CMT, around 10-20% are linked to mutations in the *MFN2* gene, encoding Mitofusin 2, and are referred to as CMT2A (3-5). The symptoms of CMT2A are mainly characterized by progressive distal muscle weakness and atrophy, foot deformities, areflexia and sensory loss (6). However, the age of disease onset and the severity of symptoms are highly variable among CMT2A patients (6).

MFN2 is a dynamin-like GTPase protein originally identified at the outer membrane of mitochondria, where it regulates mitochondrial fusion (7). Characterization of *in vitro* and *in vivo* models of the disease based on the expression of mutated MFN2, has led to substantial insights into the CMT2A pathophysiology (8-12). Multiple mouse models have been developed for CMT2A (8, 13-15), however a transgenic line overexpressing $MFN2^{R94Q}$ specifically in neurons (mitoCharc mice or *CMT2A Tg*) most closely mimics the late-onset CMT2A pathology (8). Homozygous *CMT2A Tg* mice develop locomotor dysfunction from the age of 5 months on, a pathologic effect associated at a late stage of the disease with the accumulation of mitochondria in small-caliber axons (8). However, the long-term progression of the disease, as well as the mechanisms underlying motor and/or sensory dysfunction, have not been fully characterized in this model yet. *In vitro,* primary sensory and motor neurons overexpressing mutated *MFN2*, or motoneurons differentiated from CMT2A-R94Q iPS cells, both display mild defects in mitochondrial transport as well as mitochondrial fragmentation (10-12, 14-16). In sensory neurons expressing $MFN2^{R94Q}$, overexpression of the homologous mitochondrial protein MFN1 partially restores mitochondrial fusion and rescues mitochondrial transport and axonal degeneration (10), suggesting the existence of additional mechanisms underlying the $MFN2^{R94Q}$-related pathophysiology.

Interestingly, a fraction of MFN2 is also located at the endoplasmic reticulum (ER) membrane, in particular at specialized sites of contacts with mitochondria called Mitochondria-Associated Membranes (MAM) (17). The MAM control several cellular processes such as lipid metabolism, calcium homeostasis, mitochondrial

dynamics as well as autophagy/mitophagy (18, 19). Several studies have highlighted the role of MAM in neuronal function, with important implications in various neurodegenerative disorders (20-23). MFN2 has been proposed to regulate either positively or negatively the association between the two organelles (17, 24-26). However, it is unknown how CMT2A-associated MFN2 mutations affect MAM functioning and what are the potential consequences for CMT2A pathology.

In the present study, we characterized in detail the neuropathy phenotype caused by expression of $MFN2^{R94Q}$ in both *in vitro* and *in vivo* CMT2A disease models. Our data show that overexpression of $MFN2^{R94Q}$ affects locomotion and gait in *CMT2A Tg* mice, and causes the loss of neuromuscular junctions at a late stage of the disease. In primary neurons, $MFN2^{R94Q}$ induces axonal degeneration. At the cellular level, $MFN2^{R94Q}$ expression leads to ER stress and the loss of MAM, as well as impaired mitochondrial dynamics. Importantly, we observe that pharmacological treatments to reinforce MAM function or block ER stress can rescue some of these phenotypes.

Results

CMT2A Tg mice display locomotor and gait abnormalities associated to slow-twitch muscle denervation

Previous studies showed that homozygous *CMT2A Tg* mice develop locomotion impairments in the rotarod test, starting from the age of approximately 6 months (8). As CMT2A patients display symptoms that worsen with age (27), we sought to assess the progression of both motor and sensory dysfunction in *CMT2A Tg* mice. In addition, to mimic more closely the dominant inheritance of CMT2A we used heterozygous *B6;D2-Tg* $^{(Eno2\text{-}MFN2*R94Q)/-}$ mice, described here as *CMT2A Tg* mice. We performed a battery of behavioral tests at early and late time points (6 and 12 months old). Locomotor function was evaluated using the rotarod and catwalk tests and sensory function using the Von Frey test. We did not observe any significant effect in sensory function (**Fig. 1A**). However, the performance on the rotarod was significantly affected in *CMT2A Tg* animals compared to wild-type (WT) littermates at both 6 and 12 months of age (**Fig. 1B**). *CMT2A Tg* score on rotarod did not significantly worsen between 6 and 12 months (**Fig. 1B** and **Fig. S1A**). Furthermore, gender-dependent segregation of mice showed that the motor performance was significantly decreased only in male *CMT2A Tg* mice (**Fig S1A**).

Catwalk test revealed that several gait parameters were significantly changed at both 6 and 12 months in *CMT2A Tg* mice as compared to WT mice. These parameters were classified as indicators of the pressure exerted by each paw, the area of the floor contacted by each paw, gait/posture and coordination (**Table 1**). Intensity variables reflecting paw pressure during contact with the glass walkway floor were reported to be affected by peripheral nerve injury (28). Here, forepaw intensity values were significantly decreased in *CMT2A Tg* animals at both time points (**Table 1**). Print size of the right forepaw was also reduced in 6-month-old *CMT2A Tg* mice suggesting a misplacement of the paw (**Table 1**). Dynamic catwalk variables that evaluate gait/posture as well as coordination were also affected in *CMT2A Tg* mice. At the age of 6 months, right forepaw terminal dual stance and left forepaw duty cycle mean were increased, whereas two other variables (left hindpaw stand mean and 'support three') also indicating gait impairment were significantly changed in 12-month-old *CMT2A Tg* animals (**Table 1**). These observations indicate that *CMT2A Tg*

mice maintain some of their paws longer on the glass plate. Finally, the right forepaw and right hindpaw inter-paw coordination reflected by the phase dispersions and couplings parameters, were altered in *CMT2A Tg* mice only at 12 months (**Table 1**).

To assess whether these locomotor defects were linked to muscle weakness, we monitored muscle strength using the grid test (29, 30). No decrease in muscle strength score was observed in *CMT2A Tg* mice compared to WT at either 6 (WT: 2308 ± 96.2 and *CMT2A Tg*: 2328 ± 144.8) or 12 months (WT: 1886 ± 107.7 and *CMT2A Tg*: 1852 ± 155.2).

As defects in locomotion can reflect subtler neuromuscular dysfunctions, we evaluated motoneuron survival and NMJ innervation. We did not observe loss of motoneuron in *CMT2A Tg* spinal cord at 12 months (**Fig. 1C**). Similarly, there was no significant loss of proximal motor axons in the ventral roots or sensory neurons in the dorsal root (**Fig. S1B, C**). However, we observed a significant decrease in the proportion of fully innervated NMJ at the age of 12 months in the slow-twitch soleus muscle of *CMT2A Tg* mice (innervated NMJ WT: 79 ± 5.8 %, *CMT2A Tg*: 48.2 ± 7 %) (**Fig. 1D, E**). Remarkably, at the same age, the loss of NMJ occupancy was not significantly reduced in the fast-twitch tibialis muscle (**Fig. S1D**). Moreover, NMJ innervation was not affected at 6 months (**Fig. S1E**), suggesting that additional mechanisms may underlie the behavioral dysfunctions already observed at this age.

MFN2^{R94Q} overexpression leads to alteration of the neurite length of primary motoneurons

To characterize the mechanisms underlying neuronal dysfunction in CMT2A, we used primary embryonic cultures of either motor or sensory neurons, the two neuronal populations that are typically affected by the disease. To evaluate the effects of mutated CMT2A, we overexpressed either the wild-type (*MFN2^{WT}*) or R94Q mutated form of MFN2 (*MFN2^{R94Q}*) using AAV6 vectors (**Fig. S2A**). In accordance with our *in vivo* data, the overexpression of either *MFN2^{WT}* or *MFN2^{R94Q}* did not reduce the survival of motor or sensory neurons at 4, 6 or 8 days post-infection (**Fig. 2A, B**). However, the overexpression of *MFN2^{R94Q}* led to a significant reduction of neuritic length at 6 dpi. This effect was evident in motoneurons (non-infected: 1982.6 ± 220.9, *MFN2^{WT}*: 2056.8 ± 175.7 µm, *MFN2^{R94Q}*: 1419.5 ± 110.5 µm), but not in sensory neurons (*MFN2^{WT}* 3810 ± 648 µm, *MFN2^{R94Q}*: 3547 ± 897 µm) (**Fig. 2C, D**). Moreover, in both motor and sensory neurons expressing *MFN2^{R94Q}* we observed the

presence of axonal swellings and spheroids, as revealed by peripherin staining (**Fig. 2D**).

MFN2^{R94Q} impairs ER-mitochondria tethering both *in vitro* and *in vivo*

MFN2 has been shown to regulate either positively or negatively ER-mitochondria connections (17, 24-26). We therefore quantified ER-mitochondria contacts in neurons overexpressing either WT or mutated MFN2. We used an *in vitro* proximity ligation assay (PLA) based on the interaction of the mitochondrial VDAC1 protein and the ER protein IP3R, as previously described (20) (**Fig. S2B**). The number of dots reflecting ER-mitochondria contacts was significantly decreased in both motor and sensory neurons overexpressing MFN2^{R94Q}, as compared to both non-infected neurons and neurons overexpressing MFN2^{WT} (**Fig. 3A, B**). Importantly, we also observed a decreased number of ER-mitochondria contacts in CMT2A patient-derived fibroblasts as compared to control (**Fig. 3C, D**).

Next, we further evaluated by electron microscopy the contacts between mitochondria and ER in the motoneuron soma, in the lumbar spinal cord of 12 month-old WT and *CMT2A Tg* mice. In WT mice, 37.8 ± 2.1 % of the mitochondria made at least one contact with the ER, whereas this proportion was significantly decreased in *CMT2A Tg* motoneurons (31.3 ± 2.1%) (**Fig. 3E, G**). Furthermore, the length of these contacts was significantly decreased in *CMT2A Tg* motoneurons, representing 6.0 ± 0.3 % of mitochondrial perimeter, as compared 9.6 ± 0.4 % in their WT counterparts (**Fig. 3F, G**). We did not notice any significant change in the level of expression of SIGMAR1 or VAPB, two constituents of MAM, in the spinal cord of CMT2A mice, supporting a specific role of mutated MFN2 in the observed MAM defects (**Fig. S2C, D**). To determine whether the altered contacts between ER and mitochondria played a functional role in neurite shortening following MFN2^{R94Q} expression, we treated motoneurons with Pre-084, a selective agonist of SIGMAR1, a chaperone protein located at the MAM which controls calcium transfer from the ER towards mitochondria (20). Remarkably, exposure of primary motoneurons to Pre-084 almost completely prevented neurite degeneration induced by MFN2^{R94Q}, as shown by significant increase in neuritic length when compared to untreated neurons (MFN2^{R94Q}: 1479 ± 162 µm, MFN2^{R94Q} + Pre-084: 2087.5 ± 187.9 µm) (**Fig. 3H**).

Expression of MFN2^{R94Q} leads to unfolded protein response activation and intracellular calcium defects

MAM defects have been previously linked to ER malfunction leading to an unfolded protein response (UPR) and calcium homeostasis impairments (20, 31). We therefore analyzed the level of ER stress markers *in vitro* (phosphorylated eIF2A, P-eIF2α; the ER chaperone PDI). The levels of both P-eIF2α and PDI were significantly increased in motoneurons overexpressing mutated MFN2 relative to the non-infected controls or MFN2^{WT} (PDI MFN2^{R94Q}: +81 ± 11.7 % compared to non-infected; P-eIF2α MFN2^{R94Q}: +134 ± 53.4 % compared to MFN2^{WT}) (**Fig. 4A, B**). In sensory neurons, there was no significant effect of MFN2^{R94Q} on the level of both PDI and P-eIF2α (**Fig. 4A**).

To confirm these findings *in vivo*, we analyzed the level of P-eIF2α, PDI and Activating Transcription Factor 6 (ATF6) in lumbar motoneurons of 12-month-old *CMT2A Tg* animals. Compared to WT littermates, we observed a significant increase in PDI expression similar to the changes seen *in vitro* (**Fig. 4C, E**). Although there was a clear trend towards increased level of P-eIF2α, the difference did not reach statistical significance (**Fig. 4C**). We also analyzed the nuclear translocation of ATF6 as an additional early marker of ER stress in motoneurons of WT and *CMT2A Tg* mice. The proportion of motoneurons with a predominant nuclear versus cytosolic ATF6 staining was significantly higher in the *CMT2A Tg* lumbar spinal cord (WT: 24 ± 3.2 %, *CMT2A Tg*: 47.4 ± 5.2 %) (**Fig. 4D, E**).

Interestingly, exposure of primary motoneurons to the ER stress inhibitor Salubrinal (20) almost completely prevented neurite degeneration induced by MFN2^{R94Q}, as shown by a significant increase in neuritic length when compared to untreated neurons (MFN2^{R94Q}: 1270.7 ± 77.8 µm, MFN2^{R94Q} + Salubrinal: 1685.5 ± 115.6 µm) (**Fig. 4F**). These results show that ER stress plays a functional role in neuronal degeneration following MFN2^{R94Q} expression.

As defects in calcium homeostasis have been previously associated with ER stress activation (20), we monitored intracellular calcium variation using ratiometric Fura-Red AM (F490/F440 ratio) before, during and after 25 mM KCl exposure, as previously described (32). In basal conditions, we did not detect any difference in the ratiometric fluorescence of the calcium indicator when comparing motoneurons overexpressing either MFN2^{WT} or MFN2^{R94Q} (**Fig. 4G**). However, we found a lower amplitude in the KCl-evoked calcium rise in MFN2^{R94Q} motoneurons, as compared to

cells expressing $MFN2^{WT}$, which reflects perturbed calcium dynamics (**Fig. 4H**). Furthermore, $MFN2^{R94Q}$ motoneurons displayed a shorter time to return to basal calcium levels (**Fig. S3A**) further indicating impairment of calcium buffering in motoneurons expressing $MFN2^{R94Q}$.

Mitochondrial transport and clustering are altered in axons expressing $MFN2^{R94Q}$

Previous studies reported contradictory results regarding abnormalities of mitochondrial transport following mutated MFN2 expression (10, 12, 15). We monitored axonal mitochondrial transport by time-lapse microscopy *in vivo*, in the mouse sciatic nerve. Mitochondria were classified according to their velocities, moving at either very slow (<0.3 µm/min), slow (>0.3 and <0.6 µm/min), medium (>0.6 and <0.9 µm/min) or fast (>0.9 µm/min) speed (**Fig. 5A, B and Fig. S3B**). The frequency distribution showed more very slow moving and less moving mitochondria in axons of the sciatic nerve of 1-month-old *CMT2A Tg* mice compared to control mice (**Fig. S3B**). In addition, very slow moving mitochondria were significantly slower in *CMT2A Tg* mice, as compared to WT littermates (mean speed of very slow mitochondria, WT: 0.24 ± 0.011 µm/min, *CMT2A Tg*: 0.11 ± 0.01 µm/min) (**Fig. 5B**). This actually translated into a sharp increase in the proportion of stationary mitochondria (WT: 3.4 %, *CMT2A Tg*: 50.7 %). Mitochondrial velocity was not affected towards any specific direction, since there was no difference in the average anterograde or retrograde mitochondrial transport speeds (**Fig. 5C**). However, the proportion of mitochondria moving anterogradely or retrogradely was different between control and *CMT2A Tg* mice (WT: 32 % retrograde and 68 % anterograde moving mitochondria, *CMT2A Tg*: 55 % retrograde and 44 % anterograde moving mitochondria). The formation of mitochondria accumulations/clusters have previously been observed *in vitro* and could potentially be linked to mitochondrial transport defects induced by $MFN2^{R94Q}$ (14, 16). Therefore, we measured the diameter of mitochondria clusters in axons relative to the average diameter of a single mitochondrion. We noticed a significant overrepresentation of individual mitochondria as well as small mitochondria clusters with a decrease in the numbers of large-size clusters in *CMT2A Tg* axons as compared to WT axons (**Fig. 5D**). Overall, these observations suggest defects in mitochondrial dynamics following $MFN2^{R94Q}$ overexpression.

MFN2^{R94Q} induced changes in mitochondrial morphology can be partially reverted by preventing ER stress

MFN2 is one of the main proteins controlling mitochondrial fusion (33). Mitochondrial length is reduced in sensory neurons expressing MFN2^{R94Q} (10). Altered ER-mitochondria contact could be implicated in this phenotype since MAM participate in regulation of mitochondria dynamics (18). We analyzed mitochondria morphology *in vitro*, by loading motor neurons and sensory neurons with Mitotracker red allowing to label more than 90 % of axonal mitochondria (20). We noticed a significant decrease in mitochondria length in both motor and sensory neurons overexpressing MFN2^{R94Q} (motoneurons: MFN2^{WT}: 1.76 ± 0.14 µm, MFN2^{R94Q}: 1.36 ± 0.09 µm; sensory neurons: MFN2^{WT}: 1.79 ± 0.09 µm, MFN2^{R94Q}: 1.43 ± 0.09 µm) (**Fig. 6A, B**). Mitochondria morphology was also evaluated using *in vivo* imaging, in axons of the sciatic nerve of 1-month-old WT and *CMT2A Tg* mice. In this experiment, axonal mitochondria were labeled with mito-Dsred2 expressed following injection of AAV9-CAG-mitoDsred2 into the spinal cord at postnatal day 1. In *CMT2A Tg* mice, mitochondrial length was again significantly reduced as compared to WT littermates (WT: 3.7 ± 0.1 µm, *CMT2A Tg*: 3.2 ± 0.12 µm) (**Fig. 6C, D**). The diameter of mitochondria was not significantly changed (WT: 0.49 ± 0.13 µm, *CMT2A Tg*: 0.56 ± 0.1 µm). Furthermore, we also used transmission electron microscopy to assess mitochondrial morphology in the soma of spinal cord motoneurons (**Fig. S3C**). In 12-month-old *CMT2A Tg* mice, consistent significant decrease in mitochondria length was observed (WT: 0.64 ± 0.014 µm, *CMT2A Tg*: 0.58 ± 0.02 µm). Together, these results suggest that mutated MFN2 may affect mitochondrial fusion leading to smaller mitochondria.

Since perturbations of ER-mitochondria contacts affect mitochondrial dynamics, we sought to explore if treatments with either Pre-084 to reinforce MAM function, or Salubrinal to prevent ER stress, had beneficial effects on mitochondrial morphology in neurons expressing MFN2^{R94Q}. We measured mitochondria length in primary motoneurons expressing MFN2^{R94Q} as previously described, and found that both treatments restored mitochondrial length to values similar to the control MFN2^{WT} condition (**Fig. 6E**). By performing electron microscopy on the distal sciatic nerve of 6-month-old *CMT2A Tg* mice, we also measured a significant rescue of mitochondrial size and density after 4 weeks of daily Salubrinal injections (**Fig. 6F-**

H). Overall, these results demonstrate that the modulation of MAM and ER stress support proper function of mitochondria and could prevent some defects in mitochondria caused by MFN2^{R94Q}.

Discussion

We used both *in vitro* and *in vivo* models of CMT2A diseases in order to gain insight into the pathophysiology of $MFN2^{R94Q}$-induced axonopathy. Overexpression of $MFN2^{R94Q}$ led to progressive locomotor impairments in mice, whereas overt distal axonal degeneration was apparent only at later stages of the disease. Decreased numbers of ER-mitochondria contacts, as well as ER and mitochondria dysfunction were detected in motor and sensory neurons expressing $MFN2^{R94Q}$, either preceding or concomitant to axonal degeneration. We also observed that the number of MAM was reduced in patient-derived fibroblasts carrying MFN2 mutations when compared to age-matched controls.

Although muscle strength can be affected to different degrees in CMT2A patients depending on the age of disease onset, clinical data also indicate that sensory function is generally less affected (6, 34, 35). Here, we characterized the motor and sensory functions of *CMT2A Tg* mice at early and late stages of the disease (6 vs 12 months). We confirmed that locomotor dysfunction is an early feature of *CMT2A Tg* mice, detectable with the rotarod test in 6- and 12-month-old mice. However, rotarod phenotype does not worsen with age. In addition, the *CMT2A Tg* mice do not display neither muscle weakness, nor sensory impairments in the Von Frey test. Locomotion as well as gait defects were more precisely assessed in the catwalk test (36), previously used in another CMT2A model (13). This test has revealed several parameters altered in *CMT2A Tg* mice, which highlight changes in the pressure and the surface of contact of the paw (spatial parameters), in gait/posture (temporal parameter) and coordination. Spatial parameters are consistently decreased at 6 and 12 months, whereas temporal parameters and coordination tend to deteriorate over time. Similarly, foot misplacement and deformation, as well as toe muscle weakness, are observed in CMT2A patients and lead to steppage gait (6). In *CMT2A Tg* mice, gait parameters such as terminal dual stance and duty cycle mean are already changed at 6 months. At 12 months, parameters including left hindpaw stand mean and 'support three' are significantly changed, which could suggest posture alterations with an increased duration of the postural phase (37). In addition, inter-paw coordination of the right limb pair reflected by the phase dispersion and couplings parameters, are altered in 12-month-old *CMT2A Tg* animals. All together, these results indicate

walking difficulties in *CMT2A Tg* mice, with symptoms slightly progressing between 6 and 12 months, which is consistent with the clinical data from CMT2A patients (6).

Quantification of NMJ occupancy showed that between 6 and 12 months of age, the proportion of fully innervated junctions significantly declines to 50 % in the slow-twitch soleus muscle of *CMT2A Tg* mice. In contrast, denervation does not reach statistical significance in the fast-twitch tibialis muscle. Soleus muscle is mainly involved in walking and maintenance of standing posture (38), two parameters altered in *CMT2A Tg* mouse model. In contrast, tibialis muscle is involved in functions such as running and jumping, which require strength. Slowly progressing locomotor deficits combined to late muscle denervation indicate that *CMT2A Tg* mice replicate the phenotype of late-onset CMT2A neuropathy. When compared to early-onset disease, late-onset CMT2A is indeed characterized by milder and more slowly progressing symptoms (34). Moreover, axonal degeneration is almost absent in these patients, which is in line with the normal numbers of motoneurons and proximal axons measured in *CMT2A Tg* mice until month 12.

In agreement with the *in vivo* data, we observed no decrease in the survival of primary motor and sensory neurons induced to overexpress $MFN2^{R94}$ for up to 8 days *in vitro*. However, we detected substantial neurite shortening and the presence of axonal swellings and spheroids indicating ongoing neurite degeneration. As no motoneuron death is observed, reduction in neuritic length of $MFN2^{R94Q}$ motoneurons may reflect a dying back process which has already been described in motoneuron diseases (20, 39). Similar to previously published observations, sensory neurons also display signs of axonal degeneration without any reduction in neuritic length (10).

MFN2 regulates ER-mitochondria associations as well as calcium transfer from ER towards mitochondria (17). The connection between these organelles is maintained via interaction of $MFN2^{mitochondrial}$-$MFN2^{ER}$ homodimers or $MFN1^{mitochondrial}$-$MFN2^{ER}$ heterodimers (17, 24, 33). It is still unclear whether MFN2 regulates positively or negatively the formation of MAM (17, 24, 25). Recent work has discriminated the role of short and long-range ER-mitochondria contacts based on a split green fluorescent protein-based contact site sensor (40). Using this system, it was shown that downregulation of MFN2 increases short-range ER-mitochondria connections whereas it reduces the long-range ones, arguing the observed discrepancy regarding the role of MFN2 at MAM. Our data demonstrate that the neuronal overexpression of $MFN2^{R94Q}$ affects ER-mitochondria contacts both *in vitro* and *in*

vivo. In addition, we observed that the number of MAM is reduced in fibroblasts derived from CMT2A-R94Q patients. Since $MFN2^{R94Q}$ is expressed at a level similar to $MFN2^{WT}$ (8, 17), it is unlikely that the observed defects are due to specific changes in $MFN2^{R94Q}$ abundance at the level of the ER or mitochondria. Alternatively, altered capacity of $MFN2^{R94Q}$ to interact with MFN2 (9) may contribute to the observed decrease in ER-mitochondria contacts. Interestingly, it has been shown that in contrast to MFN2, MFN1 is able to make functional interactions with $MFN2^{R94Q}$ (9). However, since MFN1 localization is restricted to mitochondria, it cannot complement $MFN2^{ER}$ and may therefore only partially rescue the effects of the mutation at the level of ER-mitochondria contacts.

Disruption of MAM has emerged as a key process in several neurodegenerative diseases (20, 23, 41). MAM regulate various processes essential for neuronal function, such as calcium transfer between ER and mitochondria, which controls ATP production (42). MAM also control lipid synthesis and transfer, as well as mitochondrial dynamics (18). Interestingly, stimulation of the MAM protein SIGMAR1 with the Pre-084 agonist prevented axonal degeneration in motoneurons overexpressing $MFN2^{R94Q}$. SIGMAR1 is an ER chaperone protein involved in the stabilization of IP3R, thereby controlling ER calcium efflux (42). SIGMAR1 inhibition or loss has been connected to MAM defects and axonal degeneration in motoneurons (20, 41).

Disconnection of ER and mitochondria can affect the function of both organelles. We therefore evaluated pathological changes in ER and measured an increase of ER stress markers that occurred in motoneurons both *in vitro* and *in vivo*. The potential link between MFN2 and ER stress remains poorly studied. MFN2 depletion in liver and skeletal muscle leads to an increase in P-eIF2α, CHOP, IRE-1, ATF6 and the ER chaperone BIP (43). In cardiac myocytes, the deletion of MFN2, but not MFN1, enhances ER stress (44). UPR aims at re-establishing proper ER function by promoting ER chaperone synthesis and ER-associated protein degradation, as well as decreasing protein translation. However, in case of sustained activation, UPR can lead to cell degeneration (45). MFN2 modulates UPR sensors by direct interaction with PERK (direct activator of P-eIF2α), preventing its constitutive activation (46). Our observation that the ER-stress inhibitor Salubrinal prevents axonal degeneration in motoneurons expressing $MFN2^{R94Q}$ suggests that ER stress is likely to contribute to axonal dysfunction in CMT2A.

We have also evaluated the levels of ER stress in CMT2A patient-derived fibroblasts (data not shown). However, the levels of P-eIF2α and CHOP were highly variable in both control and patients' cells making it difficult to interpret a possible effect of MFN2 mutation on the basal and induced ER stress. The observed variability may reflect differences between used fibroblast culture that are likely to be linked to their proliferative capacity and/or their number of passages. Alternatively, fibroblasts might also be able to recover more easily from ER stress than neurons in culture conditions.

Mitochondria can adjust to stress conditions by dividing or fusing. Mitochondrial fusion enables mitochondria to exchange components and rescue mitochondria while mitochondrial fission promotes axonal transport and cell apoptosis (47). Mitochondrial fragmentation has been reported in axons of sensory neurons or motoneurons overexpressing $MFN2^{R94Q}$ (10, 14, 16). We indeed observed decreased mitochondria length *in vitro*, in axons of both motoneurons and sensory neurons overexpressing $MFN2^{R94Q}$, consistent with defects in mitochondrial fusion. Live imaging of mitochondria in intact sciatic nerves of 1-month-old *CMT2A Tg* mice also showed a reduction in mitochondria length as well as overabundance of small mitochondria clusters. This could indicate that mitochondria tend to be fragmented already in the axons of young *CMT2A Tg* mice. Altered mitochondria dynamics may also underlie some of the behavioral and structural phenotypes seen in older mice, as confirmed by electron microscopy in motoneurons of 12-month-old *CMT2A Tg* mice.

Defects in mitochondria positioning have been observed in sensory neurons expressing $MFN2^{R94Q}$ (10, 14, 16). However, other reports found mild or no axonal transport defects using *in vitro* models of CMT2A, such as motoneurons differentiated from CMT2A-R94Q human iPS cells and sensory neurons expressing $MFN2^{R94W}$ (11, 12, 15). By measuring mitochondrial transport *in vivo*, we noticed that the velocity of slow-moving mitochondria, that could be defined as oscillation movements, was significantly decreased, which corresponds to an increase in the number of stationary mitochondria in *CMT2A Tg* mice. As oscillatory movements require ATP production (48), the strong reduction observed in *CMT2A Tg* axons may reflect reduced levels of available ATP. Although the levels of ATP have not been measured in the sciatic nerve, OXPHOS complexes and ATP levels are decreased in the brain of 9-month-old *CMT2A Tg* mice (49). In addition, mitochondria tend to form a higher number of small clusters in the axons of *CMT2A Tg* mice. Accumulations of

mitochondria have also been observed in the soma and axons of both sensory and motor neurons in models of CMT2A (8, 13, 14, 16), which may further contribute to mitochondrial transport defects.

Noteworthy, we observed differences between motor and sensory neurons in the cellular response to $MFN2^{R94Q}$ overexpression. Although the number of MAM and length of mitochondria were decreased in both neuron types, UPR markers and neuritic length remained unchanged in the sensory neurons. This selective vulnerability of motor versus sensory neurons is consistent with previous reports, which showed perturbations of the MAM protein SIGMAR1 in motoneurons only (20), and ER stress to be specifically induced in motoneurons of amyotrophic lateral sclerosis mice expressing mutated SOD1 (50). The finding that motoneurons may be more vulnerable than sensory neurons to defects of the ER-mitochondria system may clarify why the motor function is generally more affected than the sensory function in CMT2A patients (35).

In conclusion, our results show that altered interplay between ER and mitochondria contribute to the axonopathy present in *CMT2A Tg* mice. Therefore, modulation of these mechanisms should be considered as a potential future therapeutic strategy to prevent or delay the onset of CMT2A neuropathy.

Materials and Methods

For fully detailed methods, please refer to SI Appendix.

Animals

In vivo work was performed using the mouse strain B6;D2-Tg (Eno2-MFN2*R94Q) L51Ugfm/J previously described by (8) (alternative name *MitoCharc1*, purchased from Jackson Laboratories, stock No: 012812). Animals were maintained as heterozygous by crossing B6;D2-Tg $^{(Eno2\text{-}MFN2*R94Q)/-}$ males with B6;D2F1 females (Janvier).

Neuronal cultures were prepared from embryos (Swiss Rj Orl mouse strain, purchased from Janvier) collected at gestational day 12.5. Animals were housed in an animal facility with 12 h light / 12 h dark environment, and *ad libitum* access to water and normal diet. All experiments were done in accordance with Swiss legislation and the European Community Council directive (86/609/EEC) for the care and use of laboratory animals and were approved by the Veterinarian Office of the canton of Vaud and a local ethics committee.

Behavioral Studies

In accordance with dominant CMT2A inheritance, all animals studies were performed on heterozygote B6;D2-Tg $^{(Eno2\text{-}MFN2*R94Q)/-}$ mice (described here as *CMT2A Tg*) or matched control animals (described as wild-type).

Muscle strength was evaluated with the grid test as previously described (29). Sensory function was evaluated using the plantar Von Frey test. The touch sensitivity following mechanical stimulation of the mouse hindpaw was measured using a dynamic plantar aesthesiometer (Ugo Basile). Locomotion was evaluated by the rotarod and CatWalk tests. Latency to fall was tested on an accelerating rotarod (4-40 rpm) with a maximum latency of 300 sec. Each mouse was tested twice and the best score was kept (51). Experiments on the CatWalk walkway apparatus (Noldus, The Netherlands) were performed as described in (52).

Fibroblast lines

Skin biopsies were obtained from two normal controls and two CMT2A patients (PN198.1 and PN198.3) with a p.Arg94Gln missense mutation in the

Mitofusin 2 gene (*MFN2*). Clinical, electrophysiological and neuropathological characteristics of these patients were reported by (53). Five-millimeter punch forearm glabrous skin biopsies were obtained and used to prepare primary fibroblast cells. Appropriate consent was obtained from participants and the Institutional Review Board from the University of Antwerp approved the study.

Constructs and production of AAV vectors

Plasmid containing Myc-Human *MFN2* was generously provided by Dr. Darren Moore. Myc-hMFN2 cassette was subcloned in a pAAV-hsyn-MCS plasmid for expression under the control of the hSyn1 promoter. Arginine-to-glutamine substitution at position 94 of *MFN2* was generated using Quickchange site-directed mutagenesis kit (Agilent). For AAV2/6 vector production, pAAV plasmids (AAV-hsyn-hMFN2^{WT}, AAV-hsyn-hMFN2^{R94Q}, AAV-CMV-GFP) were co-transfected with pDP6 helper plasmid into HEK293-AAV cells (Agilent). Cells were lysed 48 h after transfection and viral particles were purified using iodixanol gradient followed by separation on heparin affinity columns. The infectivity titer of each virus (expressed as Transduced Units/mL) was determined by real time PCR.

Primary neuronal cultures

Motor and sensory neurons cultures were prepared from E12.5 mouse embryos as previously described (20).

For analysis of neuronal survival, mitochondrial transport and ER stress, neuronal cultures were infected with AAV6-hsyn-MFN2^{WT} or AAV6-hsyn-MFN2^{R94Q} (10 TU/cell) 48 h after plating and analyzed at indicated time points (4, 6 or 8 days post-infection (dpi)). For quantification of neuritic length, neurons were co-infected with AAV2/6-hsyn-MFN2^{WT} or AAV2/6-hsyn-MFN2^{R94Q} (10 TU/cell) and AAV2/6-CMV-GFP (1 TU/cell) to label neuronal processes with GFP.

Reagents

Mitotracker Red CMXRos was purchased from Life technologies. Pre-084 was purchased from Tocris Biosciences and used at 50 nM on primary neurons. For *in vitro* experiments, neurons were treated with 5 µM of Salubrinal (Sigma Aldrich). For *in vivo* experiments, Salubrinal diluted in sterile saline solution was intraperitoneally injected daily at a dose of 1 mg/kg.

Immunocytochemistry

Neuronal and fibroblasts cultures collected at indicated time-points were fixed and incubated with the following primary antibodies: rabbit anti-IP3R (Abcam, 1/250), mouse anti-VDAC1 (Abcam, 1/250), rabbit anti-peripherin (Millipore, 1/1000), rabbit anti-GFP (Invitrogen, 1/500), rabbit anti-phospho-eIF2α (Invitrogen, 1/250), mouse anti-non-phosphorylated neurofilament H (SMI32, Biolegend, 1/500) and anti-mouse neurofilament 200 (Sigma Aldrich, 1/500). Coverslips were next incubated with appropriate fluorochrome-conjugated secondary antibodies (Molecular Probes) and mounted in Mowiol Medium. Fluorescence was observed under a Zeiss Axioplan fluorescence microscope with a 63x objective and images were analyzed using Fiji or Axiovision software.

Proximity Ligation Assay

Fixation and blocking were performed as described for immunocytochemistry. To label MAM, neurons or fibroblasts were incubated with rabbit anti-IP3R and mouse anti-VDAC1 primary antibodies in the antibody reagent buffer provided in the proximity ligation assay (PLA) kit (Duolink, Sigma-Aldrich) as previously described (Bernard-Marissal *et al.*, 2015).

Calcium Imaging

Quantitative changes of $[Ca^{2+}]i$ in motoneurons were monitored using a Fura-Red acetoxymethyl ester (AM) dye (Invitrogen) that allows effective ratiometric fluorescence measurements. At 6 dpi, motoneurons were rinsed with an external solution containing (in mM):150 NaCl, 2 KCl, 2 $MgCl_2$, 2 $CaCl_2$, 10 HEPES, and 10 glucose, pH 7.4, and incubated in the same solution containing 4 µM Fura-Red AM for 30 min in the dark at 20 °C. The dye was washed off and the coverslips reincubated in the dark for a further 30 min at RT. To selectively visualize Ca^{2+} in motoneurons, we acquired fluorescent images of Fura-Red. Fura-Red was alternately excited at 440 (10) nm and 490 (10) nm using a xenon light source (Sutter Instruments), and emission collected at 660 (50) nm using a CCD camera (Hamamatsu). During experiments, neurons were continuously perfused with external solution. Fifteen sec after beginning the experiment, neurons were activated by a brief (8 sec) application of the external solution containing 25 mM KCl (replacing

equimolar amount of NaCl in the external solution), applied via a fast perfusion system. After KCl application, the cells were perfused with the KCl-free solution for an additional 3 min to let them recover. To analyze $[Ca^{2+}]i$, we drew regions of interest on motoneurons and then applied these regions of interest for analysis of Fura-Red images. $[Ca^{2+}]i$ values are presented as the 490/440 nm ratio.

Mitochondrial axonal transport

AAV2/9-CAG-mitoDsred2 vector was transdermally introduced into the spinal cord of 1-day-old mice. One month after injection, mice were anesthetized and the sciatic nerve was exposed and imaged as previously described (48). Mitochondria images were acquired by time-lapse recording, varying from one image every min to one image every 5 min during 1 h using 920 nm wavelength as excitation light (48). To analyze mitochondrial parameters in peripheral axons, we used ImageJ software to project parts of the axon, located in different Z-layers, in a single maximum intensity image. The multiple time-point images were aligned using the Template Matching plugin in ImageJ. To measure size of a single mitochondrion, we drew a line along the axis of the smallest isolated object and measured the line length using Image J software. To measure the size of mitochondrial clusters we drew a similar line through individually identified objects. To measure mitochondrial speed, we defined a ROI encompassing individual mitochondrion using Image J and the movement of each ROI was calculated using the MTrackJ plugin of Image J software. Speed is expressed as µm/min. 3D images were reconstructed using Bitplane Imaris 8.3.1. software.

Immunohistochemistry

Mice were sacrificed and transcardially perfused with PBS followed by 4 % PFA. Spinal cord and muscles were dissected out and postfixed during 2-3 h at 4 °C or 20 min respectively. Generated tissue sections were incubation with the following antibodies: mouse anti-ATF6 (Novus Biologicals, 1/150), rabbit anti-P-eIF2α (Invitrogen, 1/150), mouse anti-PDI (Abcam, 1/150), mouse anti-NeuN (Millipore, 1/500) and goat anti-ChAT (Millipore, 1/500). Immunodetection was made with appropriate secondary antibodies (Alexa Fluor 488 or Cy3, Molecular Probes; or secondary biotinylated antibody, Vector BA-9500) combined with Vectastain ABC-

Elite kit (Vector Labs) and 0.05 % 3,3′ -diaminobenzidine (DAB, Sigma Aldrich) staining. Fluorescent-labelled sections were mounted in Mowiol mounting medium and imaged on Axioplan fluorescence microscope (Zeiss). Integrated density of fluorescence signal was analyzed in 15-20 motoneurons per animal using Fiji software and expressed as a ratio Protein-of-interest/NeuN. Motoneuron survival was directly evaluated under a transmitted light Olympus CX41 microscope.

Neuromuscular Junctions (NMJ) occupancy was quantified on 25-µm and 16-µm thick longitudinal tibialis and soleus sections, respectively. Muscle sections were incubated with mouse anti-SV2 (Developmental Hybridoma Bank, 1/50). Sections were next incubated with goat anti-mouse IgG1 Cy3-conjugated antibody (Jackson ImmunoResearch, 1/500) and Bungarotoxin-488 (Molecular Probes, 1/500), and mounted in Mowiol mounting medium. NMJ were imaged on Axioplan fluorescence microscope (Zeiss) with a 20x objective.

Western blot

Western blots were done on lysates from lumbar spinal cord dissected from 12-month-old wild-type or *CMT2A Tg* mice as previously described (Bernard-Marissal *et al.*, 2015). Membranes were incubated with the following antibodies: goat anti-SIGMAR1 1/500 (Santa Cruz), rabbit anti VAPB 1/500 (Novus Biologicals) and goat anti-GAPDH 1/1000 (Santa-Cruz Biotechnology, #sc-48167). Blots were then incubated with donkey anti-rabbit IRDye 800 and donkey anti-goat IRDye 680, (Li-Cor Biosciences, diluted at 1/10000). Acquisition of results was done using the LI-COR Odyssey system. Immunoblot images were quantified using the software ImageJ and normalized relative to GAPDH levels.

Electron microscopy

Animals were sacrificed and transcardially and spinal cords, sciatic nerves and dorsal and ventral roots were dissected out and kept in fixative solution at 4 °C overnight. Coronal 80-µm thick sections were obtained from the lumbar spinal cord and distal part of the sciatic nerve using vibratome and processed as previously described (Bernard-Marissal *et al.*, 2015). Photographs of ultra-thin sections were obtained using transmission FEI Tecnai Spirit BioTWIN microscope.

The number of mitochondria apposed to ER, forming a MAM, was evaluated in the lumbar spinal cord of 12 month-old WT (n=33 motoneurons from 3 mice) and *CMT2A Tg* mice (n=33 motoneurons from 3 mice). Length of MAM was quantified in the same cells by measuring the length of the mitochondrial surface associated with the ER (<30 nm) reported to the circumference of each mitochondria and the proportions of the mitochondrial surface (circumference) as previously described (54).

Semi-thin (0.5 mm) cross-sections of dorsal and ventral roots were stained with 1 % toluidine blue and digitalized using Axioskop 40 with AxioCam MRc5 (Zeiss). Axon number was evaluated with Fiji software.

Statistical analyses and experimental design

Animals were matched by gender, genotype, age and weight. Mice were randomly assigned to experimental groups and all behavioral experiments as well as processing and analyzes of the tissues were performed in blind.

Size of the cohort for behavioral studies was estimated based on previous experiments using the *CMT2A Tg* model (8).

For histology, we analyzed at least 3 mice per condition. *In vitro* results display the data averaged from at least 3 independent cultures. For behavioral studies, we performed either two-tailed student's t-test, one-way, two-way ANOVA or repeated-measures two-way ANOVA with Sidak, Tukey's or Newman-Keuls post-hoc tests, depending on the experimental design. Significance of the results for histology, electron microscopy, *in vivo* mitochondrial transport and primary cultures was evaluated with one-way, two-way ANOVA or two-tailed student's t-test according to experimental design. In Fig. 6F-G, non-parametric Kruskal-Wallis test with Dunn's post-hoc test was applied as the values did not follow normal distribution (D'Agostino and Pearson normality test). Statistical analyses were performed using the GraphPad Prism or Statistica software. All data are presented as mean ± standard error of the mean (sem) or using box-and-whisker plots (showing median, first and third quartiles and minimal/maximal values). The alpha level of significance was set at 0.05. Levels of significance are indicated as follows: *$p<0.05$, **$p<0.01$, ***$p<0.001$ and ****$p<0.0001$.

Acknowledgments

We thank Philippe Colin and Christel Voize for their technical support in animal experimentation and histology. We also thank Aline Aebi, Fabienne Pidoux and Viviane Padrun for viral vector production. We wish to thank the electron microscopy platform of EPFL, CIME, for the processing of the tissues and imaging. We also thank Romain Cartoni and Jean-Claude Martinou for their help with *CMT2A tg* mice. We thank Hassan Boukhaddaoui, the Montpellier Resources Imaging facility and the animal facility staff of SMARTY platform of the Réseau des Animaleries de Montpellier.

This work was supported by Swiss National Science Foundation grant (310030L_156460/1 to B.S.), by ERANET E-Rare FaSMALS (Grant 3ER30_160673, to B.S.), by The Neuromuscular Research Association Basel grant (to B.S., R.C. and N.B.M), by the Swedish StratNeuro program grant (to R.C.), by the Swedish Research Council grant (2015-02394 to R.C.), by the Labex EpiGenMed (to G.v.H.), by the European research council (FP7-IDEAS-ERC 311610 to N.T.), by AFM-Téléthon research grant (20044 to N.T. and R.C.), by the Fund for Scientific Research (FWO-Flanders, grants G036814N and G041416N to V.T.), the Queen Elisabeth Medical Foundation (to V.T) and the Association Belge contre les maladies neuromusculaires (ABMM, to M.J.).

References

1. Azzedine H, Senderek J, Rivolta C, & Chrast R (2012) Molecular genetics of charcot-marie-tooth disease: from genes to genomes. *Molecular syndromology* 3:204-214.
2. Weis J, *et al.* (2017) Towards a functional pathology of hereditary neuropathies. *Acta neuropathologica* 133:493-515.
3. Feely SM, *et al.* (2011) MFN2 mutations cause severe phenotypes in most patients with CMT2A. *Neurology* 76:1690-1696.
4. Rossor AM, Polke JM, Houlden H, & Reilly MM (2013) Clinical implications of genetic advances in Charcot-Marie-Tooth disease. *Nature reviews Neurology* 9:562-571.
5. Zuchner S, *et al.* (2004) Mutations in the mitochondrial GTPase mitofusin 2 cause Charcot-Marie-Tooth neuropathy type 2A. *Nature genetics* 36:449-451.
6. Stuppia G, *et al.* (2015) MFN2-related neuropathies: Clinical features, molecular pathogenesis and therapeutic perspectives. *Journal of the neurological sciences* 356:7-18.
7. Chan DC (2006) Dissecting mitochondrial fusion. *Developmental cell* 11:592-594.
8. Cartoni R, *et al.* (2010) Expression of mitofusin 2(R94Q) in a transgenic mouse leads to Charcot-Marie-Tooth neuropathy type 2A. *Brain* 133:1460-1469.
9. Detmer SA & Chan DC (2007) Functions and dysfunctions of mitochondrial dynamics. *Nature reviews. Molecular cell biology* 8:870-879.
10. Misko AL, Sasaki Y, Tuck E, Milbrandt J, & Baloh RH (2012) Mitofusin2 Mutations Disrupt Axonal Mitochondrial Positioning and Promote Axon Degeneration. *J Neurosci* 32:4145-4155.
11. Rizzo F, *et al.* (2016) Selective mitochondrial depletion, apoptosis resistance, and increased mitophagy in human Charcot-Marie-Tooth 2A motor neurons. *Human molecular genetics* 25:4266-4281.
12. Saporta MA, *et al.* (2015) Axonal Charcot-Marie-Tooth disease patient-derived motor neurons demonstrate disease-specific phenotypes including abnormal electrophysiological properties. *Experimental neurology* 263:190-199.
13. Bannerman P, Burns T, Xu J, Miers L, & Pleasure D (2016) Mice Hemizygous for a Pathogenic Mitofusin-2 Allele Exhibit Hind Limb/Foot Gait Deficits and Phenotypic Perturbations in Nerve and Muscle. *PloS one* 11:e0167573.

14. Detmer SA, Vande Velde C, Cleveland DW, & Chan DC (2008) Hindlimb gait defects due to motor axon loss and reduced distal muscles in a transgenic mouse model of Charcot-Marie-Tooth type 2A. *Human molecular genetics* 17:367-375.
15. Strickland AV, *et al.* (2014) Characterization of the mitofusin 2 R94W mutation in a knock-in mouse model. *JPNS* 19:152-164.
16. Baloh RH, Schmidt RE, Pestronk A, & Milbrandt J (2007) Altered axonal mitochondrial transport in the pathogenesis of Charcot-Marie-Tooth disease from mitofusin 2 mutations. *J Neurosci* 27:422-430.
17. de Brito OM & Scorrano L (2008) Mitofusin 2 tethers endoplasmic reticulum to mitochondria. *Nature* 456:605-610.
18. Krols M, *et al.* (2016) Mitochondria-associated membranes as hubs for neurodegeneration. *Acta neuropathologica* 131:505-523.
19. Rowland AA & Voeltz GK (2012) Endoplasmic reticulum-mitochondria contacts: function of the junction. *Nature reviews. Molecular cell biology* 13:607-625.
20. Bernard-Marissal N, Medard JJ, Azzedine H, & Chrast R (2015) Dysfunction in endoplasmic reticulum-mitochondria crosstalk underlies SIGMAR1 loss of function mediated motor neuron degeneration. *Brain* 138:875-890.
21. De Vos KJ, *et al.* (2012) VAPB interacts with the mitochondrial protein PTPIP51 to regulate calcium homeostasis. *Human molecular genetics* 21:1299-1311.
22. Hedskog L, *et al.* (2013) Modulation of the endoplasmic reticulum-mitochondria interface in Alzheimer's disease and related models. *Proceedings of the National Academy of Sciences of the United States of America* 110:7916-7921.
23. Paillusson S, *et al.* (2016) There's Something Wrong with my MAM; the ER-Mitochondria Axis and Neurodegenerative Diseases. *Trends in neurosciences* 39:146-157.
24. Cosson P, Marchetti A, Ravazzola M, & Orci L (2012) Mitofusin-2 independent juxtaposition of endoplasmic reticulum and mitochondria: an ultrastructural study. *PloS one* 7:e46293.
25. Filadi R, *et al.* (2015) Mitofusin 2 ablation increases endoplasmic reticulum-mitochondria coupling. *Proceedings of the National Academy of Sciences of the United States of America* 112:E2174-2181.

26. Naon D, *et al.* (2016) Critical reappraisal confirms that Mitofusin 2 is an endoplasmic reticulum-mitochondria tether. *Proceedings of the National Academy of Sciences of the United States of America* 113:11249-11254.
27. Cartoni R & Martinou JC (2009) Role of mitofusin 2 mutations in the physiopathology of Charcot-Marie-Tooth disease type 2A. *Experimental neurology* 218:268-273.
28. Lin KL, *et al.* (2010) DuraSeal as a ligature in the anastomosis of rat sciatic nerve gap injury. *The Journal of surgical research* 161:101-110.
29. Bernard-Marissal N, Sunyach C, Marissal T, Raoul C, & Pettmann B (2015) Calreticulin levels determine onset of early muscle denervation by fast motoneurons of ALS model mice. *Neurobiology of disease* 73:130-136.
30. Saxena S, Cabuy E, & Caroni P (2009) A role for motoneuron subtype-selective ER stress in disease manifestations of FALS mice. *Nature neuroscience* 12:627-636.
31. Bernard-Marissal N, Chrast R, & Schneider BL (2018) Endoplasmic reticulum and mitochondria in diseases of motor and sensory neurons: a broken relationship? *Cell death & disease* 9:333.
32. Bernard-Marissal N, *et al.* (2012) Reduced calreticulin levels link endoplasmic reticulum stress and Fas-triggered cell death in motoneurons vulnerable to ALS. *J Neurosci* 32:4901-4912.
33. Chen H, *et al.* (2003) Mitofusins Mfn1 and Mfn2 coordinately regulate mitochondrial fusion and are essential for embryonic development. *The Journal of cell biology* 160:189-200.
34. Chung KW, *et al.* (2006) Early onset severe and late-onset mild Charcot-Marie-Tooth disease with mitofusin 2 (MFN2) mutations. *Brain* 129:2103-2118.
35. Zuchner S & Vance JM (2006) Molecular genetics of autosomal-dominant axonal Charcot-Marie-Tooth disease. *Neuromolecular medicine* 8:63-74.
36. Hamers FP, Koopmans GC, & Joosten EA (2006) CatWalk-assisted gait analysis in the assessment of spinal cord injury. *Journal of neurotrauma* 23:537-548.
37. Wang XH, *et al.* (2012) Quantitative assessment of gait and neurochemical correlation in a classical murine model of Parkinson's disease. *BMC neuroscience* 13:142.
38. Kanning KC, Kaplan A, & Henderson CE (2010) Motor neuron diversity in development and disease. *Annual review of neuroscience* 33:409-440.

39. Selvaraj BT, Frank N, Bender FL, Asan E, & Sendtner M (2012) Local axonal function of STAT3 rescues axon degeneration in the pmn model of motoneuron disease. *The Journal of cell biology* 199:437-451.
40. Cieri D, *et al.* (2018) SPLICS: a split green fluorescent protein-based contact site sensor for narrow and wide heterotypic organelle juxtaposition. *Cell death and differentiation* 25:1131-1145.
41. Watanabe S, *et al.* (2016) Mitochondria-associated membrane collapse is a common pathomechanism in SIGMAR1- and SOD1-linked ALS. *EMBO molecular medicine* 8:1421-1437.
42. Hayashi T, Rizzuto R, Hajnoczky G, & Su TP (2009) MAM: more than just a housekeeper. *Trends in cell biology* 19:81-88.
43. Sebastian D, *et al.* (2012) Mitofusin 2 (Mfn2) links mitochondrial and endoplasmic reticulum function with insulin signaling and is essential for normal glucose homeostasis. *Proceedings of the National Academy of Sciences of the United States of America* 109:5523-5528.
44. Ngoh GA, Papanicolaou KN, & Walsh K (2012) Loss of mitofusin 2 promotes endoplasmic reticulum stress. *The Journal of biological chemistry* 287:20321-20332.
45. Xiang C, Wang Y, Zhang H, & Han F (2017) The role of endoplasmic reticulum stress in neurodegenerative disease. *Apoptosis : an international journal on programmed cell death* 22:1-26.
46. Munoz JP, *et al.* (2013) Mfn2 modulates the UPR and mitochondrial function via repression of PERK. *The EMBO journal* 32:2348-2361.
47. Milone M & Benarroch EE (2012) Mitochondrial dynamics: general concepts and clinical implications. *Neurology* 78:1612-1619.
48. Gonzalez S, *et al.* (2015) In vivo time-lapse imaging of mitochondria in healthy and diseased peripheral myelin sheath. *Mitochondrion* 23:32-41.
49. Guillet V, *et al.* (2011) Bioenergetic defect associated with mKATP channel opening in a mouse model carrying a mitofusin 2 mutation. *FASEB journal : official publication of the Federation of American Societies for Experimental Biology* 25:1618-1627.
50. Taiana M, Sassone J, & Lauria G (2016) Mutant SOD1 accumulation in sensory neurons does not associate with endoplasmic reticulum stress features:

Implications for differential vulnerability of sensory and motor neurons to SOD1 toxicity. *Neuroscience letters* 627:107-114.

51. Dirren E, *et al.* (2015) SOD1 silencing in motoneurons or glia rescues neuromuscular function in ALS mice. *Annals of clinical and translational neurology* 2:167-184.
52. Caballero-Garrido E, Pena-Philippides JC, Galochkina Z, Erhardt E, & Roitbak T (2017) Characterization of long-term gait deficits in mouse dMCAO, using the CatWalk system. *Behavioural brain research* 331:282-296.
53. Verhoeven K, *et al.* (2006) MFN2 mutation distribution and genotype/phenotype correlation in Charcot-Marie-Tooth type 2. *Brain* 129:2093-2102.
54. Stoica R, *et al.* (2014) ER-mitochondria associations are regulated by the VAPB-PTPIP51 interaction and are disrupted by ALS/FTD-associated TDP-43. *Nature communications* 5:3996.

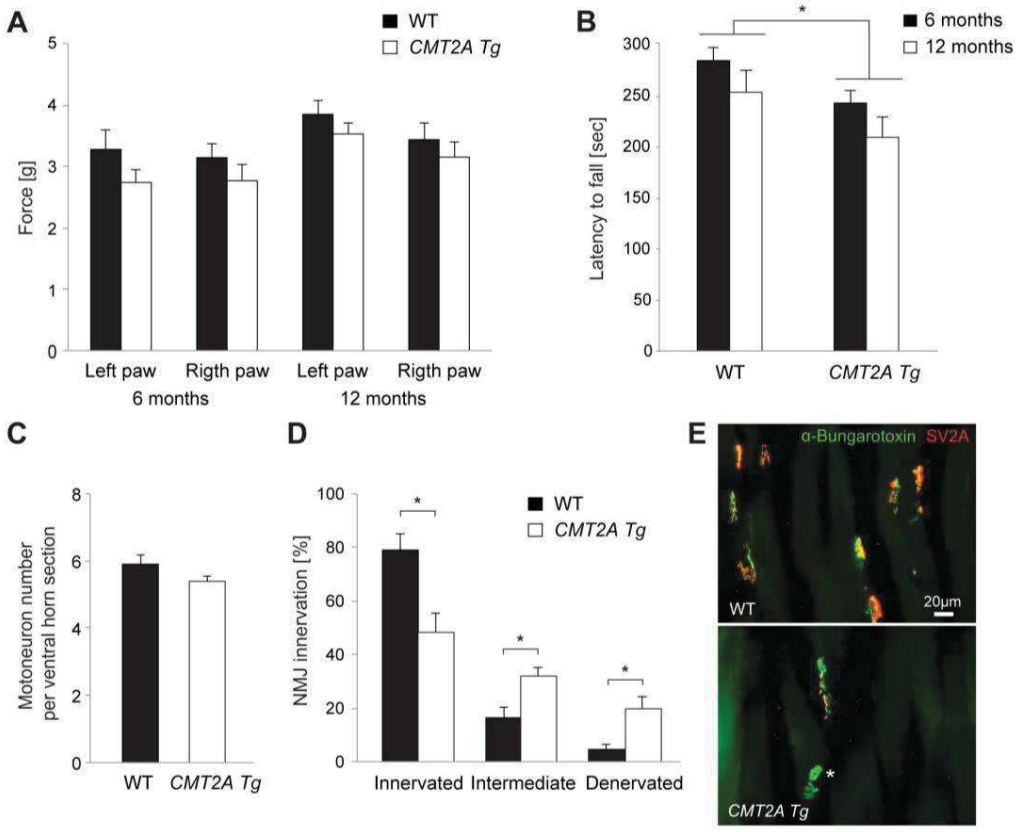

Fig. 1. *CMT2A Tg* mice show locomotor defects and muscle denervation but no detectable motoneuronal death

(A) Evaluation of sensory function with the von Frey test at the age of 6 and 12 months (WT: n=11 and *CMT2A Tg*: n=12). Statistical analysis: two-way repeated-measures ANOVA (group x time) with Newman-Keuls post-hoc test. **(B)** Evaluation of motor function with rotarod test at the age of 6 and 12 months (WT: n=11 and *CMT2A Tg*: n=12). Statistical analysis: two-way repeated-measures ANOVA (group x time, significant group effect) with Newman-Keuls post-hoc test. **(C)** Number of motoneurons in lumbar spinal cord of 12 month-old animals (n=4 for both WT and *CMT2A Tg*). Statistical analysis: two-tailed unpaired student's t-test. **(D)** Level of innervation of soleus muscle evaluated based on the co-localization of the nerve terminal marker SV2A and acetylcholine receptor marker α-bungarotoxin in 12 month-old WT (n=5) and *CMT2A Tg* (n=7) mice. Statistical analysis: two-tailed unpaired student's t-test. **(E)** Representative photomicrographs of NMJ in WT and *CMT2A Tg* soleus muscle, stained with anti-SV2A antibodies and α-bungarotoxin. Note the presence of unoccupied NMJ positive for α-bungarotoxin only (indicated by an asterisk) in the *CMT2A Tg* mice. *$p<0.05$.

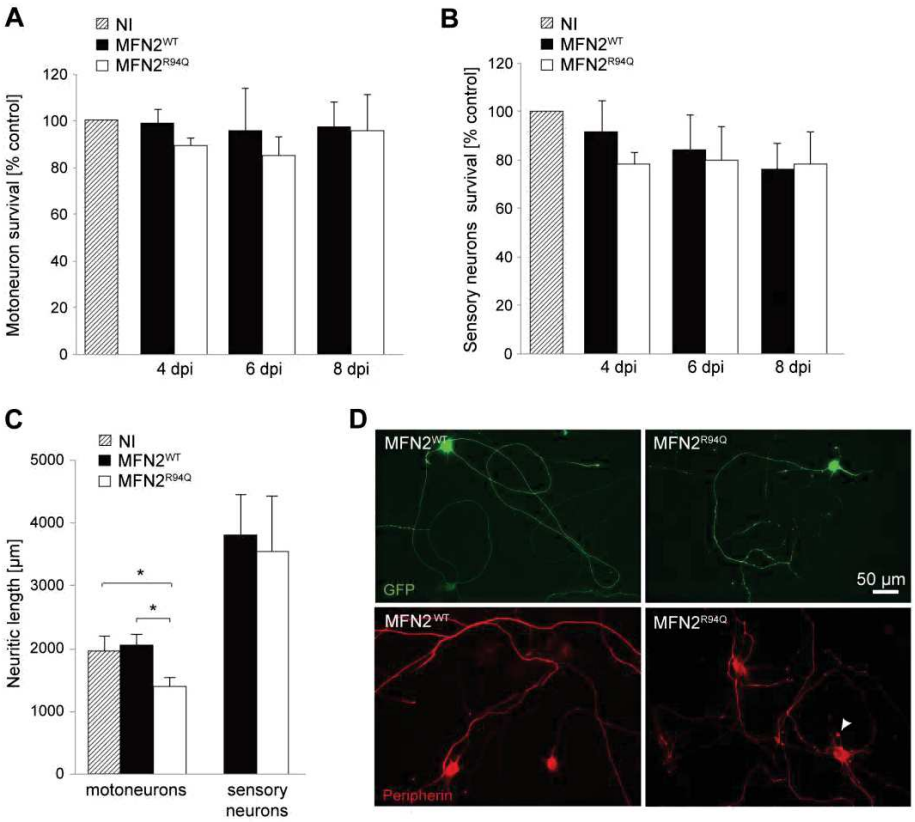

Fig. 2. Overexpressing MFN2^{R94Q} induces neurite degeneration in the absence of neuronal death

(A, B) Motor and sensory neurons were infected for 4, 6 and 8 days (days post-infection, dpi) with AAV6-hsyn-hMFN2^{WT} or AAV6-hsyn-hMFN2^{R94Q}. Survival of motor and sensory neurons was evaluated following SMI32 and NF-200 staining. Non-infected (NI) motoneuron cultures were used as a control to evaluate the effect of MFN2 overexpression. Data are expressed as mean percentage ± sem as compared to the non-infected (NI) control cultures (n=3 independent neuronal cultures). Statistical analysis: two-way ANOVA (group x time), with Tukey's post-hoc test. **(C)** Neuritic length was quantified at 6 dpi in motor and sensory neurons infected with AAV6-hsyn-hMFN2^{WT} or AAV6-hsyn-hMFN2^{R94Q}. Neurons were co-transduced with AAV6-CMV-GFP to label neurites. Values are expressed as mean (µm) ± sem from 6 independent cultures. Statistical analysis: two-way ANOVA (group x time), with Tukey's post-hoc test. **(D)** Upper panels show GFP-labeled neurites in motoneurons expressing either MFN2^{WT} or MFN2^{R94Q}. Lower panels illustrate peripherin staining in the same conditions. Arrowhead indicates a peripherin-positive axonal swelling. *$p<0.05$.

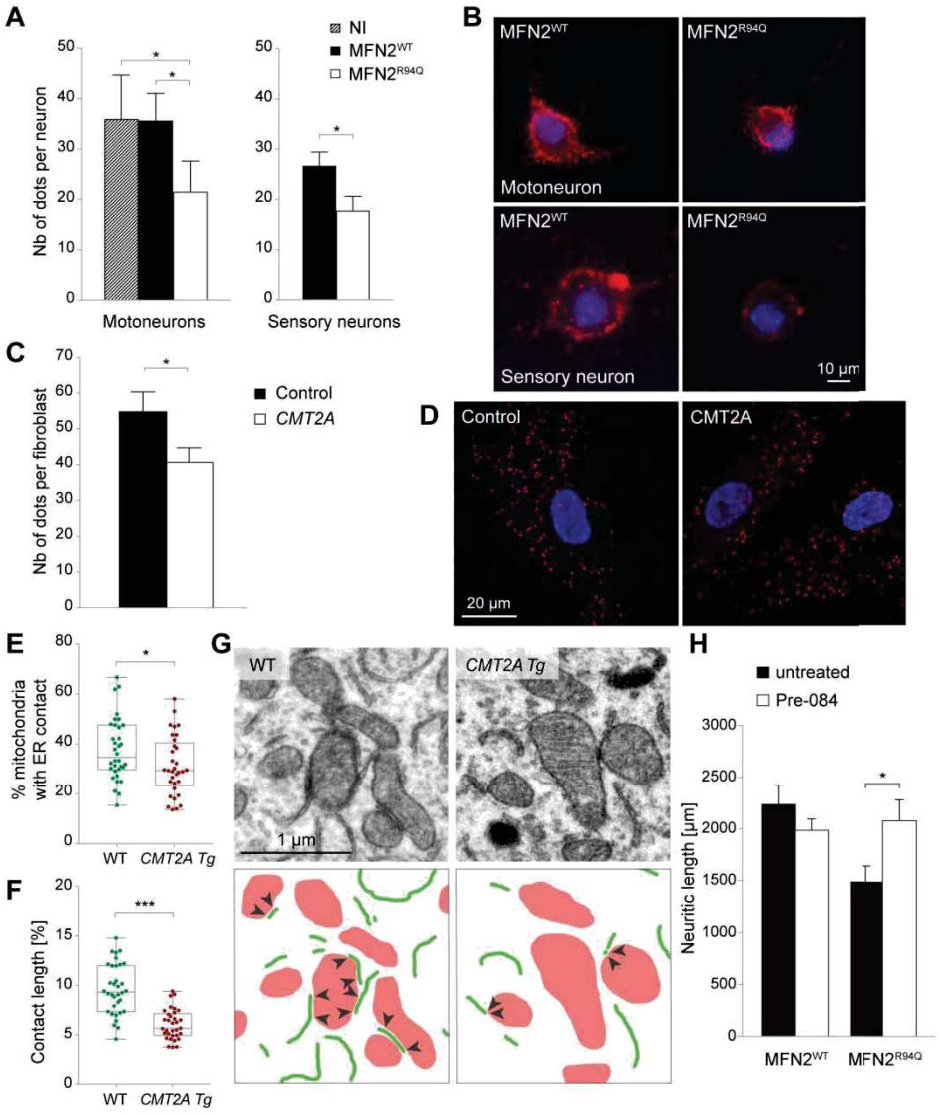

Fig. 3. MFN2^{R94Q} affects neuronal ER-mitochondria contacts *in vitro* and *in vivo*
(A) Quantification of ER-mitochondria contacts using PLA at 6 dpi in motor (n=5 independent cultures) and sensory neurons (n=3), infected with AAV6-hsyn-hMFN2^{WT} or AAV6-hsyn-hMFN2^{R94Q} (n=6 independent cultures). Data are expressed as the mean number of contacts ± sem per neuron detected by a proximity ligation assay. Statistical analysis: repeated measures one-way ANOVA with Tukey's post-hoc test (motoneurons) and two-tailed paired student's t-test (sensory neurons). **(B)** Photomicrographs of proximity ligation assay between the ER protein IP3R and the mitochondrial protein VDAC1 in motor and sensory neurons. Red dots indicate ER-mitochondria proximity. Nuclei are stained with DAPI. **(C)** Quantification of ER-mitochondria contacts using proximity ligation assay in fibroblasts from control and CMT2A-R94Q individuals (n=39 and n=40 cells, respectively, from two independent

cell lines for each condition). Data are expressed as the mean number of contacts ± sem per cell. Statistical analysis: two-tailed unpaired student's t-test. **(D)** Photomicrographs of control and *CMT2A* human fibroblasts. Intracellular red dots indicate the presence of ER-mitochondria proximity revealed by the proximity ligation assay. Nuclei are stained with DAPI. **(E)** Electron microscopy quantification of the percentage of mitochondria with ER contact in motoneuron soma in the lumbar spinal cord of 12 month-old WT (n=34 motoneurons from 3 mice) and *CMT2A Tg* mice (n=33 motoneurons from 3 mice). Statistical analysis: two-tailed unpaired student's t-test. **(F)** Analysis of the length of the mitochondria-ER contacts, expressed as the percentage of the mitochondrial perimeter (n=34 motoneurons from 5 WT mice and n=33 motoneurons from 5 *CMT2A Tg* mice). Statistical analysis: two-tailed unpaired student's t-test. **(G)** Electron microscopy pictures illustrating ER-mitochondria contacts in motoneuron soma of WT and *CMT2A Tg* mice. ER segments are delineated in green and mitochondria are shown in red. Arrowheads indicate the mitochondria-ER contacts. **(H)** Neuritic length quantified at 6 dpi in motoneurons overexpressing either $MFN2^{WT}$ or $MFN2^{R94Q}$. Motoneurons treated with a SIGMAR1 agonist (Pre-084, 50 nM) are compared to the untreated condition. Note the significant rescue of neuritic length in $MFN2^{R94Q}$ motoneurons treated with Pre-084. Mean values are obtained from 4 independent cultures. Statistical analysis: two-way ANOVA (group x treatment) with Sidak post-hoc test. *$p<0.05$, ***$p<0.001$.

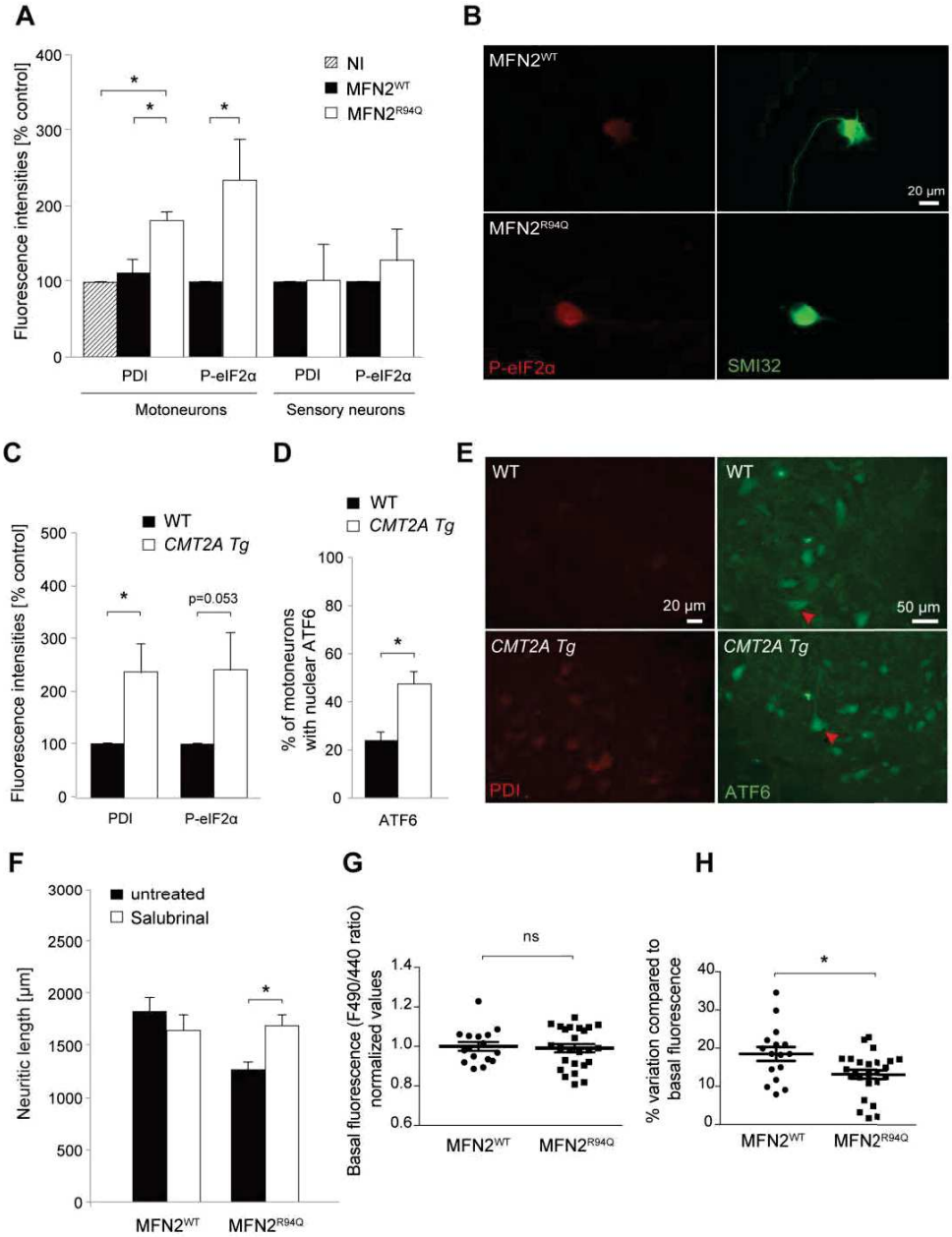

Fig. 4. MFN2^{R94Q} induces ER stress both *in vitro* and *in vivo*

(A) Immuno-quantification of level of ER stress in motor and sensory neurons infected with AAV6-hsyn-hMFN2^{WT} or AAV6-hsyn-hMFN2^{R94Q} at 6 dpi (n=3 independent cultures). Levels of PDI or P-eIF2α were normalized to the level of either the motoneuronal marker SMI32 or the sensory neuron marker NF-200. Data are expressed as percentage ± sem relative to non-infected (NI), (PDI) or MFN2^{WT} condition (all other measurements). Statistical analysis: repeated measures one-way ANOVA with Tukey's post-hoc test. **(B)** Representative stainings for P-eIF2α and SMI32 in motoneurons expressing MFN2^{WT} or MFN2^{R94Q}. **(C)** Immuno-quantification of ER stress markers in motoneurons in the lumbar spinal cord of 12 month-old WT (n=6) and *CMT2A Tg* mice (n=6). Levels of P-eIF2α and PDI were

normalized to the neuronal marker NeuN. Data are expressed as percentage ± sem relative to WT. Statistical analysis: two-tailed unpaired student's t-test. **(D)** The percentage of motoneurons with nuclear versus cytoplasmic ATF6 was evaluated in the spinal cord of 12 month-old WT (n=6) and *CMT2A Tg* mice (n=5). Statistical analysis: two-tailed unpaired student's t-test. **(E)** Representative photomicrographs of PDI (left panels) and ATF6 staining (right panels) in WT and *CMT2A Tg* spinal cord sections. Cytoplasmic and nuclear ATF6 staining is indicated by arrowheads. **(F)** Neuritic length quantified at 6 dpi in motoneurons overexpressing either $MFN2^{WT}$ or $MFN2^{R94Q}$. Motoneurons were treated with Salubrinal (5 µM). Values represent the mean of 4 independent cultures. Statistical analysis: two-way ANOVA (group x treatment) with Sidak post-hoc test *$p<0.05$. **(G-H)** Intracellular calcium measurement evaluated by Fura-Red ratiometric imaging (F490/F440) before (**G**) and during (**H**) KCl (25mM) exposure in $MFN2^{WT}$ (n=16) and $MFN2^{R94Q}$ cells (n=25). Amplitude of the response (**H**) is expressed as the percentage of variation relative to basal fluorescence obtained in (**G**). Data are expressed as mean ± sem. Each dot represents one cell. Statistical analysis: two-tailed unpaired student's t-test.

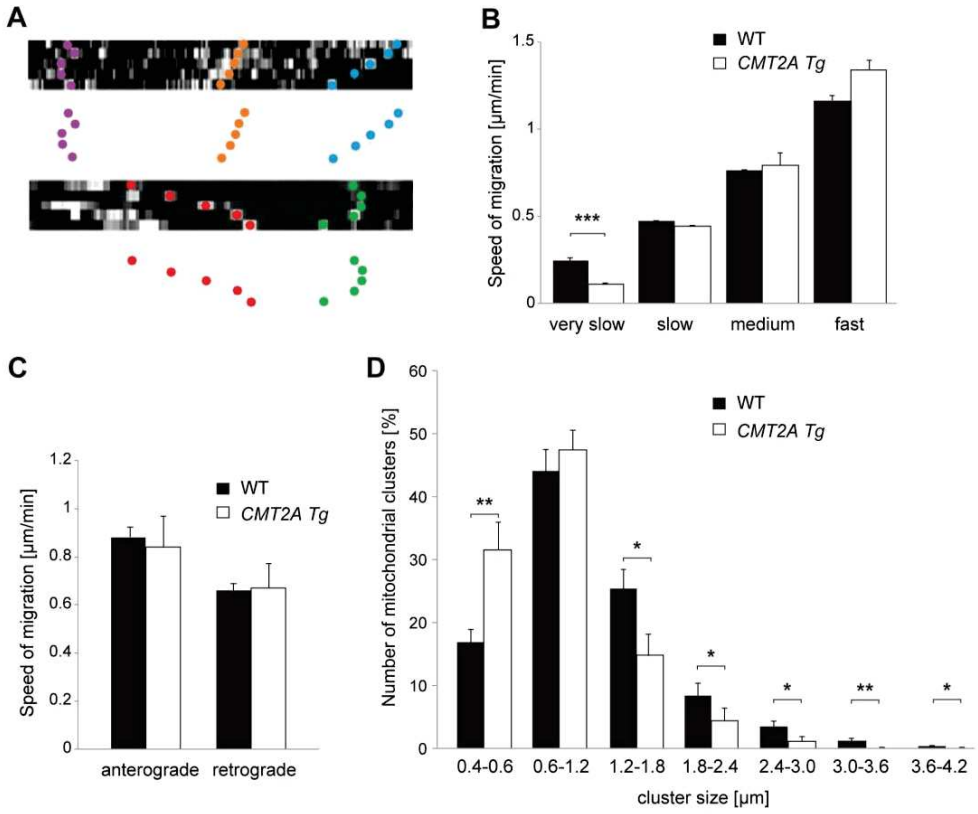

Fig. 5. MFN2^{R94Q} impairs mitochondrial transport and leads to overabundance of small mitochondria clusters *in vivo*

(A) Examples of kymographs used to determine mitochondrial velocity in sciatic nerve axons of 1-month-old animals. Colored dots represent different types of mitochondrial movements. **(B)** mitochondria are classified according to very slow (<0.3 µm/min), slow (>0.3 and <0.6 µm/min), medium (>0.6 and <0.9 µm/min) and fast (>0.9 µm/min) transport velocities. Statistical analysis: two-tailed unpaired student's t-test. **(C)** Mitochondrial anterograde and retrograde transport velocities were evaluated in the sciatic nerve of WT (n=74 mitochondria from 7 mice) and *CMT2A Tg* (n=29 mitochondria from 6 mice) mice. **(D)** Number of mitochondrial clusters according to cluster size in axons of WT (n=23 axons from 10 mice) and *CMT2A Tg* (n=16 axons from 6 mice) mice. Statistical analysis: two-tailed unpaired student's t-test. *p<0.05, ** p<0.01, ***p<0.001.

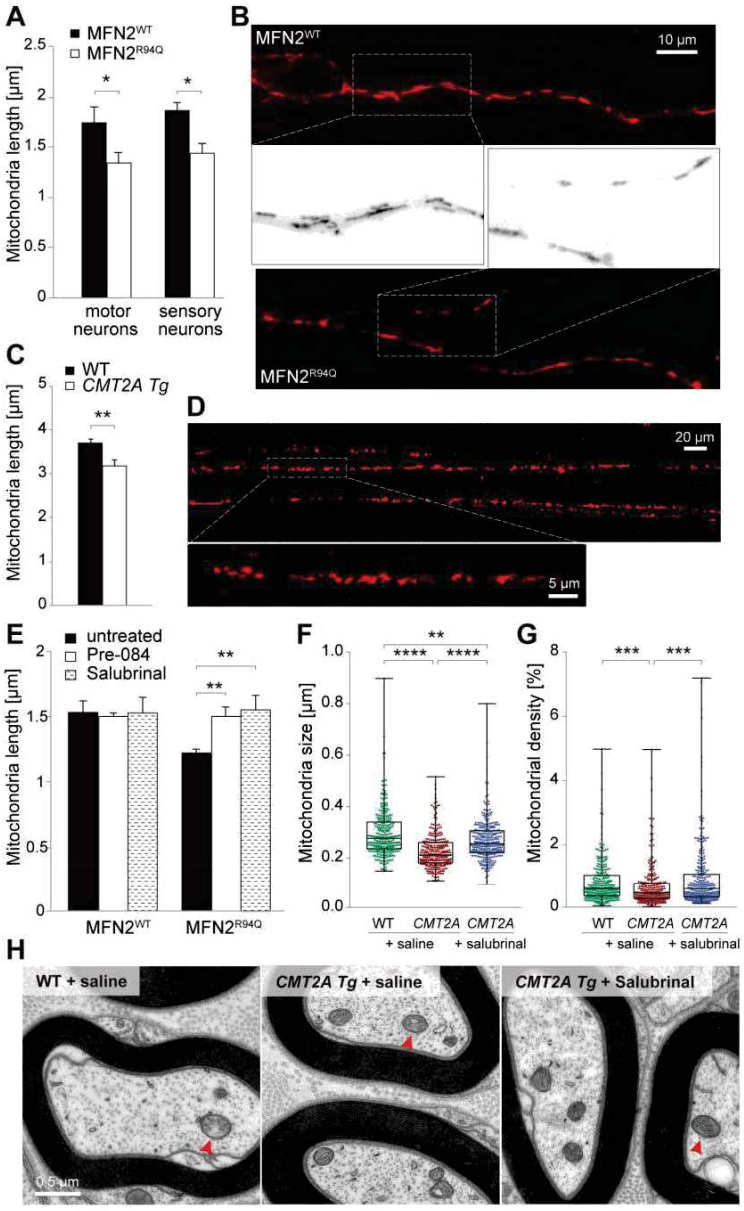

Fig. 6. Mitochondrial morphology is affected by MFN2^{R94Q} both *in vitro* and *in vivo*

(A, B) Motor and sensory neurons infected with AAV6-hsyn-hMFN2^{WT} or AAV6-hsyn-hMFN2^{R94Q} were stained at 6 dpi with Mitotracker Red to assess mitochondria morphology. **(A)** Mitochondrial length quantified in the proximal part of axons (n=5 independent motoneuron cultures and n=3 independent sensory neuron cultures). Statistical analysis: two-tailed unpaired student's t-test. **(B)** Mitotracker Red stained-mitochondria in axons of motoneurons expressing either MFN2^{WT} or MFN2^{R94Q}. Higher magnifications of Mitotracker Red-stained mitochondria are shown in the middle panels. **(C)** Mitochondrial length in sciatic nerve axons of 1-month-old WT

(n=767 mitochondria from 10 mice) and *CMT2A Tg* (n=395 mitochondria from 6 mice) mice. Statistical analysis: two-tailed unpaired student's t-test. **(D)** Representative images of axonal mitochondria stained with AAV9-CAG-mitoDsred2. Images taken with 20x and 63x objectives are from the same area but are time-shifted due to mitochondria movement. **(E)** Mitochondrial length (visualized with Mitotracker Red) quantified at 6 dpi in motoneurons expressing either $MFN2^{WT}$ or $MFN2^{R94Q}$. Motoneuron cultures were treated with either Pre-084 (50 nM) or Salubrinal (5 µM). Results represent n=3 independent cultures. Statistical analysis: repeated-measure two-way ANOVA with Tukey's post-hoc test. **(F)** Box-and-whisker plot of mitochondrial size measured by electron microscopy in distal sciatic nerve axons of 6 month-old WT (n=291 mitochondria from 3 mice), *CMT2A Tg* mice (n=287 mitochondria from 3 mice), and *CMT2A Tg* mice daily treated for 4 weeks with 1mg/kg Salubrinal (n=315 mitochondria from 3 mice). **(G)** Box-and-whisker plot of mitochondrial density measured in the same samples by determining the percentage of axoplasm occupied by mitochondria. Statistical analysis for (f) and (g): Kruskal-Wallis test with Dunn's multiple comparison post-hoc test. **(H)** Representative electron microscopy images of axonal mitochondria (red arrowheads) in distal sciatic nerve axons of 6 month-old WT and *CMT2A Tg* mice. *$p<0.05$, **$p<0.01$, ***$p<0.001$, ****$p<0.0001$.

Parameters	6 months-old		
Paw intensity measures	**WT**	***CMT2A Tg***	***P-value***
Right forepaw Max contact max intensity (a.u)	196.6 ± 2.4	183.1 ± 2.9	0.001
Right forepaw Max intensity mean (a.u)	201.5 ± 1.9	191.7 ± 2.6	0.005
Right forepaw Mean intensity (a.u)	174 ± 3	161.9 ± 3	0.007
Left forepaw Mean intensity (a.u)	172 ± 3.7	162.4 ± 2.5	0.03
Paw size			
Right forepaw Print length mean (cm)	1.03 ± 0.018	0.97 ± 0.014	0.009
Right forepaw Print width mean (cm)	0.93 ± 0.02	0.86 ± 0.02	0.023
Right forepaw Print area mean (cm^2)	0.58 ± 0.02	0.51 ± 0.014	0.013
Gait/Posture			
Right forepaw Terminal dual stance (sec)	0.036 ± 0.005	0.057 ± 0.007	0.046
Left forepaw Duty cycle mean (%)	60.2 ± 1.07	64.3 ± 1.28	0.021
Parameters	12 months-old		
Paw intensity measures	**WT**	***CMT2A Tg***	***P-value***
Right forepaw Max contact max intensity (a.u)	201.1 ± 1.9	191.9 ± 2.9	0.013
Right forepaw Max intensity mean (a.u)	205 ± 1.1	197.5 ± 2.2	0.005
Right forepaw Mean intensity (a.u)	93.7 ± 1.5	89.4 ± 1.1	0.025
Right forepaw Mean intensity of the 15 most intense pixels mean (a.u)	180.8 ± 3.2	169.7 ± 3.6	0.025
Right hindpaw Max intensity mean (a.u)	211.4 ± 1.2	203.5 ± 3.1	0.029
Left forepaw Max contact max intensity (a.u)	201.3 ± 1.7	193.5 ± 2.4	0.011
Left forepaw Max intensity mean (a.u)	205.2 ± 1	199.3 ± 1.9	0.013
Gait/Posture			
Left hindpaw Stand mean (sec)	0.21 ± 0.012	0.27 ± 0.02	0.047
Support three (%)	27.4 ± 2.8	36.5 ± 2.6	0.021
Coordination			
Phase dispersions Right forepaw> Right hindpaw mean (%)	51 ± 1.4	55.7 ± 1.5	0.027
Couplings Right forepaw> Right hindpaw mean (%)	50.9 ± 1.4	56.8 ± 1.7	0.012

Table 1. Catwalk locomotion parameters affected in *CMT2A Tg* mice
Summary of the parameters affected in 6 and 12 month-old *CMT2A Tg* mice (6 month-old: n=23; 12 month-old: n=17) compared to WT mice (6 month-old: n=18; 12 month-old: n=15). Parameters were classified according to paw intensity, paw size, gait/posture and coordination. Statistical analysis: two-tailed unpaired student's t-test.

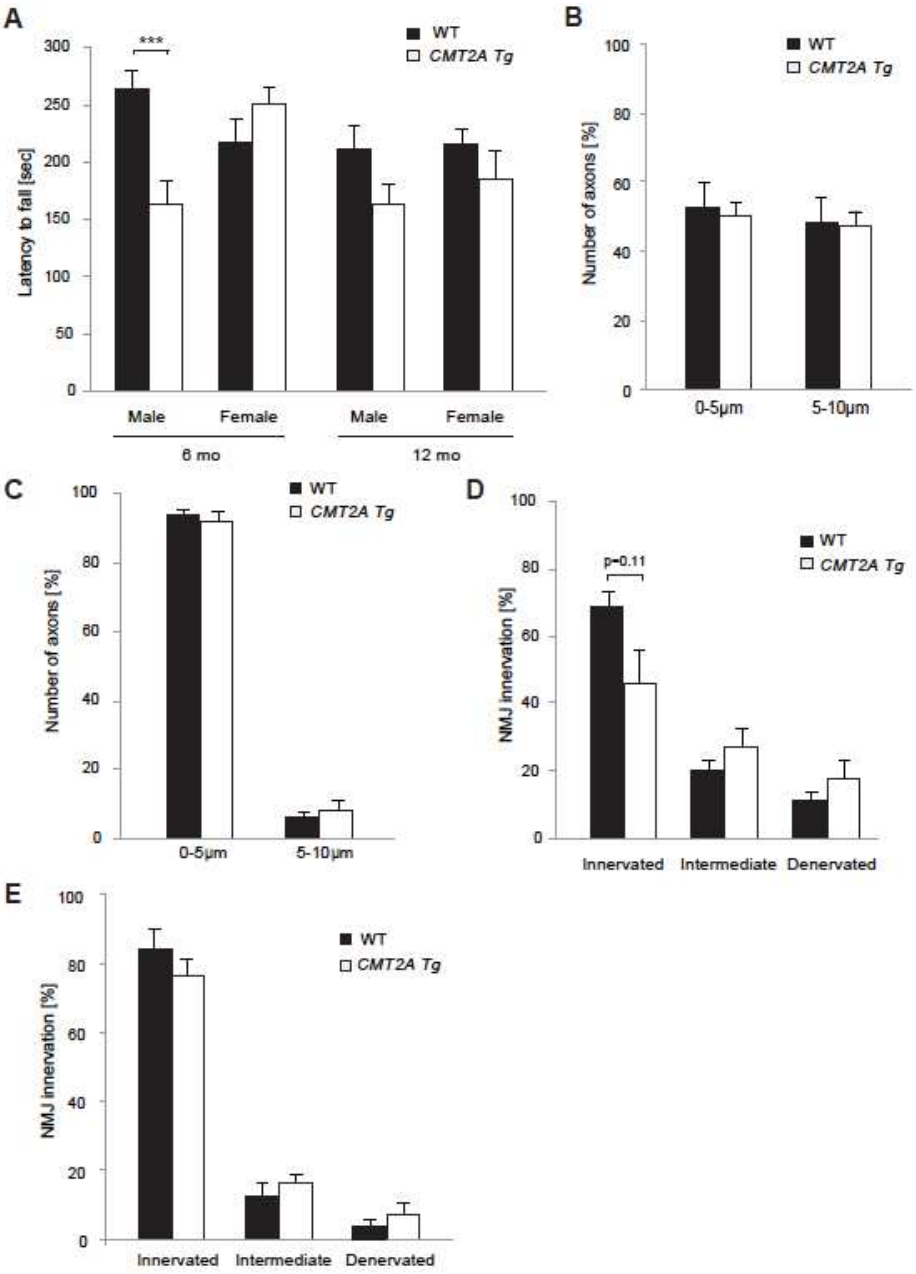

Figure S1. CMT2A Tg mice display locomotion defects but no proximal axonal degeneration or tibialis muscle denervation

(A) Evaluation of motor function with rotarod test at 6 months (WT: n=21; CMT2A Tg: n=23) and 12 months of age (WT: n=17; CMT2A Tg: n=19). Statistical analysis: repeated-measures three-way ANOVA (group x gender x time) with Newman-Keuls post-hoc test. Note the significant loss of performance in 6 month-old male CMT2A Tg mice. (B) Number of motor axons in ventral roots of 12 month-old WT (n=2) and CMT2A Tg (n=3) mice. Axons were classified according to small (<5 µm) and large (>5 µm) calibers. Statistical analysis: two-tailed unpaired student's t-test. (C) Number of sensory axons in dorsal roots of 12 month-old WT (n=3) and CMT2A Tg (n=3) mice. Axons were classified according to small (<5 µm) and large (>5 µm) calibers. Statistical analysis: two-tailed unpaired student's t-test. (D) Levels of NMJ occupancy in the tibialis muscle at 12 months of age in WT (n=5) and CMT2A Tg mice (n=6). (E) Levels of NMJ occupancy in the soleus muscle at 6 months of age in WT (n=3) and CMT2A Tg mice (n=3). Statistical analysis for (c) and (d): two-tailed unpaired student's t-test.

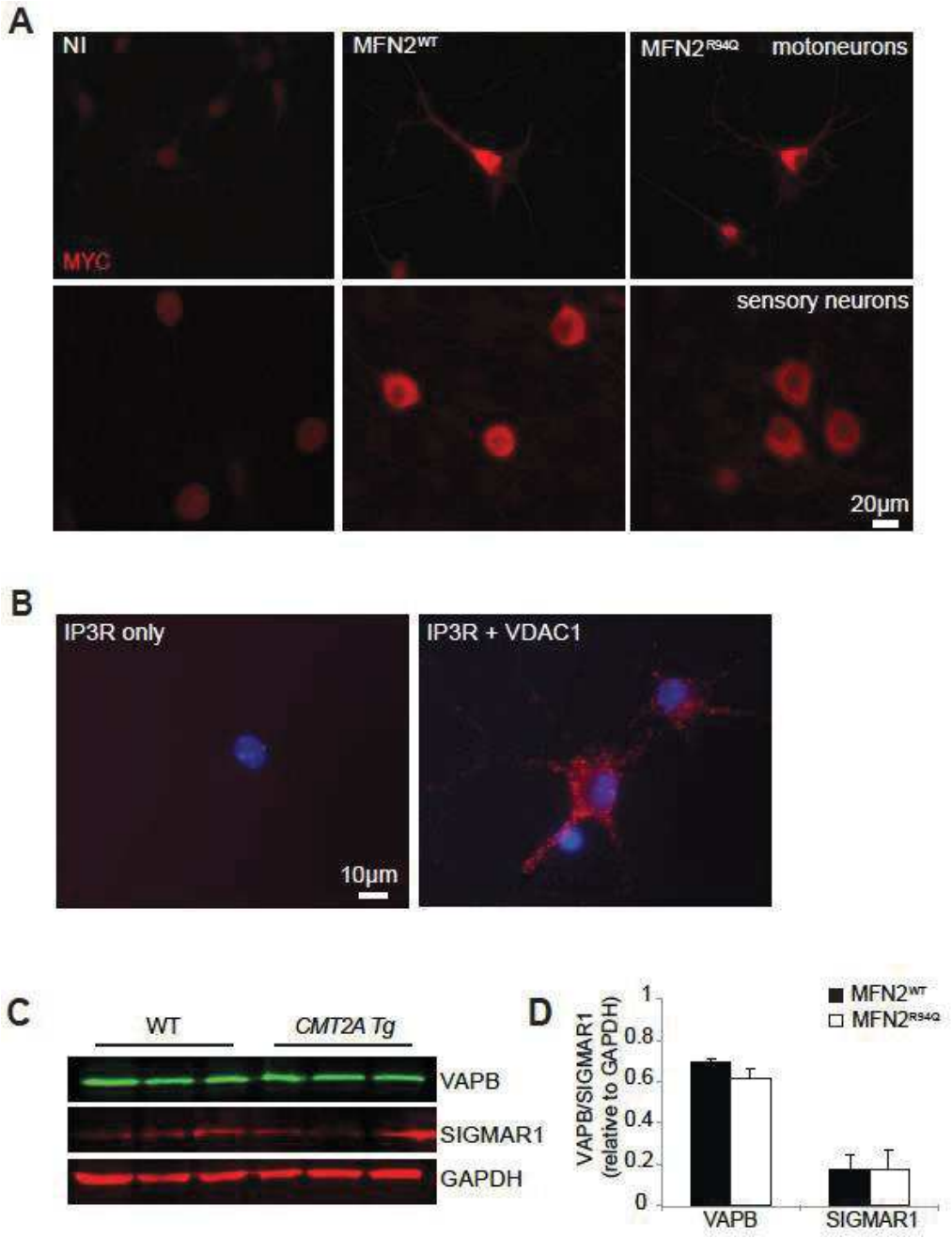

Figure S2. Characterization of consequences of the overexpression of MFN2 WT or MFN2^{R94Q} in motor and sensory neurons

(A) Motor and sensory neurons were infected with AAV6-hsyn-hMFN2WT or AAV6-hsyn-hMFN2^{R94Q} (10 TU per cell), 2 days after plating. Level of expression of MYC-tagged-MFN2 was evaluated at 8 dpi with anti-myc staining. (B) As a control for specificity of antibodies used for proximity ligation assay, the experiment was performed without VDAC1 antibody, using only the IP3R antibody. No signal was detected under this condition as compared to experiment performed in presence of both antibodies (IP3R + VDAC1). (C-D) Western blot on spinal cord extracts from 12 month-old WT (n=3) and 12 month-old CMT2A Tg (n=3) mice. (C) Proteins levels of two MAM proteins: VAPB and SIGMAR1 and GAPDH as a reference protein. (D) Levels of expression of VAPB and SIGMAR1 relative to GAPDH. Values are expressed as mean intensity ratio (protein of interest/GAPDH) ± sem (from n=3 animals). Statistical analysis: two-tailed unpaired student's t-test.

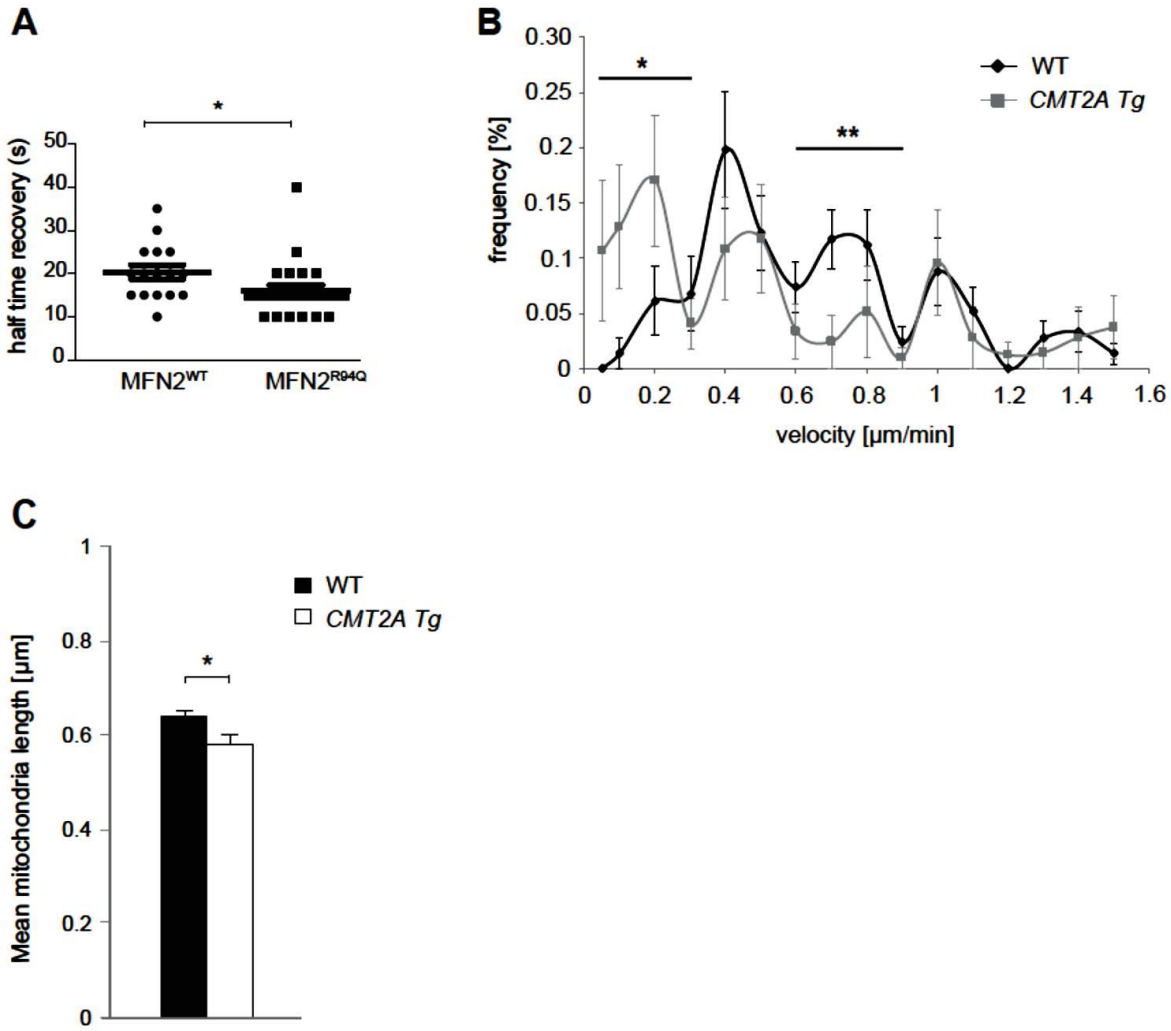

Figure S3. **Characterization of parameters related to ER and mitochondria biology**
(A) Intracellular calcium measurements using Fura-Red ratiometric imaging (F490/F440) after KCl (25mM) exposure in MFN2WT (n=16) and MFN2R94Q cells (n=25). Half time recovery (sec) to basal values was calculated for each cell. Data are expressed as mean ± sem. Each dot represents one cell. Statistical analysis: two-tailed unpaired student's t-test. (B) Velocity histogram showing mitochondrial transport in sciatic nerve axons of 1-month-old WT (n=24 axons from 7 mice) and CMT2A Tg (n=12 axons from 6 mice) mice. Mitochondria are classified according to fast (>0.9 µm/min), medium (>0.6 and <0.9 µm/min), slow (>0.3 and <0.6 µm/min) and very slow (<0.3 µm/min) transport velocities. Statistical analysis: repeated-measure two-way ANOVA (C) Electron microscopy assessment of mitochondrial length in lumbar spinal cord motoneurons of 12 month-old WT (n=76 mitochondria from 5 mice) and CMT2A Tg mice (n=76 mitochondria from 5 mice). Statistical analysis: two-tailed unpaired student's t-test. *p<0.05.

Chapter 8) Dynamics of ATP and ROS production in healthy and neuropathological peripheral nerves

ATP and ROS production are two main functions of axonal mitochondria within peripheral nerves. However, mitochondrial activity is not stable over time, because their environment is constantly changing due to constant depolarization and repolarization of the cell membrane, which changes the composition of the cytosol in respect to glucose, lactate, calcium and other molecules. In addition, mitochondria encounter spatial differences, such as differences between nodes of Ranvier and internodes, during their migration through the axon, which may change mitochondrial ATP and ROS production.

Besides these changes in healthy conditions, mitochondria also respond to pathological changes. In the previous chapter, I described how MFN2 deficient mitochondria show impaired ER-mitochondria interactions and altered morphology and decreased migration velocity through axons. However, changes in ATP and ROS production in the CMT2A pathology have not yet been established. Furthermore, in what way pathologic demyelination changes mitochondrial ATP and ROS production *in vivo* is not known.

In this chapter, I will present my results on mitochondrial function in healthy peripheral nerves, in MFN2 deficient peripheral nerves and in demyelinated axons *in vivo*.

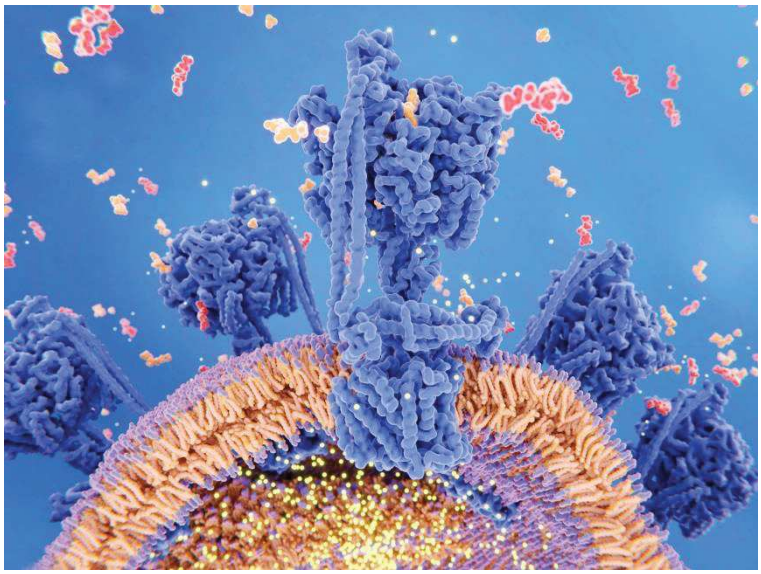

ATP synthases

CMT disease 2A and demyelination decouple ATP and ROS production by axonal mitochondria

Running title: pathological decoupling of axonal mitochondria

Gerben van Hameren[1]*, Graham Campbell[1], Marie Deck[1], Jade Berthelot[1], Roman Chrast[2], Nicolas Tricaud[1]*

[1] Institut des Neurosciences de Montpellier, INSERM U1051, Université de Montpellier, Montpellier, France

[2] Departments of Neuroscience and Clinical Neuroscience, Karolinska Institutet, Stockholm, Sweden

* Corresponding authors: gerben.van-hameren@inserm.fr

nicolas.tricaud@inserm.fr

Keywords: axonal activity, demyelination, MFN2, mitochondria, ROS

Abstract

Mitochondria are critical for the function and maintenance of myelinated axons notably through ATP production. A by-product of this activity is reactive oxygen species (ROS), which are highly deleterious for neurons. While ROS and metabolism are involved in several neurodegenerative diseases, it is still unclear how axonal activity or myelin modulates ATP and ROS production in axonal mitochondria. We imaged and quantified mitochondrial ATP and hydrogen peroxide (H_2O_2) in resting or stimulated peripheral nerve myelinated axons *in vivo,* using genetically-encoded fluorescent probes, two-photon time-lapse and CARS imaging. ATP and H_2O_2 productions are intrinsically higher in nodes of Ranvier even in resting conditions. Axonal firing increased both ATP and H_2O_2 productions but with different dynamics. In neuropathic $MFN2^{R94Q}$ mice, mimicking Charcot-Marie-Tooth 2A disease, defective mitochondria failed to upregulate ATP production following axonal activity. However, H_2O_2 production was dramatically sustained. Mimicking demyelinating peripheral neuropathy resulted in a reduced production of ATP while H_2O_2 level soared. Taken together, our results suggest that ATP and ROS productions are decoupled under neuropathic conditions, which may compromise axonal function and integrity.

1. Introduction

While the nervous system, and the brain in particular, represents around 2% of the body mass, it consumes up to 20% of the glucose we mobilize every day [1]. This high energy expenditure in the nervous system is firstly due to the synaptic activity that requires high amounts of adenosine tri-phosphate (ATP) [1]. A second energy demanding process is the propagation of action potentials (APs) along axons. Indeed, conduction of APs involves ion

exchanges through the plasma membrane, first through voltage-gated ion channels to depolarize, then through the sodium-potassium ATPase to repolarize [2,3]. Therefore, the production of ATP in axons is crucial for repeated regeneration of APs. Both in the central nervous system (CNS) and in the peripheral nervous system (PNS), myelination significantly reduces the energy cost of AP propagation through the sequestration of the AP firing machinery at the node of Ranvier and axon initial segment [4].

Mitochondria appear to be the main source of cellular ATP and these organelles are abundant in CNS [5,6] and PNS [7] axons. Some reports indicated that mitochondria were more abundant in the node of Ranvier [8]. In addition, axonal AP activity and axo-glial junctions regulates the recruitment of mitochondria in the nodal area [9]. Therefore, a well-accepted idea is that axonal AP activity could locally stimulate ATP production in axonal mitochondria [10]. However, this nodal enrichment in mitochondria remains controversial [11] and the dynamic of local mitochondrial ATP production following AP is actually unknown.

As an intrinsic by-product of ATP production, mitochondria also produce reactive oxygen species (ROS) [12,13]. The mitochondrial electron transport chain (ETC) and NAPDH oxidases are the major sources of superoxide ($O_2^{\bullet -}$), a highly reactive type of ROS, within cells [14]. $O_2^{\bullet -}$ is rapidly converted to H_2O_2 by superoxide dismutase (SOD) and H_2O_2 is then reduced to H_2O and O_2 by mitochondrial glutathione peroxidase (GPx) and cytosolic enzymes [15]. H_2O_2 can also react with iron or $O_2^{\bullet -}$ to form hydroxyl radicals (OH•), which is then reduced by molecular hydrogen to H_2O [16]. If not reduced by antioxidants, all types of ROS are highly toxic for the cell and in particular for mitochondria, where they are produced. Indeed ROS can directly oxidize and damage DNA, carbohydrates, proteins or lipids [17].

In several neurodegenerative diseases and axonopathies, such as Parkinson's disease [18], multiple sclerosis (MS) [19] and Charcot-Marie-Tooth diseases (CMT) [20], mitochondrial dysfunction and increased levels of ROS have been shown to be involved. Whether axonal mitochondria are involved is still unclear and investigating the production of ATP and ROS by these mitochondria in active or diseased axons in real time *in vivo* would constitute a first answer.

The importance of mitochondrial homeostasis for the normal function of myelinated axons [9,21] is highlighted by mutations in the *mitofusin 2* (*MFN2*) gene. Indeed, MFN2 has several functions in mitochondria physiology, among which mitochondrial fusion [22] and transport along axons [23], and mutations in its gene result in axonal form of peripheral neuropathy (CMT2A) in humans and in mice [24,25]. In particular, MFN2 loss-of-function in axonal mitochondria decreases the expression of oxidative phosphorylation subunits [26], suggesting that *MFN2* mutations also affect ATP and ROS production. However, this remains to be shown *in vivo*.

MS is a chronic inflammatory disease affecting myelinated tracts in the brain [27]. MS is characterized by demyelinated lesions resulting from the loss of the myelin sheath and the progressive form of MS shows successive events of myelin degeneration and regeneration that damage axons [27]. A common hypothesis is that demyelinated axons are more demanding in ATP in order to maintain their functions and their integrity [28]. Recent data showed that axonal mitochondria complex IV activity is increased in MS lesions and the total mitochondrial mass is increased [29], suggesting that axonal mitochondria are indeed producing more ATP. In addition, while activated microglia and macrophages are thought to be the initial source of ROS, axonal mitochondria dysfunction and an increase of

mitochondrial ROS contribute to progressive MS [30]. Taken together this suggests that the myelin sheath plays a significant role in the maintenance of axonal mitochondria homeostasis and in particular in the production of ATP and ROS in mitochondria.

To answer these questions, we set up an *in vivo* approach using a H_2O_2-sensitive GFP (roGFP-Orp1) [31] and a fluorescent ATP sensor (ATeam) [32] targeted to mitochondria to image and measure the dynamics of ATP and H_2O_2 production in mitochondria of myelinated axons in myelinated axons of the PNS. Using this approach, we show that both ATP and H_2O_2 levels are increased in mitochondria residing in nodes of Ranvier and that nerve stimulation sharply increases ATP and H_2O_2 production by mitochondria in few minutes. While MFN2 mutations had no effect on basal levels of ATP and H_2O_2 in axons, it prevented the increase of ATP production after nerve stimulation. At the opposite, an increased H_2O_2 production was observed. Moreover, pathological demyelination reduced ATP production while enhancing mitochondrial ROS, showing that both neuropathic conditions decoupled the production of ATP from the production of ROS.

2. Results

2.1. Validation of the mito-roGFP-Orp1 and mito-ATeam probes

We used ATeam, which is a genetically-encoded fluorescence probe based on fluorescence resonance energy transfer (FRET), to detects ATP [32]. This probe consists of the cyan fluorescent protein (CFP) mseCFP, the yellow fluorescent protein (YFP) variant monomeric Venus, both linked at the ε-subunit of the Bacillus subtilis FoF1-ATP synthase. In the presence of ATP, the ε-subunit retracts to bring the two fluorescent proteins close to each

other, thereby increasing FRET efficiency. The conformational change is reversible. Relative ATP levels are measured using the Venus/CFP fluorescence ratio.

Redox sensitive GFPs (roGFPs) harbor an engineered dithiol/disulfide switch on their surface, which determines their wavelength of excitation [33]. RoGFP2 has been converted into an H_2O_2 specific probes by fusion with the microbial H_2O_2 sensor Oxidant Receptor Peroxidase 1 (Orp1) [31]. The reaction is reversible via reduction by cellular thioredoxin (Trx) or GRx/GSH [34]. Relative H_2O_2 levels are measured using the ratio of emitted fluorescence lights when excited at 800nm (oxidized form) or 940nm (reduced form). All experiments were done in the same imaging conditions and analysis. As both probes are ratiometric, the measured values are independent of the number of mitochondria or of the absolute fluorescence intensity of the probe. Both probes were targeted to the mitochondrial matrix.

We first validated mito-roGFP-Orp1 and mito-ATeam probes *in vivo*. Injection of AAV9-mito-roGFP-Orp1 and AAV9-mito-ATeam in the spinal cord of mouse pups one day after birth (P1) resulted in expression of the fluorescent probes in multiple axons that are part of sciatic and saphenous nerves (Fig 1a). Coherent Anti-stokes Raman Scattering (CARS) microscopy uses the non-linear interactions between light and molecules to generate light from lipids without labeling [35]. As myelin is enriched with lipids, CARS microscopy allows visualizing the myelin sheath around axons *in vivo* [36,37,38]. Using this technique, we observed that the fluorescent probe signal was encompassed by the myelin sheath, which shows the probes are expressed in myelinated axons (Fig 1a). We then performed an immunostaining of teased fibers for the mitochondrial marker TOM20 and observed a partial colocalisation between fluorescent probes and mitochondria (Fig 1b), showing probes are expressed in axonal mitochondria, but not all of them. Consistently, mitochondria located in

Schwann cells surrounding axons were labeled with TOM20 antibody but not with fluorescent probes. Both probes could be detected in axons of the mouse saphenous and sciatic nerves *in vivo*.

Then the ratio of the fluorescent intensity of oxidized/reduced roGFP-Orp1 (R) was followed over time (Fig 1c), showing a small and slow increase of the ratio (0.206 ± 0.002 per hour) probably due to air oxidation. Addition of reducer DTT on the nerve resulted in a significant decrease of the fluorescence ratio, while injection of oxidizer diamide resulted in a significant increase of fluorescence ratio (Fig 1d). These results show that the dithiol/disulfide switch of mito-roGFP-Orp1 is an efficient and reliable indicator of relative redox changes in axonal mitochondria of mouse peripheral nerves *in vivo*. The fluorescence ratio Venus/CFP of mito-ATeam (R) was very stable over time (Fig 1e). Injection of 0.4M and 1M ATP into the sciatic nerve in an increase of ATeam fluorescence ratio (Fig 1f), showing this probe is also functional *in vivo*.

2.2 The effect of nerve stimulation on ATP and H_2O_2 production

While ATP is supposed to be critical for the firing of axons, ATP production in mitochondria of functionally active axons has never been observed *in vivo*. We used the real-time imaging approach previously described in combination with a setup for electrical nerve stimulation based on previous work [39] (Fig 2a-d). We used the saphenous nerve, which is mostly composed of sensory axons, hence its stimulation leads to only limited unwanted contraction of the paw's muscles [40]. After recording the probe fluorescence for at least 20 minutes without stimulation, APs were induced by an electrical burst stimulation protocol including 3 bursts of 50Hz for 30 seconds spaced by a 60 second recovery period (Fig 2e).

The fluorescent signal of mito-ATeam was recorded every 5 minutes for 20 minutes after stimulation (Fig 3a). At each time point the fluorescence ratio (R) was corrected for the mean fluorescence ratio of that same axon before nerve stimulation (R0). After a first stimulation, the fluorescence ratio of mito-ATeam increased in several axons, but not in all of them (44%), resulting in a slight non-significant average increase (Fig 3a). After the second stimulation, all axons responded significantly increasing mitochondrial ATP production (Fig 3a). In the same conditions, nerve stimulations significantly increased mitochondrial H_2O_2 production just 1 minute after the stimulation period (Fig 3b). H_2O_2 level then quickly went back and stabilized at pre-stimulation values (Fig 3b). These data show that axonal mitochondria very quickly adapt to the axonal activity up-regulating their production of ATP. Spikes in mitochondrial H_2O_2 production were also observed just before the surge of ATP in mitochondria (Fig 3c), suggesting that this H_2O_2 production reflects the oxidative phosphorylation process.

2.3. ATP and H_2O_2 production are altered in CMT2A neuropathic mice

We recently showed that $MFN2^{R94Q}$ mice, a model for CMT2A disease [25] where MFN2 is defective, displayed altered mitochondria motility and clustering in peripheral nerve axons [41]. We used this model to measure the level of ATP in axonal mitochondria of myelinated axons in neuropathic conditions. In non-stimulated conditions, control and mutant mice axonal mitochondrial ATP production were similar (Fig 4a). After the first stimulation, similar to control mice, mitochondrial ATP production increased in some axons whereas others did not respond, resulting in statistically non-significant variation (Fig 4b). However, after a second period of nerve stimulation, as opposed to controls, $MFN2^{R94Q}$ axonal mitochondria failed to upregulate ATP production (Fig 4b-c). This indicates that

dysfunctional MFN2 does not hinder the basal production of ATP by axonal mitochondria but impairs their ability to up-regulate their production in response to axonal activity.

Similar to ATP, we found no difference between controls and $MFN2^{R94Q}$ mice in the basal H_2O_2 levels (Fig 4d). When nerves were stimulated, mitochondrial H_2O_2 significantly increased after each stimulation period (Fig 4e). However, this increase was delayed compared to controls and H_2O_2 levels remained high for longer time (Fig 4f), showing that axonal mitochondria produce more deleterious H_2O_2 than control mice in response to axonal activity. Since ROS production in the mitochondrial matrix reflects the oxidative phosphorylation process [42,43], these data indicate that oxidative phosphorylation is decoupled from ATP production in mitochondria of these neuropathic mice.

2.4. ATP and H2O2 production in nodes of Ranvier and internodes

The enrichment of mitochondria at the node of Ranvier and whether these nodal mitochondria are more metabolically active remains controversial. In order to detect potential spatial differences between nodal and internodal mitochondria, we used CARS microscopy. Gaps in CARS signal between two myelinated internodes are nodes of Ranvier (Fig 5a) [38,43,44]. Combining two-photon imaging of fluorescent probes with CARS imaging allowed us to analyze mitochondrial physiology in nodes of Ranvier versus internodes defined as areas distant of more than 5 µm from the node (Fig 5a). In all observed nodes of Ranvier, probes-labeled mitochondria were present, but they were not more abundant or larger than in internodes (Fig 5a). However, when measuring the mito-ATeam and mito-roGFP-Orp1 fluorescence ratio, we found significantly higher ATP and H_2O_2 levels in node of Ranvier mitochondria (Fig 5b-c). These data, obtained in resting animal without nerve stimulations, indicate that nodal mitochondria are intrinsically more metabolically active than internodal

ones. In neuropathic $MFN2^{R94Q}$ mice, nodal mitochondria did not show a higher level of ATP versus internodal mitochondria (Fig 5b). However, they still had higher level of H_2O_2 (Fig 5c), suggesting again a decoupling between oxidative phosphorylation and the production of ATP in mitochondria of these mutant mice.

2.5. ATP and H_2O_2 production in mitochondria of demyelinated axons

The myelin sheath is critical to maintain the node of Ranvier on myelinated axons and is therefore likely to play a significant role in the homeostasis of axonal mitochondria. As demonstrated in Fig 5a, the myelination state of the axons in the mouse sciatic nerve can be assessed *in vivo* by CARS imaging. We therefore investigated how this demyelination affects axonal mitochondria physiology *in vivo*. To induce demyelination we used lyso-phosphatidylcholine (LPC) and we followed the production of mitochondrial ATP and H_2O_2 in axons during demyelination and during the restoration of the myelin sheath (remyelination). LPC, which is a signaling molecule resulting from the hydrolysis of phophatidylcholine by phospholipase A2 [45] acts in mSC and oligodendrocytes as a demyelinating signal [46,47,48]. LPC was injected in the sciatic nerve of adult mice and demyelination occurred immediately to culminate one week after the injection with the formation of myelin ovoids and debris as seen using CARS (Fig 6a, week 1) [37,49]. As soon as two weeks after LPC injection, remyelination occurred and some thin myelin sheaths reappeared around axons (Fig 6a, week 2). Axons were completely remyelinated three weeks after injection of LPC (Fig 6a, week 3). No demyelination occurred in control mice injected with PBS (Fig 6a last panel). Axonal integrity is not directly affected by LPC (EV Figure 1) [50] and axonal mitochondria remained visible using either mito-ATeam or mito-roGFP-Orp1 probes during the entire process of demyelination and remyelination (Fig 6a inserts).

We therefore measured the fluorescence ratio for these probes in non-stimulated axonal mitochondria during the process. One week after LPC injection, when axons are completely demyelinated, ATP production was slightly lower than before demyelination, but not significantly (Fig 6b), while H_2O_2 levels peaked (Fig 6c). ATP levels were significantly lower in axonal mitochondria at two weeks after LPC injection, while H_2O_2 levels were back to control and pre-demyelination levels (Fig 6b-c). Finally, three weeks after injection, when remyelination is completed, ATP levels were back to control and pre-demyelination levels as are the H_2O_2 levels (Fig 6b-c). No change either in ATP or H_2O_2 levels were detected at one week after injection with PBS in control mice (Fig 6b-c). Moreover, increase in ROS did not result from a general oxidative stress in the demyelinated nerve, since CellRox dye did not show any significant increase, except at the LPC injection site where we did not image our probe (EV Fig 2). Taken together, these data indicate that the myelin sheath has a profound impact on axonal mitochondria physiology. Mitochondria manage to maintain their ATP production during myelin break-down, but they generate more H_2O_2. The process of remyelination leads to decreased production of ROS, while ATP production is temporally diminished before full remyelination. These data therefore indicate that demyelination induces the decoupling of ATP production from oxidative phosphorylation.

3. Discussion

Although it has been shown that PNS axonal mitochondria, like most mitochondria, produce both ATP and ROS, the regulations of their production are still not well understood *in vivo* and *in situ*. We used a combination of viral delivery of mitochondria-targeted fluorescent probes to active peripheral neurons and two-photon and CARS live imaging in mice to fill

that gap. The mito-ATeam and mito-roGFP-Orp1 fluorescent probes had been previously validated *in vitro* [51] and *in vivo* [33] in other systems but we also validated them *in vivo* in our system. We did not attempt to measure absolute values of ATP or H_2O_2 with each probe fluorescence *in vivo* because firstly, this was difficult as probes are targeted to mitochondrial matrix and secondly, it was not necessary as we aimed to compare different genotypes and conditions in particular with time. So only relative values obtained in the same imaging conditions are shown here. We found that the range of detection was large enough to cover the changes occurring in axonal mitochondria *in vivo*. Moreover the probe sensitivity was sufficient to observe variations in real-time using a 5 minutes delay between measures. This delay was partly imposed by relative low speed of our imaging system (1 minute to create 10 scans of 200μm^2 over 40 μm depth for each wavelength), but also by the intrinsic limits of our set-up: electrical stimulation induced slight contractions of saphenous nerve surrounding muscles which made the pictures blurred during the stimulation. The probes alterations were also reversible fast enough to observe changes in both directions. Mito-ATeam was stable, but mito-roGFP-Orp1 showed a slight increase of its fluorescence ratio over time under our experimental settings. These results are not explained by photobleaching or degradation of the probe, since the total fluorescent signal does not decrease. This change in ratio of fluorescence may be caused by air oxidation [52]. However, buffered artificial cerebrospinal fluid as an incubation medium for the saphenous nerve did not prevent the probe oxidation. Nonetheless, this slow oxidation of mito-roGFP-Orp1 had negligible effects on our experiments, since it was too slow to cause significant changes in our relatively short term imaging.

Axonal activity induced stereotypic changes in ATP and H_2O_2 production by axonal mitochondria. Shortly after the stimulation, H_2O_2 production increased and dropped

immediately and then ATP increased for several minutes. This was stereotypic, because it occurred almost identically after both stimulations we did. After the first stimulation, not all axonal mitochondria produced more ATP, suggesting that either our stimulation protocol was not mobilizing enough axons or axonal mitochondria are deactivated, similar to some ion channels. This limitation was lifted by the second stimulation. On the attempts we did for further stimulations, sometimes the ATP level was maintained at high range and sometimes mitochondria did not respond anymore. The reason for these variations in the long term is unknown and we did not pursue this further. However, taken together, this suggests that ATP production in axonal mitochondria is positively correlated with the level of axonal activity and can eventually reach a plateau in our conditions. Due to technical reasons we could not measure H_2O_2 levels in mitochondria after several stimulations. However, looking at the first two stimulations, we conclude that H_2O_2 production in mitochondria is also positively correlated with axonal activity but not cumulative. It would be interesting to look further for the molecular mechanisms that allow mitochondria to detect axolemma depolarization or ion channels activity on a very short period of time (around one minute in our detection capacities). This fast kinetic suggests the role of ions, such as calcium ions, which are mobilized during AP firing at the node of Ranvier [53], or kinases. A mechanism involving calcium has been shown to anchor mitochondria at the node of Ranvier [54], suggesting that mitochondria are associated with the axolemma there. Consistently, we found nodal mitochondria to be more metabolically active than internodal ones. However, our data following stimulations were recorded on mitochondria independently of their location on axons. As the node is much smaller than the internodes (1 μm versus 600 μm in average in the mouse nerve) the probability we recorded nodal mitochondria is extremely small. So the molecular mechanism that mobilizes mitochondria after AP firing has to exist also in internodal mitochondria.

Looking at the known origin of ROS in mitochondria, our data suggest that the H_2O_2 production we detected in axonal mitochondria reflects the loading of the mitochondrial matrix with protons before the production of ATP. However, since the H_2O_2 production drops very quickly and, contrary to the ATP production, it is not cumulative, a more complex scheme has to be taken in consideration. Indeed, H_2O_2 is formed by SOD enzyme from $O_2^{\bullet-}$, which directly results from the ETC. Moreover, H_2O_2 is then changed in H_2O and O_2 by several reducing enzymes, such as mitochondrial GPx, so actually the amount of H_2O_2 we detected is the result of equilibrium between $O_2^{\bullet-}$ production and SOD and reducing enzymes' activities. As these enzymes are highly expressed in mitochondria [55], they probably do not constitute a limiting factor and the H_2O_2 levels we detected still reflect axonal mitochondria metabolic activation. However, H_2O_2 levels drop quickly, probably because reducing enzymes are removing it quickly. In addition, these enzymes' activities change following fast post-translational modifications such as phosphorylation [56] or environmental changes [57]. While this may explain why H_2O_2 levels are not incremental following several stimulations, further investigation will be needed to clarify underlying mechanisms.

Several CNS and PNS neuropathies are linked to mitochondrial dysfunctions in neurons [18,19,20]. Our data show that the electrical activity of neurons directly regulates the physiology and the respiration of axonal mitochondria. As axonal mitochondria are the most abundant among neuronal mitochondria, this suggests that axonal mitochondria dysfunctions may severely impact neuronal physiology and survival. We evaluated this hypothesis using a couple of peripheral neuropathy mouse model, such as a model of CMT2A disease expressing mutant $MFN2^{R94Q}$ [25]. While *in vitro* data had shown increased H_2O_2 levels [58], but no change in ATP production [59] in neuronal mitochondria of these mice, *in vivo* we did not measure significant differences in these parameters between resting $MFN2^{R94Q}$ mice and

control mice. A first explanation for this discrepancy is that cultured cells are living in an environment that is significantly different from the *in vivo* conditions. This is especially true in terms of metabolism [60]. Another explanation is that mitochondria physiology is altered, but this can only be seen when mitochondria are challenged. Environmental changes in culture may constitute this challenge, while more physiologically relevant challenges have to be found *in vivo*. Our electrical stimulations were physiologically meaningful challenges for axons and, similar to control mice, we observed ATP levels increasing in several axons of mutant mice, but not all, after a first nerve stimulation. However, while control mice mitochondria increased their ATP production further following a second stimulation, no increase was observed in mutant mice mitochondria. We have shown that Mitochondria Associated Membranes (MAM), which mediate interactions between the endoplasmic reticulum and mitochondria [41], are impaired in these mutant mice. So we suggest that an impaired Ca^{2+} uptake by mitochondria through MAM [61] could alter the ATP production as it has been shown that calcium is required for the TCA cycle [62]. However, mutant mice mitochondria were still able to produce a large amount of H_2O_2 following both stimulations, suggesting the ETC and therefore the TCA cycle are working properly. Yet this H_2O_2 production was completely abnormal: it was largely delayed and was sustained for over at least 10 minutes. As discussed before the levels of H_2O_2 result from an equilibrium between several parameters, so it is difficult to explain this abnormal production. Nevertheless, a relationship between mitochondrial shape and ROS has been shown *in vitro* [63]. It has been suggested that smaller mitochondria result in intra-mitochondrial redistribution of cytochrome c and the pro-aging molecule p66shc that acts trough ROS upregulation [64,65]. Smaller fragmented mitochondria, such as MFN2 mutants [63], correlate with a malfunctioning antioxidant system and an increased production of ROS [58,64]. In any case, our data show that an altered MFN2 function lead to the dysfunction of axonal mitochondria only when

axons are firing. This dysfunction is strongly deleterious as mitochondria don't produce more ATP but show a sustained production of deleterious ROS. This functional decoupling between ATP and H_2O_2 production, occurring in the most abundant mitochondria of the neurons and in conditions of normal firing activity, is likely to be a significant cause of the neuronal dysfunction in this peripheral neuropathy.

Looking at the node of Ranvier of MFN2 mutant mice, we found that, similar to control mice, nodal mitochondria were more metabolically active than internodal ones. As MFN2 mutant mitochondria do not increase ATP production in active axons, this suggests that nodal mitochondria are intrinsically more active even in absence of firing. This is consistent with the fact that motile mitochondria slow down in the nodes of Ranvier [6] and that they have a different morphology [66]. Moreover, nodal mitochondria may participate to axonal degeneration since this process starts in nodes of Ranvier due to high ROS levels [67]. It would have been interesting to investigate changes occurring in ATP and H_2O_2 production of nodal mitochondria after electrical stimulation but this was impossible due to the small size of the node and the change of focus that occurs following stimulations.

The myelin sheath that covers axons appears to be an important regulator of axonal metabolism and of mitochondria physiology. Indeed in MS, demyelination alters axonal mitochondria [19,29,68] and we show here that nodes of Ranvier devoid of myelin house more metabolically active mitochondria. To go further, we therefore investigated the impact of the loss of myelin on axonal mitochondria. LPC was the right tool because it induced demyelination without destroying axons [46,47,48]. LPC-induced demyelination resulted in a decrease of ATP levels in axonal mitochondria. This decrease was strongest after two weeks and was reversed by 3 weeks, showing that ATP production within neurons is impaired until

complete remyelination. This decrease was unexpected, since AP propagation in demyelinated axons is more energy demanding: the nodal machinery and the Na^+/K^+ ATPase are diffused all along the axolemma and all the energy-effective benefits of myelination are lost [69]. In demyelinated area of brains affected by MS, an upregulation of ETC complexes protein expression and more complexes I and IV activity [68] was observed. Moreover, demyelinated axons showed more mitochondria [29], which is consistent with a higher energy demand.

Nevertheless, H_2O_2 levels strongly increased in axonal mitochondria of fully demyelinated axons in absence of general oxidative stress in the tissue. This decoupling of mitochondrial oxidative phosphorylation and ATP production is in accordance with previous studies that reported a decreased ATP production, together with increased ROS levels in demyelinating diseases [70]. This suggests that actually, mitochondrial ETC complexes are more active and produce more ROS, but this does not lead to more ATP production. Such a mechanism has been shown in particular conditions where the goal of mitochondrial activity is to produce heat. Uncoupling proteins such as UCP2 permeabilize the inner mitochondrial membrane to dissipate the proton gradient [71]. This may not be the sole utility of uncoupling as this process has been shown to occur in several neurodegenerative diseases [72]. However, so far we failed to detect unusual UCP2 expression in demyelinated nerves. The high production of H_2O_2 during demyelination is probably not without consequences as ROS can alter the function of the ATP synthase [73]. This may explain why ATP production remains weak in mitochondria of axons that are being remyelinated two weeks after LPC injection, despite that ROS production is back to normal. This suggests that during demyelination, axons may recruit more mitochondria [29], or use another metabolism, such as aerobic glycolysis, in order to cover their need in ATP.

While very little amount of data exists on the homeostasis of axonal mitochondria in demyelinated axons of the PNS, in the CNS, demyelination in progressive MS results in axonal mitochondria dysfunction and ROS increase [74]. The data we collected in PNS myelinated axons on ROS production by axonal mitochondria are consistent with this. This suggests that, despite the large difference that exists between PNS and CNS myelinating glia, their similar role in segregating axonal firing machinery at nodes of Ranvier is essential for mitochondria homeostasis in axons. Nevertheless, the electrical isolation of the axon and the formation of the node of Ranvier is not the only function of the myelin sheath as it also largely participates to the metabolic homeostasis of the axon through the lactate shuttle process [75,76]. This is particularly true for the CNS myelin [76]. In addition, MS disease is significantly different from peripheral nerve diseases, in particular because of the important role played by CNS glial cells astrocytes and microglia. So, it would be essential to confirm the data we obtained in PNS myelinated axons in CNS myelinated axons *in vivo*, in order to definitely conclude on the alteration of ATP and ROS production by axonal mitochondria in demyelinated lesion of progressive MS.

To conclude, combining several novel techniques such as two-photon and CARS non-linear live imaging coupled to electrical nerve stimulation and genetically-encoded fluorescent probes delivered by AAV vectors, we were able to observe the production of ATP and H_2O_2 by axonal mitochondria in real time and in living and active axons of mouse peripheral nerves. We demonstrated that mitochondria are more metabolically active at the node of Ranvier and we characterized the role of AP firing in the dynamics of mitochondrial ATP and H_2O_2 production. Moreover we show the deleterious alterations that occur in axonal mitochondria physiology of two mouse models of neuropathy, peripheral axonal CMT2A and

demyelinating peripheral neuropathies. Together, our data thus provide new insight into the role of axonal mitochondria under physiological and pathological conditions.

4. Materials and methods

4.1. Cloning

pLPCX mito-roGFP-Orp1 (Addgene; #64992) was digested with XhoI/ClaI, blunted and cloned into pAAV-MCS (Cell Biolabs, Inc.) under the control of a CMV promoter. Clones were validated by sequencing. Likewise, pcDNA-mito-ATeam (from H. Imamura, Tokyo, Japan) was digested with XhoI/HindIII, blunted and cloned into the CMV promoter controlled pAAV-MCS. Mitochondria-targeting tags were CoxVIII for roGFP-Orp1 and two tandem copies of CoxVIII for mito-ATeam. AAV viral particles were produced at the viral vector production centre at the Centre de Biotecnologia Animal I Teràpia Gènica in Barcelona, Spain or the University of Nantes, France.

4.2. Mouse strains

Either Swiss mice (Janvier, France) or $MFN2^{R94Q}$ mice [25] were used in the performed experiments. Mice were kept in the animal facility of the Institute for Neurosciences of Montpellier in clear plastic boxes and subjected to standard light cycles. All animal experiments were conducted in accordance with the French Institutional and National Regulation CEEA-LR-11032.

4.3. In vivo virus injection in spinal cord

A thin borosilicate glass capillary (Harvard Apparatus, Ref. 30-0016) was pulled with a Vertical Micropipette Puller (Sutter Instruments, P30-682) to form a glass needle. The glass needle was filled with viral solution (1 µl) and a 1 day old mouse is restrained in a position that exposes the lower back. The needle is injected through the skin using a micromanipulator and introduced into the spinal cord. The viral solution was injected over 2 minutes with short pressure pulses using a Picopump (World Precision Instrument) coupled to a pulse generator. After injection, the injection site is cleaned with betadine solution (Vetoquinol, cat. no. 3042413) for disinfection and the pup is placed back with its mother and littermates.

4.4. Immunohistochemistry

One month after the viral injection, the sciatic nerve was dissected and fixed in Zamboni's fixative [77] for 10 min at room temperature. After fixation, the dissected sciatic nerves are washed in PBS and incubated in successive glycerol baths (15, 45, 60, 66% in PBS) for 18 to 24 h each before freezing at −20 °C. The nerves were cut in small pieces in 66% glycerol and the epineurium sheaths removed. Small bundles of fibers were teased in double-distilled water on Superfrost slides and dried for 3 hours at room temperature. Some nerves were frozen in O.C.T. Compound (Tissue-Tek, Ref. 4583) and longitudinal sections were cut using a cryostat (Leica Biosystems, CM3050). For immunostaining, the teased fibers or longitudinal sections were incubated for 1 h at room temperature in blocking solution (10% goat serum and 0.3% TritonX100 in PBS). Then, the samples were incubated with TOM20 (FL-145) primary rabbit antibody (1/500, Santa Cruz, Ref. sc-11415), mouse anti-Myelin Basic Protein (1/500, Merck, Ref. NE1019) or rabbit NF-200 (1/500, Sigma, Ref. N4142) in blocking solution overnight at

4 °C. The next day, the samples were washed in PBS and incubated for 1h at room temperature with secondary donkey antibodies coupled to Alexa568 (1/1000, Invitrogen, Ref. A10042) or Alexa488 (1/1000, Invitrogen, Ref. A21202). Finally the samples were washed in PBS and mounted in Immu-mount (Thermo Scientific). Images were acquired at room temperature using a 20× or 40× objective, a Zeiss confocal microscope LSM710, and its associated software.

4.5. Imaging of sciatic nerve in living mice

One month after the viral injection, the mice were anesthetized with a constant flow (1.5 l/min) of oxygen + 5% of isoflurane in an anesthesia box (World Precision Instruments, Ref. EZ-B800) for 5 min. Thereafter the anesthesia was maintained with a mask delivering 2% isoflurane at 0.8 l/min. The eyes were protected by eye protection gel (Ocry-gel, TVM, cat. no. 48026T613/3). Intraperitoneal injection of 0.1 mg/kg buprenorphine was used for pre-surgery analgesia. The mouse was placed in a silicone mold, lying on its belly, shaved on his hind paw and the paws immobilized using small pins. The incision area was disinfected with betadine solution (Vetoquinol, cat. no. 3042413). The skin was cut using scissors, fat tissue removed, the gluteus superficialis and biceps femoris muscles were separated to reveal a cavity crossed by the sciatic nerve, and the sciatic nerve was lifted up using a small spatula. A long plastic strip was placed underneath the sciatic nerve and this strip fixed using magnets. The sciatic nerve was kept in an aqueous environment of either sterile PBS buffer or artificial cerebrospinal fluid (148 mM NaCl, 3 mM KCl, 1.4 mM $CaCl_2$•$2H_2O$, 0.8 mM $MgCl_2$•$6H_2O$, 0.2 mM $NaPO_4$•H_2O in sterile H_2O) to prevent drying. At that point the mouse was placed under the two-photon microscope objective lens, a glass, 12mm diameter, 0.25mm thick microscope coverslip put on top of the nerve and a drop of deionized water placed on it to

immerse the objective lens (20X, Carl Zeiss Microscopy, LD CApochromat, Ref. 421887–9970).

4.6. Demyelination procedure

After imaging of the sciatic nerve in vivo for at least 30 minutes, 5 µl of 1 mg/ml lysophotphatidyl choline (LPC) was injected directly into the sciatic nerve using a Hamilton syringe (Ref. 80930) to induce demyelination. Injection of 5 µl PBS is used as a negative control. After injection, the nerve was placed back to its original location in the body. The skin of the incision was realigned together using a blunt scalpel and stapled along the wound with two clips (Fine Science Tools; 12020-00). The area around the wound was disinfected again with betadine solution. The anesthesia mask was removed and the mouse was monitored until it had woken up. Motor function of the injected and non-injected hindlimb was followed by lifting the animal by the tail. At 1 week after LPC injection, the non-injected hindlimb showed a normal postural reflex characterized by spreading of leg whereas the injected hindlimb showed abnormal reflexes such as tremors, clasping or retracting of the paw. This behavior has been described and linked to deficient myelination in the PNS in previous studies [78]. The severity of abnormal hindlimb function decreased at 2 weeks after LPC injection and no difference in leg function between the injected and non-injected hindlimb could be observed anymore at 3 weeks after LPC injection.

4.7. Saphenous nerve stimulation in living mice

After skin incision and removal of connecting tissue, the saphenous nerve is lifted up and isolated using a plastic strip (Fig 2a). To stimulate the saphenous nerve, two platinum kapton

microelectrodes (World Precision Instruments, PTM23B05KT) were inserted at the posterior side of the plastic strip using a micromanipulator (Fig 2A). One hook-shaped recording electrode (AD Instruments, MLA 1203) was placed at the anterior side (Fig 2A). The ground electrode was inserted in the tail of the mouse and the negative electrode in the groin area (Fig 2B). The mouse was placed under the two-photon microscope (Fig 2C), a microscope glass coverslip was placed on top of the nerve and the electrodes were connected to a Powerlab 26T (AD Instruments; ML4856). A drop of deionized water was then placed on top of the microscope glass to immerse the 20× objective lens.

4.8. Two-photon image acquisition

All in vivo images were obtained with a two-photon microscope LSM 7 MP OPO (Zeiss, France) coupled to a dark microscope incubator (L S1 Dark, Zeiss) in which the temperature was maintained at 37 °C (Heating Unit XL S, Zeiss, France). Mitochondria images were acquired by time-lapse recording varying from one image every minute to one image every 5 minutes during 1 hour. Each image is a stack at Maximum Intensity (ZEN software, Zeiss) of 10 scans over 40 μm depth. For ATeam imaging, a single track at 850 nm excitation wavelength is used to obtain both the CFP (em. 475 nm) and Venus (em. 527 nm) image at the same time point. For roGFP imaging, the two images were acquired for each time point using alternating tracks at 940nm and 800nm. Change of track was set after each stack. For Coherent Anti-Stokes Raman Scattering (CARS) imaging, 2 synchronized laser lines at excitation wavelengths 836 nm and 1097 nm are used simultaneously thanks to the OPO system. Each scan was acquired with constant laser intensity (20% for 940 nm, 10% for 850 nm, 10% for 800nm, 15% for 836nm, 4% 1097nm) at a 512 × 512 pixel resolution and

microscope imaging parameters were maintained over all different regions we imaged. Images, acquired with ZEN software (Zeiss), were saved in .czi format.

4.9. Data and statistical analysis

We used ImageJ software to analyze the relative ATP or H_2O_2 levels in mitochondria of peripheral axons. The acquired images for each wavelength were aligned using the Template Matching plugin. We defined a Region of Interest (ROI) encompassing all labeled mitochondria of the same axon and the mean fluorescent intensity on the ROI was measured on both images. These light intensities were then corrected for background light intensity determined as an area within the nerve where no fluorescent signal from the viral probe can be observed. Either the ATeam Venus/CFP ratio or the oxidized roGFP/reduced roGFP ratio was then calculated from the 2 values for mean light intensity.

Statistical significance for the effect of time on probe stability was determined using linear regression. The effects of the positive controls and negative controls on probe validation were determined using Student two-tailed T-tests. The effect of nerve stimulation was determined using one-way ANOVA and Dunnett's post-hoc tests. In addition, the threshold for a responding axon was set at 20% change in probe fluorescence ratio. The differences between MFN2 mutants and wild-type mice were determined using either Student two-tailed T-tests or two- way ANOVA with Sidak post-hoc tests. Differences between internodes and node of Ranvier mitochondria were determined using paired two-tailed T-tests. The effect of demyelination was determined using paired two-tailed T-tests.

4.10. Data availability

The data that support the findings of this study are available from the corresponding author upon reasonable request.

5. Acknowledgements

In addition we thank the MRI imaging platform, supported by the French National Research Agency (ANR-10-INBS-04), in particular Hassan Boukhaddaoui, and the Animal Facility of the INM. We also would like to thank Patrice Quintana for his help with the nerve stimulation protocol and Volker Baeker for the image analysis protocol.

This work has been supported by the European Research Council grant (FP7-IDEAS-ERC #311610) to N.T., the Association Française contre les Myopathies AFM-Téléthon research grant (#20044) to N.T. and R.C., The Neuromuscular Research Association Basel grant to R.C., by the Swedish StratNeuro program grant to R.C., by the Swedish Research Council grant (#2015-02394) to R.C., and by the Labex EpiGenMed ANR-10-LABX-12-01 to G.H.

6. Author contributions

GvH conducted the experiments. GvH and NT designed the experiments and wrote the paper with contributions from GC and RC. GC, MD and JB contributed to the experiments and to the design of the experiments. NT supervised the project.

7. Competing interests

The authors declare that the research was conducted in the absence of any commercial or financial relationships that could be construed as a potential conflict of interest.

8. References

1. Harris JJ, Jolivet R, Attwell D. Synaptic Energy Use and Supply. Neuron. 2012 Sep 6;75(5):762–77.
2. Attwell D, Laughlin SB. An Energy Budget for Signaling in the Grey Matter of the Brain. J Cereb Blood Flow Metab. 2001 Oct 1;21(10):1133–45.
3. Ames A. CNS energy metabolism as related to function. Brain Res Rev. 2000 Nov 1;34(1):42–68.
4. Salzer JL, Zalc B. Myelination. Curr Biol. 2016 Oct 24;26(20):R971–5.
5. Fischer TD, Dash PK, Liu J, Waxham MN. Morphology of mitochondria in spatially restricted axons revealed by cryo-electron tomography. PLOS Biol. 2018 Sep 17;16(9):e2006169.
6. Misgeld T, Kerschensteiner M, Bareyre FM, Burgess RW, Lichtman JW. Imaging axonal transport of mitochondria in vivo. Nat Methods. 2007 Jun 10;4:559.
7. Zhou B, Yu P, Lin M-Y, Sun T, Chen Y, Sheng Z-H. Facilitation of axon regeneration by enhancing mitochondrial transport and rescuing energy deficits. J Cell Biol. 2016;214(1):103–119.
8. Ohno N, Kidd GJ, Mahad D, Kiryu-Seo S, Avishai A, Komuro H, et al. Myelination and axonal electrical activity modulate the distribution and motility of mitochondria at CNS nodes of Ranvier. J Neurosci Off J Soc Neurosci. 2011 May 18;31(20):7249–58.
9. Perkins GA, Ellisman MH. Mitochondrial Configurations in Peripheral Nerve Suggest Differential ATP Production. J Struct Biol. 2011 Jan;173(1):117–27.
10. Tarasov AI, Griffiths EJ, Rutter GA. Regulation of ATP production by mitochondrial Ca(2+). Cell Calcium. 2012 Jul;52(1):28–35.
11. Edgar JM, McCulloch MC, Thomson CE, Griffiths IR. Distribution of mitochondria along small-diameter myelinated central nervous system axons. J Neurosci Res. 2008;86(10):2250–7.
12. Giorgio M, Trinei M, Migliaccio E, Pelicci PG. Hydrogen peroxide: a metabolic by-product or a common mediator of ageing signals? Nat Rev Mol Cell Biol. 2007 Sep 1;8:722.
13. Murphy MP. How mitochondria produce reactive oxygen species. Biochem J. 2009 Jan 1;417(Pt 1):1–13.
14. Hamanaka RB, Chandel NS. Mitochondrial reactive oxygen species regulate cellular signaling and dictate biological outcomes. Trends Biochem Sci. 2010 Sep;35(9):505–13.

15. Tormos KV, Chandel NS. Seeing the Light: Probing ROS In Vivo Using Redox GFP. Cell Metab. 2011 Dec 7;14(6):720–1.
16. Dixon BJ, Tang J, Zhang JH. The evolution of molecular hydrogen: a noteworthy potential therapy with clinical significance. Med Gas Res. 2013;3:10–10.
17. Tomanek L. Proteomic responses to environmentally induced oxidative stress. J Exp Biol. 2015;218(12):1867–1879.
18. Dauer W, Przedborski S. Parkinson's disease: mechanisms and models. Neuron. 39th ed. 2003;889–909.
19. Su KG, Banker G, Bourdette D, Forte M. Axonal degeneration in multiple sclerosis: The mitochondrial hypothesis. Curr Neurol Neurosci Rep. 2009 Sep;9(5):411–7.
20. Palau F, Estela A, Pla-Martín D, Sánchez-Piris M. The Role of Mitochondrial Network Dynamics in the Pathogenesis of Charcot-Marie-Tooth Disease. In: Espinós C, Felipo V, Palau F, editors. Inherited Neuromuscular Diseases: Translation from Pathomechanisms to Therapies [Internet]. Dordrecht: Springer Netherlands; 2009. p. 129–37.
21. Smith GM, Gallo G. The role of mitochondria in axon development and regeneration. Dev Neurobiol. 2017 Oct 14;78(3):221–37.
22. Chen H, Chan DC. Emerging functions of mammalian mitochondrial fusion and fission. Hum Mol Genet. 2005 Oct 15;14(suppl_2):R283–9.
23. Misko A, Jiang S, Wegorzewska I, Milbrandt J, Baloh RH. Mitofusin 2 is necessary for transport of axonal mitochondria and interacts with the Miro/Milton complex. J Neurosci Off J Soc Neurosci. 2010 Mar 24;30(12):4232–40.
24. Züchner S, Mersiyanova IV, Muglia M, Bissar-Tadmouri N, Rochelle J, Dadali EL, et al. Mutations in the mitochondrial GTPase mitofusin 2 cause Charcot-Marie-Tooth neuropathy type 2A. Nat Genet. 2004 Apr 4;36:449.
25. Cartoni R, Arnaud E, Médard J-J, Poirot O, Courvoisier DS, Chrast R, et al. Expression of mitofusin 2R94Q in a transgenic mouse leads to Charcot–Marie–Tooth neuropathy type 2A. Brain. 2010 May 1;133(5):1460–9.
26. Pich S, Bach D, Briones P, Liesa M, Camps M, Testar X, et al. The Charcot–Marie–Tooth type 2A gene product, Mfn2, up-regulates fuel oxidation through expression of OXPHOS system. Hum Mol Genet. 2005 Jun 1;14(11):1405–15.
27. Frohman EM, Racke MK, Raine CS. Multiple Sclerosis — The Plaque and Its Pathogenesis. N Engl J Med. 2006 Mar 2;354(9):942–55.
28. Sedel F, Bernard D, Mock DM, Tourbah A. Targeting demyelination and virtual hypoxia with high-dose biotin as a treatment for progressive multiple sclerosis. Oligodendrocytes Health Dis. 2016 Nov 1;110:644–53.
29. Mahad DJ, Ziabreva I, Campbell G, Lax N, White K, Hanson PS, et al. Mitochondrial changes within axons in multiple sclerosis. Brain J Neurol. 2009 May;132(Pt 5):1161–74.

30. Campbell G, Mahad DJ. Mitochondrial dysfunction and axon degeneration in progressive multiple sclerosis. FEBS Lett. 2018 Feb 17;592(7):1113–21.
31. Gutscher M, Sobotta MC, Wabnitz GH, Ballikaya S, Meyer AJ, Samstag Y, et al. Proximity-based Protein Thiol Oxidation by H(2)O(2)-scavenging Peroxidases. J Biol Chem. 2009 Nov 13;284(46):31532–40.
32. Imamura H, Huynh Nhat KP, Togawa H, Saito K, Iino R, Kato-Yamada Y, et al. Visualization of ATP levels inside single living cells with fluorescence resonance energy transfer-based genetically encoded indicators. Proc Natl Acad Sci U S A. 2009 Sep 15;106(37):15651–6.
33. Albrecht SC, Barata AG, Großhans J, Teleman AA, Dick TP. In Vivo Mapping of Hydrogen Peroxide and Oxidized Glutathione Reveals Chemical and Regional Specificity of Redox Homeostasis. Cell Metab. 2011 Dec 7;14(6):819–29.
34. Ren W, Ai H-W. Genetically Encoded Fluorescent Redox Probes. Sensors. 13th ed. 2013;15422–33.
35. Tu H, Boppart SA. Coherent anti-Stokes Raman scattering microscopy: overcoming technical barriers for clinical translation. J Biophotonics. 2014 Jan;7(0):9–22.
36. Mytskaniuk V, Bardin F, Boukhaddaoui H, Rigneault H, Tricaud N. Implementation of a Coherent Anti-Stokes Raman Scattering (CARS) System on a Ti:Sapphire and OPO Laser Based Standard Laser Scanning Microscope. J Vis Exp. 113th ed. 2016;doi: 10.3791/54262.
37. Hajjar H, Boukhaddaoui H, Rizgui A, Sar C, Berthelot J, Perrin-Tricaud C, et al. Label-free non-linear microscopy to measure myelin outcome in a rodent model of Charcot-Marie-Tooth diseases. J Biophotonics. 2018 Aug 9;0(ja):e201800186.
38. Huff TB, Cheng J-X. In vivo coherent anti-Stokes Raman scattering imaging of sciatic nerve tissue. J Microsc. 2007 Feb;225(Pt 2):175–82.
39. Gonzalez S, Fernando R, Berthelot J, Perrin-Tricaud C, Sarzi E, Chrast R, et al. In vivo time-lapse imaging of mitochondria in healthy and diseased peripheral myelin sheath. Mitochondrion. 2015 Jul 1;23:32–41.
40. Ino D, Sagara H, Suzuki J, Kanemaru K, Okubo Y, Iino M. Neuronal Regulation of Schwann Cell Mitochondrial Ca2+ Signaling during Myelination. Cell Rep. 2015 Sep 29;12(12):1951–9.
41. Bernard-Marissal N, Van Hameren G, Juneja M, Pellegrino C, Rochat C, El Mansour O, et al. Endoplasmic reticulum and mitochondria dysfunction underlies reversible Charcot–Marie–Tooth type 2A neuropathy.
42. Bazil JN, Beard DA, Vinnakota KC. Catalytic Coupling of Oxidative Phosphorylation, ATP Demand, and Reactive Oxygen Species Generation. Biophys J. 2016 Feb 23;110(4):962–71.
43. Cadenas E, Davies KJA. Mitochondrial free radical generation, oxidative stress, and aging. Free Radic Biol Med. 2000 Aug 1;29(3):222–30.

44. Bélanger E, Henry FP, Vallée R, Randolph MA, Kochevar IE, Winograd JM, et al. In vivo evaluation of demyelination and remyelination in a nerve crush injury model. Biomed Opt Express. 2011 Sep;2(9):2698–2708.
45. Cooper MF, Webster GR. The differentiation of phospholipase A1 and A2 in rat and human nervous tissues. J Neurochem. 1970 Nov;17(11):1543–54.
46. Allt G, Ghabriel MN, Sikri K. Lysophosphatidyl choline-induced demyelination. Acta Neuropathol (Berl). 1988 Sep 1;75(5):456–64.
47. Plemel JR, Michaels NJ, Weishaupt N, Caprariello AV, Keough MB, Rogers JA, et al. Mechanisms of lysophosphatidylcholine-induced demyelination: A primary lipid disrupting myelinopathy. Glia. 2017 Oct 25;66(2):327–47.
48. Kiryu-Seo S, Ohno N, Kidd GJ, Komuro H, Trapp BD. Demyelination increases axonal stationary mitochondrial size and the speed of axonal mitochondrial transport. J Neurosci Off J Soc Neurosci. 2010 May 12;30(19):6658–66.
49. Tricaud N, Park H. Wallerian demyelination: chronicle of a cellular cataclysm. Cell Mol Life Sci. 74th ed. 2017;4049–57.
50. Meiri H, Steinberg R, Medalion B. Detection of Sodium Channel Distribution in Rat Sciatic Nerve Following Lysophosphatidylcholine-Induced Demyelination. J Membrane Biol. 92nd ed. 1986;47–56.
51. Hanson GT, Aggeler R, Oglesbee D, Cannon M, Capaldi RA, Tsien RY, et al. Investigating Mitochondrial Redox Potential with Redox-sensitive Green Fluorescent Protein Indicators. J Biol Chem. 2004 Mar 26;279(13):13044–53.
52. Dooley CT, Dore TM, Hanson GT, Jackson WC, Remington SJ, Tsien RY. Imaging Dynamic Redox Changes in Mammalian Cells with Green Fluorescent Protein Indicators. J Biol Chem. 2004 May 21;279(21):22284–93.
53. Samara C, Poirot O, Domènech-Estévez E, Chrast R. Neuronal activity in the hub of extrasynaptic Schwann cell-axon interactions. Front Cell Neurosci. 2013;7:228.
54. Yi M, Weaver D, Hajnóczky G. Control of mitochondrial motility and distribution by the calcium signal: a homeostatic circuit. J Cell Biol. 2004 Nov 22;167(4):661–72.
55. Fukai T, Ushio-Fukai M. Superoxide Dismutases: Role in Redox Signaling, Vascular Function, and Diseases. Antioxid Redox Signal. 2011 Sep 15;15(6):1583–606.
56. Yamakura F, Kawasaki H. Post-translational modifications of superoxide dismutase. Biochim Biophys Acta. 1804th ed. 2010;318–25.
57. Little C, Olinescu R, Reid KG, O'Brien PJ. Properties and Regulation of Glutathione Peroxidase. J Biol Chem. 1970 Jul 25;245(14):3632–6.
58. Nie Q, Wang C, Song G, Ma H, Kong D, Zhang X, et al. Mitofusin 2 deficiency leads to oxidative stress that contributes to insulin resistance in rat skeletal muscle cells. Mol Biol Rep. 2014 Oct 1;41(10):6975–83.

59. Baloh RH, Schmidt RE, Pestronk A, Milbrandt J. Altered Axonal Mitochondrial Transport in the Pathogenesis of Charcot-Marie-Tooth Disease from Mitofusin 2 Mutations. J Neurosci. 2007;27(2):422–430.
60. Zilberter Y, Zilberter T, Bregestovski P. Neuronal activity in vitro and the in vivo reality: the role of energy homeostasis. Trends Pharmacol Sci. 2010 Sep 1;31(9):394–401.
61. Ainbinder A, Boncompagni S, Protasi F, Dirksen RT. Role of Mitofusin-2 in Mitochondrial Localization and Calcium Uptake in Skeletal Muscle. Cell Calcium. 2015 Jan;57(1):14–24.
62. Chen Y, Csordás G, Jowdy C, Schneider TG, Csordás N, Wang W, et al. Mitofusin 2-containing Mitochondrial-Reticular Microdomains Direct Rapid Cardiomyocyte Bioenergetic Responses via Inter-Organelle Ca(2+) Crosstalk. Circ Res. 2012 Sep 14;111(7):863–75.
63. Yu T, Robotham JL, Yoon Y. Increased production of reactive oxygen species in hyperglycemic conditions requires dynamic change of mitochondrial morphology. Proc Natl Acad Sci U S A. 2006 Feb 21;103(8):2653–8.
64. de Brito OM, Scorrano L. Mitofusin 2: A Mitochondria-Shaping Protein with Signaling Roles Beyond Fusion. Antioxid Redox Signal. 2007 Dec 20;10(3):621–34.
65. Giorgio M, Migliaccio E, Orsini F, Paolucci D, Moroni M, Contursi C, et al. Electron Transfer between Cytochrome c and p66Shc Generates Reactive Oxygen Species that Trigger Mitochondrial Apoptosis. Cell. 2005 Jul 29;122(2):221–33.
66. Chen H, Chan DC. Mitochondrial dynamics–fusion, fission, movement, and mitophagy–in neurodegenerative diseases. Hum Mol Genet. 2009 Oct 15;18(R2):R169–76.
67. Bros H, Millward JM, Paul F, Niesner R, Infante-Duarte C. Oxidative damage to mitochondria at the nodes of Ranvier precedes axon degeneration in ex vivo transected axons. Exp Neurol. 2014 Nov 1;261:127–35.
68. Witte ME, Bø L, Rodenburg RJ, Belien JA, Musters R, Hazes T, et al. Enhanced number and activity of mitochondria in multiple sclerosis lesions. J Pathol. 2009 May 26;219(2):193–204.
69. Young EA, Fowler CD, Kidd GJ, Chang A, Rudick R, Fisher E, et al. Imaging correlates of decreased axonal Na+/K+ ATPase in chronic multiple sclerosis lesions. Ann Neurol. 2008;63(4):428–35.
70. Gilgun-Sherki Y, Melamed E, Offen D. The role of oxidative stress in thepathogenesis of multiple sclerosis: The need for effectiveantioxidant therapy. J Neurol. 2004 Mar 1;251(3):261–8.
71. Rousset S, Alves-Guerra M-C, Mozo J, Miroux B, Cassard-Doulcier A-M, Bouillaud F, et al. The Biology of Mitochondrial Uncoupling Proteins. Diabetes. 2004;53(suppl 1):S130–S135.
72. Dalgaard LT, Pedersen O. Uncoupling proteins: functional characteristics and role in the pathogenesis of obesity and Type II diabetes. Diabetologia. 2001 Aug 1;44(8):946–65.

73. Rexroth S, Poetsch A, Rögner M, Hamann A, Werner A, Osiewacz HD, et al. Reactive oxygen species target specific tryptophan site in the mitochondrial ATP synthase. Biochim Biophys Acta BBA - Bioenerg. 2012 Feb 1;1817(2):381–7.
74. Yin X, Kidd GJ, Ohno N, Perkins GA, Ellisman MH, Bastian C, et al. Proteolipid protein–deficient myelin promotes axonal mitochondrial dysfunction via altered metabolic coupling. J Cell Biol. 2016 Nov 21;215(4):531–42.
75. Yellen G. Fueling thought: Management of glycolysis and oxidative phosphorylation in neuronal metabolism. J Cell Biol. 2018;217(7):2235–2246.
76. Funfschilling U, Supplie LM, Mahad D, Boretius S, Saab AS, Edgar J, et al. Glycolytic oligodendrocytes maintain myelin and long-term axonal integrity. Nature. 2012 Apr 29;485(7399):517–21.
77. Stefanini M, Martino CD, Zamboni L. Fixation of Ejaculated Spermatozoa for Electron Microscopy. Nature. 1967 Oct 14;216:173.
78. Hung H, Kohnken R, Svaren J. The NURD chromatin remodeling complex is required for peripheral nerve myelination. J Neurosci. 2012 Feb 1;32(5):1517–27.

9. Figure legends

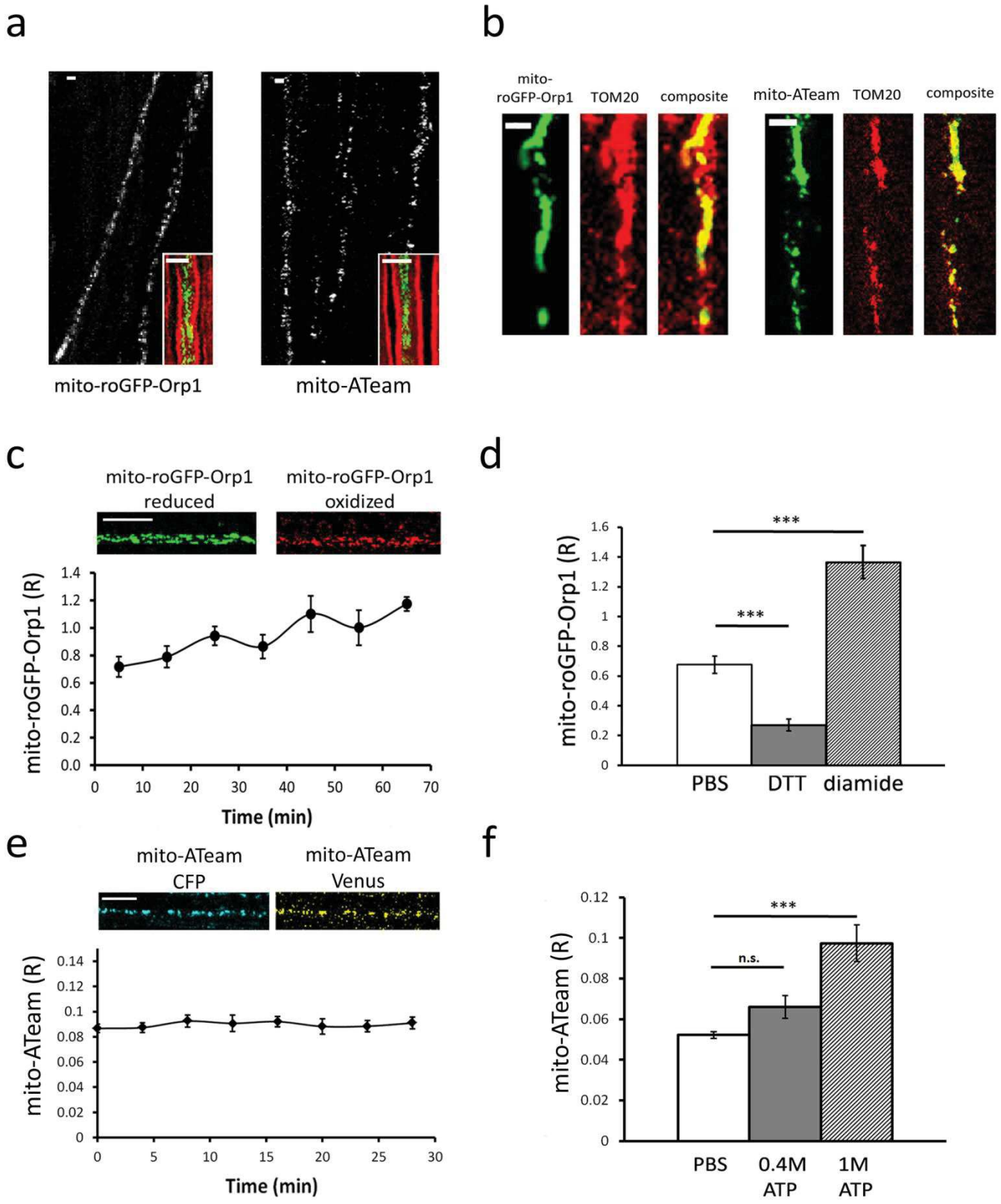

Figure 1

Figure 1: *In vivo* validation of the fluorescent probes.

(A) Several axons expressing mito-roGFP-Orp1 or mito-ATeam probe can be observed in teased fibers of mouse sciatic nerve 1 month after the virus injection. CARS imaging (inserts) shows that axons expressing mito-roGFP-Orp1 or mito-ATeam (green) are surrounded by a myelin sheath (red). Scale bars = 3 µm. **(**B) mito-roGFP-Orp1 expression (green) partially colocalizes with mitochondrial marker TOM20 (red) in the axon. Similarly, mito-ATeam partially colocalizes with TOM20 in axonal mitochondria. Scale bars = 3 µm. (C) A fluorescent signal of mito-roGFP-Orp1 is detected when the probe is reduced and when it is oxidized by H_2O_2. The ratio of mito-roGFP-Orp1 fluorescence measured *in vivo* (n=6 axons; 6 mice) shows a slight increase over time. Scale bar = 10 µm **(**D) Mito-roGFP-Orp1 fluorescence ratio decreases with DTT (p=0.006; n=3 axons, 3 mice) and increases after injection of diamide into the nerve (p=0.003; n=4 axons, 4 mice). (E) A fluorescent signal of the CFP subunit and Venus subunit of mito-ATeam is detected. Mito-ATeam fluorescence ratio measured *in vivo* shows no significant change over time (n=18 axons; 3 mice). Scale bar = 10 µm. (F) Mito-ATeam fluorescence ratio increases after injection of 0.4M (p=0.06; n=3 axons, 3 mice) and 1M (p=7.5E-4; n=6 axons, 4 mice) ATP into the sciatic nerve. All error bars show SEM. Statistical analysis shows Student two-tailed T-tests.

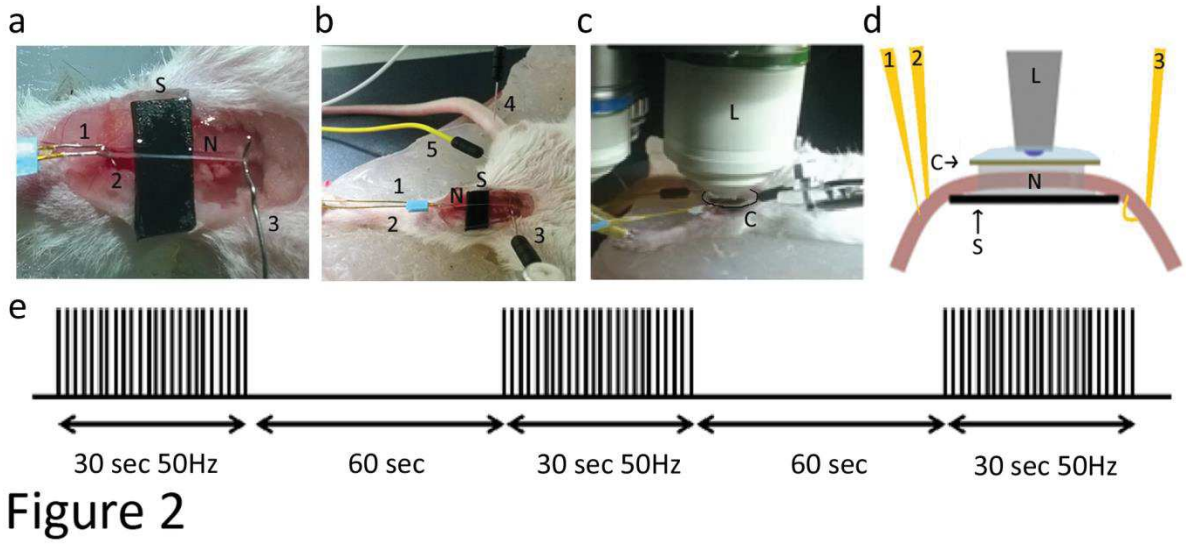

Figure 2: Setup of the saphenous nerve imaging experiment.

(A) After deep anesthesia, the mouse is placed on its back, the skin of its left inner tight is removed and the saphenous nerve (N) is placed on a plastic strip (S). Two stimulation microelectrodes (1 and 2) are inserted on both sides of the nerve on the plastic strip and one hook-shaped recording electrode (3) is holding the nerve on the opposite side. (B) The ground electrode (4) is inserted in the mouse tail and the negative electrode (5) in the groin area. (C) A glass coverslip (Co) is then placed on the nerve soaked in PBS and the mouse is then placed under the two-photon microscope immersion lens 20X (L) in water. (D) Schematic view of the imaging setup. (E) Schematic representation of the nerve stimulation pattern used to induce APs. The generation of APs was verified using the recording electrode. Negative electrode was used to correct for background signal.

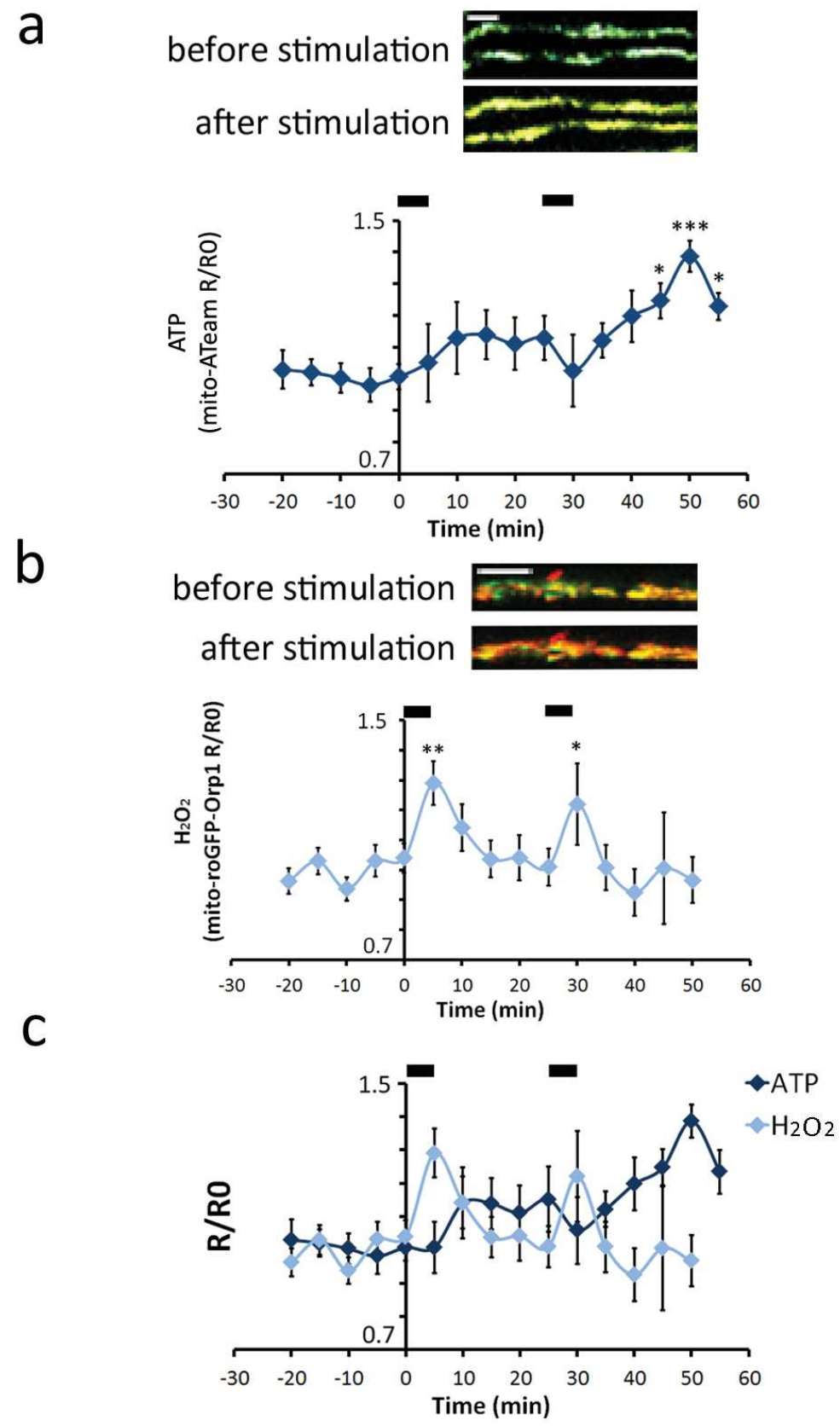
a
before stimulation
after stimulation
ATP
(mito-ATeam R/R0)
1.5
0.7
***
*
*
-30 -20 -10 0 10 20 30 40 50 60
Time (min)
b
before stimulation
after stimulation
H2O2
(mito-roGFP-Orp1 R/R0)
1.5
0.7
**
*
-30 -20 -10 0 10 20 30 40 50 60
Time (min)
c
R/R0
1.5
0.7
ATP
H2O2
-30 -20 -10 0 10 20 30 40 50 60
Time (min)

Figure 3

Figure 3: Effect of burst nerve stimulation on mitochondrial ATP and H_2O_2 levels.

(A) Upper panels: Nerve stimulation induced changes in the fluorescence signal of both the CFP and Venus subunit of mito-ATeam as illustrated by the Venus/CFP overlay pictures. Lower panel: graph showing mito-ATeam fluorescence ratio normalized to pre-stimulation values (R/R0) following two successive nerve stimulation period (black bars at the top). The first stimulation results in a slight, non-significant increase; a significant increase is measured after a second stimulation (p=0.0171 at t=45, p=0.0001 at t=50, p=0.049 at t=55; F-value = 2.872; Df=15; n=9 axons in 3 mice). (B) Upper panels: Nerve stimulation induced changes in the fluorescence signal of both the oxidized and reduced forms of GFP in mito-roGFP-Orp1 as illustrated by the overlay pictures. Lower panel: graph showing mito-roGFP-Orp1 fluorescence ratio normalized on pre-stimulation values (R/R0) following two successive nerve stimulation (black bars at the top). Both stimulations result in a significant increase 5 minutes after the stimulation (p=0.007; p=0.04; F-value = 2.804; Df=14; n=14 axons in 7 mice). (C) Graphs described in a and b were overlaid to show the relative dynamics of ATP and ROS levels after nerve stimulations. Scale bars= 5 µm. Error bars show SEM. Statistical tests are one-way ANOVA.

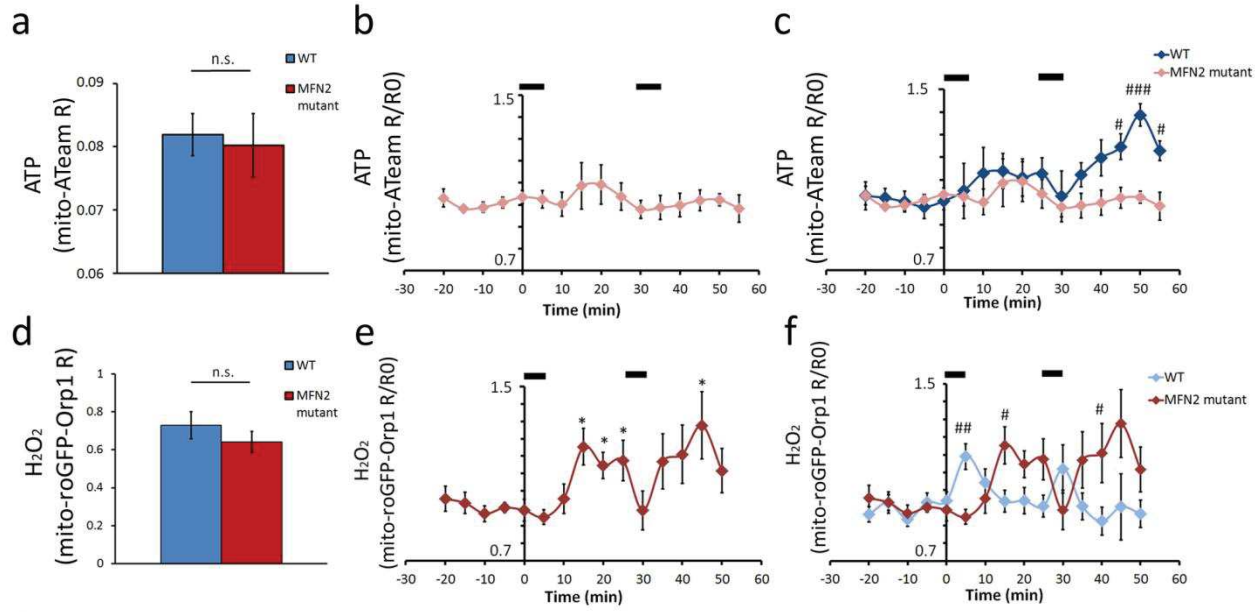

Figure 4

Figure 4: ATP and H_2O_2 levels of MFN2^{R94Q} mice.

(A) Graph showing mito-ATeam fluorescence ratio in resting axonal mitochondria of wild-type or mutant MFN2^{R94Q} mice (Student two-tailed T-test p=0.809; n=18 axons, 7 mice per group). (B) Graph showing mito-ATeam fluorescence ratio normalized on pre-stimulation values (R/R0) following two successive nerve stimulation periods (black bars at the top). The first period of stimulation resulted in a slight, non-significant increase; the second stimulation period did not generate any change (n=14 axons in 5 mice). (C) Graphs showing mito-ATeam R/R0 in wild-type (Fig. 3A) and mutant MFN2^{R94Q} mice (B panel) were overlaid to show the relative dynamics of ATP levels in both genotypes after nerve stimulations (Two way

ANOVA, p=0.011 at t=45, p=4.8E-5 at t=50, p=0.02 at t=55, F-value=19,27; Df=1). (D) Graph showing mito-roGFP-Orp1 fluorescence ratio in resting axonal mitochondria of wild-type or mutant MFN2^{R94Q} mice (Student two-tailed T-test p=0.337; n=16 axons, 8 mice per group). (E) Graph showing mito-roGFP-Orp1 fluorescence ratio normalized on pre-stimulation values (R/R0) following two successive nerve stimulation periods (black bars at the top). Both stimulations result in a significant increase (p=0.013 at t=15, p=0.020 at t=20, p=0.044 at t=25 and p=0.038 at t=45; F-value=3.095; Df=14; n=11 axons in 4 mice). (F) Graphs showing mito-roGFP-Orp1 R/R0 in wild-type (Fig. 3B) and mutant MFN2^{R94Q} mice (E panel) were overlaid to show the relative dynamics of H_2O_2 levels in both genotypes after nerve stimulations. A significant higher H_2O_2 level is detected in wild-type first (Two way ANOVA, p=0.007 at t=5, F-value= 5,484; Df=1), then a higher H_2O_2 level is detected in mutant MFN2^{R94Q} (p=0.014 at t=15, p=0.047 at t=40). Error bars show SEM. # = p-value<0.05. ## = p-value<0.01. ### = p-value<0.001.

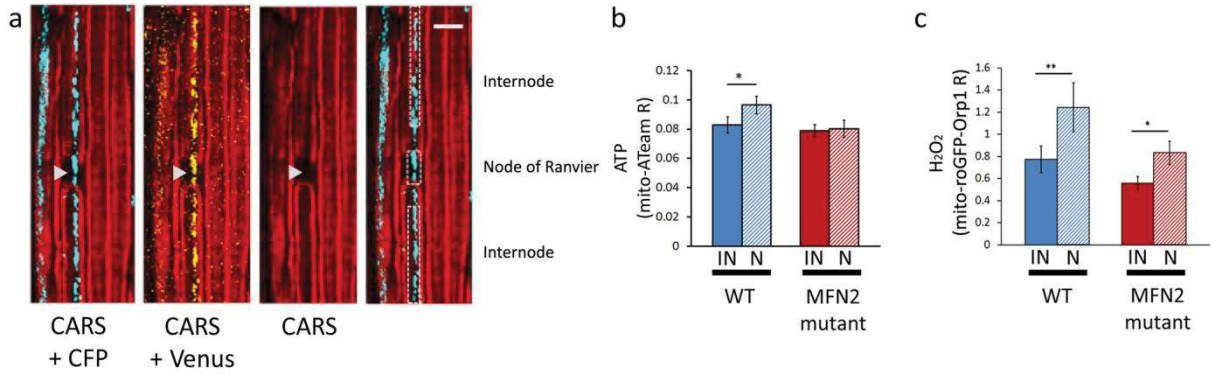

Figure 5

Figure 5: ATP and H_2O_2 levels are different along axons.

(A) Two-photons imaging of CFP (blue) and Venus (yellow) fluorescence of mito-ATeam was combined with CARS imaging of the myelin sheath (red). CARS imaging gap shows a node of Ranvier (arrowhead). Using the combined images, mitochondria located in the node of Ranvier and mitochondria located in internodes can be identified (right panel). Scale bar = 10 µm (B) Graph showing mito-ATeam fluorescence ratio in axonal mitochondria located in nodes of Ranvier (N) or internodes (IN) of wild-type (WT) or MFN2^{R94Q} mice (MFN2 mutant). In wild-type mice, ATP levels are higher in mitochondria in nodes of Ranvier than in internodes (p=0.035; n=14 axons in 7 mice). In MFN2^{R94Q} mice, ATP levels in node of Ranvier mitochondria are equal to internode mitochondria (n=7 nodes in 3 mice). (C) Graph showing mito-roGFP-Orp1 fluorescence ratio in axonal mitochondria located in nodes of Ranvier or internodes of wild-type or mutant MFN2^{R94Q} mice. In both wild-type mice and mutant MFN2^{R94Q} mice, H_2O_2 levels are higher in mitochondria in nodes of Ranvier than in internodes (WT: p=0.009; n=8 axons in 3 mice. MFN2^{R94Q}: p=0.019; n=9 axons in 3 mice). Error bars show SEM. Statistical tests are paired two-sided T-tests.

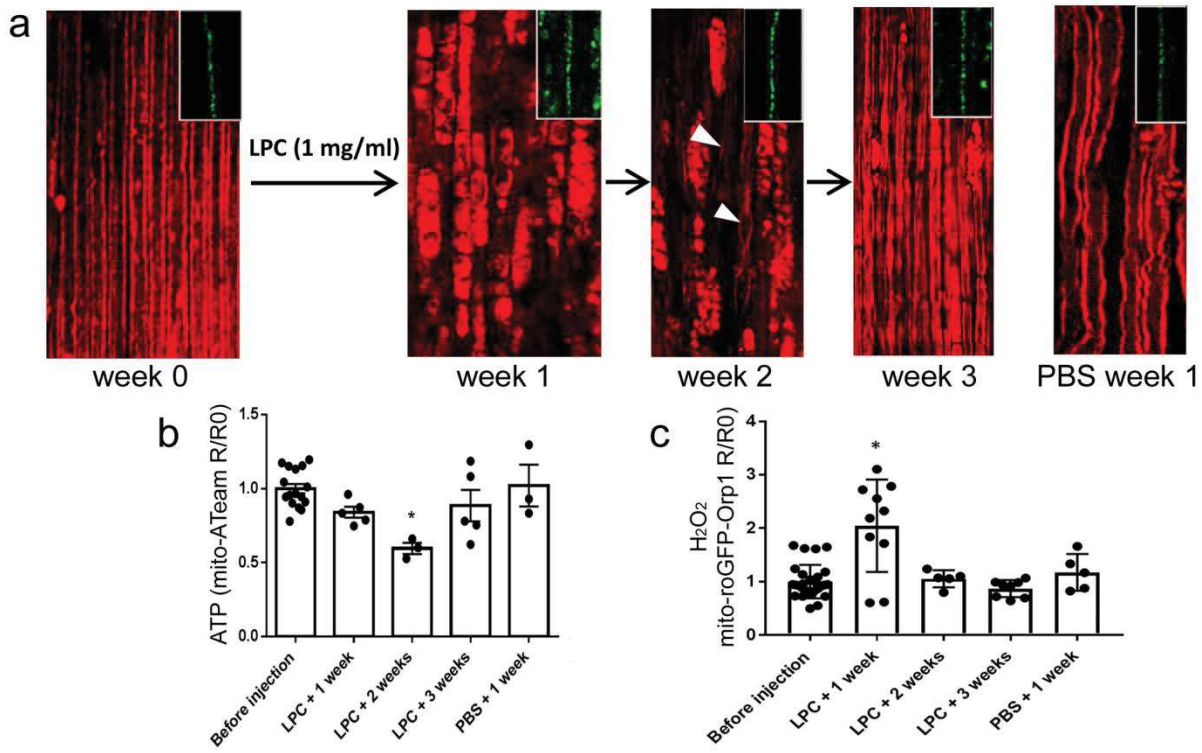

Figure 6

Figure 6: Impact of demyelination on axonal mitochondria ATP and H_2O_2.

(A) CARS imaging is used to visualize myelin. At week 0, before injection of LPC, most axons are myelinated. 1 week after LPC injection, axons are demyelinated and myelin debris and ovoids are observed. At week 2, thinly myelinated axons are observed in between the myelin debris (arrowheads) and at week 3, almost all axons are myelinated again, thus resembling a healthy nerve. PBS injection induces small conformational changes, but no formation of ovoids or debris. Inserts show that neuronal mitochondria remain visible throughout the whole process. (B) Graph showing mito-ATeam fluorescence ratio (R) in axonal mitochondria normalized on pre-demyelination values (R0) following demyelination. Following LPC injection, ATP levels are unchanged after 1 week (p=0.085; n=5 mice; 27 axons), decreased after 2 weeks (p=0.019; n=3 mice, 24 axons) and restored after 3 weeks (p=0.491; n=5 mice; 31 axons). PBS injection results in no significant change (p=0.799; n=3 mice; 23 axons). (C) Graph showing mito-roGFP-Orp1 fluorescence ratio (R) in axonal mitochondria normalized on pre-demyelination values (R0) following demyelination. Following LPC injection, H_2O_2 levels are increased after 1 week (p=0.031; n=10 mice, 17 axons), and unchanged after 2 weeks (p=0.663; n=5 mice, 9 axons) and after 3 weeks (p=0.450; n=8 mice, 13 axons). PBS injection results in no significant change (p=0.121; n=3 mice, 5 axons).

10. Expanded view figure legends

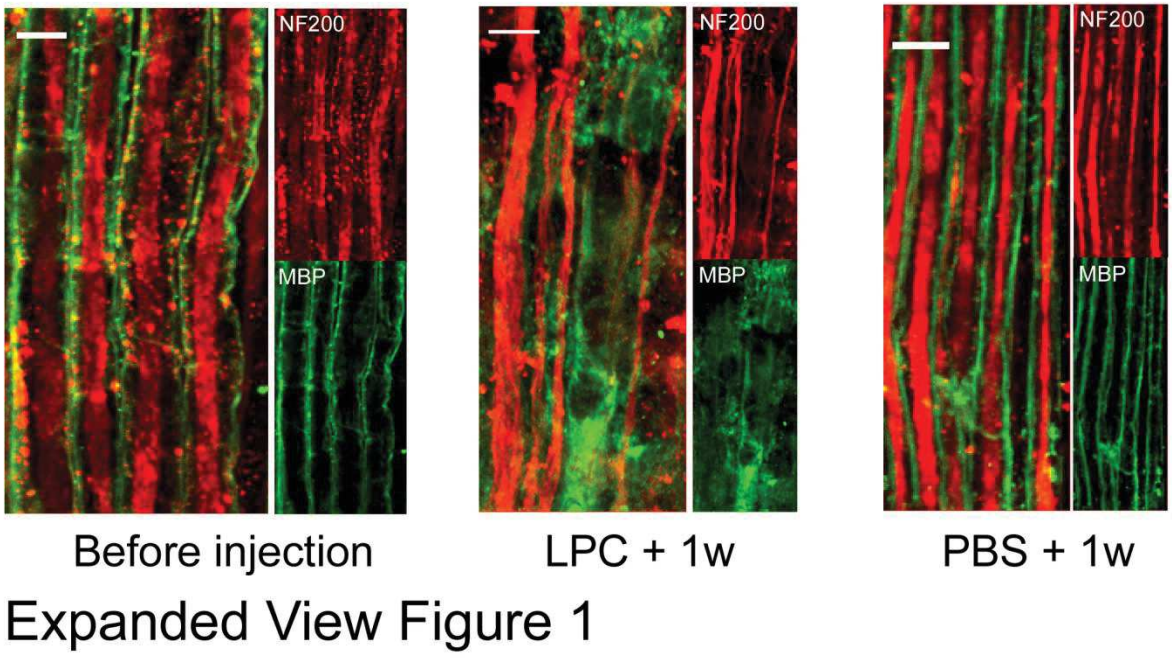

Expanded View Figure 1: LPC injection induces degeneration of the myelin sheath, but not axonal degeneration.

In a healthy sciatic nerve (Before injection), axons (red) are surrounded by a myelin sheath (green). This myelin sheath is severely damaged following injection of LPC into the sciatic nerve (LPC + 1w), but no sign of axonal degeneration. Injection of PBS (PBS + 1w) does not affect axon or myelin sheath physiology. Scale = 10 μm.

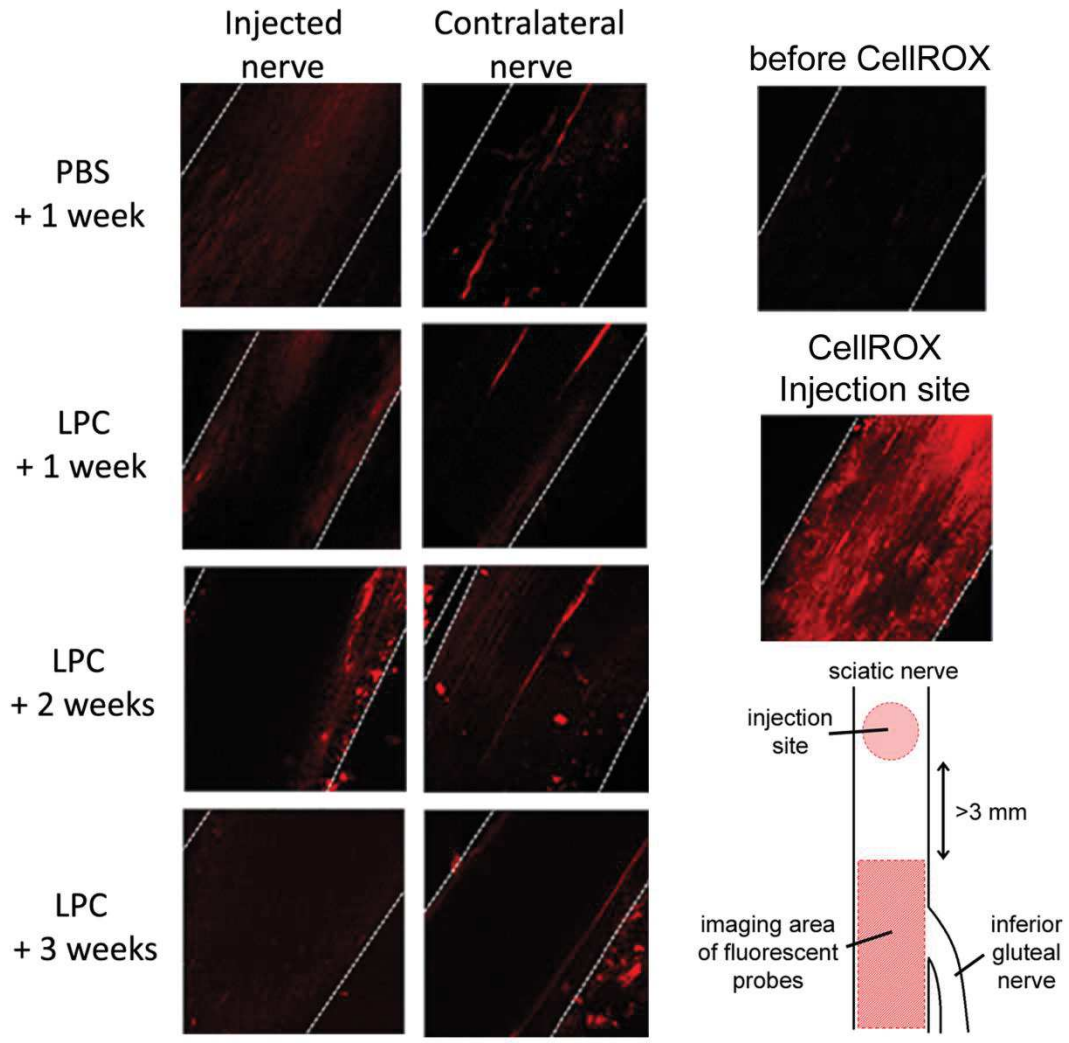

Expanded View Figure 2

Expanded View Figure 2: Impact of extramitochondrial ROS on mito-roGFP-Orp1 during demyelination.

Upon injection of CellROX deep red into the sciatic nerve, fluorescence signal could be detected indicative of oxidative stress. No significant differences were observed between the time points of the demyelination process, nor nerves injected with PBS. In the contralateral nerves, which were not injected with LPC or PBS, a fluorescence signal was detected as well. Before CellROX injection, no fluorescence signal was observed. At the injection site, where tissue is locally damaged due to insertion of the syringe, a much stronger fluorescence signal is observed than at the region where mitochondrial H_2O_2 was measured (Fig. 6C).

Chapter 9) *In vivo* introduction of viral vectors into mouse sciatic nerves

Next to the expression of fluorescent probes in the neurons to observe the axonal cytosol or axonal mitochondria, fluorescent probes can be expressed in myelinating Schwann cells as well.

In this chapter, I provide a protocol to inject viral vectors into the sciatic nerve of mice in order to infect Schwann cells. In this protocol, a distinction is made between sciatic nerve injection in adult mice and mouse pups. This protocol has been published in Methods of Molecular Biology - Myelin in 2018.

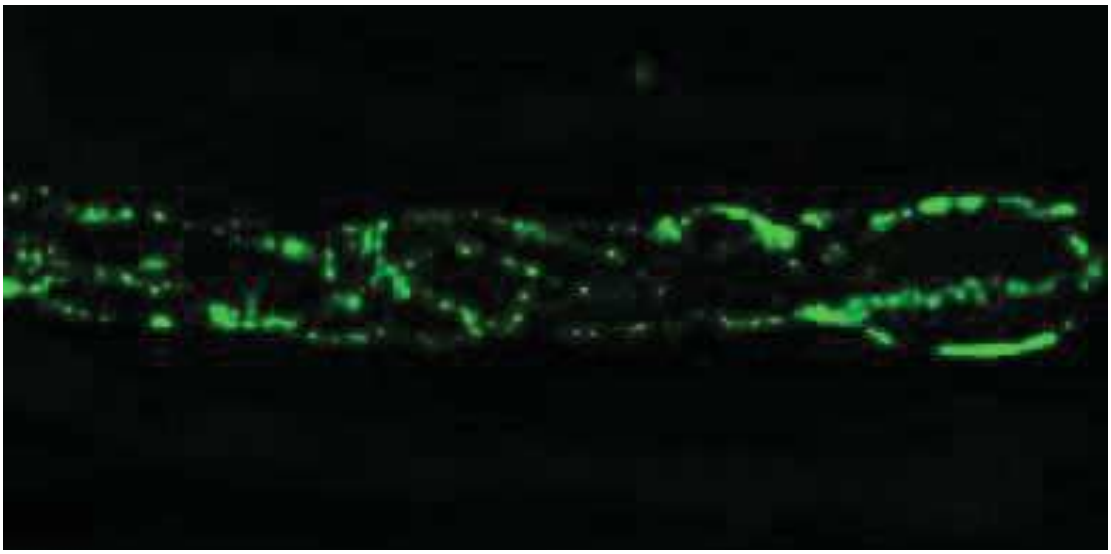

Expression of fluorescent probes in Schwann cell mitochondria

In Vivo Introduction of Transgenes into Mouse Sciatic Nerve Cells Using Viral Vectors

Gerben Van Hameren, Sergio Gonzalez, Ruani N. Fernando, Claire Perrin-Tricaud, and Nicolas Tricaud

Abstract

Myelinated fibers are essential for the rapid and efficient propagation of nerve information throughout the body. These fibers result from an intimate crosstalk between myelinating glia and the myelinated axons and, because it is difficult to fully reproduce these interactions in vitro, the basic molecular mechanisms that regulate myelination, demyelination, and remyelination remain unclear. Schwann cells produce myelin in the peripheral nervous system (PNS) and remain associated with the axons of peripheral neurons throughout axonal migration to the target. In order to investigate more closely the biology of myelinated fibers, we developed a local transgenesis approach based on the injection of engineered viral vectors in the sciatic nerve of mice to locally transduce peripheral nerve cells. This approach represents an alternative to germline modifications as it facilitates and speed up the investigation of peripheral nerve biology in vivo. Indeed the protocol we describe here requires just 3 weeks to complete. The injection of engineered viral vectors in the sciatic nerve of mice is a reproducible and straightforward method for introducing exogenous factors into myelinating Schwann cells and myelinated axons in vivo in order to investigate specific molecular mechanisms.

Key words Peripheral nerve, Viral transduction, Schwann cells, Axons, Transgenesis, Sciatic nerve

1 Introduction

The rise of mouse genetic techniques has revolutionized neurosciences with the creation of mouse models for human peripheral pathology [1–3]. These mouse models are really invaluable to understand the etiology of diseases; however, the time and resources invested to obtain a conditional knockout are important. Moreover despite the commercial availability of an increasing number of embryonic stem cells with specifically floxed genes, it usually takes 18–24 months to generate a conditional mutant [4]. In addition, obtaining a single mutant requires the use of 10–20 other mice. So the production and characterization of an allelic series in a single gene is a significant effort requiring several years. Recently

Ashwin Woodhoo (ed.), *Myelin: Methods and Protocols*, Methods in Molecular Biology, vol. 1791,
https://doi.org/10.1007/978-1-4939-7862-5_21,

new technologies such as zinc-finger nucleases (ZFNs), Transcription Activator-Like Effector Nucleases (TALENs), or Crispr-Cas9 to edit the mouse genome have emerged as valuable and effective alternatives to conventional gene targeting using ES cells, enabling faster and cheaper creation of genetically modified models [5–7]. Nevertheless, while the mouse genetic approach is useful for the study of specific disease-related genes, it is less appropriate for the analysis of fast and complex mechanisms such as cell interactions or differentiation.

Myelination is essential for a fast propagation of action potentials along axons in peripheral (PNS) and central (CNS) nervous systems. In the PNS, myelinating Schwann cells (mSC) [7] wrap around axons to form myelin segments. The molecular machinery required to propagate action potentials is concentrated between the segments at regular sites in structures known as nodes of Ranvier. Regarding the importance of myelinated fibers very little amount of data is available concerning the axon–glia relationships in peripheral nerves. This underscores the complexity of this cell–cell interaction and the relative inadequacy of the current technical approaches used in peripheral nerve research. Recent data have highlighted the role of cellular organelles and molecular factors in the interaction between Schwann cells and axons [8]. So the interdependence between the axon and the myelinating glia is so deep that CNS and PNS neuropathies cannot be correctly addressed without understanding the extent and complexity of the relationship between neurons and glial cells [9].

Avoiding arduous mouse genetics projects, we developed and successfully applied a viral strategy to introduce exogenous factors into Schwann cells and neurons of PNS [10]. The strategy takes advantage of the receptivity of axons and mSC to viral infection. By injecting engineered viral constructs into the sciatic nerve of wild-type or mutant mice many proteins can rapidly be silenced or overexpressed in the mSC in vivo. The impact of these modifications on myelination can be analyzed and quantified using light and electron microscopy [11]. The viral strategy described here allows for reliable and reproducible manipulation of multiple cellular factors in vivo [10–14]. The protocol is straightforward and less time- and resource-consuming than genetic approaches. Moreover, mRNA silencing facilitates acute downregulation of gene expression, thus preventing the adaptation and compensation that frequently occurs in mice with genetic modifications.

Early studies demonstrated that the injection of adenoviral particles into the sciatic nerve of anesthetized mice infects both axons and Schwann cells [11, 15, 16]. However, if the viral infection itself does not affect myelination, adenovirus infection is strongly immunogenic, so these vectors can only be used in immunodeficient mice. We later broadened this approach by developing a strategy to inject viral particles to locally silence (short hairpin RNA) or overexpress a

gene of interest at earlier time points (up to P3-P5 postnatal pups), which allows perturbation of the gene of interest at the beginning of myelination [13]. The same approach in young adult mice (4–8 weeks old) allows to study myelin sheath maintenance and, after nerve crush, demyelination. In addition, this approach can be used with both integrating (lentivirus) and non-integrating viruses (adenovirus and adeno-associated virus). In both cases the expression of the transgene was maintained for a long time in mSC in vivo without a significant decrease suggesting that the integration is not necessary to maintain expression in these cells [10–12, 14].

We also tested the tropism of various viral vectors following their injection in the sciatic nerve of mice at different ages (Table 1). Another option is to choose a specific promoter that can restrict the expression to a specific subset of cells. It is therefore important to select the correct mouse strain, viral particle, and promoter depending on the factor being studied and the cell type you wish to infect (Table 1). In addition, parallel control injections with a control shRNA as an example (non-target or scramble) is essential. Finally, adenoviral vectors and immunodeficient mice cannot be used to

Table 1
Comparison of viral vectors, age of infection, promoters, infected cells, applications, and mouse strains

Viral particle	Age	Promoter	Target cell type	Application	Mouse strain
Adenovirus	P3-P5 postnatal	U6 or CMV[a]	Myelinating SC (30%)[b]	Myelin formation	Immunodeficient such as CB17/SCID, Rag 1 or Rag 2 negative
			Non-myelinating SC (70%)[b]	Demyelination	
	Adult	U6 or CMV[a]	Myelinating SC (30%)[b]	Myelin maintenance	
			Non-myelinating SC (70%)[b]	Demyelination	
	P3-P5 postnatal or Adult	Synapsin 1[c]	Neurons (100%)	Axonal studies	
Lentivirus	P3-P5 postnatal	U6 or CMV[a]	Myelinating SC (70%) [11, 13]	Myelin formation	Swiss or any strain
			Non-myelinating SC (30%)	Demyelination	

[a]shRNA are commonly expressed using a U6 polIII promoter. Proteins are commonly expressed using a CMV polII promoter. However, in specific conditions the CMV promoter can be used to express a shRNA [13]
[b]These cells can easily be distinguished morphologically
[c]Synapsin I promoter is specifically expressed in neurons [11]

study demyelinating neuropathies or Wallerian degeneration because these biological events require an active immune system. In this context only lentivirus can be used to introduce exogenous factors into myelinating Schwann cells and myelinated axons.

For optimal results, we strongly recommend the use of high titer viral particles (between 10^{10} and 10^{11} cfu/ml). We used to produce high titer adenovirus or lentivirus in-house using the methods proposed by He et al. [17] or Cotter et al. [10], respectively. However commercial companies also offer high titer virus production services.

2 Materials

2.1 Reagents

1. Newborn SWISS strain mouse pups (P3-P5 postnatal) or adult (6 weeks to 3 months old) from immunodeficient strains such as CB17/SCID, Rag 1, or Rag 2 negative (*see* **Note 1**).
2. Bactrim. Sulfamethoxazole/Trimethoprim (Roche, cat no. 10130293 FR-S FY 1106.1071). Bactrim solution: Add 3 mL of Bactrim (200 mg sulfamethoxazole/40 mg trimethoprim stock) in 250 ml of drinking water. This solution must be freshly prepared per cage and changed every week.
3. 0.1% Fast Green solution: Dissolve 0.01 g of Fast Green FCF in 10 mL of PBS pH 7.4. Store at 4 °C for up to 6 months.
4. Viral particles (high titer: lentiviral particles $\geq 10^{10}$ cfu/mL and adenoviral particles $\geq 10^{10}$ cfu/mL): Make 8 µL aliquots of the viral particles and add 2 µL of 0.1% Fast Green solution (final concentration 0.01%). After mixing, the solution will appear blue. Store the aliquots at −80 °C for up to 12 months (*see* **Note 2**).
5. Isoflurane 1000 mg/mL.
6. Medical Oxygen bottle with an oxygen regulator.
7. Nitrogen gas bottle.
8. Betadine solution (Povidone iodine 10 g/L).
9. Leibovitz's L15 Medium (1×): Store the medium at 4 °C for up to 6 months.
10. Eye protection gel.
11. Buprenorphine 0.3 mg/mL solution: Dilute buprenorphine in sterile PBS pH 7.4 to a final concentration of 100 µg/mL. Keep away from direct light and store at 4 °C for up to 1 month.
12. Disinfectant solution. Add one tablet of disinfectant Relyton Virkon to 500 mL of sterile deionized water. Store at room temperature (20–25 °C) for up to 1 week.
13. Histoacryl tissue glue.

2.2 Equipment

1. Isoflurane-processing anesthesia system (Datex Ohmeda Isotec 5) with mouse nose cone.
2. Microinjector (Pneumatic Picopump PV820, World Precision Instruments or Picospritzer III, Parker-Hannifin).
3. Function pulse generator 3 MHz.
4. Dissecting kit comprising a scissors, forceps, spatula for adult surgery, spatula for pup surgery, retractors, wound clip system.
5. Surgery table.
6. Animal cage changing hood.
7. Disposable scalpels.
8. Instrument sterilizer.
9. Instrument beaker with silicone bottom.
10. Cotton buds.
11. Borosilicate glass capillaries 1.0 mm O.D. × 0.58 mm I.D.
12. Clipper Oster Turbo 111.
13. Micromanipulator IM—3C.
14. Hamilton glass pipette holder.
15. RN compression fitting 1 mm.
16. Insulin syringe 0.5 mL.
17. Stereomicroscope Zeiss Stemi 2000.
18. Cold light source Zeiss KL200.
19. Flaming/Brown Micropipette Puller Model P97.
20. Thermal blanket (230 V—50 W).
21. Micropipette P10 µL and P200 µL.
22. Eppendorf microloader.

2.3 Equipment Setup

1. Pulled glass capillaries: Pull the glass capillaries into fine glass needles using the flaming/brown micropipette puller. For pup injections, pull capillaries with the following parameters: heat 580 °C, pull 100 psi, velocity 50, and time 250 ms. For adult injections, the parameters are: heat 550 °C, pull 100 psi, velocity 50, and time 250 ms (*see* **Note 3**).

3 Methods

3.1 Preparing Mice for Surgery and Surgery

1. The day before surgery, add Bactrim antibiotic to the drinking water of the mice being operated on. If using pups, Bactrim antibiotic should be added to the drinking water of the pups lactating mothers. Bactrim is a broad spectrum mix of antibiotics that will be passed to the pups via lactation.

2. Set up all equipment for surgery in the animal cage changing hood. Using a hood of this style ensures adequate personal protection during viral injections while allowing optimal accessibility for equipment.
3. Switch on the thermal blanket and place it under the surgical table. The homogenous diffusion of the heat through the table will maintain optimal body temperature during surgery and injection (*see* **Note 4**)
4. Open the oxygen bottle valve and set the air compressor to a pressure of 100 bar.
5. For pups' surgery, perform the steps in Subheading 3.1.1. For adults' surgery perform the steps in Subheading 3.1.2.

3.1.1 Pups Surgery

1. Adjust the oxygen flow to 0.6% and the isoflurane distribution to 5% and turn on the mask anesthesia system.
2. Gently place the pup's head into the nose cone and maintain this position until the animal is immobile (Fig. 1a) (*see* **Note 5**).
3. Check paw and/or tail reflexes by pinching to ensure complete anesthesia.
4. Clean the region of incision with betadine solution using a sterile cotton bud.
5. Cut incision with small scissors. Be cautious to sterilize all instruments before use (Fig. 1b).
6. Pull apart the skin with small retractors to expose the cavity traversed by the sciatic nerve.
7. Using small scissors gently clear the connective tissue between the gluteus superficialis and bíceps femoris muscles, the intersection of which is commonly found just behind the top edge of a small fat deposit. This will open a small cavity beneath which lies the sciatic nerve. The appearance of the sciatic nerve will differ depending on age. At P2, the nerve will appear thin and translucent and is difficult to inject accurately. At P3, the nerve is thicker, opaque, and easier to distinguish. At P4, the nerve is thicker again and the trunks of the sciatic nerve can be clearly identified. Using forceps gently clear any connective tissue surrounding the nerve, but avoid rupturing any blood vessels.

Fig. 1 (continued) is placed in the mask for anesthesia. (f) The right thigh is shaved and prepared for surgery. The skin is incised and retracted to expose the nerve area. (g) The tip of the glass needle is carefully introduced into the nerve at a <45° acute angle to the nerve surface via the micromanipulator. The colored viral solution (in blue) is injected in the nerve. (h) Staples close the wound after surgery. All experiments using mice were performed under institutional guidelines (approval number CEEA-LR-11032) and according to all relevant regulations

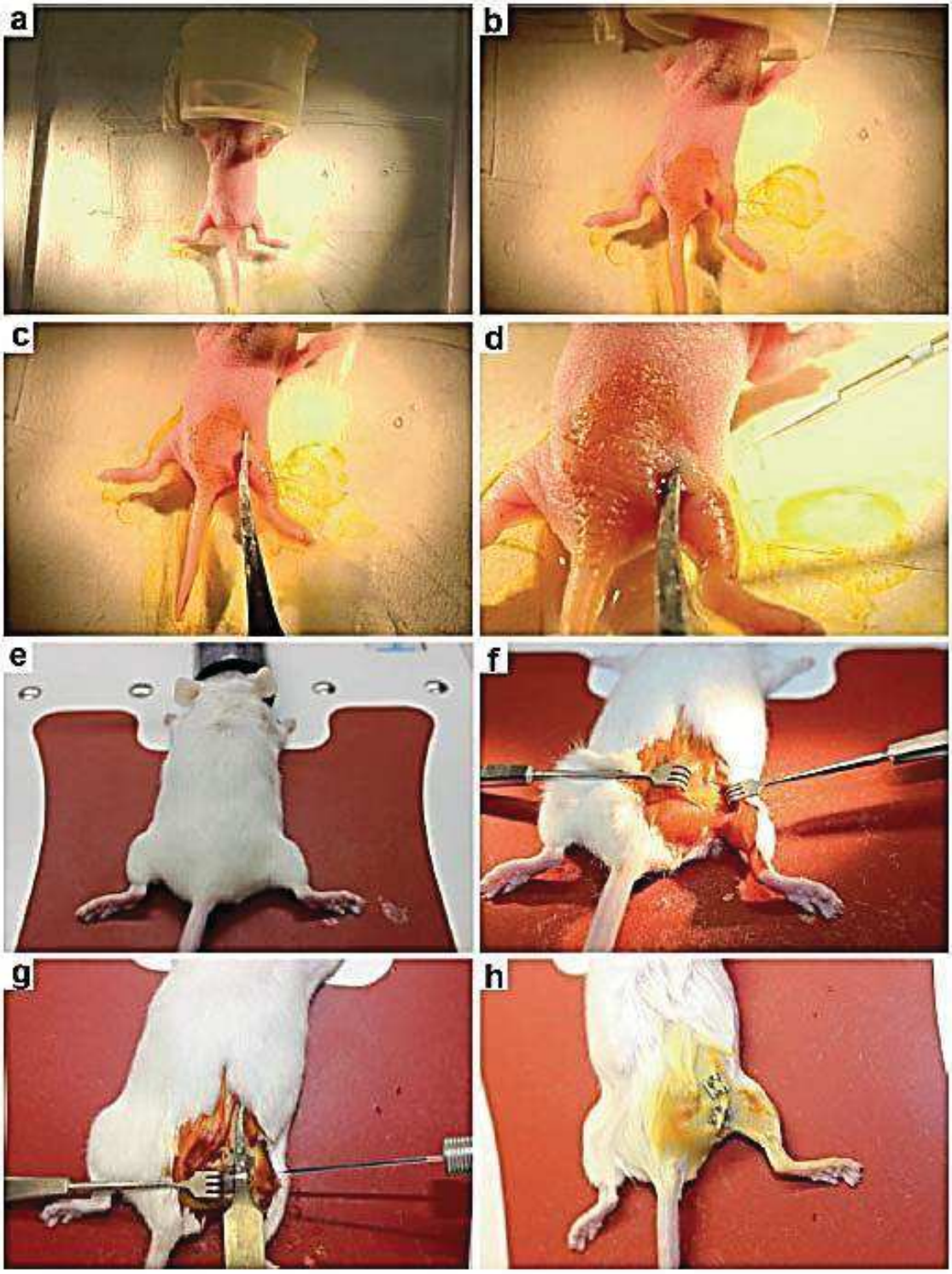

Fig. 1 (a) Successive steps of the adult and pup surgery, and injection. The nose of the pup is placed in the mask cone before surgery. (b) A small vertical incision is made in the thigh of the mouse pup with scissors. (c) The sciatic nerve is lifted out by using a fine spatula. (d) The tip of the glass needle is carefully introduced into the nerve at a <45° acute angle to the nerve surface via the micromanipulator. (e) The nose of the adult mouse

Using a thin spatula gently lift out the sciatic nerve (Fig. 1c). To avoid nerve lesions don't force the sciatic nerve.

8. Keep the cavity and surrounding tissue moist with L15 Medium using a P200 micropipette.
9. Reduce isoflurane to 3–2% to maintain anesthesia (*see* **Note 6**).

3.1.2 Adults Surgery

1. Weigh the mouse before starting anesthesia and note the weight (this is necessary to dose the analgesic in the coming days). Adjust the oxygen flow to the anesthesia induction box to 1.5% and turn on the isoflurane system to 5%. Put the mouse into the box for 2–3 min.
2. Switch off the isoflurane flow to the box, adjust the oxygen flow to 1% and turn on the mask anesthesia system.
3. Place mouse nose into the mask cone and check tail and paw reflexes by pinching to ensure complete anesthesia is reached (Fig. 1e).
4. Apply a drop of eye protector-gel on each eye.
5. For presurgical analgesia, administer buprenorphine/PBS solution (100 μg/kg) using an insulin syringe 0.5 mL, intraperitoneally (I.P).
6. Prepare the incision region for surgery: shave the incision area using the clippers. Apply betadine to the shaved area to clear loose hairs. Next clean the area with ethanol 70% and finally reapply betadine to the specific area of incision using sterile cotton buds (*see* **Note 7**).
7. Reduce isoflurane to 2–1.5% to maintain anesthesia and adjust flow oxygen to 0.2%. If the animal stirs during the surgery do not hesitate to increase the anesthesia to 5% isoflurane again for few minutes, but reduce to 2–1.5% once strong anesthesia is re-achieved.
8. Cut the skin with a scalpel. The scalpel has to be handled firmly and applied to the skin with some force for a clean cut.
9. Expand the incision with retractors to expose the gluteus superficialis and bíceps femoris muscles (Fig. 1f). A small fat deposit commonly indicates the junction of the two muscles. Use a scalpel or small scissors to cut the connective tissue that connects the muscles, revealing a small cavity which is traversed by the sciatic nerve. In adults, the sciatic nerve will appear thick and white (with a wavy pattern typical of myelin) and rests on muscles at the bottom of the cavity. Carefully enlarge the cavity by cutting connective tissues between the muscles. Use a closed scissor along the edges of the sciatic nerve (top and bottom) to free it from the surrounding tissue. Do not enlarge the cavity too much as large blood vessels transverse the muscle junction and you may cut them.

10. Use a spatula for adult surgery to gently lift the sciatic nerve out (Fig. 1g). Make sure that you don't lift up the fine muscle that lies beneath the nerve. Be extremely gentle lifting the nerve out as you may break or crush it.
11. Keep the nerve and cavity and surrounding tissue moist with L15 Medium using a P200 micropipette.

3.2 Injection

1. Use microloader tips and a P10 micropipette to load pulled glass needles with the colored viral particle solution, 3 μL for pup or 8 μL for adult injections. To avoid bubbles, it is critical to insert the loaded microloader tip to the base of the glass needle (where it begins to narrow) before slowly releasing the viral solution into the glass needle while carefully withdrawing the microloader tip. Tap the glass needle gently to remove any air bubbles. You may use one glass needle loaded with 6–7 μL of viral particles to inject two pups in a row. In this case note the half-way point of the viral solution on the glass needle with a marker. Avoid freeze and thaw cycles of viral aliquots.
2. Place the loaded glass needle into the Hamilton glass pipette holder and adjust it using the RN Compression Fitting.
3. Adjust the stereomicroscope to focus on the tip of the glass needle. Cut the flexible part of the needle tip in order to get a fine tip hole (*see* **Note 8**).
4. Use the microinjector to start the flow of the viral solution and check for a good flow from the tip (a fine drop should form at the tip of the needle).
5. Adjust the stereomicroscope to focus on the sciatic nerve at the highest possible magnification. A good view of the injection site at high magnification is essential to control the injection and to detect any leak out of the nerve.
6. Using the micromanipulator carefully introduce the tip of the glass needle into the nerve at <45° acute angle to the nerve surface (Fig. 1g). Puncture the perineurium and penetrate the nerve. Withdraw the glass needle slightly (but not completely) and advance again, to open an injection place. Repeat if necessary (*see* **Note 9**).
7. Start the injection of the viral particles. Virus should be injected between 200 and 300 nL/min over a 20–40 min period and for up to 10 psi of pressure to avoid the generation of high pressure in the nerve and subsequent nerve damage. We use the Function Pulse Generator set to frequency 2.1 with output 50 Ω and the Pneumatic Picopump with amplitude of 100 ms and 10 psi of pressure. The regulator dial of the Picopump can be employed to control the pressure with which the viral solution is expelled. Repetitive pumping of nanoliters of viral solution through the same injection site is critical to obtain a fully

loaded sciatic nerve. This loading of the nerve using pulsed microinjection takes time, but this process allows a good spread of the viral particles along the sciatic nerve which is critical for optimal transduction efficiency.

8. Adjust the stereomicroscope to visualize the glass needle inside the nerve to control the rate and volume injected. Ideally you should be able to visualize the solution entering and filling the nerve, the sciatic nerve should appear blue during and after injection (Fig. 1d). You should ideally see flow of blue liquid into nerve upstream and downstream of injection place (*see* **Note 10**).
9. Although harmless, do not allow any nitrogen gas to enter the nerve and stop pumping just before the glass needle is completely empty.

3.3 Closing

1. Clean the injection area with L15 Medium and remove excess liquid with a sterile cotton bud.
2. Replace the sciatic nerve at the bottom of the cavity and replace the muscles on top of the nerve. The muscles should sit easily back in place covering the nerve and, as they were not cut, they do not need sutures.
3. For pups' closure surgery, perform option Subheading 3.3.1. For adults' closure surgery perform the option Subheading 3.3.2.

3.3.1 Pups' Closure Surgery

1. Use forceps to lightly realign the skin either side of the incision. Apply a small amount of histoacryl glue along the incision to seal the wound (*see* **Note 11**).
2. Reduce isoflurane flow to 0% and allow the pups to inhale 100% oxygen for one or 2 min to facilitate good revival.
3. Allow the pup to fully recover before replacing with the mother (allow 5–10 min in warm conditions to allow the pup to fully wake and recover mobility). It is possible to prep the next pup to be injected in this time (*see* **Note 12**).
4. Switch off the anesthesia system. Disinfect dissecting tools using the disinfectant solution Relyton Virkon (no more than 10 min) and wash them with distillated water.

3.3.2 Adults' Closure Surgery

1. Use blunt forceps to realign the skin of the incision together and staple with two clips along the wound (Fig. 1h). Before closing the incision, remove all air from the point of closure.
2. Reduce isoflurane flow to 0% and allow the adults to inhale 100% oxygen for 2 min to facilitate good revival. Keep the adult mouse warm until fully awake and then house in a new cage.

3. Switch off the anesthesia system. Disinfect dissecting tools using the disinfectant solution Relyton Virkon (no more than 10 min) and wash them with distillated water.

3.4 Maintenance

1. For adults, administer I.P injections of buprenorphine/PBS solution (100 µg/kg) every 12 h for 2 days. Due to their small weigh pups cannot be treated safely with buprenorphine in IP. Maintain Bactrim antibiotic in the drinking water for 3 weeks both for pups and adults. Seven to ten days after surgery, remove clips from the injected adult mice.
2. From 3 weeks after injection, if desired, collect the nerve for analysis and immunohistochemistry using standard techniques. An example of the analysis we have performed can be found in Tricaud et al. [14]. Before this time point the long mSC may not be fully filled with the fluorescent marker protein. However demyelination phenotypes may appear and be detectable as early as 2 weeks after injection. We estimate that the transgene expression (shRNA or reporter protein) can be detected a few days after the injection but requires about a week to be fully efficient (*see* **Note 13**).

4 Notes

1. All experiments using mice must be performed in accordance with all institution and government ethics and animal handling requirements.
2. Caution: Viral particles have to be handled carefully. Avoid freeze and thaw cycles to guarantee the quality of viral particles.
3. As these parameters are highly dependent on the pipette puller we recommend that the appropriate parameters are determined by successive trials. Take note that the final diameter of the orifice is not important but instead the glass needle should be long enough enable free hand trimming to different lengths to achieve the correct diameter and dimensions for each injection.
4. Electrical heating blankets can be very hot on localized areas and cause burns. Don't put the animal directly on the blanket. Take particular care with pups as they are more sensitive to the heating blanket. We recommend extra layers of absorbent paper, or similar, between pups and heating blanket.
5. To adjust the nose cone to optimally fit the pup's head and reduce loss of isoflurane, cut a small piece of latex glove and affix it to the nose cone with a rubber band. Cut a small hole with scissors, enough to comfortably fit the pup's head without

any gaps. It is common for the pup to become immobile before full anesthesia is achieved. It is important to maintain 5% isoflurane inhalation for at least 5 min as pups are more resistant to isoflurane anesthesia than adults.

6. Anesthesia of mouse pups is tricky at this early age. While pups are more resistant to isoflurane anesthesia, an overdose is lethal. If the pup stirs during the surgery do not hesitate to increase the anesthesia to 5% isoflurane again for few minutes, but reduce to 3–2% once strong anesthesia is re-achieved. The most common cause of pup mortality during injection is an overdose of isoflurane. To avoid this do not maintain 5% isoflurane for too long and visually monitor the pups' respiration rate. Decrease the anesthesia to 3–2% if the diaphragm's movements become intermittent.
7. CB17/SCID mice are immunodeficient, so sterile conditions are recommended to avoid infection.
8. Cut just the flexible part of the tip to control the injection volume. If too much is cut, the orifice diameter will be too large, resulting in a high injection volume so most of the viral solution will leak out and not enter the nerve. If you break the glass needle tip or you cut it too much, remove the viral solution using a fresh microloader tip and a P10 micropipette. Discard the defective glass needle and load another one.
9. It is better to avoid multiple injection sites. If the glass needle bends and doesn't puncture the perineurium, this means the glass needle tip is too flexible. Withdraw the glass needle and cut the tip with small scissors to attain a firmer tip.
10. If no visible flow of virus particles from the glass needle, this means or the glass needle diameter hole is too small, or it is clogged by precipitates in the viral solution or by nerve tissue. First completely withdraw the glass needle from the sciatic nerve and try to reinject at a different site. If it does not work, then cut the tip with small scissors and try again. Finally, load a new glass needle.
11. The histoacryl glue often attracts the interest of the mother. Occasionally the mothers will try to 'clean' the glue away from the wound, which on the rare instance can result in pup mortality. To minimize this risk, always use fresh glue and limit the application to a minimum.
12. Keep enough littermates (injected or not) to occupy the mother. We inject as many as eight pups of the same litters and keep them together. Additionally, some mouse strains display poorer maternal care than others, which can affect the survival of the weakened pups. In this situation, we recommend the use of a lactating foster mother from the SWISS strain.

13. If you obtain a low number of infected cells then the titer of viral particles may be too low. Alternatively, not enough viral particles were injected. During and after injection, monitor the color of sciatic nerve. If an adequate amount of viral solution is injected, the nerve should appear blue. If you use adenoviral vectors, remember that adenoviral infection in an immunocompetent strain will induce the destruction of infected cells. Use a lentiviral vector or an immunodeficient strain. If you obtain cells weakly fluorescent, then the marker protein may be weakly expressed or not stable. Alternatively, fast and robust demyelination induced by the transgene may remove highly fluorescent cells. You can change the marker protein or sacrifice animals earlier to catch healthy fluorescent cells. If infected cells are not fully filled with the marker, animals were sacrificed too early before the marker completely fills the cell. Wait longer before sacrifice.

Acknowledgements

N.T. is grateful for the support of European research council (FP7-IDEAS-ERC 311610) and ATIP-Avenir program. R.F. work was supported by Fondation pour la Recherche Médicale and the Marie-Curie fellowship program. G.H. work has benefited from support by the Labex EpiGenMed.

References

1. Suter U, Scherer SS (2003) Disease mechanisms in inherited neuropathies. Nat Rev Neurosci 4:714–726. https://doi.org/10.1038/nrn1196
2. McGoldrick P, Joyce PI, Fisher EMC, Greensmith L (2013) Rodent models of amyotrophic lateral sclerosis. Biochim Biophys Acta 1832:1421–1436. https://doi.org/10.1016/j.bbadis.2013.03.012
3. Höke A (2012) Animal models of peripheral neuropathies. Neurotherapeutics 9:262–269. https://doi.org/10.1007/s13311-012-0116-y
4. Davey RA, MacLean HE (2006) Current and future approaches using genetically modified mice in endocrine research. Am J Physiol Endocrinol Metab 291:E429. https://doi.org/10.1152/ajpendo.00124.2006
5. Joung JK, Sander JD (2013) TALENs: a widely applicable technology for targeted genome editing. Nat Rev Mol Cell Biol 14:49–55. https://doi.org/10.1038/nrm3486
6. Sung YH, Baek I-J, Seong JK et al (2012) Mouse genetics: catalogue and scissors. BMB Rep 45:686–692
7. Sherman DL, Brophy PJ (2005) Mechanisms of axon ensheathment and myelin growth. Nat Rev Neurosci 6:683–690. https://doi.org/10.1038/nrn1743
8. Viader A, Sasaki Y, Kim S et al (2013) Aberrant Schwann cell lipid metabolism linked to mitochondrial deficits leads to axon degeneration and neuropathy. Neuron 77:886–898. https://doi.org/10.1016/j.neuron.2013.01.012
9. Nave K-A (2010) Myelination and support of axonal integrity by glia. Nature 468:244–252. https://doi.org/10.1038/nature09614
10. Cotter L, Ozçelik M, Jacob C et al (2010) Dlg1-PTEN interaction regulates myelin thickness to prevent damaging peripheral nerve overmyelination. Science 328:1415–1418. https://doi.org/10.1126/science.1187735
11. Ozçelik M, Cotter L, Jacob C et al (2010) Pals1 is a major regulator of the epithelial-like polarization and the extension of the myelin sheath in peripheral nerves. J Neurosci 30:4120–4131. https://doi.org/10.1523/JNEUROSCI.5185-09.2010

12. Fernando RN, Cotter L, Perrin-Tricaud C et al (2016) Optimal myelin elongation relies on YAP activation by axonal growth and inhibition by Crb3/hippo pathway. Nat Commun 7:12186. https://doi.org/10.1038/ncomms12186
13. Perrin-Tricaud C, Rutishauser U, Tricaud N (2007) P120 catenin is required for thickening of Schwann cell myelin. Mol Cell Neurosci 35:120–129. https://doi.org/10.1016/j.mcn.2007.02.010
14. Tricaud N, Perrin-Tricaud C, Brusés JL, Rutishauser U (2005) Adherens junctions in myelinating Schwann cells stabilize Schmidt-Lanterman incisures via recruitment of p120 catenin to E-cadherin. J Neurosci 25:3259–3269. https://doi.org/10.1523/JNEUROSCI.5168-04.2005
15. Glatzel M, Flechsig E, Navarro B et al (2000) Adenoviral and adeno-associated viral transfer of genes to the peripheral nervous system. Proc Natl Acad Sci U S A 97:442–447
16. Guénard V, Schweitzer B, Flechsig E et al (1999) Effective gene transfer of lacZ and P0 into Schwann cells of P0-deficient mice. Glia 25:165–178
17. He T-C, Zhou S, da Costa LT et al (1998) A simplified system for generating recombinant adenoviruses. Proc Natl Acad Sci 95:2509–2514

Chapter 10) Discussion

Combining the data of different experiments and projects, I propose an attempt to create a model of the axon metabolism and axonal mitochondria physiology in normal and in some disease conditions. In addition, I would like to illustrate how its metabolism and energy production changes in response to different stimuli.

10.1 Energy production in peripheral nerves

The production of energy in the form of ATP is essential for healthy axonal physiology. Indeed, axons have to regenerate and propagate action potentials all along their length and they act as a major trafficking highway for mitochondria and vesicles between the cell body and the presynaptic terminals. However, axons are very fine structures (up to 2-3µm) compared to a full cell (more than 20µm usually), isolated in middle of the nervous system, so finding and storing metabolic resources may be difficult. Indeed CNS axons are known to be unable to store glucose, such as glycogen.
So where do those metabolites come from? Also, what happens to the neuron when metabolites are scarce? We have shown that myelinating Schwann cells shift from a PKM1 driven mitochondrial respiration metabolic state to a PKM2 aerobic glycolysis metabolic state when they enter a mature state, maintaining myelin and nurturing axons. When PKM2, the enzyme that favors lactate instead of pyruvate as glycolysis end product, is knocked down in Schwann cells, the Warburg effect is suppressed and pyruvate, which remains the sole glycolysis end product, is only used for oxidative phosphorylation. As a consequence, less lactate is produced by mSC. This leads to an abnormal metabolism in axons. Indeed, the cytosolic content of lactate decreases in axons upon successive stimulations of the nerve, indicating that the lactate that is used during the firing of action potentials is not replenished in absence of the Warburg effect in Schwann cells. Meanwhile, cytosolic glucose is recruited as an alternative energy source, but this is not sufficient to allow the upregulation of mitochondrial ATP production. As a result, oxidative phosphorylation is affected as we have shown by decreased ATP production in axonal mitochondria of PKM2 knockout mice.

What are the functional consequences of this glial lactate-starvation metabolism in the axon? The abnormal axonal metabolism and decreased ATP production by axonal mitochondria result in the development of motor problems over time. These motor problems are not the result of impaired myelin function as shown by normal nerve conduction velocity, but rather due to impaired neuronal function. This result was verified using DCA to decrease the levels of lactate even further. We showed that addition of DCA results in a drop of motor performance in both PKM2 mutants and controls due to a global shortage of lactate, but controls were able to recover motor performance after halting DCA administration, whereas mutants could not. This result indicates that motor performance is indeed dependent on Schwann cell lactate production through Warburg effect.
The glial lactate-starvation axonal metabolism causes impaired motor performance, but how exactly? While we could not detect any significant change in the propagation of action potentials, We found that the nerve endings retracted in PKM2 knockout mice, indicating that the maintenance of nerve endings at the neuromuscular junction is impaired. In addition we show an increased percentage of motorneurons showing caspase 3 expression, indicating they experience stress. Finally, the transport of mitochondria along the axon was also affected as more mitochondria were found to be stuck in mutant mice axons.

This represents the first confirmation that lactate shuttle is also essential in the PNS to provide SC lactate to the myelinated axons. Indeed so far only the expression of MCT transport has

been reported to support this theory in the PNS. In addition, this work provides the first demonstration of the existence of an aerobic glycolysis metabolism in a glial cell that supports axonal function. Indeed, while several indications exist that astrocytes and oligodendrocytes are glycolytic cells, suggesting they may use Warburg effect, we show here that PKM2, the enzyme required to produce Warburg effect, is expressed in mature mSC and is required there for the maintenance of functional axons in the PNS. This discovery has several implications for the understanding of the PNS biology and by extrapolation of the CNS. Indeed the Warburg effect may be a useful target for therapeutic strategies against PNS and CNS diseases, especially in neurodegenerative diseases in which cell fate is determined by pro-survival and apoptotic signals. Stimulating the Warburg effect and the subsequent delivery of lactate to the axon could be a strong pro-survival signal, which could prevent neurodegeneration.

10.2 The environment changes the metabolic rate of mitochondria

So we showed that ATP production by axonal mitochondria relies on the production and transport of lactate by Schwann cells. This indicates that axonal mitochondria activity is regulated by external and eventually internal stimuli. By extension we also reasoned that reactive oxygen species produced by active mitochondria as the other product of oxidative phosphorylation could also be influenced by these stimuli.

For a long time, mitochondria at the nodes of Ranvier were supposed to be more active based on structural differences observed between internodal and nodal mitochondria and on the important role of ATP in the maintenance of the action potential propagation process that occurs at the node. However, as no one had ever seen ATP production in these mitochondria, this remained merely an assumption. We looked at the production of ATP in axonal mitochondria and compared different spatial locations of these mitochondria within the axon of the same neuron. We found that the location of mitochondria changes the intrinsic ATP and ROS production. Mitochondria that are located in the node of Ranvier, an area where the axon is not myelinated, is rich in ion channels and where the electric signal of action potentials are reinitiated, produce more ATP and ROS than in mitochondria located in the internodes. This observation suggests that these mitochondria are intrinsically more active, possibly because the need for ATP is higher in this region. Why the energy need in nodes of Ranvier is higher than in internodes is not clear yet. Nodes of Ranvier are rich in voltage gated ion channels, but these channels do not require ATP. Na^+/K^+ ATPase activity does require ATP, but whether Na^+/K^+ ATPase is enriched in the node of Ranvier is under debate. Another hypothesis is that in nodes of Ranvier more ATP is used for calcium buffering by the ATP-utilizing calcium pump SERCA of the endoplasmic reticulum.

Then, what happens to ATP production by axonal mitochondria when the axon is active and conducts action potentials? We showed that after multiple successive periods of induced action potentials, mitochondria upregulate their ATP production. Likely, this upregulation of ATP production is an adaptation to an increased energy dependency of the axon during action potential firing. However, the upregulation of ATP is not limited to mitochondria located in the nodes of Ranvier, which shows that action potential firing has an effect on mitochondria in internodes as well.

In addition to increased ATP production, mitochondrial ROS production increases for a short period of time after each period of induced action potential firing. Naturally, these ROS are the byproducts of ATP production as it immediately precedes the increase in mitochondrial ATP. However, because ROS have signaling effects, these increase of ROS levels potentially

results in downstream effects. For example, ROS levels have an influence on gene expression. However, the mitochondria in our model are located in the axon, thus far away from the nuclear DNA that is in the cell body. Therefore, the effect of ROS produced by axonal mitochondria on neuronal gene expression in neurons is nihil. The signaling roles of ROS more probably influence local proteins activity. The elevated ROS levels may as well have signaling effects on Schwann cells, because of the close physical interaction they have with the axons.

While mitochondrial activity increases, they also slow down. This docking of axonal mitochondria may be the result of ROS signaling, because the motor protein KIF5 is sensitive to ROS levels and therefore, elevated ROS levels can cause a disconnect of mitochondria from the microtubule. In parallel, neuronal firing causes an influx of calcium into the cytosol though voltage-dependent Ca^{2+} channels. These calcium ions interact with Miro, hence causing the docking of mitochondria. Possibly, mitochondria halt their migration to replenish cytosolic ATP locally.

Our results show that indeed mitochondrial physiology is influenced by multiple stimuli such as spatial differences and nerve activity. However, the levels of ATP and ROS, the two main products of mitochondria, are influenced in an independent matter. Whereas ROS production shows spikes, the increase in ATP production happens gradually, showing that the dynamics between ATP and ROS levels are not the same. Since mitochondrial ROS production is the result of proton translocation by the electron transport chain, this implies that a formation of a stronger proton gradient precedes increased ATP production. Furthermore, the level of H_2O_2 is not elevated any longer once ATP production is upregulated, probably because the antioxidant defenses that are present inside mitochondria are sufficient to adapt to elevated ROS levels and reduce those levels quickly. Together, these results show that the level of ROS cannot simply be extrapolated from the amount of ATP produced or vice versa. The model of mitochondrial physiology is more complex than often is assumed.

10.3 Axonal mitochondria in pathological conditions

So mitochondria can change their ATP production depending on their location or on nerve activity. Moreover, this increase of ATP production is without too many negative ramifications for we showed that ROS levels are increased for only a very short period of time. However, pathologic conditions change the healthy adaptation of mitochondria to physiological stimuli.

Deficient mitofusin 2, a protein involved in mitochondrial fusion, results in CMT2A or CMT6A disease, which characterized by motor and sensory deficits. We have shown that in mice the morphology of these fusion-deficient mitochondria changes: they are shorter in length and abnormally clustered in peripheral nerve axons. MFN2 deficient mitochondria also show decreased transport velocity. This may be the result of MFN2 no longer interacting with the Miro-Milton complex, the main protein complex that connects mitochondria to the cytoskeleton. Now, we have shown how this altered morphology correlates with pathologic physiology too. First, we have demonstrated that the contact area of MFN2 mutant mitochondria with the endoplasmic reticulum becomes impaired, which may result in decreased transport of calcium from the ER to mitochondria. Since calcium is a co-factor for oxidative phosphorylation, decreased calcium transport may cause impaired mitochondrial ATP production. Indeed, MFN2 mutant mitochondria fail to upregulate ATP production upon action potentials, even though basal ATP levels are the same. Interestingly, MFN2 mutations

have critical consequences for ROS production too. The upregulation of ROS was delayed compared to littermates that did not express the MFN2 mutation, but elevated levels of ROS were maintained in mitochondria for a longer period of time, probably resulting in increased oxidative stress. In short, mitochondrial ATP levels were maintained while ROS levels soared. This shows that the MFN2 mutation causes a pathological decoupling of ATP and ROS production. These results also imply that mitochondrial shape correlates with mitochondrial physiology.
Even though we show that MFN2 mutations affect the contact between mitochondria and ER, mitochondrial shape, transport and physiology in peripheral axons, these data do not prove a causal relationship between ER-mitochondria contact and mitochondrial physiology. Possibly, the observed changes are independent effects of the MFN2 mutation.

A second pathological condition was mimicked through the induction of demyelination. This mimics multiple sclerosis and CMT1 pathology that affects the myelin sheath around axons in the CNS and PNS respectively. In this condition, ATP decreased and ROS production increased. This decoupling of ATP production and ROS production suggests or that mitochondrial ETC complexes are more active, the ETC complexes produce more ROS or the antioxidant defense are less efficient.

In first hypothesis, as increased ROS production does not correlate with more ATP production, this suggests that protons reenter the mitochondrial matrix without driving ATP production by passing through ATP synthase. Such a mechanism has been shown in particular conditions where the goal of mitochondrial activity is to produce heat. Uncoupling proteins such as UCP2 permeabilize the inner mitochondrial membrane to dissipate the proton gradient, without the production of ATP molecules. In the second hypothesis is the rate of proton translocation normal or lower, but the percentage of electrons that leak back into the matrix and form ROS is higher, possibly via reverse electron transport. This reverse electron transport could be the result of altered metabolism, because the lactate shuttle becomes impaired due to the reduced connection between mSC and axon. Mitochondrial physiology would then resemble the mice with an impaired Warburg effect. Indeed both models showed a decreased ATP production by axonal mitochondria. Unfortunately we did not check the production of ROS in PKM2 knockout mice. In the third hypothesis, an increased ROS production is the result of a less efficient antioxidant defense. Indeed, myelin has antioxidant capacities, but an absence of this antioxidant defense should not affect the antioxidant capacity within mitochondria, which is where we measured the ROS levels. Nonetheless, decreased SOD levels have been measured in demyelinating disorders and SOD2 may even switch into a pro-oxidant in manganese deprived conditions.

Taken together our combined data show that the presence of a myelin sheath is an essential factor that determines the function of axonal physiology and mitochondria. Indeed, a healthy myelin sheath allows for neuronal maintenance and salutatory conduction, while it regulates mitochondrial activity.

10.4 Perspectives to neuropathies

In order to find a solution for diseases that involve an impaired function of the nervous system, a better understanding of the dynamics between ATP and ROS production is lacking. In the model that I lay out in this thesis, we show that interaction between cell types is an important factor in neuronal function, and these interactions between cell types have often been overlooked or ignored.

Indeed, the role of the Warburg effect in the nervous system has never been directly investigated and its role in the development of neurodegenerative diseases is a research field that is practically untouched. In addition, the interaction between myelinating cells and axons has widespread downstream consequences, as observed with the change in mitochondrial physiology in axons and the subsequent behavioral defects.

Secondly, for future research it should be understood that the physiology of axonal and, by extrapolation, neuronal mitochondria is highly sensitive to their environment and since alterations in their ROS and ATP production have such widespread impact on neuronal function, mitochondria play without a doubt a central role in the development or progression of symptoms of many neuropathies of the PNS.

Furthermore, we showed that mitochondrial function is not as static as often is assumed. In many research projects, either ROS or ATP is measured, but detection of both ATP and ROS in the same experimental setup is seldom. Generally, ROS has been considered as a by-product of ATP production and it is assumed that ROS levels always increase when ATP production is upregulated. We demonstrated that this common assumption is much too reductive. When these ATP and ROS productions become decoupled, this may have critical consequences for the development of neuropathies.

Taken together I strongly believe our experiments and results provide a next big step towards a better understanding of the peripheral nervous system in health and disease.

Conclusion

In the presented research, I provided a dynamic mechanism how the peripheral nerve axons function and how axons work together with neighboring cell types such as Schwann cells, with a focus on mitochondria.

A key element in axons is energy, because all the major axonal cellular processes require energy, especially the continuous depolarization and repolarization of the neuronal membrane and organelles trafficking. This energy is produced in the form of ATP and it is likely that energy cannot efficiently be stored in axons (under a glycogen form for example) due to the lack of space eventually. In addition, the scarcity of space probably result in the production of energy in active axons having negative consequences: the production of reactive oxygen species, which are eager to react with the molecules in their environment and cause damage.

As a consequence, complex pathways regulate ATP and ROS production in axons. First, the correlation between mitochondrial shape and mitochondrial function is revealed when mitochondrial shape is abnormal. I used a model in which mitochondria are unable to fuse due to mutations in MFN2 genes, resulting in an abnormal shape, because mitochondria are decreased in length. I have shown that these abnormally shaped mitochondria also differ in their production of ATP and ROS and in the function of MAMs, although the nerve needs to be challenged first.

The second factor influencing mitochondrial function is the intracellular environment. We show that upon nerve stimulation, mitochondria are able to upregulate ATP production. Meanwhile ROS production also increases but with a different dynamic: a spike in ROS production just before a gradual ATP increase. This suggests that the concentration of antioxidant enzymes is an important factor in the pathway of mitochondrial bioenergetics. Next to the interplay between ATP production and ROS production, the interplay between mitochondria and other organelles appears to be another factor in mitochondrial physiology. Through MAM, calcium may enter mitochondria from the endoplasmic reticulum, which changes enzymatic activity in oxidative phosphorylation.

The presence of metabolites in the axonal cytoplasm involves a third type of interplay being the influence of other cell types. Especially mSCs appeared to have a major effect on mitochondrial physiology in the axon. Indeed, first they use the Warburg effect to produce more lactate, which is then transported into the neuron through MCT transporters via the lactate shuttle. Additionally, mSCs produce a myelin sheath, which presence strongly influences axonal mitochondrial function. Mitochondria in regions where the axon is not myelinated produce more ATP and more ROS. Moreover, pathological myelin loss results in decreased ATP production and elevated levels of ROS.

Factors that determine axonal function often involve counterparts that influence each other: ATP with ROS, axon with Schwann cell, endoplasmic reticulum with mitochondrion, oxidative phosphorylation with glycolysis, ATP synthase with uncoupling proteins, glucose with lactate, node of Ranvier with internode. These counterparts allow an energy-efficient function of the nerve and enable adaptation to changing environments to a certain extent.

In conclusion, mitochondria are dynamic organelles that are sensitive to their environment and respond accordingly by changing its physiology. This is essential when mitochondria need to adapt to changing environments, such as action potential firing. However, pathologic

stimuli can result in mitochondria that work in disbalance. Unbalanced mitochondria physiology can have disastrous effects for the nerve, because ROS are often damaging for cell components and enough ATP production is essential for axonal function. These malfunctioning mitochondria may be central players in developing symptoms of neurodegenerative diseases, such as multiple sclerosis, CMT2A, Alzheimer disease or Parkinson's.

In this thesis, I elaborated a model for ATP and ROS production by axonal mitochondria in vivo. To sum up this model, the following statements reflect the original discoveries from my research:

- The Warburg effect in Schwann cells is essential for healthy axonal metabolism and ATP production in mitochondria (1).
- Blocking the Warburg effect affects neuronal physiology characterized by decreased synaptic contact at the neuromuscular junction and increased cellular stress in motor neurons (2).
- Blocking the Warburg effect causes motor problems caused by neuronal failure, but not Schwann cell or myelin sheath deficiencies (3).
- Demyelination results in a pathologic decoupling of ATP and ROS production by axonal mitochondria (4).
- Following induced action potentials, mitochondrial ATP and ROS production increase, but with separate dynamics (5).
- Mitochondria located in the node of Ranvier intrinsically are more active than mitochondria located in internodes (6).
- Mitofusin2-deficient neurons show mitochondria with a different morphology in vivo, together with an affected transport (7).
- Mitofusin2-deficient motorneurons show shorter dendritic length (8).
- Mitofusin2-deficient neurons show decreased contact area between endoplasmic reticulum and mitochondria (9).
- Mitofusin2-deficient mitochondria do not produce altered levels of ATP or ROS in rest, but in active nerves, affected mitochondrial physiology is revealed (10).

In conclusion, mitochondrial physiology within myelinated axons is an energetic interplay involving a multitude of counterparts.

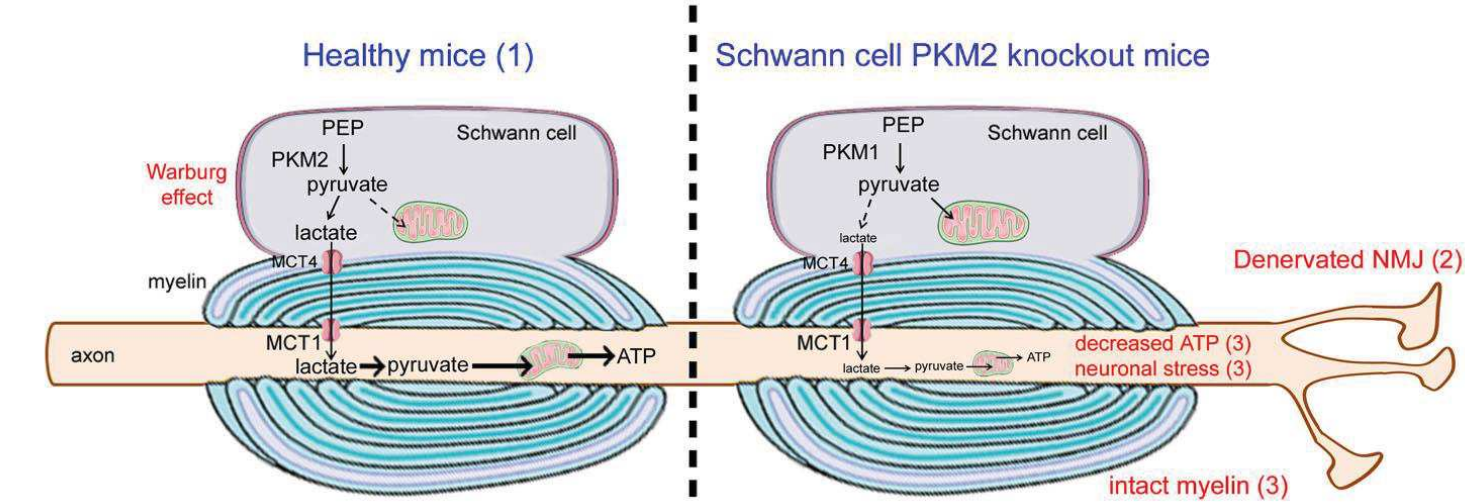
Healthy mice (1)
Schwann cell PKM2 knockout mice
PEP
Schwann cell
PKM2
pyruvate
lactate
Warburg effect
myelin
MCT4
MCT1
axon
lactate
pyruvate
ATP
PKM1
Denervated NMJ (2)
decreased ATP (3)
neuronal stress (3)
intact myelin (3)

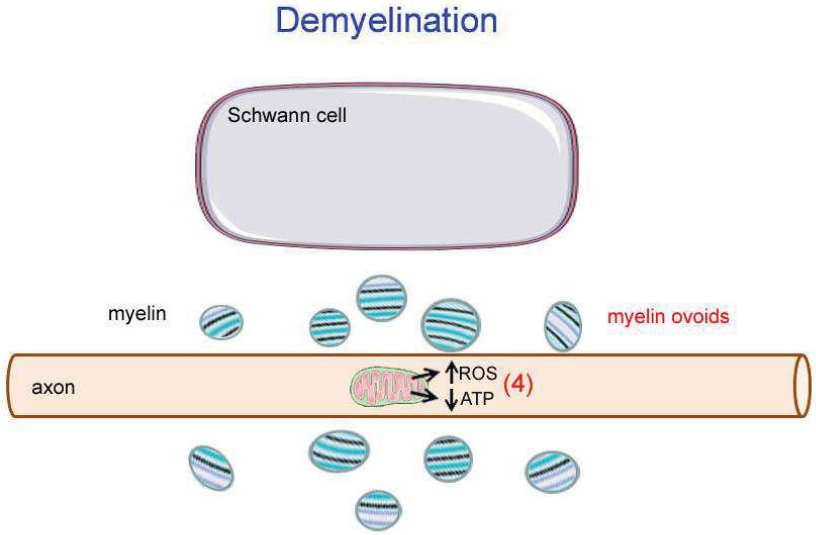
Demyelination
Schwann cell
myelin
myelin ovoids
axon
ROS
ATP
(4)

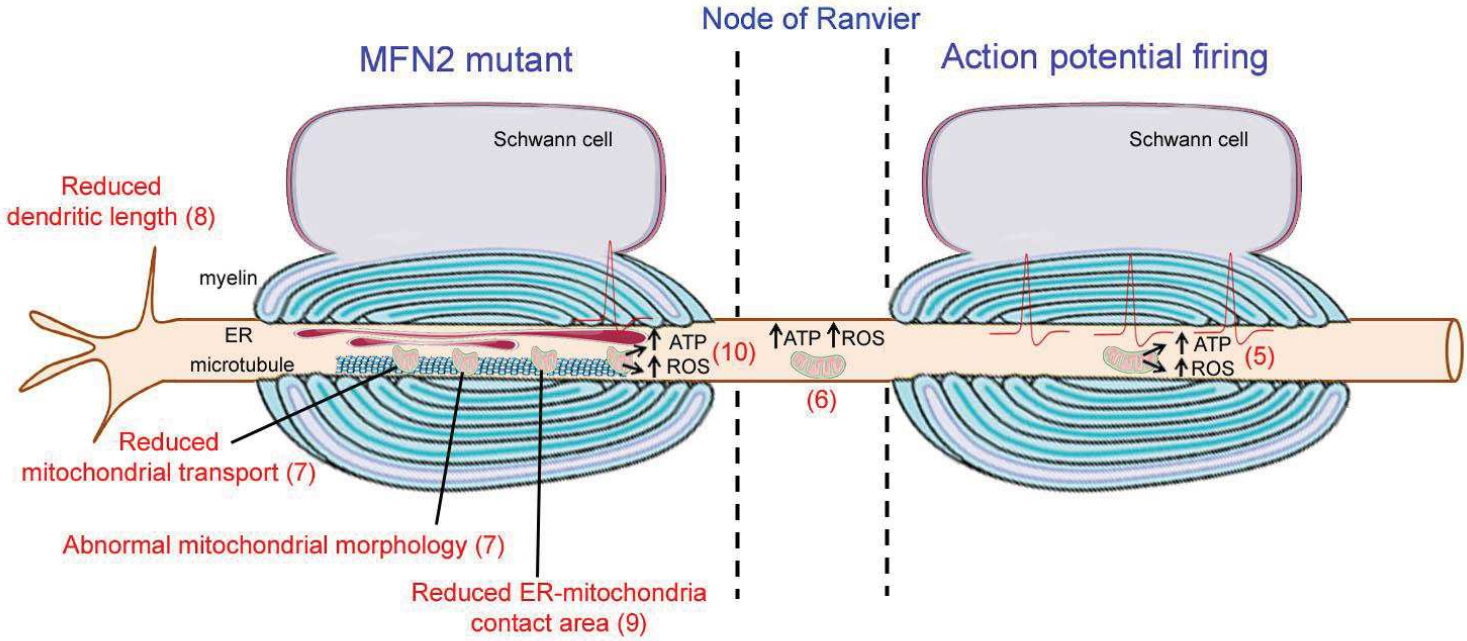
Node of Ranvier
MFN2 mutant
Action potential firing
Schwann cell
Reduced dendritic length (8)
myelin
ER
microtubule
ATP
ROS
(10)
ATP ROS
(6)
(5)
Reduced mitochondrial transport (7)
Abnormal mitochondrial morphology (7)
Reduced ER-mitochondria contact area (9)

Acknowledgements

To every single person who has helped me during my time in Montpellier, helped preparing me in the years before arriving in France, I would like to say:

THANK YOU!

First, I'd like to thank my promoter Dr. Nicolas Tricaud, who has helped me over the whole process of the project. The project that was initially designed looked very different than what is the end result here before you. These changes in direction were based on unexpected results that often arise in challenging projects like these. Thanks to the guidance of Dr. Tricaud, I was able to continue the project by trying to answer our research questions in a different way or pursue more important or more interesting hypotheses. Also he has shown me how to anticipate multiple results and how to respond accordingly. Finally, thanks to him I was able to improve my scientific writing enormously.

Also the other members of team 6, past or present, I would like to thank for their help with my work, especially Marie Deck and Graham Campbell, who have seen the development of this project closely and were able to give me countless technical or theoretical advice. I thank Benoit Gautier for his training in several experimental techniques and help with the presentation of my data. Thanks to Jade Berthelot for her help within the lab and for all her French lessons. I will never forget the difference between un moule and une moule! Hélène, with whom I have shared the PhD experience in parallel, Scarlette Abbou and Elisa Gonzalez are to be thanked for the help with several experiments as well. Furthermore, I would like Jerôme Devaux and Heather Richardson for their advice and for our interesting discussions. Also I would like thank Mallory Poncelet, Alise Lattard, Sophie Guelfie, Sergio Gonzalez, Aymeline Staigre and Jérémie El Bechir, and in particular Liz Tavares, for the comments during lab meetings and for the good vibes both in the lab and outside.

However, research cannot be possible without the support from the platforms. I would like to thank the employees from the animal facility platform for taking good care of the mice, especially Laura Cerramon and Jerôme Sarniguet. Also, the help from Hassan Boukhaddaoui from the imaging platform was essential for the use of the multiphoton microscope.

My work was also highly influenced by the advice that I got from the weekly joint-meetings with the Jeanneteau lab from the IGF. Freddy Jeanneteau, Marga Arango-Lievano, Amelie Borie and Yann Dromard: thank you for this. Other guidance from external advisors showed to be key moments to push the projects to a next phase. For this, great thanks to Marie-Luce Vignais, Benedicte Dargent, Roman Chrast and Nathalie and Bernard-Marissal.

But also the (mental) support of the other people working at the INM was very much appreciated, especially the other researchers working on the first floor. Pascalle Bomont, Karolina Campbell, Zoe Geraghty, Léa Lescouzères, Aurora Scrivo, Simona Torriano, Mikhaela Diakitou, Gregor Dubois, Viki Kalatzis, Carla Sanjurjo-Sorriano, Nejla Erkilic and Dasha Mamaeva, thank you for the good atmosphere. Special thanks to Laura Dumas for her corrections in my French writing.

Next to people that supported me with my science, I also would like to thank a group of people that made sure I had a great time during my stay in Montpellier. First, Hannah Emlein from Labex EpiGenMed. Also Leentje den Ceuninck, Alexandra Miliu, Ksenia Semenovskaya and Annika Urbanek. I want to thank my team mates from M.A.R.C.

Montpellier as well for the countless good times at Stade Philippides, but also other (running) events around Montpellier and even as far as Edinburgh: Alexis Aufore, Mathieu Brydniak, Marion Béchard, Jean-Michel Blenet, Gabriël Carvalho, Remy Choquet, Odile Conrardy, Guilhem Debarros, Joao Ferreira, Tom Gaudy, Catherine Grimal, Jean-Pierre Grimal, Manon Grimal, Lorna Handley, Jeff Holley, Sophie Imus, Julien Jeanjean, Julie Jerome, Raphael Lamiral, Gabriël Lecat, Marie Loury, Atica Mamoudi, Jennifer Mercier, Sophie Noel, Franc Puyoo, Florie Seznec, Zaina Tazeroualti, Sylvain Téchené and le coach Jean-Luc.

My stay in Montpellier would not have been possible without the people that taught me the necessary skills in preparation of becoming a PhD student. My stay Coleman lab at Sun City, Arizona was a very influential period in my life and for that I want to thank Dr. Paul Coleman, Diego Mastroeni, Elaine Delvaux, Jennifer Nolz, Amanda Lewis and Yuyan Tan. Also former supervisors at Maastricht University had played a crucial role, especially Daniël van den Hove, Jos Prickaerts and Guido Haenen.

Special thanks to my dearest friends during the Research Master at Maastricht, Netherlands. Artemis Iatrou, Koen Meuwissen, Dila Suay and Britt van Hagen: the saying out of sight, out of mind definitely does not apply to you guys!

Finally, I want to thank the homefront, my family. Wim van Hameren, Paul van Hameren, Henriëtte van Hameren and Wim van der Linden: Thank you for everything. Also thanks to the developers of Skype and Whatsapp for making regular contact with them possible.

References

1. Gray, M. W. Mitochondrial Evolution. *Cold Spring Harb Perspect Biol* a011403 (2012).
2. Koonin, E. V. The origin and early evolution of eukaryotes in the light of phylogenomics. *Genome Biology* 209 (2010).
3. Martin, W. & Müller, M. The hydrogen hypothesis for the first eukaryote. *Nature* 37–41 (1998).
4. Calvo, S. E. & Mootha, V. K. The Mitochondrial Proteome and Human Disease. *Annu Rev Genomics Hum Genet.* 25–44 (2010).
5. Baker, M. J., Frazier, A. E., Gulbis, J. M. & Ryan, M. T. Mitochondrial protein-import machinery: correlating structure with function. *TRENDS in Cell Biology* 456–464 (2007).
6. Li, X., Fang, P., Mai, J., Choi, E. T. & Yang, X.-F. Targeting mitochondrial reactive oxygen species as novel therapy for inflammatory diseases and cancers. *Journal of Hematology & Oncology* 19 (2013).
7. Perkins, G. A. & Ellisman, M. H. Mitochondrial Configurations in Peripheral Nerve Suggest Differential ATP Production. *Journal of structural biology* **173**, 117–127 (2011).
8. Aufschaiter, A., Kohler, V., Diessl, J. & Büttner, S. Mitochondrial lipids in neurodegeneration. *Cell Tissue Res* 125–140 (2017).
9. Seo, A., Joseph, A., Dutta, D. & Leeuwenburgh, C. New insights into the role of mitochondria in aging: mitochondrial dynamics and more. *J Cell Sci.* 2533–42 (2010).
10. Pareyson, D., Saveri, P., Sagnelli, A. & Piscosquito, G. Mitochondrial dynamics and inherited peripheral nerve diseases. *Neuroscience Letters* 66–77 (2015).
11. Benard, G. & Karbowski, M. Mitochondrial fusion and division: regulation and role in cell viability. *Semin Cell Dev Biol.* 365–374 (2009).

12. Lee, H.-C. & Wei, Y.-H. Mitochondrial biogenesis and mitochondrial DNA maintenance of mammalian cells under oxidative stress. *The International Journal of Biochemistry & Cell Biology* 822–834 (2005).
13. St-Pierre, J., Drori, S., Uldry, M. & Spiegelman, B. Suppression of reactive oxygen species and neurodegeneration by the PGC-1 transcriptional coactivators. *Cell* 397–408 (2006).
14. Yoboue, E. D. & Devin, A. Reactive Oxygen Species-Mediated Control of Mitochondrial Biogenesis. *International Journal of Cell Biology* 403870 (2012).
15. Jornayvaz, F. R. & Shulman, G. I. Regulation of mitochondrial biogenesis. *Essays Biochem.* 69–84 (2010).
16. Shadel, G. & Clayton, D. Mitochondrial DNA maintenance in vertebrates. *Annu Rev Biochem.* 409–35 (1997).
17. Chen, H., Vermulst, M., Wang, Y. E. & Chan, D. C. Mitochondrial fusion is required for mtDNA stability in skeletal muscle and tolerance of mtDNA mutations. *Cell* 280–289 (2010).
18. Mathur, D., Lopez-Rodas, G., Casanova, B. & Burgal Marti, M. Perturbed Glucose Metabolism: Insights into Multiple Sclerosis Pathogenesis. *Front Neurol.* 250 (2014).
19. Li, X., Gu, J. & Zhou, Q. Review of aerobic glycolysis and its key enzymes – new targets for lung cancer therapy. *Thoracic Cancer* 17–24 (2015).
20. Castro, M. A., Beltran, F. A., Brauchi, S. & Concha, I. I. A metabolic switch in brain: glucose and lactate metabolism by ascorbic acid. *Journal of Neurochemistry* 423–440 (2009).
21. Lowry, O., Passonneau, J., Hasselberger, F. & Schulz, D. Effect of Ischemia on Known Substrates and Cofactors of the Glycolytic Pathway in Brain. *Journal of Biological Chemistry* 18–30 (1964).

22. Casson, R. J., Wood, J. P. M., Han, G. & Chidlow, G. M-Type Pyruvate Kinase Isoforms and Lactate Dehydrogenase A in the Mammalian Retina: Metabolic Implications. *Invest Ophthalmol Vis Sci.* 66–80 (2016).
23. Dong, G., Mao, Q. & Jiang, F. PKM2 and cancer: The function of PKM2 beyond glycolysis. *Oncology letters* 1980–1986 (2016).
24. Liemburg‐Apers, D. C., Willems, P. H. G. M. & Koopman, W. J. H. Interactions between mitochondrial reactive oxygen species and cellular glucose metabolism. *Arch Toxicol* 1209–1226 (2015).
25. Osellame, L. D., Blacker, T. S. & Duchen, M. R. Cellular and molecular mechanisms of mitochondrial function. *Best Practice & Research Clinical Endocrinology & Metabolism* 711–723 (2012).
26. Mailloux, R. J., Bériault, R. & Appanna, V. D. The Tricarboxylic Acid Cycle, an Ancient Metabolic Network with a Novel Twist. *PLoS ONE* e690 (2007).
27. Nijland, P. G., Molenaar, R. J., Van der Pol, S. M. A. & Van Horssen, J. Differential expression of glucosemetabolizing enzymes in multiple sclerosis lesions. *Acta Neuropathologica Communications* 79 (2015).
28. Mullarky, E. & Cantley, L. C. Innovative Medicine. in *Diverting Glycolysis to Combat Oxidative Stress* 3–23 (Nakao K., Minato N., Uemoto S., 2015).
29. Pierce, J. T. & Phypers, B. Lactate physiology in health and disease. *Continuing Education in Anaesthesia Critical Care & Pain* **6**, 128–132 (2006).
30. Gray, L. R., Tompkins, S. C. & Taylor, E. B. Regulation of pyruvate metabolism and human disease. *Cellular and molecular life sciences : CMLS* **71**, 2577–2604 (2014).
31. Warburg, O., Wind, F. & Negelein, E. THE METABOLISM OF TUMORS IN THE BODY. *The Journal of general physiology* **8**, 519–530 (1927).

32. Potter, M., Newport, E. & Morten, K. J. The Warburg effect: 80 years on. *Biochemical Society transactions* **44**, 1499–1505 (2016).

33. Liberti, M. V. & Locasale, J. W. The Warburg Effect: How Does it Benefit Cancer Cells? *Trends in Biochemical Sciences* **41**, 211–218 (2016).

34. DeBerardinis, R. J., Lum, J. J., Hatzivassiliou, G. & Thompson, C. B. The Biology of Cancer: Metabolic Reprogramming Fuels Cell Growth and Proliferation. *Cell Metabolism* **7**, 11–20 (2008).

35. Estrella, V. *et al.* Acidity Generated by the Tumor Microenvironment Drives Local Invasion. *Cancer Res* **73**, 1524 (2013).

36. Sun, Q. *et al.* Mammalian target of rapamycin up-regulation of pyruvate kinase isoenzyme type M2 is critical for aerobic glycolysis and tumor growth. *Proc Natl Acad Sci USA* **108**, 4129 (2011).

37. Christofk, H. R. *et al.* The M2 splice isoform of pyruvate kinase is important for cancer metabolism and tumour growth. *Nature* **452**, 230 (2008).

38. Murphy, M. P. How mitochondria produce reactive oxygen species. *Biochem. J.* 1–13 (2009).

39. Schägger, H. & Pfeiffer, K. The Ratio of Oxidative Phosphorylation Complexes I–V in Bovine Heart Mitochondria and the Composition of Respiratory Chain Supercomplexes. *Journal of Biological Chemistry* 37861–37867 (2001).

40. Bianchi, C., Genova, M. L., Castelli, G. P. & Lenaz, G. The Mitochondrial Respiratory Chain Is Partially Organized in a Supercomplex Assembly. *Journal of Biological Chemistry* 36562–36569 (2004).

41. Lopez-Fabuel, I., Le Douce, J., Logan, A. & Bolanos, J. P. Complex I assembly into supercomplexes determines differential mitochondrial ROS production in neurons and astrocytes. *PNAS* 13063–13068 (2016).

42. Runswick, M. J., Bason, J. V., Montgomery, M. G. & Walker, J. E. The affinity purification and characterization of ATP synthase complexes from mitochondria. *Open Bio* 120160 (2013).

43. Walker, J. E. ATP Synthesis by Rotary Catalysis. *Angew. Chem. Int. Ed.* 2308–2319 (1998).

44. Zhou, Z. D. & Tan, E.-T. Iron regulatory protein (IRP)-iron responsive element (IRE) signaling pathway in human neurodegenerative diseases. *Molecular Neurodegeneration* 75 (2017).

45. Horowitz, M. P. & Greenamyre, J. T. Mitochondrial Iron Metabolism and Its Role in Neurodegeneration. *J Alzheimers Dis* S551–S568 (2010).

46. Poulos, T. Heme Enzyme Structure and Function. *Chem Rev.* 3919–3962 (2014).

47. Ajioka, R. S., Phillips, J. D. & Kushner, J. P. Biosynthesis of heme in mammals. *Biochimica et Biophysica Acta (BBA) - Molecular Cell Research* 723–736 (2006).

48. Brookes, P. S., Yoon, Y., Robotham, J. L. & Sheu, S.-S. Calcium, ATP, and ROS: a mitochondrial love-hate triangle. *Am J Physiol Cell Physiol* C817–C833 (2004).

49. McCormack, J. & Denton, R. Mitochondrial Ca2+ transport and the role of intramitochondrial Ca2+ in the regulation of energy metabolism. *Dev Neurosci.* 165–73 (1993).

50. Das, A. & Harris, D. Control of mitochondrial ATP synthase in heart cells: inactive to active transitions caused by beating or positive inotropic agents. *Cardiovasc Res.* 411–7 (1990).

51. Wernette, M. E., Ochs, R. S. & Lardy, H. A. Ca2* Stimulation of Rat Liver Mitochondrial Glycerophosphate Dehydrogenase. *Journal of Biological Chemistry* 12767–12771 (1981).

52. Mildaziene, V., Baniene, R., Nauciene, Z. & Kolodenko, B. N. Calcium indirectly increases the control exerted by the adenine nucleotide translocator over 2-oxoglutarate oxidation in rat heart mitochondria. *Arch Biochem Biophys.* 130–4 (1995).

53. Williams, G., Boyman, L. & Lederer, W. Mitochondrial calcium uptake. *PNAS* 10479–10486 (2013).

54. Simmen, T., Lynes, E. M., Gesson, K. & Thomas, G. Oxidative protein folding in the endoplasmic reticulum: Tight links to the mitochondria-associated membrane (MAM). *Biochimica et Biophysica Acta* 1465–1473 (2010).

55. Hedskog, L., Moreira Pinho, C., Filadi, R. & Ankarcrona, M. Modulation of the endoplasmic reticulum– mitochondria interface in Alzheimer's disease and related models. *PNAS* 7916–7921 (2013).

56. Court, F. A. & Coleman, M. P. Mitochondria as a central sensor for axonal degenerative stimuli. *Trends in Neurosciences* 364–372 (2012).

57. Hunter, D. & Haworth, H. The Ca2+-induced membrane transition in mitochondria. II. Nature of the Ca2+ trigger site. *Arch Biochem Biophys* 460–467 (1979).

58. Brini, M., Cali, T., Ottolini, D. & Carafoli, E. Neuronal calcium signaling: function and dysfunction. *Cellular and Molecular Life Sciences* 2787–2814 (2014).

59. Pawlowski, J. & Kraft, A. S. Bax-induced apoptotic cell death. *Proceedings of the National Academy of Sciences* **97**, 529–531 (2000).

60. Beckhauser, T. F., Francis-Oliveira, J. & De Pasquale, R. Reactive Oxygen Species: Physiological and Physiopathological Effects on Synaptic Plasticity. *Journal of Experimental Neuroscience* 23–48 (2016).

61. Lubos, E., Loscalzo, J. & Handy, D. E. Glutathione Peroxidase-1 in Health and Disease: From Molecular Mechanisms to Therapeutic Opportunities. *Antioxidants & Redox Signaling* 1957–1997 (2011).

62. Lloyd, R. V., Hanna, P. M. & Mason, R. P. The origin of the hydroxyl radical oxygen in the Fentin reaction. *Free Radical Biology & Medicine* 885–888 (1997).

63. Thomas, C., Mackey, M. M., Diaz, A. A. & Cox, D. P. Hydroxyl radical is produced via the Fenton reaction in submitochondrial particles under oxidative stress: implications for diseases associated with iron accumulation. *Redox Report* 102–108 (2009).

64. Lacza, Z., Pankotai, E. & Busija, D. W. Mitochondrial nitric oxide synthase: current concepts and controversies. *Frontiers in bioscience (Landmark edition)* **14**, 4436–4443 (2009).

65. Radi, R., Cassina, A., Hodara, R., Quijano, C. & Castro, L. Peroxynitrite reactions and formation in mitochondria. *Free Radical Biology & Medicine* 1451–1464 (2002).

66. Romero, N., Denicola, A., Souza, J. M. & Radi, R. Diffusion of Peroxynitrite in the Presence of Carbon Dioxide. *Archives of Biochemistry and Biophysics* 23–30 (1999).

67. Schöpfer, F., Riobo, N., Cadenas, E. & Poderoso, J. J. Oxidation of ubiquinol by peroxynitrite: implications for protection of mitochondria against nitrosative damage. *Biochem J.* 35–42 (2000).

68. Cassina, A. & Radi, R. Differential Inhibitory Action of Nitric Oxide and Peroxynitrite on Mitochondrial Electron Transport. *Arch Biochem Biophys.* 309–16 (1996).

69. Selivanov, V. A., Votyakova, T. V. & Cascante, M. Reactive Oxygen Species Production by Forward and Reverse Electron Fluxes in the Mitochondrial Respiratory Chain. *PLoS Computational Biology* e1001115 (2011).

70. Scialò, F., Fernández-Ayala, D. J. & Sanz, A. Role of Mitochondrial Reverse Electron Transport in ROS Signaling: Potential Roles in Health and Disease. *Frontiers in Physiology* **8**, 428 (2017).

71. Quinlan, C. L. *et al.* Mitochondrial complex II can generate reactive oxygen species at high rates in both the forward and reverse reactions. *Journal of Biological Chemistry* (2012).

72. Grimm, S. Respiratory chain complex II as general sensor for apoptosis. *Biochimica et Biophysica Acta (BBA) - Bioenergetics* **1827**, 565–572 (2013).

73. Bezawork-Geleta, A., Rohlena, J., Dong, L., Pacak, K. & Neuzil, J. Mitochondrial Complex II: At the Crossroads. *Trends in Biochemical Sciences* **42**, 312–325 (2017).

74. Yu, E. P. K. & Bennett, M. R. Mitochondrial DNA damage and atherosclerosis. *Trends in Endocrinology and Metabolism* 481–487 (2014).

75. Muller, F. L., Liu, Y. & Van Remmen, H. Complex III Releases Superoxide to Both Sides of the Inner Mitochondrial Membrane. *Journal of Biological Chemistry* **279**, 49064–49073 (2004).

76. Srinivasan, S. & Avadhani, N. G. Cytochrome c Oxidase Dysfunction in Oxidative Stress. *Free radical biology & medicine* **53**, 1252–1263 (2012).

77. Popović, D. M. Current advances in research of cytochrome c oxidase. *Amino Acids* **45**, 1073–1087 (2013).

78. Lambeth, J. D. NOX enzymes and the biology of reactive oxygen. *Nat Rev Immunol.* 181–9 (2004).

79. Dikalov, S. Cross talk between mitochondria and NADPH oxidases. *Free Radical Biology & Medicine* 1289–1301 (2011).

80. Andrukhiv, A., Costa, A. D., West, I. C. & Garlid, K. D. Opening mitoKATP increases superoxide generation from complex I of the electron transport chain. *Am J Physiol Heart Circ Physiol* H2067–H2074 (2006).

81. Dikalova, A. E., Bikineyeva, A. T., Harisson, D. G. & Dikalov, S. I. Therapeutic Targeting of Mitochondrial Superoxide in Hypertension. *Circ Res.* 106–16 (2010).

82. Park, L., Anrather, J., Zhou, P. & Iadecola, C. NADPH-oxidase-derived reactive oxygen species mediate the cerebrovascular dysfunction induced by the amyloid beta peptide. *J Neurosci.* 1769–77 (2005).

83. Williamson, L., Saponaro, M., Boeing, S. & Svejstrup, J. Q. UV Irradiation Induces a Non-coding RNA that Functionally Opposes the Protein Encoded by the Same Gene. *Cell* 843–855 (2017).

84. Fleming, A. M., Ding, Y. & Burrows, C. J. Oxidative DNA damage is epigenetic by regulating gene transcription via base excision repair. *PNAS* 2604–2609 (2017).

85. Cadet, J. & Wagner, J. R. DNA Base Damage by Reactive Oxygen Species, Oxidizing Agents, and UV Radiation. *Cold Spring Harb Perspect Biol* a012559 (2013).

86. Wagner, J. R., Van Lier, J. E., Berger, M. & Cadet, J. Thymidine Hydroperoxides: Structural Assignment, Conformational Features, and Thermal Decomposition in Water. *J. Am. Chem. Soc.* 2235–2242 (1994).

87. Cadet, J., Douki, T. & Ravanat, J. L. Oxidatively generated damage to the guanine moiety of DNA: mechanistic aspects and formation in cells. *Acc Chem Res.* 1075–83 (2008).

88. Duarte, V., Gasparutto, D., Jaquinod, M. & Cadet, J. In vitro DNA synthesis opposite oxazolone and repair of this DNA damage using modified oligonucleotides. *Nucleic Acids Research* **28**, 1555–1563 (2000).

89. Cadet, J., Douki, T. & Ravanat, J. L. Oxidatively generated base damage to cellular DNA. *Free Radic Biol Med.* 9–21 (2010).

90. Vieira, A. & Steenken, S. Pattern of OH radical reaction with adenine and its nucleosides and nucleotides: Characterization of two types of isomericOHadduct and their unimolecular transformation reactions. *J Am Chem Soc* 6986–6994 (1990).

91. Woodbine, L., Brunton, H., Goodarzi, A. A., Shibata, A. & Jeggo, P. A. Endogenously induced DNA double strand breaks arise in heterochromatic DNA regions and require ataxia telangiectasia mutated and Artemis for their repair. *Nucleic Acids Research* **39**, 6986–6997 (2011).

92. Castillo, W. & Aristizabal-Pachon, A. Galantamine protects against beta amyloid peptide-induced DNA damage in a model for Alzheimer's disease. *Neural Regen Res* **12**, 916–917 (2017).

93. Cecarini, V., Gee, J., Fioretti, E., Eleuteri, A. M. & Keller, J. N. Protein oxidation and cellular homeostasis: Emphasis on metabolism. *Biochimica et Biophysica Acta* 93–104 (2007).

94. Stadtman, E. R. & Levine, R. L. Free radical-mediated oxidation of free amino acids and amino acid residues in proteins. *Amino Acids* 207–218 (2003).

95. STADTMAN, E. R. & LEVINE, R. L. Protein Oxidation. *Annals of the New York Academy of Sciences* **899**, 191–208

96. Stadtman, E. R. Protein Oxidation in Aging andAge-Related Diseases. *Ann N Y Acad Sci.* 22–38 (2001).

97. Castro, J. P., Jung, T., Grune, T. & Siems, W. 4-Hydroxynonenal (HNE) modified proteins in metabolic diseases. *Free Radical Biology and Medicine* 309–315 (2017).

98. Ayala, A., Munoz, M. F. & Argüelles, S. Lipid Peroxidation: Production, Metabolism, and Signaling Mechanisms of Malondialdehyde and 4-Hydroxy-2-Nonenal. *Oxidative Medicine and Cellular Longevity* (2014).

99. Niedernhofer, L. J., Daniels, J. S., Rouzer, C. A., Greene, R. E. & Marnett, L. J. Malondialdehyde, a Product of Lipid Peroxidation, Is Mutagenic in Human Cells. *Journal of Biological Chemistry* **278**, 31426–31433 (2003).

100. Esterbauer, H., Eckl, P. & Ortner, A. Possible mutagens derived from lipids and lipid precursors. *Mutation Research* 223–233 (1990).

101. Zhang, Y., Sano, M. & Shinmura, K. 4-Hydroxy-2-nonenal protects against cardiac ischemia-reperfusion injury via the Nrf2-dependent pathway. *Journal of Molecular and Cellular Cardiology* 576–586 (2010).

102. Fukai, T. & Ushio-Fukai, M. Superoxide Dismutases: Role in Redox Signaling, Vascular Function, and Diseases. *Antioxidants & Redox Signaling* 1583–1606 (2011).

103. Ganini, D., Santos, J. H., Bonini & Mason, R. P. Switch of Mitochondrial Superoxide Dismutase into a Prooxidant Peroxidase in Manganese-Deficient Cells and Mice. *Cell Chemical Biology* 413–425 (2018).

104. Miao, L. & St. Clair, D. K. Regulation of Superoxide Dismutase Genes: Implications in Diseases. *Free Radic Biol Med.* 344–356 (2009).

105. Xu, Y., Kiningham, K. & St. Clair, D. An intronic NF-kappaB element is essential for induction of the human manganese superoxide dismutase gene by tumor necrosis factor-alpha and interleukin-1beta. *DNA Cell Biol.* 709–22 (1999).

106. Mastrangelo, I., Courey, A. & Hough, P. DNA looping and Sp1 multimer links: a mechanism for transcriptional synergism and enhancement. *Proc Natl Acad Sci USA* 5670–5674 (1991).

107. Zhu, C., Huang, Y., Weydert, C., Oberley, L. & Domann, F. Constitutive activation of transcription factor AP-2 is associated with decreased MnSOD expression in transformed human lung fibroblasts. *Antioxid Redox Signal* 387–395 (2001).

108. Rojo, A., Salinas, M., Martin, D. & Cuadrado, A. Regulation of Cu/Zn-superoxide dismutase expression via the phosphatidylinositol 3 kinase/Akt pathway and nuclear factor-kappaB. *J Neurosci* 7324–7334 (2004).

109. Fukui, M. & Zhu, B. T. Mitochondrial Superoxide Dismutase SOD2, but not Cytosolic SOD1, Plays a Critical Role in Protection against Glutamate-Induced Oxidative Stress and Cell Death in HT22 Neuronal Cells. *Free radical biology & medicine* **48**, 821–830 (2010).

110. Esposito, L. A., Kokoszka, J. E., Waymire, K. G. & Wallace. Mitochondrial oxidative stress in mice lacking the glutathione peroxidase-1 gene. *Free Radic Biol Med* 754–766 (2000).

111. Kinnula, V. & Crapo, J. Superoxide dismutases in malignant cells and human tumors. *Free Radic Biol Med* 718–744 (2004).

112. Margis, R., Dunand, C., Teixeira, F. K. & Margis-Pinheiro, M. Glutathione peroxidase family – an evolutionary overview. *The FEBS Journal* **275**, 3959–3970 (2008).

113. Handy, D. E., Lubos, E., Yang, Y. & Loscalzo, J. Glutathione Peroxidase-1 Regulates Mitochondrial Function to Modulate Redox-dependent Cellular Responses. *Journal of Biological Chemistry* 11913–11921 (2009).

114. Kirkman, H. N., Rolfo, M., Ferraris, A. M. & Gaetani, G. F. Mechanisms of Protection of Catalase by NADPH: KINETICS AND STOICHIOMETRY. *Journal of Biological Chemistry* **274**, 13908–13914 (1999).

115. Young, I. S. & Woodside, J. V. Antioxidants in health and disease. *J Clin Pathol* 176–186 (2001).

116. Kowaltowski, A. J., Castilho, R. F. & Vercesi, A. E. Opening of the mitochondrial permeability transition pore by uncoupling or inorganic phosphate in the presence of Ca 2+ is dependent on mitochondrial-generated reactive oxygen species. *FEBS Letters* 150–152 (1996).

117. Naziroglu, M. Molecular role of catalase on oxidative stressinduced Ca2+ signaling and TRP cation channel activation in nervous system. *Journal of Receptors and Signal Transduction* 134–141 (2012).

118. Starkov, A. A., Andreyev, A. Y., Zhang, S. F. & Popov, V. N. Scavenging of H2O2 by mouse brain mitochondria. *J Bioenerg Biomembr.* 471–477 (2014).

119. Drechsel, D. & Patel, M. Respiration-dependent H2O2 removal in brain mitochondria via the thioredoxin/peroxiredoxin system. *J Biol Chem.* 27850–8 (2010).

120. Kodydková, J., Vávrová, L., Kocík, M. & Žák, A. Human Catalase, Its Polymorphisms, Regulation and Changes of Its Activity in Different Diseases. *Folia Biol (Praha)* 153–67 (2014).

121. Veal, E. A., Day, A. M. & Morgan, B. A. Hydrogen Peroxide Sensing and Signaling. *Molecular Cell* 1–14 (2007).

122. Sies, H. Hydrogen peroxide as a central redox signaling molecule in physiological oxidative stress: Oxidative eustress. *Redox Biology* 13–619 (2017).

123. Minatel, I., Francisqueti, F., Corrêa, C. & Pereira Lima, G. Antioxidant Activity of γ-Oryzanol: A Complex Network of Interactions. *Int. J. Mol. Sci.* 1107 (2016).

124. Sablina, A., Budanov, A. & Chumakov, P. The antioxidant function of the p53 tumor suppressor. *Nat. Med.* 1306–1313 (2005).

125. Storz, G., Tartaglia, L. & Ames, B. Transcriptional regulator of oxidative stress-inducible genes: direct activation by oxidation. *Science* 189–194 (1990).

126. Kim, S., Merchant, K., Nudelman, R. & Stamler, J. OxyR: a molecular code for redox-related signaling. *Cell* 383–396 (2002).

127. Aslund, F., Zheng, M., Beckwith, J. & Storz, G. Regulation of the OxyR transcription factor by hydrogen peroxide and the cellular thiol-disulfide status. *Proc. Natl. Acad. Sci. USA* 6161–6165 (1999).

128. Herbig, A. & Helmann, J. Roles of metal ions and hydrogen peroxide in modulating the interaction of the Bacillus subtilis PerR peroxide regulon repressor with operator DNA. *Mol. Microbiol.* 849–859 (2001).

129. Lee, J. & Helmann, J. The PerR transcription factor senses H(2)O(2) by metal-catalysed histidine oxidation. *Nature* 363–367 (2006).

130. Bossis, G. & Melchior, F. Regulation of SUMOylation by reversible oxidation of SUMO conjugating enzymes. *Mol. Cell* 349– 357 (2006).

131. Pajares, M., Jiménez-Moreno, N., Dias, I. H. K. & Cuadrado, A. Redox control of protein degradation. *Redox Biology* 409–420 (2015).

132. Reinheckel, T., Sitte, N., Ullrich, O. & Grune, T. Comparative resistance of the 20S and 26S proteasome to oxidative stress. *Biochemical Journal* 637–642 (1998).

133. Soubannier, V., McLelland, G., Zunino, R. & Braschi, E. A Vesicular Transport Pathway Shuttles Cargo from Mitochondria to Lysosomes. *Current Biology* 135–141 (2012).

134. Ghosh, M., Carlsson, F., Laskar, A., Yuan, X.-M. & Li, W. Lysosomal membrane permeabilization causes oxidative stress and ferritin induction in macrophages. *FEBS Letters* **585**, 623–629 (2011).

135. Schieber, M. & Chandel, N. S. ROS Function in Redox Signaling and Oxidative Stress. *Current Biology* R453–R462 (2014).

136. Wang, D., Malo, D. & Hekimi, S. Elevated mitochondrial reactive oxygen species generation affects the immune response via hypoxia-inducible factor-1alpha in long-lived Mclk1+/- mouse mutants. *J Immunol* 582–590 (2010).

137. Kong, X., Thimmulappa, R., Craciun, F. & Biswal, S. Enhancing Nrf2 pathway by disruption of Keap1 in myeloid leukocytes protects against sepsis. *Am J Respir Crit Care Med.* 928–938 (2011).

138. Chaudhari, P., Ye, Z. & Jang, Y. Roles of reactive oxygen species in the fate of stem cells. *Antioxid. Redox Signal* 1881– 1890 (2014).

139. Borquez, D. A., Urrutia, P. J., Wilson, C. & Gonzalez-Billault, C. Dissecting the role of redox signaling in neuronal development. *Journal of Neurochemistry* 506–517 (2016).

140. Yan, Y., Wei, C. & Liu, J. Cross-talk between calcium and reactive oxygen species signaling. *Acta Pharmacologica Sinica* 821–826 (2006).

141. Koerie, J. Interaction of reactive oxygen species with ion transport mechanisms. *Am J Physiol* C1–24 (1998).

142. Cheng, H., Lederer, W. & Cannell, M. Calcium sparks: the elementary events underlying excitation-contraction coupling in heart muscle. *Science* 740–4 (1993).

143. Gauron, C., Rampon, C., Volovitch, M. & Vriz, S. Sustained production of ROS triggers compensatory proliferation and is required for regeneration to proceed. *Scientific Reports* 2084 (2013).

144. Rieger, S. & Sagasti, A. Hydrogen Peroxide Promotes Injury-Induced Peripheral Sensory Axon Regeneration in the Zebrafish Skin. *PLOS Biology* e1000621 (2011).

145. Niethammer, P., Grabher, C., Look, T. A. & Mitchison, T. J. A tissue-scale gradient of hydrogen peroxide mediates rapid wound detection in zebrafish. *Nature* 996–999 (2009).

146. Suzuki, N. & Mittler, R. Reactive oxygen species-dependent wound responses in animals and plants. *Free RadicalBiologyandMedicine* 2269–2276 (2012).

147. Smith, G. M. & Gallo, G. The Role of Mitochondria in Axon Development and Regeneration. *Dev Neurobiol.* 221–237 (2017).

148. Misgeld, T., Kerschensteiner, M., Bareyre, F. M., Burgess, R. W. & Lichtman, J. W. Imaging axonal transport of mitochondria in vivo. *Nature Methods* 559–561 (2007).

149. Hockfield, S. & McKay, R. D. G. Identification of Major Cell Classes in the Developing Mammalian Nervous System. *The Journal of Neuroscience* (1985).

150. Tessier-Lavigne, M. & Goodman, C. S. The molecular biology of axon guidance. *Science* 1123–1133 (1996).

151. Kaplan, S., Odaci, E., Unal, B., Sahin, B. & Fornaro, M. Development of the peripheral nerve. *International Review of Neurobiology* 9–26 (2009).

152. Monk, K. R., Feltri, L. & Taveggia, C. New Insights on Schwann Cell Development. *Glia* 1376–1393 (2015).

153. Shah, N., Marchionni, M., Isaacs, I., Stroobant, P. & Anderson, D. Glial Growth Factor Restricts Mammalian Neural Crest Stem Cells to a Glial Fate. *Cell* 349–360 (1994).

154. Doddrell, R. *et al.* Regulation of Schwann Cell Differentiation and Proliferation by the Pax-3 Transcription Factor. *Glia* 1269–1278 (2012).

155. Jacob, C. *et al.* HDAC1 and HDAC2 Control the Specification of Neural Crest Cells into Peripheral Glia. *The Journal of Neuroscience* 6112– 6122 (2014).

156. Jessen, K. R. & Mirsky, R. The origin and development of glial cells in peripheral nerves. *Nature Reviews Neuroscience* **6**, 671 (2005).

157. Dong, Z., Brannan, A., Liu, N., Mirsky, R. & Jessen, K. Neu Differentiation Factor Is a Neuron-Gila Signal and Regulates Survival, Proliferation, and Maturation of Rat Schwann Cell Precursors. *Neuron* 585–596 (1995).

158. Newbern, J. & Birchmeier, C. Nrg1/ErbB signaling networks in Schwann cell development and myelination. *Seminars in Cell & Developmental Biology* 922–928 (2010).

159. Brill, M. S., Kleele, T., Ruschkies, L., Kneussel, M. & Misgeld, T. Branch-Specific Microtubule Destabilization Mediates Axon Branch Loss during Neuromuscular Synapse Elimination. *Neuron* 845–856 (2016).

160. Todd, K. J., Darabid, H. & Robitaille, R. Perisynaptic Glia Discriminate Patterns of Motor Nerve Activity and Influence Plasticity at the Neuromuscular Junction. *The Journal of Neuroscience* 11870 –11882 (2010).

161. Ko, C.-P. & Robitaille, R. Perisynaptic Schwann Cells at the Neuromuscular Synapse: Adaptable, Multitasking Glial Cells. *Cold Spring Harb Perspect Biol* a020503 (2015).

162. Darabid, H., Arbour, D. & Robitaille, R. Glial Cells Decipher Synaptic Competition at the Mammalian Neuromuscular Junction. *The Journal of Neuroscience* 1297–1313 (2013).

163. Morell, P. & Quarles, R. The Myelin Sheath. in *Basic Neurochemistry: Molecular, Cellular and Medical Aspects.* (Siegel GJ, Agranoff BW, Albers RW, et al., 1999).

164. Boiko, T. & Winckler, B. Myelin under construction—teamwork required. *The Journal of Cell Biology* **172**, 799–801 (2006).

165. Sherman, D. L., Wu, L. M. N., Grove, M., Gillespie, C. S. & Brophy, P. J. Drp2 and Periaxin Form Cajal Bands with Dystroglycan But Have Distinct Roles in Schwann Cell Growth. *Journal of Neuroscience* **32**, 9419–9428 (2012).

166. Snaidero, N. & Simons, M. Myelination at a glance. *Journal of Cell Science* **127**, 2999–3004 (2014).

167. Bunge, M. B., Bunge, R. P. & Ris, H. ULTRASTRUCTURAL STUDY OF REMYELINATION IN AN EXPERIMENTAL LESION IN ADULT CAT SPINAL CORD. *J Cell Biol* **10**, 67 (1961).

168. Segura-Anaya, E., Martinez-Gomez, A. & Dent, M. A. R. Localization of Aquaporin 1 water channel in the schmidt-lantermann incisures and the paranodal regions of the rat sciatic nerve. *Neuroscience* 119–127 (2015).

169. Balice-Gordon, R., Bone, L. & Scherer, S. Functional Gap Junctions in the Schwann Cell Myelin Sheath. *J Cell Biol* 1095–1104 (1998).

170. Rasband, M. & Peles, E. The Nodes of Ranvier: Molecular Assembly and Maintenance. *Cold Spring Harb Perspect Biol.* a020495 (2015).

171. Samara, C., Poirot, O., Domenèch-Estévez, E. & Chrast, R. Neuronal activity in the hub of extrasynaptic Schwann cell-axon interactions. *FrontiersinCellularNeuroscience* 228 (2013).

172. Ichimura, T. & Ellisman, M. Three-dimensional fine structure of cytoskeletal-membrane interactions at nodes of Ranvier. *J Neurocytol* 667–681 (1991).

173. Ariyasu, R. G., Nichol, J. A. & Ellisman, M. H. Localization of Sodium/Potassium Adenosine Triphosphatase in Multiple Cell Types of the Murine Nervous System with Antibodies Raised Against the Enzyme from Kidney. *The Journal of Neuroscience* 2581–2596 (1985).

174. Cooper, E. Made for "anchorin": Kv7.2/7.3 (KCNQ2/KCNQ3) channels and the modulation of neuronal excitability in vertebrate axons. *Semin Cell Dev Biol* 185–192 (2011).

175. Berghs, S., Aggujaro, D., Dirkx, R. & Ort, T. bIV spectrin, a new spectrin localized at axon initial segments and nodes of Ranvier in the central and peripheral nervous system. *J Cell Biol* 985–1002 (2000).

176. Bréchet, A., Fache, M., Brachet, A. & Dargent, B. Protein kinase CK2 contributes to the organization of sodium channels in axonal membranes by regulating their interactions with ankyrin G. *J Cell Biol* 1101–1114 (2008).

177. Yang, Y., Lacas-Gervais, S., Morest, D. & Rasband, M. bIV spectrins are essential for membrane stability and the molecular organization of nodes of Ranvier. *J Neurosci* 7230–7240 (2004).

178. Schafer, D., Custer, A., Shrager, P. & Rasband, M. Early events in node of Ranvier formation during myelination and remyelination in the PNS. *Neuron Glia Biol* 69–79 (2006).

179. Ching, W., Zanazzi, G., Levinson, S. & Salzer, J. Clustering of neuronal sodium channels requires contact with myelinating Schwann cells. *J Neurocytol* 295–301 (1999).

180. Catterall, W. A. From Ionic Currents to Molecular Mechanisms: The Structure and Function of Voltage-Gated Sodium Channels. *Neuron* **26**, 13–25 (2000).

181. Patchornik, G., Goldshleger, R. & Karlish, S. J. D. The complex ATP–Fe2+ serves as a specific affinity cleavage reagent in ATP-Mg2+ sites of Na,K-ATPase: Altered ligation of Fe2+ (Mg2+) ions accompanies the E1P->E2P conformational change. *PNAS* 11954–11959 (2000).

182. Crotty, P., Sangrey, T. & Levy, W. B. Metabolic Energy Cost of Action Potential Velocity. *Journal of Neurophysiology* **96**, 1237–1246 (2006).

183. Neishabouri, A. M. & Faisal, A. A. The metabolic efficiency of myelinated vs unmyelinated axons. *BMC Neuroscience* **12**, P100–P100 (2011).

184. Harris, J. J., Jolivet, R. & Attwell, D. Synaptic Energy Use and Supply. *Neuron* **75**, 762–777 (2012).

185. Nave, K.-A. Myelination and support of axonal integrity by glia. *Nature* **468**, 244 (2010).

186. Young, E. A. *et al.* Imaging correlates of decreased axonal Na+/K+ ATPase in chronic multiple sclerosis lesions. *Annals of Neurology* **63**, 428–435 (2008).

187. Gibbs, K. L., Greensmith, L. & Schiavo, G. Regulation of Axonal Transport by Protein Kinases. *Trends in Biochemical Sciences* **40**, 597–610 (2015).

188. Maday, S., Twelvetrees, A. E., Moughamian, A. J. & Holzbaur, E. L. F. Axonal Transport: Cargo-Specific Mechanisms of Motility and Regulation. *Neuron* 292–309 (2014).

189. Devine, M. J. & Kittler, J. T. Mitochondria at the neuronal presynapse in health and disease. *Nature Reviews Neuroscience* **19**, 63 (2018).

190. Liotta, A. *et al.* Energy Demand of Synaptic Transmission at the Hippocampal Schaffer-Collateral Synapse. *J Cereb Blood Flow Metab* **32**, 2076–2083 (2012).

191. Figley, C. R. Lactate Transport and Metabolism in the Human Brain: Implications for the Astrocyte-Neuron Lactate Shuttle Hypothesis. *Journal of Neuroscience* **31**, 4768–4770 (2011).

192. Funfschilling, U. *et al.* Glycolytic oligodendrocytes maintain myelin and long-term axonal integrity. *Nature* **485**, 517–521 (2012).

193. Domènech-Estévez, E. *et al.* Distribution of Monocarboxylate Transporters in the Peripheral Nervous System Suggests Putative Roles in Lactate Shuttling and Myelination. *J. Neurosci.* **35**, 4151 (2015).

194. Saab, A. S. *et al.* Oligodendroglial NMDA Receptors Regulate Glucose Import and Axonal Energy Metabolism. *Neuron* **91**, 119–132 (2016).

195. Hutton, E. J., Carty, L., Laura, M. & Reilly, M. M. c-Jun expression in human neuropathies: a pilot study. *Journal of the Peripheral Nervous System* 295–303 (2011).

196. Parkinson, D. B., Bhaskaran, A., Arthur-Farraj, P. & Jessen, K. c-Jun is a negative regulator of myelination. *J. Cell Biol.* 625–637 (2008).

197. Arthur-Farraj, P., Latouche, M., Wilton, D., Mirsky, R. & Jessen, K. c-Jun reprograms Schwann cells of injured nerves to generate a repair cell essential for regeneration. *Neuron* 633–47 (2012).

198. Ramburrun, P., Kumar, P. & Pillay, V. A Review of Bioactive Release from Nerve Conduits as a Neurotherapeutic Strategy for Neuronal Growth in Peripheral Nerve Injury. *BioMed Research International* 132350 (2014).

199. Jessen, K., Mirsky, R. & Arthur-Farraj, P. The Role of Cell Plasticity in Tissue Repair: Adaptive Cellular Reprogramming. *Dev Cell.* 613–20 (2015).

200. Perkins, G. A. & Ellisman, M. H. Mitochondrial configurations in peripheral nerve suggest differential ATP production. *Journal of Structural Biology* 117–127 (2011).

201. Ohno, N. *et al.* Myelination and axonal electrical activity modulate the distribution and motility of mitochondria at CNS nodes of Ranvier. *The Journal of neuroscience : the official journal of the Society for Neuroscience* **31**, 7249–7258 (2011).

202. Bros, H., Milward, J. M., Friedemann, P., Raluca, N. & Infante-Duarte, C. Oxidative damage to mitochondria at the nodes of Ranvier precedes axon degeneration in ex vivo transected axons. *Experimental Neurology* 127–135 (2014).

203. Sheng, Z.-H. & Cai, Q. Mitochondrial transport in neurons: impact on synaptic homeostasis and neurodegeneration. *Nat Rev Neurosci* 77–93 (2016).

204. Course, M. M. & Wang, X. Transporting mitochondria in neurons. *F1000Research* 1735 (2016).

205. Rice, S. *et al.* A structural change in the kinesin motor protein that drives motility. *Nature* **402**, 778 (1999).

206. Lin, M.-Y. & Sheng, Z.-H. Regulation of mitochondrial transport in neurons. *Experimental Cell Research* 35 – 4 4 (2015).

207. Van Spronsen, M., Mikhaylova, M. & Lipka, J. TRAK/Milton motor-adaptor proteins steer mitochondrial trafficking to axons and dendrites. *Neuron* 485–502 (2013).

208. Franker, M. & Hoogenraad, C. Microtubule-based transport - basic mechanisms, traffic rules and role in neurological pathogenesis. *J. Cell Sci.* 2319–2329 (2013).

209. Eschbach, J., Sinniger, J., Bouitbir, J. & Dupuis, L. Dynein mutations associated with hereditary motor neuropathies impair mitochondrial morphology and function with age. *Neurobiol Dis.* 220–230 (2013).

210. Yi, M., Weaver, D. & Hajnóczky, G. Control of mitochondrial motility and distribution by the calcium signal: a homeostatic circuit. *Journal of Cell Biology* 661–672 (2004).

211. Schwartz, T. Mitochondrial Trafficking in Neurons. *Cold Spring Harb Perspect Biol* a011304 (2013).

212. Liu, X. & Hajnóczky, G. Ca2+-dependent regulation of mitochondrial dynamics by the Miro–Milton complex. *The International Journal of Biochemistry & Cell Biology* 1972–1976 (2009).

213. Raturi, A. & Simmen, T. Where the endoplasmic reticulum and the mitochondrion tie the knot: The mitochondria-associated membrane (MAM). *Biochimica et Biophysica Acta* 213–224 (2013).

214. Yang, Y. & Strittmatter, S. The reticulons: a family of proteins with diverse functions. *Genome Biol.* 234 (2007).

215. Barber, S. C., Mead, R. J. & Shaw, P. J. Oxidative stress in ALS: A mechanism of neurodegeneration and a therapeutic target. *Biochimica et Biophysica Acta* 1051–1067 (2006).

216. Zarei, S. *et al.* A comprehensive review of amyotrophic lateral sclerosis. *Surgical Neurology International* **6**, 171 (2015).

217. Rosen, D., Siddique, T., Patterson, D. & Brown Jr., R. Mutations in Cu/Zn superoxide dismutase gene are associated with familial amyotrophic lateral sclerosis. *Nature* 59–62 (1993).

218. Ferrante, R., Browne, Shinobu, A. & Beal, M. Evidence of increased oxidative damage in both sporadic and familial amyotrophic lateral sclerosis. *J. Neurochem.* 2064–2074 (1997).

219. Beal, M., Ferrante, R., Browne, S. & Brown Jr., R. Increased 3-nitrotyrosine in both sporadic and familial amyotrophic lateral sclerosis. *Ann. Neurol* 644–654 (1997).

220. Tohgi, H., Abe, T., Yamazaki, K. & Murata, T. Remarkable increase in cerebrospinal fluid 3-nitrotyrosine in patients with sporadic amyotrophic lateral sclerosis. *Ann. Neurol.* 129–131 (1999).

221. Andrus, P., Fleck, T., Gurney, M. & Hall, E. Protein oxidative damage in a transgenic mouse model of familial amyotrophic lateral sclerosis. *J. Neurochem.* 2041–2048 (1998).

222. Niu, H., Álvarez-Álvarez, I., Guillén-Grima, F. & Aguinaga-Ontoso, I. Prevalence and incidence of Alzheimer's disease in Europe: A meta-analysis. *Neurología (English Edition)* **32**, 523–532 (2017).

223. Moreira, Paula I., Santos, M. S. & Perry, G. Alzheimer Disease and the Role of Free Radicals in the Pathogenesis of the Disease. *CNS & Neurological Disorders - Drug Targets* 3–10 (2008).

224. Jiang, S., Nandy, P., Wang, W. & Zhu, X. Mfn2 ablation causes an oxidative stress response and eventual neuronal death in the hippocampus and cortex. *Molecular Neurodegeneration* 5 (2018).

225. Area-Gomez, E., del Carmen Lara Castillo, M., Tambini, M. & Schon, E. Upregulated function of mitochondria-associated ER membranes in Alzheimer disease. *EMBO J.* 4106–4123 (2012).

226. Dickson, D. W. Parkinson's Disease and Parkinsonism: Neuropathology. *Cold Spring Harbor Perspectives in Medicine* **2**, a009258 (2012).

227. Savica, R., Grossardt, B. R., Bower, J. H., Ahlskog, J. E. & Rocca, W. A. Time Trends in the Incidence of Parkinson's Disease: a 30-year Study. *JAMA neurology* **73**, 981–989 (2016).

228. Jankovic, J. Parkinson's disease: clinical features and diagnosis. *Journal of Neurology, Neurosurgery & Psychiatry* **79**, 368–376 (2008).

229. Winklhofer, K. & Haass, C. Mitochondrial dysfunction in Parkinson's disease. *Biochimica et Biophysica Acta* 29–44 (2010).

230. Davey, G. & Clark, J. Threshold effects and control of oxidative phosphorylation in nonsynaptic rat brain mitochondria. *J Neurochem* 12753–12757 (1998).

231. Muftuoglu, M., Elibol, B., Dalmizrak, O. & Ozer, O. Mitochondrial complex I and IV activities in leukocytes from patients with parkin mutations. *Mov. Disord.* 544–548 (2004).

232. Dauer, W. & Przedborski, S. Parkinson's disease: mechanisms and models. *Neuron* 889–909 (2003).

233. Perier, C. & Vila, M. Mitochondrial Biology and Parkinson's Disease. *Cold Spring Harb Perspect Med* a009332 (2012).

234. Mortiboys, H., Thomas, K., Koopman, W. & Bandmann, O. Mitochondrial function and morphology are impaired in parkin-mutant fibroblasts. *Ann. Neurol* 555–565 (2008).

235. Kamp, F., Exner, N., Lutz, A. K. & Haass, C. Inhibition of mitochondrial fusion by α-synuclein is rescued by PINK1, Parkin and DJ-1. *EMBO J.* 3571–89 (2010).

236. Vance, J. E. MAM(mitochondria-associatedmembranes) in mammalian cells: Lipids and beyond. *Biochimica et Biophysica Acta* 595–609 (2014).

237. Cali, T., Ottolini, D., Negro, A. & Brini, M. α-Synuclein Controls Mitochondrial Calcium Homeostasis by Enhancing Endoplasmic Reticulum-Mitochondria Interactions. *Journal of Biological Chemistry* 17914 –17929 (2012).

238. Foulon, S. *et al.* Prevalence and mortality of patients with multiple sclerosis in France in 2012: a study based on French health insurance data. *Journal of Neurology* **264**, 1185–1192 (2017).

239. Su, K., Banker, G., Bourdette, D. & Forte, M. Axonal degeneration in multiple sclerosis: The mitochondrial hypothesis. *Curr Neurol Neurosci Rep* 411–417 (2009).

240. Van Horssen, J., Witte, M. E., Schreibelt, G. & De Vries, H. E. Radical changes in multiple sclerosis pathogenesis. *Biochimica et Biophysica Acta* 141–150 (2011).

241. LeVine, S. M. The Role of Reactive Oxygen Species in the Pathogenesis of Multiple Sclerosis. *Medical Hypotheses* 271–274 (1992).

242. Lassmann, H. & van Horssen, J. Oxidative stress and its impact on neurons and glia in multiple sclerosis lesions. *Biochimica et Biophysica Acta (BBA) - Molecular Basis of Disease* **1862**, 506–510 (2016).

243. Mahad, D., Ziabreva, I., Campbell, G., Lax, N. & Turnbull, D. M. Mitochondrial changes within axons in multiple sclerosis. *Brain* 1161–1174 (2009).

244. Torkildsen, Ø., Brunborg, L. A., Myhr, K.-M. & Bø, L. The cuprizone model for demyelination. *Acta Neurologica Scandinavica* **117**, 72–76 (2008).

245. Acs, P., Selak, M., Komoly, S. & Kalman, B. Distribution of oligodendrocyte loss and mitochondrial toxicity in the cuprizone-induced experimental demyelination model. *Journal of Neuroimmunology* 128–131 (2013).

246. Witherick, J., Wilkins, A., Scolding, N. & Kemp, K. Mechanisms of Oxidative Damage inMultiple Sclerosis and a Cell Therapy Approach to Treatment. *Autoimmune Diseases* 164608 (2010).

247. Haile, Y., Deng, X., Ortiz-Sandoval, C., Giuliani, F. & Simmen, T. Rab32 connects ER stress to mitochondrial defects in multiple sclerosis. *Journal of Neuroinflammation* 19 (2017).

248. Sziget, K. & Lupski, J. Charcot–Marie–Tooth disease. *European Journal of Human Genetics* 703–710 (2009).

249. Berger, P., Young, P. & Suter, U. Molecular cell biology of Charcot-Marie-Tooth disease. *Neurogenetics* 1–15 (2002).

250. Hoyle, J. C., Isfort, M. C., Roggenbuck, J. & Arnold, W. D. The genetics of Charcot–Marie–Tooth disease: current trends and future implications for diagnosis and management. *The Application of Clinical Genetics* 235–243 (2015).

251. Saporta, A., Sottile, S., Miller, L. & Shy, M. Charcot-Marie-Tooth disease subtypes and genetic testing strategies. *Ann Neurol.* 22–33 (2011).

252. Hantke, J., Carty, L., Wagstaff, L. J. & Jessen, K. c-Jun activation in Schwann cells protects against loss of sensory axons in inherited neuropathy. *Brain* 2922–2937 (2014).

253. Roberts, S. L., Dun, X.-P. & Parkinson, D. B. Sox2 expression in Schwann cells inhibits myelination in vivo and induces influx of macrophages to the nerve. *Development* 3114–3125 (2017).

254. Pennuto, M., Tinelli, E., Feltri, L. & Wrabetz, L. Ablation of the UPR-Mediator CHOP Restores Motor Function and Reduces Demyelination in Charcot-Marie-Tooth 1B Mice. *Neuron* 393–405 (2008).

255. Topf, U., Wrobel, L. & Chacinska, A. Chatty Mitochondria: Keeping Balance in Cellular Protein Homeostasis. *Trends in Cell Biology* 577–586 (2016).

256. Bird, T. Charcot-Marie-Tooth Neuropathy Type 2. (2016).

257. Laura, M., Milani, M. & Pareyson, D. Rapid progression of late onset axonal Charcot–Marie–Tooth disease associated with a novel MPZ mutation in the extracellular domain. *J Neurol Neurosurg Psychiatry* 1263–1266 (2007).

258. Capponi, S., Geroldi, A. & Bellone, E. HSPB1 and HSPB8 in inherited neuropathies: study of an Italian cohort of dHMN and CMT2 patients. *Journal of the Peripheral Nervous System* 287–294 (2011).

259. Cartoni, R. & Martinou, J.-C. Role of mitofusin 2 mutations in the physiopathology of Charcot–Marie–Tooth disease type 2A. *Experimental Neurology* 268–273 (2009).

260. Polke, J. *et al.* Recessive axonal Charcot-Marie-Tooth disease due to compound heterozygous mitofusin 2 mutations. *Neurology* **77**, 168–173 (2011).

261. Cartoni, R. *et al.* Expression of mitofusin 2R94Q in a transgenic mouse leads to Charcot–Marie–Tooth neuropathy type 2A. *Brain* 1460–1469 (2010).

262. Chen, H., McCaffery, J. & Chan, D. Mitochondrial fusion protects against neurodegeneration in the cerebellum. *Cell* 548–562 (2007).

263. Chung, K., Kim, S., Park, K. & Choi, B. Early onset severe and late-onset mild Charcot–Marie–Tooth disease with mitofusin 2 (MFN2) mutations. *Brain* 2103–2118 (2006).

264. Detmer, S., Vande velde, S., Cleveland, D. & Chan, D. Hindlimb gait defects due to motor axon loss and reduced distal muscles in a transgenic mouse model of Charcot–Marie–Tooth type 2A. *Hum. Mol. Genet.* 367–375 (2008).

265. Delettre, C. *et al.* Nuclear gene OPA1, encoding a mitochondrial dynamin-related protein, is mutated in dominant optic atrophy. *Nature Genetics* **26**, 207 (2000).

266. Lenaers, G. *et al.* Dominant optic atrophy. *Orphanet Journal of Rare Diseases* **7**, 46 (2012).

267. Zanna, C. *et al.* OPA1 mutations associated with dominant optic atrophy impair oxidative phosphorylation and mitochondrial fusion. *Brain* **131**, 352–367 (2008).

268. Misko, A., Jiang, S., Wegorzewska, I., Milbrandt, J. & Baloh, R. H. Mitofusin 2 is necessary for transport of axonal mitochondria and interacts with the Miro/Milton complex. *J Neurosci* 4232–4240 (2010).

269. Kawalec, M. *et al.* Mitofusin 2 Deficiency Affects Energy Metabolism and Mitochondrial Biogenesis in MEF Cells. *PLOS ONE* e0134162 (2015).

270. Loiseau, D., Chevrollier, A., Verny, C. & Reynier, P. Mitochondrial Coupling Defect in Charcot– Marie–Tooth Type 2A Disease. *Ann Neurol* 315–323 (2007).

271. Sebastián, D. *et al.* Mitofusin 2 (Mfn2) links mitochondrial and endoplasmic reticulum function with insulin signaling and is essential for normal glucose homeostasis. *PNAS* 5523–5528 (2012).

272. Østern, R., Fagerheim, T., Ørstavik, K. & Dahl, A. Hereditary motor neuron disease in a large Norwegian family with a "H46R" substitution in the superoxide dismutase 1 gene. *Neuromuscular Disorders* (2012).

273. Sims-Robinson, C., Hur, J., Hayes, J. M. & Feldman, E. L. The Role of Oxidative Stress in Nervous System Aging. *PLoS ONE* e68011 (2013).

274. Pitceathly, R. D. S., Murphy, S. M., Cottenie, E. & Hanna, M. G. Genetic dysfunction of MT-ATP6 causes axonal Charcot-Marie-Tooth disease. *Neurology* 1145–1154 (2012).

275. Imamura, H., Huynh Nhat, K. P., Togawa, H. & Noji, H. Visualization of ATP levels inside single living cells with fluorescence resonance energy transfer-based genetically encoded indicators. *PNAS* 15651–15656 (2009).

276. Babu Sekar, R. & Periasamy, A. Fluorescence resonance energy transfer (FRET) microscopy imaging of live cell protein localizations. *Journal of Cell Biology* 629 (2003).

277. Elangovan, M., Day, R. & Periasamy, A. Nanosecond fluorescence reso-nance energy transfer-fluorescence lifetime imaging microscopy to localizethe protein interactions in a single living cell. *J. Microsc* 3–14 (2002).

278. San Martin, A., Ceballo, S., Ruminot, I. & Barros, L. F. A genetically encoded FRET lactate sensor and its use to detect the Warburg effect in single cancer cells. *PLoS ONE* e57712 (2013).

279. Takanaga, H., Chaudhuri, B. & Frommer, W. B. GLUT1 and GLUT9 as major contributors to glucose influx in HepG2 cells identified by a high sensitivity intramolecular FRET glucose sensor. *Biochimica et Biophysica Acta - Biomembranes* 1091–1099 (2008).

280. Albrecht, S. C., Barata, A. G., Großhans, J., Teleman, A. A. & Dick, T. P. In Vivo Mapping of Hydrogen Peroxide and Oxidized Glutathione Reveals Chemical and Regional Specificity of Redox Homeostasis. *Cell Metabolism* 819–29 (2011).

281. Gutscher, M. *et al.* Proximity-based protein thiol oxidation by H2O2-scavenging peroxidases. *J. Biol. Chem.* 31532–31540 (2009).

282. Dooley, C., Dore, T., Hanson, G. & Tsien, R. Imaging Dynamic Redox Changes in Mammalian Cells with Green Fluorescent Protein Indicators. *Journal of Biological Chemistry* 22284–22293 (2004).

283. Ren, W. & Ai, H.-W. Genetically Encoded Fluorescent Redox Probes. *Sensors* 15422–15433 (2013).

284. Nakai, J., Ohkura, M. & Imoto, K. A high signal-to-noise Ca2+ probe composed of a single green fluorescent protein. *Nature Biotechnology* 137–141 (2001).

285. Iguchi, M., Kato, M., Nakai, J. & Akao, M. Direct monitoring of mitochondrial calcium levels in cultured cardiac myocytes using a novel fluorescent indicator protein, GCaMP2-mt. *International Journal of Cardiology* 225–234 (2012).

286. Wu, P., Phillips, M. I., Bui, J. & Terwillinger, E. F. Adeno-Associated Virus Vector-Mediated Transgene Integration into Neurons and Other Nondividing Cell Targets. *Journal of Virology* 5919–5926 (1998).

287. Murlidharan, G., Samulski, R. J. & Asokan, A. Biology of adeno-associated viral vectors in the central nervous system. *Frontiers in Cellular Neuroscience* (2014).

288. Kotterman, M. A. & Schaffer, D. V. Engineering adeno-associated viruses for clinical gene therapy. *Nature Reviews Genetics* **15**, 445 (2014).

289. Clark, K. R. Recent advances in recombinant adeno-associated virus vector production. *Kidney International* **61**, S9–S15 (2002).

290. Hoyng, S. A., De Winter, F., Tannemaat, M. R. & Verhaagen, J. Gene therapy and peripheral nerve repair: a perspective. *Frontiers in Molecular Neuroscience* (2015).

291. Mason, M., Ehlert, E., Eggers, R. & Huseinovic, A. ComparisonofAAVserotypesforgenedeliverytodorsalroot ganglion neurons. *Mol. Ther.* 715–724 (2010).

292. Snyder, B., Gray, S., Quach, E. & Samulski, R. Comparison of adeno-associated viral vector serotypes for spinal cord and motor neuron gene delivery. *Hum. GeneTher* 1129–1135 (2011).

293. Kadulov, N., Brown, K., Walters, R. & Chiorini, J. Adeno-associated virus serotype 4 (AAV4) and AAV5 both require sialic acid binding for hemagglutination and efficient transduction but differ in sialic acid linkage specificity. *J. Virol.* 6884–6893 (2001).

294. Bell, C., Vandenberghe, L., Bell, L. & Van Vliet, K. The AAV9 receptor and its modification to improve in vivo lung gene transfer in mice. *J. Clin. Invest.* 2427–2435 (2011).

295. Ustione, A. & Piston, D. W. A simple introduction to multiphoton microscopy. *Journal ofMicroscopy* 221–226 (2011).

296. Tu, H. & Boppart, S. A. Coherent anti-Stokes Raman scattering microscopy: overcoming technical barriers for clinical translation. *J. Biophotonics* 9–22 (2014).

297. Williams, R., Piston, D. & Webb, W. Two-photon molecular excitation provides intrinsic 3-dimensional resolution for laser-based microscopy and microphotochemistry. *Faseb. J.* 804– 813 (1994).

298. Helmchen, F. & Denk, W. Deep tissue two-photonmicroscopy. *Nat. Methods* 932–940 (2005).

299. Kalies, S., Kuetemeyer, K. & Heisterkamp, A. Mechanisms of highorder photobleaching and its relationship to intracellular ablation. *Biomed. Opt. Express* 805–816 (2011).

300. Pegoraro, A., Stolow, A., Ridsdale, A., Moffatt, D. & Pezacki, J. *CARS Microscopy Made Simple*.

301. Sun, Y., Cheng, B., Dong, Y. & Zhang, Y. Time-Dependent Effects of Anesthetic Isoflurane on Reactive Oxygen Species Levels in HEK-293 Cells. *Brain Sci.* 311–320 (2014).

302. Hirata, N., Shim, Y. H., Pravdic, D. & Bienengraeber, M. Isoflurane differentially modulates mitochondrial reactive oxygen species production via forward versus reverse electron transport flow: Implications for preconditioning. *Anesthesiology* 531–540 (2011).

303. Morrison, B. M., Lee, Y. & Rothstein, J. Oligodendroglia: metabolic supporters of axons. *Trends in Cell Biology* 644–651 (2013).

Resumé en Français

Le système nerveux est composé de plusieurs types cellulaires qui interagissent entre eux pour conduire le potentiel d'action du corps cellulaire, le long de l'axone jusqu'aux synapses. Au niveau du système nerveux périphérique (SNP), les cellules de Schwann interagissent avec les neurones en s'enroulant autour l'axone et en créant une gaine de myéline. Cette gaine de myéline permet une conduction saltatoire rapide du potentiel d'action d'un petit espace non myélinisé au suivant, appelé nœud de Ranvier. De plus, les cellules de Schwann transportent du lactate vers le neurone qui l'utilise pour produire de l'énergie sous forme d'ATP via notamment les mitochondries. Cette production est primordiale car de nombreux processus cellulaires ont besoin d'ATP pour fonctionner dont la propagation de l'influx nerveux. Trois mécanismes sont impliqués dans la production d'ATP : la glycolyse dans le cytosol, le cycle de Krebs et la chaîne de transport d'électrons dans les mitochondries. Cependant, la production mitochondriale d'ATP génère également des dérivés réactifs de l'oxygène (DRO) à l'origine du stress oxydatif. Les DRO existent sous différentes formes avec des caractéristiques propres pouvant toutes endommager la cellule. Par exemple, l'ion superoxyde est très réactif donc il réagit extrêmement rapidement avec les molécules environnantes. A l'opposé, le péroxyde d'hydrogène est un DRO peu réactif pouvant diffuser sur de grandes distances et oxyder des cibles plus distales. Heureusement, les cellules sont équipées d'un système antioxydant composé d'un groupe d'enzymes antioxydantes qui transforment les DRO en eau. Malheureusement en cas de dysfonctionnement mitochondrial ou déséquilibre entre les DRO et antioxydants, des neuropathies peuvent se développer, comme la Sclérose Latérale Amyotrophique (SLA), la Sclérose En Plaques (SEP), les maladies d'Alzheimer et Parkinson. Dans le SNP, des neuropathies périphériques peuvent se développer en raison d'excès de DRO comme la maladie Charcot-Marie-Tooth (CMT).

Dans cette thèse, je propose un nouveau modèle détaillé de la production mitochondriale d'ATP et DRO *in vivo.* Je montre comment les cellules de Schwann utilisent l'effet Warburg, la transition métabolique depuis la phosphorylation oxydative vers la glycolyse aérobique, pour produire du lactate qui est ensuite transporté vers le neurone pour la production d'énergie. Je démontre également que sans l'effet Warburg des cellules de Schwann, le métabolisme neuronal est détérioré menant à la production diminuée d'ATP, des déficits neuronaux et des problèmes moteurs. Suite à l'activité nerveuse, la mitochondrie fabrique indépendemment de l'ATP mais aussi des DRO avec leurs dynamiques respectives. De plus, je montre que la physiologie mitochondriale est affectée par des les neuropathies. Chez les souris déficiente mitofusin2, un modèle pour CMT2A, le contact entre le réticulum endoplasmique et les mitochondries est diminué et s'accompagne d'un changement de la morphologie et fonction mitochondriale. D'autre part, la démyélinisation provoque un déficit de production d'ATP et de DRO, montrant une dissociation pathologique entre la production d'ATP et de DRO.

Pour obtenir ces résultats, des techniques d'imagerie avancées ont été utilisées pour observer les nerfs périphériques de souris transgéniques. Ces transgènes sont introduits par injection des vecteurs viraux qui induisent l'expression de sondes fluorescentes dans les cellules neuronales. Ces sondes fluorescentes sont détectées par microscopie multiphotonique. En plus du modèle de production d'ATP et DRO dans les nerfs périphériques, je présente un protocole de marquage du nerf sciatique par des vecteurs viraux.

Summary English

The nervous system consists of several cell types that interact with each other in order to conduct action potentials from the neuronal soma through axons to the synapse. In peripheral nerves, Schwann cells interact with neurons by wrapping around the axon and creating a myelin sheath. This myelin sheath allows for fast conduction of action potentials from node of Ranvier to node of Ranvier, which are small unmyelinated areas of the axon. In addition, Schwann cells transfer lactate to the neuron, which the axonal mitochondria use to produce energy in the form of ATP. This is necessary, because many cellular processes, such as the conduction of action potentials use ATP. The production of ATP involves three mechanisms: anaerobic glycolysis in the cytosol and the Kreb's cycle and electron transport chain within mitochondria. However, the production of ATP by mitochondria also results in the production of reactive oxygen species (ROS), which cause cell damage. ROS can be present in several different forms and these different forms have specific properties. For example, superoxide anions are highly reactive and subsequently react rapidly with the molecules in their environment. Hydrogen peroxide on the other hand is less reactive but hence can diffuse over longer distances and react with their targets more distally. Fortunately, the cell contains a competent antioxidant system, which can reduce ROS to water. When mitochondria malfunction or when the equilibrium between ROS and antioxidants becomes in disbalance, neuropathies can develop, such as amyotrophic lateral sclerosis (ALS), multiple sclerosis (MS), Alzheimer's disease or Parkinson's disease. In the PNS, peripheral neuropathies can develop such as Charcot-Marie-Tooth disease as a result from an excess of ROS.

In this thesis, I will provide an elaborate model for ATP and ROS production by axonal mitochondria *in vivo*. I will show how Schwann cells use the Warburg effect, the shift in metabolism from oxidative phosphorylation to anaerobic glycolysis, to produce lactate, which is then transported to the neuron for energy production. I also demonstrate that without the Warburg effect in Schwann cells neuronal metabolism would be impaired, leading to impaired ATP production, neuronal deficits and motor problems. Following action potential firing, not only ATP is produced by mitochondria, but also ROS, although with independent dynamics. In addition, I show that mitochondrial physiology is affected by several neuropathologies. In mitofusin2 deficient mice, a model for CMT2A, contact between the endoplasmic reticulum and mitochondria is impaired next to affected mitochondrial morphology and function. Also demyelination causes deficits in mitochondrial ATP and ROS production, showing a pathologic decoupling between ATP and ROS.

To obtain these results, advanced imaging techniques were used to image peripheral nerves of transgenic mice. These transgenes were introduced in mice via injection of viral vectors which induce expression of fluorescent probes in neuronal cells. These fluorescent probes were detected via multiphoton microscopy. Next to the model for ATP and ROS production in peripheral nerves, I provide a protocol for introducing viral vectors into mouse sciatic nerves.